Condition Monitoring and Fault Detection for Electrical Machines Using Advanced Sensing Techniques Based on Fibre Bragg Gratings

BELEMA PRINCE ALALIBO

A thesis submitted in partial fulfilment of the requirements for the degree of

Doctor of Philosophy

Aston University

December 2021

Aston University

Condition Monitoring and Fault Detection for Electrical Machines Using Advanced Sensing Techniques Based on Fibre Bragg Gratings

Belema Prince Alalibo

Doctor of Philosophy

December 2021

Abstract

Emerging techniques are being researched to expand the suite of condition monitoring solutions available for electric machines to adapt to a world of net zero carbon emissions. This research investigates the use of fibre bragg gratings (FBG) for condition monitoring and fault detection in three 2.2kW induction motors (IMs) using stray flux in a non-invasive manner. Optical fibre is immune to electromagnetic interference (EMI) which is an advantage but limits its direct use for magnetic field sensing. A magnetostrictive transducer, terfenol-D was bonded to FBG to form a composite sensor - FBG-T. The FBG-T was inserted into an acrylic tube - which is unaffected by magnetic field - and then positioned both axially and transversely relative to the machine's rotor shaft at the drive end (DE). The transverse position showed better repeatability and sensitivity over different operating frequencies. Temperature and magnetic flux calibrations of the FBG-T sensor gave sensitivities of 20.77 picometre per degree Celsius (pm/°C) and 19.38 picometre per micro-tesla (pm/μT) respectively. Various investigations were carried out at different operating frequencies and under three motor conditions viz: healthy, broken rotor and inter-turn short circuit conditions. Experimental results confirm that the FBG-T sensor reliably distinguished each of the three machine conditions using different orders of magnitudes of braggshifts. The FBG-T sensor accurately detected faults with the short circuit condition reaching braggshifts of hundreds of pm. Healthy and broken rotor conditions reached braggshifts in the low–to-mid-hundred and high-hundred pm range respectively. Fast Fourier Transform (FFT) analysis performed on the measured stray flux showed that not only its amplitude but also the harmonic component of its spectrum, affected the magnetostrictive behaviour of the magnetic dipoles of the terfenol-D transducer. This effect was translated into strain on the FBG. The investigation proved that FBG technology can reliably and accurately monitor the condition of the motors as well as detect faults in a non-intrusive manner.

Keywords

Terfenol-D, fibre bragg gratings, FBG-T, stray flux, braggshift, magnetostrictive, magnetic dipole, broken rotor, inter-turn short circuit, fault, transverse, FFT, spectral, induction motor.

Dedication

To Roseline Dawuta Alalibo…

My beloved mother.

Acknowledgement

I would like to thank the Almighty God for the strength to be able to complete this doctorate programme. My sincere thanks go to my supervisors Prof. Wenping Cao, Dr. Bing Ji and Dr Paul Harper for their patience, time, and expertise despite the constraints of resources available and the impact of the pandemic. Special thanks indeed to Prof. Wenping Cao for his unwavering support throughout the research and giving me the confidence to work independently whilst providing guidance and ensuring I remain in the right direction.

Special thanks to Dr. Adenowo Gbadebo, from Aston Institute of Photonics Technologies (AIPT) who helped and supported me through the first two years of my programme especially from the photonics viewpoint. I would like to thank my colleagues Dr. Muhannad Alshareef, Dr. Zheng Liu and Dr Lassi Aarniovuori for their encouragements and support and all my former colleagues in the Power Electronics, Machines and Power Systems (PEMPS) research group.

My deepest and heartfelt thanks go to my parents Late Ord. Golden Alalibo (of blessed memory) and my beloved mother, Mrs. Roseline Alalibo; my beloved wife Nyengibi and my lovely children Golden II and Elspeth. Without you all, it would have been impossible to complete my PhD.

Contents

Nomenclature

Alternating current	AC
Angle of incidence	θ_1
Angle of refraction	θ_2
Aston Institute for Photonics Technologies	AIPT
Average of the refractive index of the fibre core and the refractive index of the fibre cladding	η_{eff}
Bare fibre	BF
Bragg wavelength	λ_B
Broadband light source signal only	B(λ)
Broken rotor bar	BRB
Carbon Fibre Reinforced Polymer	CFRP
Change in	Δ
Change in temperature	ΔT
Critical angle	θ_c
Decibel	dB
Device-under-test	DUT
Direct current	DC
Drive end	DE
Dynamic Eccentricity	DE
Electromagnetic interference	EMI
Fast Fourier Transform	FFT
Finite Element Model	FEM
Fibre Bragg Grating	FBG
Fibre Bragg Grating with terfenol-D	FBG-T
Fibre optic sensing	FOS
Flux Spectral Analysis	FSA
Folding Flux Probe	FFProbe
Frequency	f
Giant magnetostrictive material	GMM
Hilbert Transform	HT
Hilbert-Huang Transform	HHT
Iron, Terbium, and Dysprosium	Fe, Tb and Dy
Induction Machine	IM
Inter-Turn Fault	ITF

Inter-Turn Short Circuit Fault	ITSF
kilo-volts amps reactive	kVAr
kilowatt	kW
Linear Discriminant Analysis	LDA
Longitudinal strain	ε_z
Long period grating	LPG
Long period grating with terfenol-D	LPG-T
Low Voltage Electric Machine	LVEM
micro-tesla	µT
millimetre	mm
milli-tesla	mT
Mixed Eccentricity	ME
Motor Current Spectral Analysis	MCSA
nanometre	nm
Naval Ordnance Laboratory	NOL
Normalised reflected FBG spectrum only	$C(\lambda)$
Open Loop Vector	OLV
Optical spectrum analyser	OSA
Parts per million	ppm
PEM	Power Electronics Module
Periodicity of grating	Λ
Permanent Magnet	PM
Permanent Magnet Synchronous Machine	PMSM
Photo-elastic coefficient	ρ_e
picometre	pm
Piecewise polynomial	pp
Polyetheretherketone	PEEK
Principal Component Analysis	PCA
Reflected broadband signal after introducing the FBG plus any noise	$A(\lambda)$
Refractive index	n
Reproducibility test	RT
Rotor resistance	Rr
Single mode fibre	SMF
Sensor-less Vector	SLV
Speed of light in air	c

Speed of light in a medium	v
Static Eccentricity	SE
Support Vector Machine	SVM
Synchronous Machine	SM
Tilted Fibre Bragg Grating	TFBG
Thermal expansion of silica	**α**
Thermo-optic coefficient	η
Unbalanced Magnetic Pull	UMP
Volt per Frequency	V/F
Variable speed drive/variable frequency drive	VSD/VFD
Vibration Spectral Analysis	VSA
Wavelength	λ
Wavelet Distribution	WD
Wigner Distribution Method	WDM
Wound Field Synchronous Machine	WFSM
Wound Rotor Induction Machine	WRIM

List of Figures

List of Table

Chapter 1

Introduction

Fibre Bragg Grating (FBG) is currently widely used in structural health, biomedical engineering and electric machines applications. This Chapter will highlight various FBG applications in engineering especially the body of work that has been done in the use of FBG for condition monitoring of electric machines. It will lay out the foundation for combining optical FBG technology with electrical machines in a non-invasive manner utilising stray flux and magnetostriction phenomenon for the subsequent chapters.

1.1 Overview

Electric machines are crucial for a wide range of domestic and industrial processes thus, human dependence on these machines for day-to-day activities continues to increase in a suggestively irreversible trend. Electric machines play pivotal roles in both domestic and industrial operations such as in refrigerators, washing machines, escalators, lifts, trains, aeroplanes and cars; as well as in power plants, petro-chemical and manufacturing plants, transport sector amongst others. As [1] asserts, electric motors are everywhere and efficient. Electric motor-driven systems consume about half of all global electricity accounting for about $565 billion each year for electricity costs and roughly 6,040 metric ton of CO_2 emissions [1]. According to the United States (US) Department of Energy, industrial motors account for 64% of the electricity consumed in the U.S industrial sector which is about 290 billion kilowatt hours (kWh) per year [2]. Of all the industrial motors in use globally, the polyphase IM is the most common type as at today, over 90% of which are the squirrel cage type [3]. Burgeoning demand for a reduction in global industrial carbon emissions due to concerns on climate change and global warming backed by the 2015 Paris Agreement [4], means that these electric machines continue playing crucial roles in achieving the desired target, especially in the areas of electric vehicles and renewable energy generation such as in wind farms.

Despite the very important role these electric machines play in our day to day existence, one of the biggest challenges which has persisted in many industrial operations is the susceptibility of these machines to unexpected breakdown due to the harsh and highly stressed environments [5] under which the machines are operated in order to provide the goods and services humans need. Most industrial plants run for 24 hours per day, 365 days per year, which means that these electrical machines are continuously in operation with minimal downtime for scheduled or routine maintenance. Unexpected machine failures and consequent downtimes thus, have serious operational and financial adverse impacts. The problems associated with unexpected disconnection of the electric motor include repair or replacement costs, stopping production processes with consequent economic losses, likely impact on the company's reputation, and customer dissatisfaction. According to [6], the economic losses of the process downtime arising from such unexpected machine failures, considerably exceeds the actual maintenance costs. To put into perspective, [7] opines that motor failures in an offshore oil plant can incur downtime losses of up to $25,000 per hour. Even for a single train service or flight cancellation, there are huge financial losses in addition to lots of disruptions. Based on Hewlett-Packard magazine report [8], about 1% of 200 billion dollars of the United States budget have been spent for servicing and maintenance of electric machines; with more than 70% of the aforementioned budget assigned to power plants and factories that lack fault diagnostic systems for their machines. Attempting to overcome these aforementioned issues continue to motivate the continuous evolution of maintenance strategies in parallel to the constant improvement in the design of the machines [6].

The key feature of online condition monitoring for machines is the early fault detection which requires continuous monitoring of specific signature(s) obtained from the machine while running. Many fault signature acquisition and detection techniques have been researched, each with its own pros and cons. In this research, Fibre Optic Sensing (FOS), particularly the use of FBG in electric machine fault detection and condition monitoring, is reviewed. Considerable amount of work has already been done in this research area and these are acknowledged in Chapter 2 of this thesis. Given the increasing role of wind turbines in renewable power generation in line with global efforts to achieve net zero carbon emissions, condition monitoring of not only electric machines but also other paraphernalia that are installed together becomes crucial. The use of FBG sensors in wind turbines was reported in [9]. It reports a distributed thermal monitoring scheme which has already been implemented for power electronic modules (PEMs) in wind turbine converters. Several other FBG applications are detailed in Chapter 2. The use of FBG for condition monitoring and sensing has been found to have far reaching research applications. Most recent FBG applications reported in various fields can be found in [10] – [25].

Hitherto, applications of FBG sensing for electric machines and drives condition monitoring are invasive in nature [9], [26]–[54]. Most are installed within stator slots or circumferentially around stator windings. The use of FBG sensor to measure magnetic field non-intrusively in electric machines has not been evaluated in reported papers. In situ flux monitoring in electric machines using FBG however, has been reported in [34], [51]. Non-intrusive monitoring will involve utilising external stray flux to determine an electric machine condition as well as detect faults. While non-intrusive FBG machine monitoring suggests obvious advantages compared to the intrusive option, it does pose some challenges too. Applications where other magnetic fields are present will introduce noise to the measured signal, thus can affect accuracy in such applications. Intrusive option also offers direct access to the main air gap flux when compared to the attenuated version obtained non-intrusively. Although the external stray flux is attenuated by the machine yoke, it is largely sufficient to be detected by optics given the order of magnitude of the broadband laser used for such sensors, typically in the nanometre (nm) range. FBG on its own is immune to electromagnetic field hence would require a transducer to convert the stray magnetic field into strain before the strain can be detected. Terfenol-D, a magnetostrictive alloy, is used to achieve this purpose where the FBG is bonded onto the alloy with the use of cyanoacrylate adhesive, to transfer the strain movement from the alloy to the FBG. The strain is then observed as a wavelength shift known as *Braggshift*.

In this research, the issue of the optimal positioning of the FBG-T sensor has been empirically addressed and results do agree with other reported observations in published papers. The experiments in this research have been conducted under various machine operating conditions. In this dissertation, two fault conditions have been investigated with various levels of severity: broken rotor bar (BRB) fault and inter-turn short circuit fault (ITSF). The research emulated both faults with details on how these faults were created provided in later chapters. Data obtained under faulty conditions were analysed and compared with measurements obtained under healthy condition. The FBG-T sensor showed distinct features for the various conditions despite the well-known large hysteresis behaviour of the terfenol-D alloy. Machines were also operated with intermittent ON/OFF periods to emulate presence and absence of magnetic field in order to further corroborate that these observations are only due to stray flux. Because of the impact of temperature on FBG sensors, all experiments have been conducted in a room with no air conditioning unit to keep the temperature relatively constant. This means experiments are all at mean room temperature and this was measured throughout to ensure external temperature did not affect the measurements.

1.2 Research Significance

The significance of this research work is that it investigates and provides empirical evidence that FBG technology can be used to measure electric machine stray flux in a non-invasive manner.

The research further proves the ability of the FBG sensor to discriminate between different electric machine conditions. Therefore, the research has laid the foundation for non-intrusive FBG magnetic field monitoring in electric machine applications, by providing research evidence that real time condition monitoring and fault detection of IMs can be realised.

1.3 Aim and Objectives

The aim of this research is to investigate whether a composite sensor made from terfenol-D bonded to FBG can utilise externally available stray flux (μT range) from an IM to monitor its condition and detect fault(s) in a non-intrusive manner. The objectives of this research are:

i. to undertake a review of the different faults that commonly occur in electric machines
ii. to undertake a review of the various techniques used to detect the faults that occur in electric machines and how they differ, with more focus on optical fibre techniques
iii. to fabricate a composite sensor which will be referred to as *'FBG-T sensor'* comprising FBG on a standard optical fibre, a magnetostrictive transducer, terfenol-D, and an adhesive as a strain transfer medium
iv. to investigate whether stray flux is detectable through magnetostriction of terfenol-D which can cause the straining of the FBG. This investigation is necessary because stray flux is usually attenuated by the machine yoke, hence it is usually of small amplitude
v. to empirically determine the optimal position of the FBG-T sensor when sensing stray flux from an IM as per (iv)
vi. to investigate whether the FBG-T sensor can be used for fault detection in electric machines

1.4 Key Achievements

The key achievements of this research are:

- A comprehensive review of various common fault types, their causes and fault detection techniques in electric machines is performed. Based on the current state of the art, optical sensors especially FBGs hitherto have only been applied intrusively in electric machine condition monitoring and fault detection research. Stray flux – in the μT range - is measured with FBG technology in this work, thus providing research evidence that the FBG-T sensor can reliably and accurately detect faults in real time electric machine operations. This is a proof-of-concept.
- Optimal sensor positioning being crucial to the overall performance of the entire condition monitoring technique had to be empirically determined. This is because there had been no previous work reported on FBG stray flux monitoring. It was determined with succinct empirical

results and observations that the transverse positioning of the FBG-T sensor just above the drive end of the IM relative to the rotor shaft axis provided the optimal location. This is in agreement with a similar work on FBG rotor flux monitoring in a permanent magnet (PM) machine recently reported in [51].

- ❖ This research experimentally showed that the FBG-T sensor can unambiguously detect the ITSF condition. This fault is one of the few serious machine conditions that can lead to fire and thermal damage if not detected and interrupted early. This research revealed that the FBG-T could use its pre-processed optical braggshift spectra and its post-processed time varying braggshift plots to detect the inter-turn fault condition reliably and accurately.
- ❖ This research showed that the magnitude of the stray flux was not solely responsible for braggshifts as expected based on FBG braggshift sensing theory. The research confirmed that, in agreement with published literature, the harmonic spectrum of the stray flux also affected how the magnetic dipoles of the magnetostrictive material responded. Both amplitude and frequency components of the stray flux thus, contributed to the micro-strains which were observed as braggshifts on the optical spectrum.
- ❖ Best Paper Award titled "Optical FBG-T Based Fault Detection Technique for EV Induction Machines" during the 2021 International Conference on Smart Transportation, Energy and Power

1.5 Thesis Layout

This thesis consists of six chapters and is outlined thus:

Chapter 1 provides an introduction of this work, its research significance, and outlines the aim and objectives as well as key achievements of the entire research.

Chapter 2 presents a detailed and critical review of common electric machines faults and the commonly used fault detection techniques with comparisons provided as part of the review. Optical fibre fault detection technique was particularly reviewed more in-depth as this work utilises one of the available optical techniques.

Chapter 3 describes the underpinning principle of FBGs and the various types available. It explains the phenomenon of magnetostriction and characteristics of terfenol-D, the magnetostrictive transducer used in this research. This chapter presents the step-by-step procedure on how the composite FBG-T sensor was put together and the methodology of the entire research including experimental test rig(s) set up, calibrations and optimal sensor positioning tests.

Chapter 4 demonstrates the use of the FBG-T sensor in monitoring and detecting the BRB fault condition. The chapter describes how the fault is emulated, how the data is collected and analysed. BRB fault condition was detected by comparing braggshifts obtained under this fault with those obtained under a healthy rotor condition. Magnitude of braggshifts for BRB reported were in the high tens of pm (nearer the 100pm mark) while magnitudes of braggshifts for healthy rotor were in the low tens of pm to mid-100pm mark. Fault detection was evident from the post-analysed data only, as the optical spectra for both BRB and healthy conditions were identical. The FBG-T successfully detected the BRB condition.

Chapter 5 demonstrates how FBG-T is used to monitor and detect an ITSF condition. It describes how the fault is emulated including safety incidents during the experiments, how data is collected and analysed. ITSF condition was detected by comparing braggshifts obtained under this fault with those obtained under a healthy rotor condition. Large magnitude of braggshifts were observed for the short circuit condition in the hundreds of pm range compared to magnitudes of braggshifts for healthy rotor which were in the low tens to mid-100pm mark. The optical spectra from short circuit conditions provided clear fault signature prior to numerical analysis of the data obtained from LabView. Post analysis of the numerical data was consistent too, confirming the large braggshifts due to the fault condition. This chapter also analyses fault severity between different fault types. The FBG-T accurately and reliably detect ITSF condition using stray flux in a non-intrusive manner.

Chapter 6 focuses on the effect of hysteresis on the performance of the FBG-T sensor via reproducibility tests (RTs). It concludes by highlighting the limitations of the sensor and proposes some recommendations for future work.

1.6 Chapter Summary

This chapter introduces the research study which focuses on the non-intrusive condition monitoring and fault detection of electrical machines using a composite sensor referred to as FBG-T and stray flux. The chapter covers the research significance, its aim and objectives and the key achievements of this research study. It finally provides an outline summarising the thesis content.

Chapter 2

Review of Electrical Machine Faults and Fault Detection Techniques

There is no single fault detection technique that can detect all machines faults that can occur during operation. Hitherto, a set of complementary fault detection techniques remains the best practice in industries around the world. To understand which techniques to combine for any given application is dependent on having sufficient knowledge of the various machine faults and their features. This Chapter will review common machine faults that occur during operation and the currently existing fault detection techniques. It will lay the foundation for optical fibre sensing technique and its applications.

2.1 Common Machine Faults – A Review

Electrical machines are broadly of two types in terms of operation: synchronous and asynchronous. In synchronous machines (SMs), the rotor (rotating part) and the stator (stationary part) operate at the same speed e.g., in permanent magnet synchronous machines (PMSM). Conversely in asynchronous machines, the rotor and the stator operate at slightly different speeds e.g., in IMs. The difference in speed is known as slip. Based on design, there are several designs by geometry with the conventional designs being axial and radial flux machines. In this research, the conventional radial flux geometry of squirrel cage type IMs will be used. Despite the reliability and lifetime expectation for majority of electric machine applications, four types of faults are considered most prevalent for the IM types: stator inter-turn faults, bearing failures, broken rotor bar/end-rings, and air gap eccentricity. A fifth common machine fault is demagnetisation, which is peculiar to machines that have permanent magnets as rotors such as PMSMs. It is widely believed that stator insulation failure is the incipient stage of stator inter-turn fault [5]. Critical components of IMs which are prone to the development of incipient faults are: stator and rotor windings, insulation, air-gap eccentricities, bearings, rotor bars, end rings and shaft [55]. In 2017, [56] reviewed 85 publications and observed that the machine failures distribution according to various surveys from 1985 to 2008 is as given in Table 2-1:

Table 2-1: Failures according to the engine part (%) [6]

Reference	[57]	[58]	[5]				[59]	[60]	[61]	[62]	[63]	[64]
			IEEE-IAS	**EPRI**	**Allianz**							
Bearings	41	69	44	41	13	40-50	44	51		40	40-50	42
Stator	23	21	26	36	66	28-43		26		38	30-40	31
Inter-turn short circuit							26					
Rotor	10		8	9	13	5-10				10		
BRBs/ end ring		7					8	5			5-10	9
Shaft/ coupling		3						2				
Unknown causes								10				
External causes								16				
Others	12		22	14	8	12	22		12			12

In 2016, [65] carried out a survey of the main centres for the repair of electrical machines in Valle del Cauca, Columbia where the failure distribution of about 500 electric motors with power ratings between 1-300 horse power (hp) were analysed for six months. It was observed during the survey that as a result of the experiences from manufacturers and repair centres as well as academic studies, [66]–[70] all agree that an approximate fault distribution based on percentage can be deduced as follows: bearing failures (45%), stator failures (35%), rotor failures (10%) and the remaining other failures (10%). In their reviews, [71] and [72] closely agreed with the above machine failure percentage distribution (Table 2-1) based on independent surveys carried out by Thorsen & Dalva et al. [73] similarly reports close failure percentage figures.

Table 2-2: Failure percentage for common machine faults

Fault Type	**Failure Percentage (%)**			
	[66]–[70]	[71]	[72]	[73]
Bearing Faults	45	40	52	41
Stator winding faults	35	38	24	37
Rotor faults	10	10	6	10
Miscellaneous faults	10	12	18	12

2.1.1 Stator Related Faults

Stator winding faults in addition to being the second most occurring faults as depicted in the table above, are one of the potentially harmful electrical faults in machines [55]; thus necessitating its detection at an early stage. Stator windings of IMs are often subjected to stresses caused by various factors which include thermal overload, mechanical vibrations, environmental and electrical stresses. Electrical stresses such as voltage spikes are typically caused by the increasing introduction for variable speed drives (VSDs) [74]. The two main locations for stator related faults are: the winding (turns) and the insulation. The various modes of stator related faults are: insulation fault, turn-to-turn fault, phase-to-phase and phase-to-earth faults.

2.1.1.1 Stator Winding Insulation Fault

The winding insulation fault is commonly observed due to thermal deterioration of the stator insulation material caused either by machine overload or presence of transient or steady state short circuit current. Abnormal thermal, mechanical, electrical or environmental stresses to stator windings also cause the stator winding insulations to undergo degradation. [75] described stator insulation failures as “a low-impedance path between conductors which are supposed to be insulated from each other, such as those of different turns, bars, or phases, or from phase to stator core”. Figure 2-1 shows an example of factors leading to stator winding insulation deterioration.

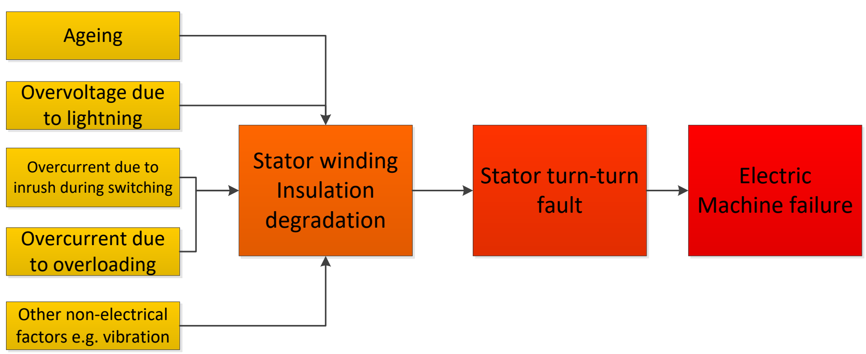

Figure 2-1: Factors leading to stator winding faults

The progressive flow of stator winding faults is that insulation degradation causes thermal hot spots in certain localised parts of the stator winding which if not attended to, will result in other severe forms of stator winding faults. There are available researched techniques for the condition monitoring and detection of various forms of partial discharge and hot spot monitoring. These techniques detect areas of localised weak points within the insulation in terms of dielectric strength prior to complete insulation breakdown. The presence of an incomplete insulation breakdown condition such as partial discharge, will not lead to sudden machine failure and disconnection. However, hot spot and stator thermal monitoring are critical for a prolonged machine lifetime as well as preventing insulation failures. Insulation failures if persistent, result in more severe stator winding faults which can lead to thermal damage of the machine including burnt windings [74]. As stated in [40], an industrially accepted rule of thumb is that for every 10°C rise in temperature above normal operating temperature, there is a corresponding reduction of insulation lifetime of about 50%. This is because of a significant reduction in the dielectric strength of the insulation.

2.1.1.2 Turn-to-Turn Winding Fault

The Turn-to-Turn fault, also called Inter-turn fault (ITF), is commonly observed between neighbour turns and causes higher than normal current flowing between adjacent turns of the stator winding. When the hot spots due to insulation degradation are not detected, they will progress into a complete breakdown of the insulation. This results in short-circuiting of the coils within 'the same' phase of the stator winding. Short circuit faults as expected, lead to huge amount of current flow thus increasing the I^2R heat dissipation. As highlighted by [74], the short circuit fault current will cause severe localised heating or hot spots resulting in the rapid spread of the fault to a larger section of the winding. Statistically, about 21% of total faults in electrical machines are specifically ITF in stator windings [58], [69], thus is considered as one of the most incident and destructive faults in electrical machines [76], [77]. Chapter 5 of this dissertation reports the detection of ITF using FBG-T sensing as part of this research.

2.1.1.3 Phase-to-Phase Winding fault

Another major type of fault is the phase-to-phase fault, which results from the breakdown of insulators separating coils between 'different phases'. For example, the ITF can lead to three phase load current unbalance and electrical asymmetry. The ITF if not detected and left unattended, will build up and progress into a further complete breakdown of surrounding insulations and even propagate the fault to coils or turns in the adjacent phase [78] leading to a phase-to-phase winding fault.

2.1.1.4 Phase-to-Earth Winding fault

The turn-to-turn fault due to stator winding insulation breakdown if allowed to progress, may lead to undesired circulating current flow between the faulty phase and some neutral terminal such as the stator core or body frame. Such fault is referred to as phase-to-earth winding fault. Large earth current flow can be caused by failure of insulation between phase winding and earth or between phases resulting in a possible irreversible damage to the machine core [78], [79]. It has been suggested that the transition between an ITF and complete insulation failure is not instantaneous [80], although there is no experimental data to indicate the time delay between the transition.

Figure2-2 shows the schematic representation of stator turn failure modes and some of the symptoms produced by stator winding turn fault as listed by [66], [74] include:

- ❖ Unbalanced phase voltages and line currents
- ❖ Increased torque pulsations
- ❖ Decreased average torque

- ❖ Noise and vibration
- ❖ Increased losses and reduction in efficiency
- ❖ Excessive heating

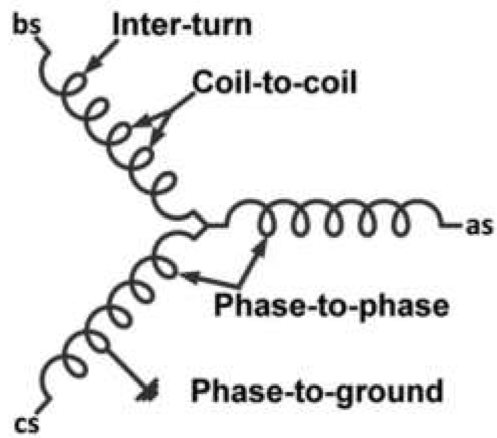

Figure2-2: Schematic representation of stator turn faults [81]

Table 2-3: Typical causes and effects of stator-related faults

Fault mode	Cause(s)	Effect(s)	Overall consequence
Winding insulation breakdown	• Over temperature • Ageing	• Hotspot • Partial discharge	• Inter-turn • inter-phase
Inter-turn	Insulation breakdown between turns of the same phase	• Overheating	• Inter-phase
Inter-phase	Insulation breakdown between turns of the different phases	• Overheating • Possible flashover	• Inter-phase • Risk of fire/explosion • Permanent damage to machine

2.1.2 Rotor Related Faults

Rotor faults are mainly caused by a combination of magnetic, thermal and mechanical stresses acting on the rotor. Because these stresses vary dynamically with loading and environmental conditions, such faults lead to rotor electrical asymmetry in machines without PM rotors [82] e.g., unbalanced voltages, currents or unbalanced magnetic pull (UMP). [82] submits that rotor asymmetries do not initially lead to machine failure. However, such phenomenon can have significant secondary effects such as increased losses, reduced efficiency and reduced machine reliability. The common forms of rotor failures are broken bar/end-ring failure, rotor field winding failure and permanent magnet demagnetisation.

2.1.2.1 Broken Rotor Bar (BRB)/End-ring

This fault occurs when there is a crack or breakage in one or more conductor bars (usually copper or aluminium) of the rotor or on the end-rings (shorting rings) which short all the bars together at both ends. This fault is common in machines having bars instead of windings such as squirrel cage IMs and damper bars in SMs as shown in Figure2-3. Although in the presence of a BRB, the machine will continue to run and more current distributed through the healthy bars. There will be increased stress and eventual shortening of the life of the healthy bars [83]. For bar breakages or cracks occurring in cast rotors, [71] believes they are almost impossible to repair and the current flow through the adjacent healthy increases up to 50% of rated current. In severe cases, the resulting increased stress can cause rotor bend and cause eccentricity fault. Torque is changed as a result of broken bar or end ring, and becomes detrimental to the smooth and safe operation of the machine [84]. Overheating, manufacturing defects and large thermo-mechanical stress have been reported by [85], [86] as the main causes of BRB faults. Other possible causes of BRBs/end-rings include [66]:

- Thermal expansion of bars due to thermal stress
- UMP and/or other magnetic stresses caused by electromagnetic forces
- Dynamic stresses due to shaft torques
- Environmental stresses due to contamination, abrasion of rotor material
- Mechanical stresses due to loosen laminations

Figure2-3: BRB on an industrial crane IM [87]

2.1.2.2 Rotor Field Winding Faults

In machines with rotor field windings such as SMs and wound rotor induction machines (WRIMs), similar stator windings faults as turn-to-turn faults do occur. As noticed by [88], there is no sufficient investigation on this fault as more focus has been on the stator winding faults. This is understandably because squirrel cage IMs which have become the principal drive in the industries and one of the most widely used machines [89] has rotor bars and end-rings instead of rotor windings. However, with the burgeoning demand for renewable energy systems, the WRIMs which are mainly used for wind turbine operations will require condition monitoring and early detection of rotor field winding faults. [90] rightly mentions that although a slight turn-to-turn rotor winding fault will not affect the normal operation of a generator unit; if undetected and persists will result in unwanted conditions such as significant increase in rotor current, rise in winding temperature, reactive power reduction, distortion in voltage waveform, vibration, and other associated mechanical faults. Possible causes of rotor winding faults include [90]: manufacturing faults; loose mounting of rotor end winding; and rotor winding insulation breakdown.

2.1.2.3 Permanent Magnet (PM) Faults

This fault is common specifically to PM machines where the permanent magnet can irreversibly lose its magnetisation known as demagnetisation. The major cause of demagnetisation is high temperature; and at a critical temperature called the Curie point, demagnetisation occurs. Other causes include corrosion, manufacturing cracks, mechanical, thermal and electrical stresses [91]. Rotor irreversible demagnetisation in PMSMs remains a persistent major concern since it adversely degrades machines performance characteristics [92] due to unbalanced rotor flux and consequent overload or increased vibrations [91]. After demagnetisation occurs in machines with high-grade magnets, the only way to recover its magnetic remanence is by removing the rotor magnet from the machines, and re-magnetising it using a large external field [92]. This consumes a lot of time for the re-magnetisation, significant machine downtime and other associated economic losses. This makes temperature a crucial signature in the condition monitoring of PMSMs i.e., both stator winding temperature and rotor PM temperature.

2.1.3 Bearing Failures

Bearing failures are common and account for more than 50% of generator faults in mega-watt range wind turbines [93] thus, require adequate monitoring to avoid costly down times. The major causes of these failures as highlighted by [5] are:

- ❖ Thermal stress – where heat from rotor shaft leading to high temperature gradually deteriorate the bearing lubrication, cause abnormal friction and eventual failure of the bearing
- ❖ Mechanical stress – where rotor shaft vibration can cause bearing failure especially with large machines having high output torque, improper bearing installation
- ❖ Electrical stress – where shaft voltage or common mode voltage in inverter output for drive-driven machines can induce current in the bearings, thus deteriorate bearing lubrication and consequently result in more intensive bearing wear or failure [94]

One of the most common ways of detecting bearing failure is an increased vibration and as [71] asserts, industrial systems heavily rely on vibration signals for bearing fault detection.

2.1.4 Air Gap Eccentricity

The air gap physically separates the stator from the rotor to prevent clash. It is the essence of the underpinning principle of electromagnetic induction discovered by Faraday with which practically electric machines work. In some machines such as SMs, the magnetic flux is set up by a separately excited field winding and not exclusively by mutual induction, hence the air gap can be larger. In other machines such as IMs, the air gap is smaller to minimise flux leakage and maximise mutual flux between stator and rotor. Regardless of the machine type, it is expected that the air gap stays uniformly distributed in a concentric manner. When a machine has a non-uniformly distributed air gap, it is referred to as eccentricity. [67] defines it simply as a condition in which the air gap between the stator and rotor is unequal. Some of the symptoms of eccentricity in IMs include [95], [96]:

- ❖ Unbalanced air gap flux density
- ❖ Increased torque and speed pulsation
- ❖ Reduction of average torque
- ❖ Increased losses and reduction of efficiency
- ❖ Increasing line current and voltage harmonics
- ❖ Excessive heating
- ❖ Increased vibration level

Larger eccentricity will result in an imbalance of the radial forces which can lead to the clashing of the stator and rotor resulting in a permanent damage [71]. It has been observed by [95], [97], [98] that the most prevalent bearing faults are those that lead to eccentricity. Three forms of eccentricity have been identified: static, dynamic, and mixed eccentricities. Figure2-4 illustrates the various forms of eccentricity as compared to a healthy air gap. As a summary, the healthy air gap has the axis of rotation coinciding with the axis of stator as well as the axis of rotor in a concentric manner. For static eccentricity (SE), the rotor is misaligned to a fixed position such that the air gap remains fixed during rotation, but it is non-uniform. It is such that the axis of rotation coincides with the rotor axis, but it is displaced from the stator axis [99]. In dynamic eccentricity (DE), the rotor is again misaligned but to varying positions away from the axis of rotation such that the air gap continuously changes during rotation. In other words, the centre of rotation overlaps with the centre of the stator, but there is a deviation of the centre of the rotor from the centre of the stator [100]. Mixed eccentricity (ME) is a condition in which both SE and DE exist together in the machine. The net or mixed effect is that there is no coincidence between the centre of rotation and the centre of stator; neither is there any coincidence between the centre of rotation and the centre of the rotor. In other words, all three centres are deviated from each other. Causes of eccentricity include:

- ❖ inaccurate positioning of the rotor or stator at the time of manufacturing and assembly of the machines
- ❖ oval design shape of the stator core or even wrong positioning or wearing of bearings [71], [99]
- ❖ inclination of rotor shaft (bent shaft), bearing wears, UMP, shaft misalignment or unbalanced torque [66], [101], [102]

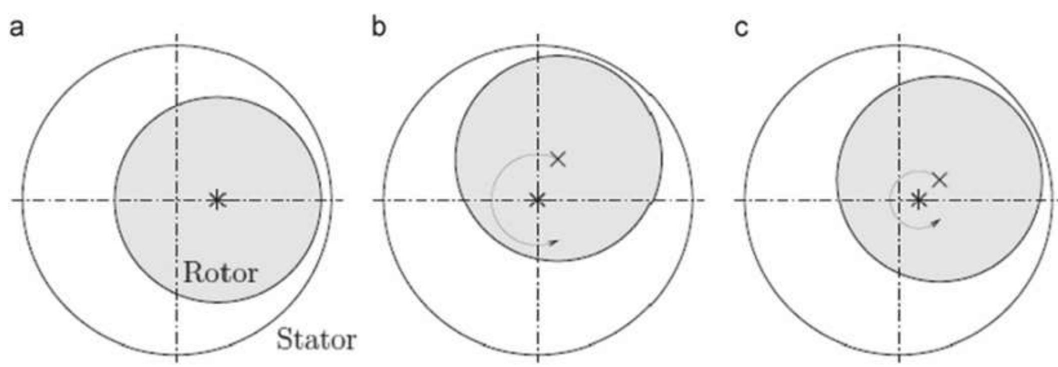

Figure2-4: Types of eccentricity a) SE b) DE and c) ME [103]

2.2. Fault Signature Extraction Techniques – A Review

Several fault signature extraction techniques exist in literature. These are mainly defined by the machine parameter being analysed to detect aberrations. Machine parameters mostly used include motor current, vibration, magnetic flux and temperature. These parameters are usually extracted via sensing or transduction, after which they are then subjected to some form of signal conditioning and processing for analysis. The commonest form of signal processing is the harmonic spectral analysis. Although several specific signal processing techniques are adopted to perform the harmonic analysis, the mostly used one is the FFT. The mostly used signature extraction techniques can be categorised into motor current spectral analysis (MCSA), vibration spectral analysis (VSA) and flux spectral analysis (FSA). Continuous temperature monitoring is often implemented alongside one or more of these techniques because heat is an inherent by-product of current flow (electrical) and friction for rotating parts (mechanical) of an electric motor. [104] presents a tabular summary of the various fault detection techniques and how they compare against each other in terms of pros and cons.

2.2.1 Motor Current Spectral Analysis (MCSA)

MCSA as a fault detection technique offers a non-intrusive condition monitoring advantage by directly measuring the motor current signal and then sending it to signal processor for spectral analysis. The reliability of this technique is dependent on both the absence of any EMI that may distort the current spectrum prior to analysis and the complexity of the signal processing stage. These two factors affect both the sensitivity and resolution of the sensors to be used for this technique. There are several different signal processing methods with pros and cons and various degrees of complexity, thus the MCSA often requires a high-resolution signal processor for high reliability on the technique. The presence of EMI and spectral noise could result in relatively low sensitivity due to attenuation or interference, thus a signal conditioner is usually required as part of the current pre-analysis stage. MCSA is also subject to false diagnosis when used with machines under low load variations [104]. Figure 2-5 and Figure 2-6 respectively show the block diagram and set up for the MCSA technique. MCSA is widely accepted and one of the most commonly used condition monitoring techniques in electric machines.

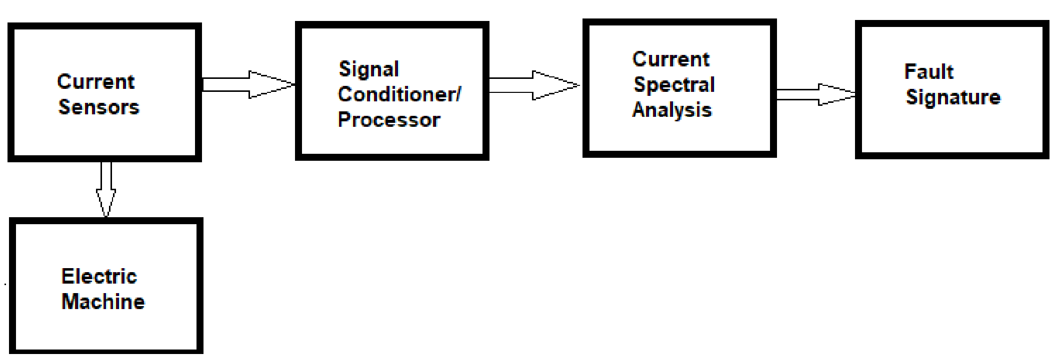

Figure 2-5: Block diagram of MCSA technique

Amongst several researchers [39], [89], [105]–[112] that adopted MCSA as the machine fault detection technique, FFT was most commonly used. It was used either as a stand-alone signal processing algorithm as in [108] and [111] or as a complementary algorithm in a set of more complex signal processing algorithm. There was no clear and persuasive evidence that there was a relationship between increased signal processing complexity with the overall accuracy of fault detection. [108] demonstrated that the motor instantaneous square current carries more information than the motor current alone, hence provides a better fault signature characteristic. [111] investigated the feasibility of bearing fault detection by spectral analysis of a single phase of the stator current of an IM using a correlation relationship between frequencies of vibration and current. To mitigate the effects of EMI and enhance the reliability of the spectral output, other researchers used the FFT in combination with other advanced signal processing techniques. Some of the signal processing methods other than FFT used as part of the MCSA technique amongst the reviewed literature include:

- ✓ Hilbert Transform (HT) - [89]
- ✓ Linear Discriminant Analysis (LDA) - [109]
- ✓ Hilbert-Huang Transform (HHT) - [112]
- ✓ Support Vector Machine (SVM) - [107], [110]
- ✓ Fuzzy SVM, Wavelet Decomposition (WD), Principal Component Analysis (PCA) - [55]
- ✓ Wigner Distribution method - [57]

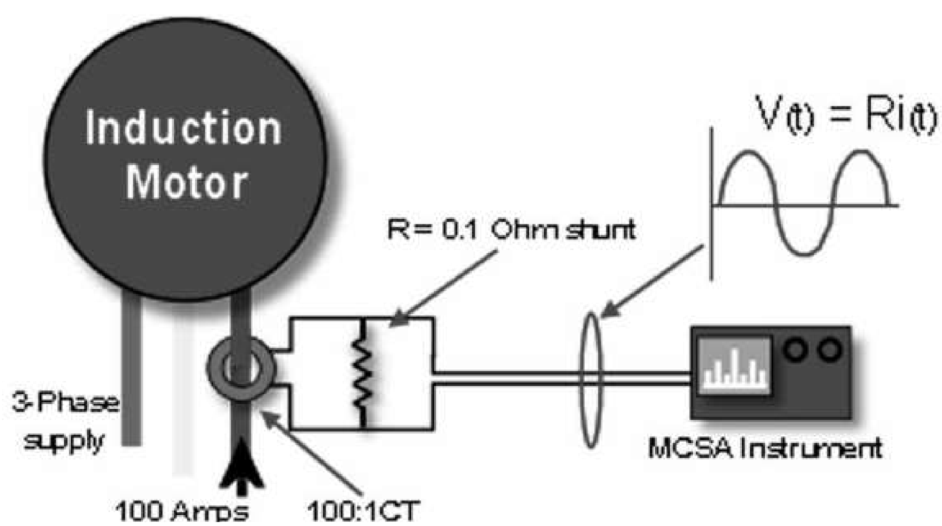

Figure 2-6: Basic MCSA instrumentation system [87]

2.2.2 Vibration Spectral Analysis (VSA)

Vibration has proved to be one of the oldest signatures for machine condition monitoring applications and depending on its amplitude, usually serves as the primary effect for fault detection. This is because both mechanical and electrical faults can cause increased vibration. Vibration detection technique is cost effective and can be utilised under varying frequency and load conditions without impacting significantly on its performance. It is particularly reliable for detecting eccentricity and bearing failures, however, the major challenge with this technique is the optimal positioning of the vibration sensors. Sensitivity of sensors used in the VSA technique is easily influenced by their positioning as there is no known theoretical method to decide where best to position these sensors. Oftentimes, VSA has no direct relation to a fault and could be a consequence of some distortion of a different machine parameter that is causing increased vibration. For example, a non-uniform magnetic field due to non-uniform air gap (eccentricity) or high levels of harmonic distortion can cause huge amounts of vibration. However, a damaged bearing can produce the same result. Although the overall consequence is unacceptable amplitudes of vibration, complementary detection methods would have to be used to further investigate the fault. The set up for the use of VSA is similar to that of MCSA with the difference being the sensor or transducer and the signal analyser (see Figure 2-7).

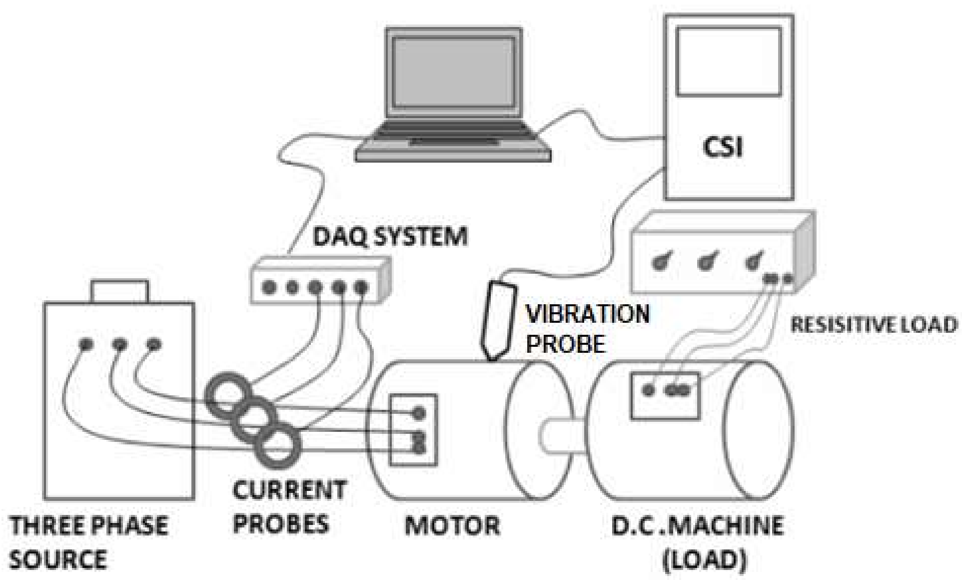

Figure 2-7: Typical VSA and MCSA instrumentation system [113]

VSA is widely used and is one of the few condition monitoring techniques that boasts of a long history of reliability in industrial machines diagnostics. One of the reasons for its common use is its capability in detecting the widest range of mechanical faults [114]. The eventual non-stationary nature of the captured vibration signal makes it unsuitable for accurate FFT analysis [115]–[117]. However, this is not unique to VSA as MCSA is also affected by non-stationary current signals. [117] further explained that in FFT, the major drawback is to go through numerous frequency lines to come to an analytical decision, and many times these lines are missed due to the non-stationary nature of the vibration signal. Thus, this spectral leakage makes the energy values at different frequencies inconsistent. Another interesting submission by [116] is that because vibration signal is non-stationary and its levels alter by variation of shaft speed, certain stationary signal analysers become unsuitable. Such stationary signal analysers typical implement algorithms such as FFT, power spectrum density (PSD), high order spectra, invasive FFT and autoregressive methods. Similar typical signal processing methods highlighted in MCSA are also used with VSA but there are other methods as well. A general limitation for the fault detection by VSA is the positioning of the transducers utilised for signature extraction, hence the need to use tri-axial accelerometers. Research has shown that some specific harmonic components are associated with certain fault types as shown in Table 2-4. Some harmonic components are present in different fault types which poses the challenge of fault discrimination to ascertain which fault is present in the machine.

Table 2-4: Harmonic component of vibration signal for fault diagnosis [116]

Type of fault	Harmonic component
Unbalance rotor and shaft	*fr, 2fr, 3fr, 4fr*
Short circuit	*nfr. Nfs*
Broken rotor bar	*fs, 2fs, 4fs*
Eccentricity	*2fs, 4fs, 6fs, ωm*

2.2.3 Flux Spectral Analysis (FSA)

The extraction of magnetic flux as a fault signature is common in both literature and industry as the machine flux is the interface between mechanical and electrical forces. This makes it straightforward to identify electrical and mechanical forces by flux monitoring [118]. Generally, the magnetic flux can be extracted from the internal or external part of the machine. The internal magnetic flux is the air gap flux generated between the rotor and the stator of the machine. The external flux is the stray flux which is oftentimes described as the remnant of the airgap flux that has been attenuated by the machine stator frame and made its way out of the machine. This technique requires magnetic flux sensors as well as signal processing units with similar set up to MCSA and VSA. In [54], a chart of various sensors and signal processing methods that have been used with FSA are highlighted. A major advantage of the use of external FSA over internal

FSA is its non-intrusive nature. Given the mechanical and electrical stresses electrical machines experience, this means that maintenance and replacement of sensor when required, will not result in machine downtime. However, external FSA relies on an attenuated copy of the main air gap flux. External FSA makes sensors susceptible to EMI unless extra precautionary measures are put in place to mitigate this. In addition to external flux sensors being susceptible to EMI, their correct location is a crucial factor in the reliability of the use of the stray flux signature. In a typical industrial environment, the presence of several machines in proximity will further enervate the stray fluxes as well as poses serious problems with flux-flux interaction as they are radiated into free space. Overall, depending on machine application, an assessment would be required to determine whether external FSA or internal FSA is more suitable.

2.2.3.1 Internal/Air Gap Flux Spectroscopy

For the main air gap flux analysis technique, the sensor is internally located usually around the stator winding as shown in Figure 2-8. Although conventional flux sensors have been used for a long time, there has been recent research utilising FBGs for internal flux measurement [51]. The use of fibre sensors for machine condition monitoring applications will be reviewed later in this chapter. Commonly used internal flux sensors include: search coils, hall effect sensors and folding flux probes (FFProbe).

Figure 2-8: Commercial air gap search coils installed on stator tooth for fault detection [119]

2.2.3.2 External/Stray Magnetic Flux Spectroscopy

[120] describes the stray flux as the image of the airgap flux density which is enervated by the stator laminations and the machine's external frame. To investigate the relationship between the main air gap flux and the stray flux, [121] proposed that the coefficient of attenuation is given by:

$$K = K^{sl}K^{ef}K^{air} \tag{2-1}$$

where $K^{sl}, K^{ef}, and\ K^{air}$ are the coefficients of the stator laminations, external frame and the external air respectively. The emergence of the stray flux is illustrated in Figure 2-9. [121] demonstrated both analytically and experimentally that regardless of the significant decrease in the amplitude of the stray flux relative to the main air gap flux, the frequency spectral content remains the same. This submission has been demonstrated by other researchers too.

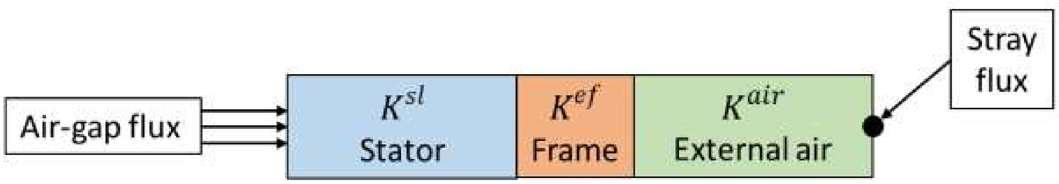

Figure 2-9: Decoupling of main air gap attenuation factors that give rise to stray flux [121]

Figure 2-10 shows the test rig for stray flux condition monitoring which is identical to the previous set up for internal FSA, MCSA and VSA with the sensing unit located outside the machine. This also means that it can be implemented easily on already commissioned and yet to be commissioned machines without disrupting machine operations. However, stray flux sensing is more susceptible to EMI as well as environmental factors implying a low signal-to-noise ratio despite already being attenuated by the machine cast frame. The reliability of the use of stray flux is yet to be widely accepted. In a typical industrial environment with several machines in close proximity, the use of stray flux may be unrealistic unless additional measures are put in place to screen such EMI from the stray flux sensors. Sensitivity and accuracy are thus critical in the successful implementation of external FSA.

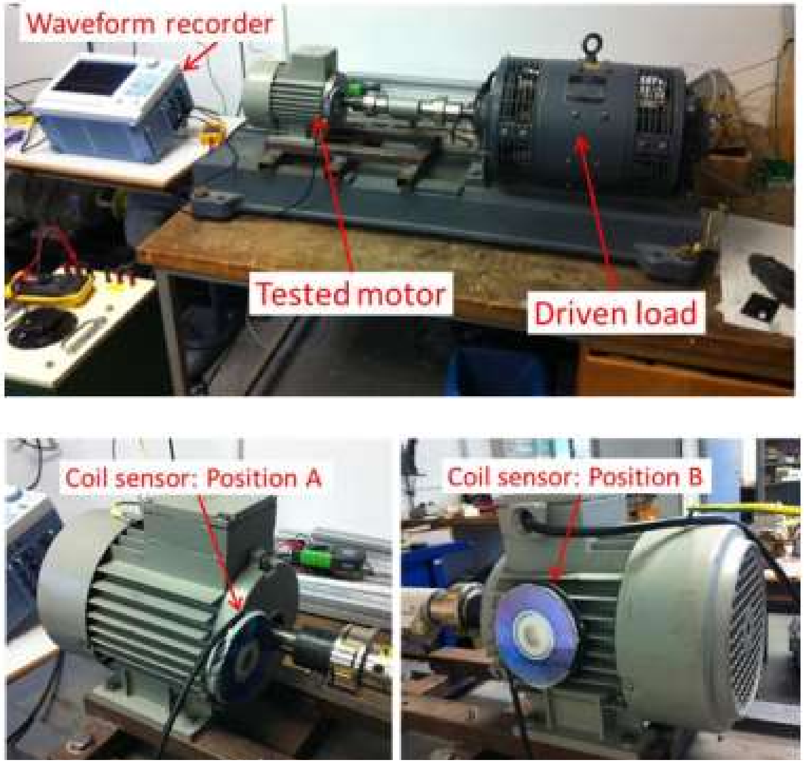

Figure 2-10: Test rigs used for stray flux monitoring [122]

Given that the amplitude of the stray flux is already small, any further noise interference can result in error in measurements. Aside the EMI issue, stray flux owing to its attenuated amplitude require flux sensors with very high sensitivity and resolution to be able to utilise the signal optimally for condition monitoring. Alternatively, slightly more sophisticated sensor with integrated signal conditioning sub-units for signal amplification and filtering can be used. However, this then compromises the cost effectiveness and simplicity flux sensors are generally known for. [104] corroborates that stray flux have low sensitivity for a small number of turns when used with wound field synchronous machine (WFSM) and requiring high resolution. Having been used for internal FSA, optical fibres are immune to EMI and can serve as an excellent complementary sensor for the use of stray flux for condition monitoring. However, as alluded by [104], "the feasibility of the use of FBG sensors to acquire low amplitude magnetic flux signals (e.g. stray fluxes) has not yet been demonstrated". Fibre optics works beyond the ultra-high frequency range which makes it an excellent candidate for ultra-small measurements provided the right transducer is available for such micro and nano range measurements. Some of the work done with conventional sensors around stray flux sensing can be found in [55], [78], [123]–[127].

A range of flux sensors have been used to acquire stray flux depending on different physical factors. These include: giant magnetostrictive resistance (GMR) sensor ([78]), magnetic antenna ([128]), hall probe ([129]), micro coil or flux probe ([120], [123]–[126]), and Rogowski coil ([130]). Table 2-5 compares some commonly used flux sensors and their range of applications.

Table 2-5: Properties of common magnetic field sensors [131]

	Hall with field concentrators (Sentron CSA-IVG)	AMR (Phillips KMZ 51, Honeywell,HMC1001)	AMR flipped+feedback (KMZ 51)	Fluxgate Billingsley TFM100
Linear range	5mT	300µT	300µT	100µT
Size	6mm	6mm	6mm	15mm
Linearity	0.1<0.2%	1%	40ppm	20ppm
Sensitivity TC	200ppm/K	600ppm/K	20ppm/K	20ppm/K
offset@25ºC	50µT	<10µT	<1µT	10nT
Offset TC	600nT/K	100nT/K	2nT/K	0.2nT/K
$noise_{RMS}$ (0.1-10Hz)	1µT	10nT(1nT)	10nT	<100pT
Perming, hysteresis	1µT	300nT	10nT	<1nT
BW	100kHz	100kHz	100Hz	3.5kHz
Power consumption	55mW	30mW	100mW	350mW

2.2.4 Temperature Condition Monitoring and Thermography

Temperature monitoring is critical to any electrical and mechanical system and is akin to vibration in terms of its causative nature as several faults can lead to a rise in temperature. Within an electric motor, the parts that regularly produce heat are the winding (copper winding I^2R losses), the core (eddy current I^2R and magnetic hysteresis losses) and shaft bearings (friction). Condition monitoring of temperature is reasonably universal and industry wide as excessive temperatures in machines can lead to fire and severe thermal damage if protection systems are not in place. Temperature sensors are known to be cost effective and reliable with very long service records. Their sensitivity and accuracy are generally not crucial for machine condition monitoring because temperature readings only serve as indicators and precursors for activating other remedial systems installed such as cooling systems or protection systems. A typical temperature condition monitoring system is shown in Figure 2-11.

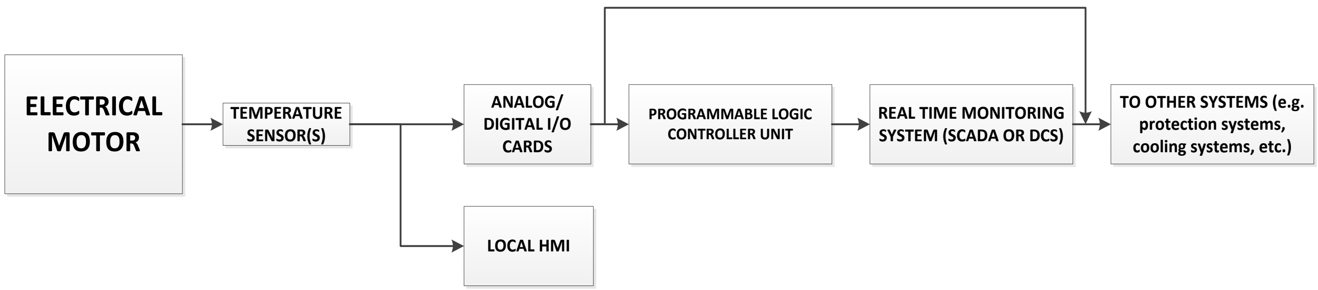

Figure 2-11: Block diagram for a typical temperature condition monitoring set up

Temperature as a signature is not an excellent fault detection tool but can provide an overall condition for the machine. According to [132] temperature monitoring method does not directly detect the fault or its cause, but rather provides an indication of a looming fault. Faulty (short circuit, bearing defects), transient (inrush phenomenon)) and even no-fault overload conditions can lead to rise in temperature in a machine. If temperature is solely used as a fault indicator, it can raise false alarms (issues of fault discrimination). Thus, temperature monitoring is usually a complementary condition monitoring technique to another available technique within the same application. Another option which is increasingly being implemented either as stand-alone or as a complementary technique with other detection techniques is the Infrared (IR) Thermography. In their opinion [133], [134] suggest that IR thermography could play an excellent role to diagnose certain failures or to complement the other techniques in order to make diagnostics conclusions. Temperature as a machine condition monitoring signature is incredibly important because excessive temperature give rise to the incipient stage of more severe faults. Hotspots due to insulation degradation and eventual breakdown start with excessive localised temperature. Very high temperatures can also lead to demagnetisation of permanent magnets in PMSMs. Three approaches to temperature monitoring as described by [135] are: local point temperature measurements using surface or embedded temperature detectors; thermal imaging or thermography; and distributed temperature measurements. Reported works which focused on temperature when used with other condition monitoring techniques can be found in [132] – [133], [136] – [146].

2.2.6 Fibre Optics Sensing (FOS) Technique

Although FOS has been around for a long time, research in this area is still very much active. This is the case in the electrical power industry where, in recent years ongoing research works have been reported on FOS applications in electric machine condition monitoring. The numerous advantages of using FOS according the industrial giant, ABB Ltd [147] include:

- high accuracy
- high bandwidth
- wide temperature range
- full digital processing
- uni- or bi-directional measurements possible
- analogue and digital outputs
- easy to install and does not require recalibration
- adaptable shape of sensing head
- small size and weight
- no magnetic centring necessary
- no magnetic overload problem
- immune to EMI
- electronics fully insulated from bus bars, hence it is possible to place them very close or even over high potential conductors without necessarily requiring electrical power at the sensor location[148]. This makes them also suitable for use in hazardous environments which usually require intrinsically safe instrumentation
- low power consumption

Other advantages highlighted by [148] include:

- easy maintenance
- chemically inert even against corrosion
- work over long distances
- several sensors can be multiplexed on the same fibre

The Faraday effect and Bragg sensing principles are the two commonly invoked principles in the power industry depending on the specific application be it sensing or fault detection. The mostly used fibre optic sensors are the FBGs whose principle will be explained in more details in the next chapter.

Commercially, ABB Ltd in 2013 introduced a fibre optic current sensor for monitoring the bus bar of a power distribution system based on the magneto-optic effect (also known as Faraday effect). This current sensor was in a single-ended optical fibre placed around the bus bar [149]. The fibre optic current sensor was reportedly able to measure uni-or bi-directional dc currents up to 500kA with an accuracy of 0.1 percent of the measured value. [35], [150]–[155] utilised FOS for fault detection in electrical machines. Table 2-6 summarises some fibre optic sensing application in electrical machines. Research relating to internal flux sensing in electric machine using FBG has also been reported in [34], [51], [156].

Table 2-6: Fibre optic applications in electrical machines

Authors [Ref]	Parameters monitored	Summary of research
Fabian et al [157]	Vibration, Temperature	Monitored the vibration response of the stator core of an IM as a function of the spatial modulation of the air gap flux
Mohammed et al [27], [38]	Temperature	Investigated the influence of FBG sensor packaging material on in situ hot spot monitoring based on the submission that bare sensing fibre is fragile and cannot be effectively inserted or wound into the coil architecture due to constraints imposed by the coil construction and the associated mechanical stress
Dreyer et al [45]	Temperature	Measured the temperature of stator bars inside a large electric generator using quasi-distributed FBG with the goal of testing the influence of the temperature on the FBG inside a package
Martelli et al [158]	Temperature	The surface temperature is measured using six FBG sensors evenly placed on the stator surface and embedded into the insulation material of a 175MW synchronous electric generator
Sousa et al [159]	Temperature	Temperature in the stator slots were monitored using two sets of FBG sensors in each fibre with a special encapsulation of the sensors to minimize mechanical disturbances in the fibre due to motor operation
Sun et al [160]	Multi parameter	Reviewed various industrial applications of FBG sensing
Sasic et al [161]	Vibration	Discussed suggestive requirements for selection of sensors and effect of temperature on modal test results
Theune et al [162]	Temperature	Reports on the first realisation of embedding FBG temperature sensors inside the stator bars and onto the leads of a 200MVA air cooled power generator including the sensor packaging requirements
Ping et al [163]	Temperature	Investigated the dynamic thermal response of standard single-mode optical fibre instrumented on a compact transformer core by using an optical frequency-domain reflectometry (OFDR) scheme

Johny et al [164]	Strain	This paper investigates the effect of FBG sensor positions on the reflected sensing signal, to optimise the sensor positioning plan for structural health monitoring of offshore structures
Marignetti et al [165]	Electric field	This paper reports proof-of-principle of an optical FBG operating as an electric field sensor and demonstrated that based on the electrostriction property of silica, by using a number of interferometric structures in the optical fibre, the component of the electric field E in the direction of the optical fibre can be measured in the points where the interferometric structures are placed

Of all the reviewed literature for FOS technique, most research works were based on the Bragg shifting principle or the use of FBG sensing, with the exception of four researchers who utilised other optical principles such as: Raman scattering Optical Time Domain Reflectometry (ROTDR) [166], Fabry-Perot Interferometry (FPI) [151], [167] and Optical Frequency Domain Reflectometry (OFDR) [163].

2.2.7 FBG in Electrical Machine Condition Monitoring

The typical test rig set up for FOS application in electrical machines is as shown in Figure 2-12. The set up comprises two machines, 30kW IM as generator and 15kW PMSM as a motor, a light source and interrogator (sometimes two separate devices), and a data acquisition system

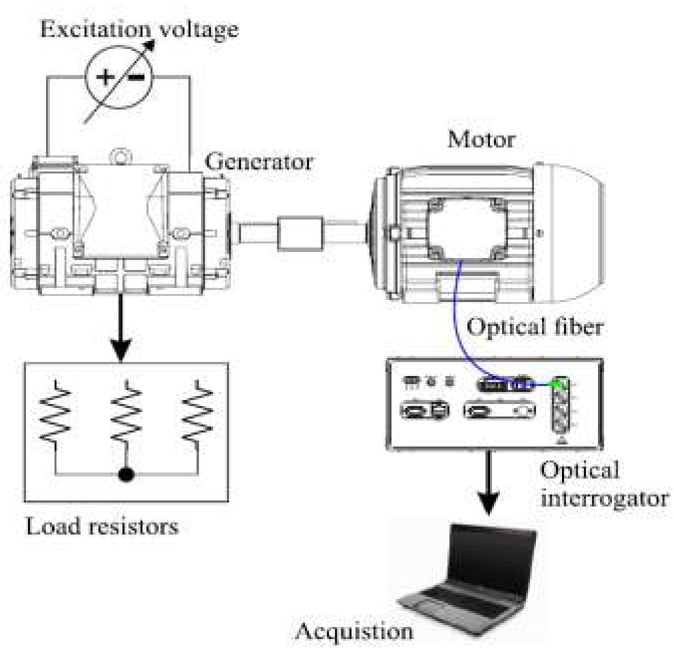

Figure 2-12: Typical FOS-machine experimental set up [155]

In [33] stator open winding fault detection was carried out by strain sensing of the stator frame of an IM using FBG as shown in Figure2-13. The presence of new frequency spikes in the faulty spectral output was used as a fault signature after processing of the acquired optical signal using FFT. It was reported that the fault effects were clearly visible at the integer multiples of the healthy reference frequencies.

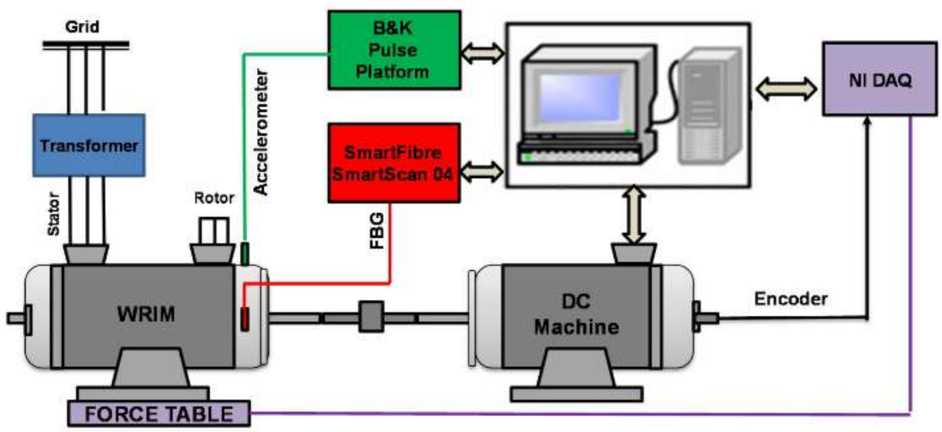

Figure2-13: FBG machine frame strain as faulty signature [33]

Bearing fault was similarly detected with FBG following FFT processing of the acquired strain signal in [168]. Here, it was reported that for vibration measurements at high frequencies, strain rather than temperature mostly affects the spectral shifts. [35] utilised FBG sensing to detect two faults viz: bearing and winding faults in a WRIM by vibration signature extraction and FFT processing of the acquired signature. Different severity levels of bearing defects were experimented through varying the diameter of a hole machined on the outer bearing race. Observations from the measured data, also revealed clearly visible fault induced frequency components on the vibration spectrum extracted by the fibre. Recently, [155], [169] investigated BRB and rotor eccentricity using the same strain extraction and FFT signal processing on a four pole, 220V motor. The BRB fault was emulated by drilling a hole on a rotor bar as shown in Figure2-14, while the eccentricity was emulated by attaching an unbalanced load to the rotor shaft. In [155], a set of four FBG sensors separated by 90° from each other were used and two regions of the stator strain frequency spectrum (near the rotational frequency, *fr* and near 2 x supply frequency, *2fs*) were the subject of focus. The amplitude of the fault frequencies were observed to be related to the fault severity and the number of broken bars. Under no-load condition, the slip, s was almost zero, thus, the BRB frequency overlapped with the two frequencies of focus (*fr* and *2fs*). This made it difficult to identify the fault at no load.

Figure2-14: Emulation of BRB in induction motor [170]

The temperature dynamic response of FBG to unbalanced power supply and losses which are of mechanical, electrical and magnetic nature, in a three-phase IM, was investigated in [154]. An encapsulation of the FBG sensor was done prior to fixing the sensor on the motor stator to reduce the influence of mechanical disturbances.

Multi parameter sensing was performed by [153], [171], [172] where mainly condition monitoring was carried out for electrical machines. Parameters such as torque, temperature, vibration and phase shifts (direction of rotation), speed and position were monitored in the related work by [171], [172]. For torque, two FBGs attached to the rotor shaft at ±45° with respect to its axis of rotation were used. The difference between both FBG reflection peak wavelengths gave a measure for torque whilst their mid-point gave an indication for temperature at that location. DC components of the transient signals were reportedly used for thermal and torque analysis, whereas the AC components were for vibrations and phase shifts analysis. Phase shifts between multiple FBGs was used to determine the rotor direction of rotation [171]. In a related work in [172], three fibres were installed on the machine stator, each having 12 FBGs. The FBGs were such that two fibres are placed between the stator teeth covering the entire length of the machine in alternate slot manner. The remaining one fibre was mounted circumferentially around the stator teeth. The two fibres routed along the stator winding were for thermal profiling, whereas the third fibre that was circumferentially mounted on the stator core was to measure vibration, rotor speed, rotor position, stator wave frequency and the spinning direction as shown in Figure2-15.

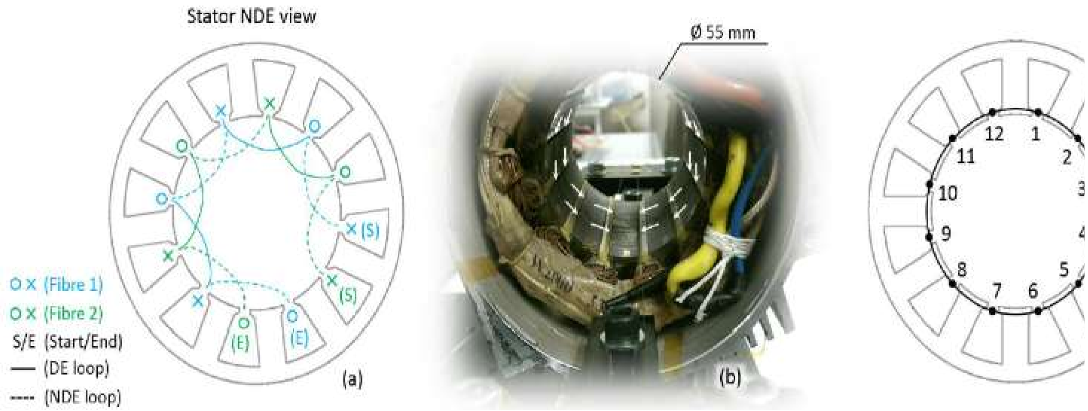

Figure2-15: FBG Positioning for multi-parameter sensing
a. Schematic and b. photograph of the distribution of 24 FBGs along the stator windings for their thermal profiling. (c) Schematic of the 12 circumferentially mounted FBGs [171]

[153] on the other hand, measured the dynamic strain on the main rotor bearings, pressure and temperature of the lubrication oil, distributed temperature through the motor stator windings and vibration of the motor housing. The sensing was for a subsea twin-screw pump and two fibres with nine FBGs on each fibre were used. Bearing fault was detected in the experiment. [173] in a separate work applied strain sensing to determine rotating speed. A centrifugal method was used to transform the rotating speed to the strain of FBG, with the FBG sensor distributed along the axial direction. An analytical method was used to show via an equation that the strain of the FBG is proportional to square of rotating speed. Based on the derived assumption, two FBG sensors were pasted on a Ā90mm shaft, with 40mm distance between the two pasting points. The initial results showed a large difference between both FBGs which was interpreted as due to pasting error, symmetry centre error and pre-tightening force error. With the addition of a sleeve type sensing structure to correct the discrepancy, the result was slightly improved.

Hot spot and thermal monitoring was investigated by [27], [29], [38], [42], [158], [159], [166], [174] in various electrical machines. [27], [29], [38] specifically investigated the influence of packaging on the FBG hot spot sensing performance using polyetheretherketon (PEEK) tubing as shown in Figure2-16. Their work assessed the attainable hot spot thermal monitoring performance of an FBG thermal sensor embedded in the structure of a current carrying random wound coil.

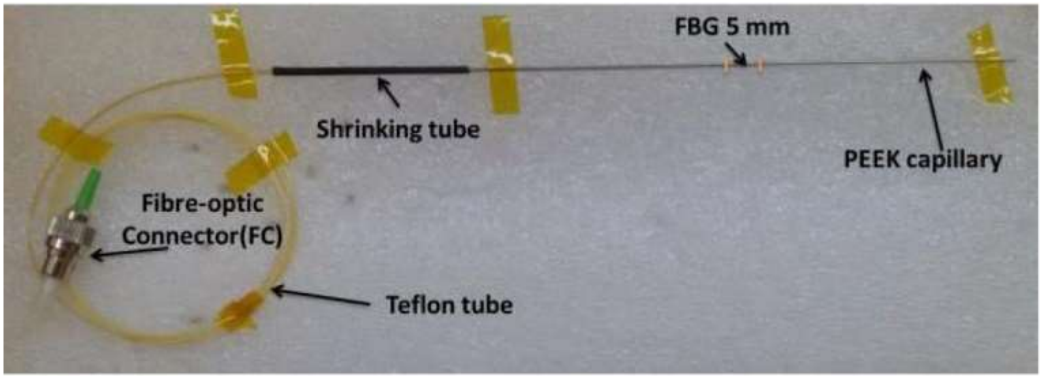

Figure2-16: FBG packaging using PEEK tubing [27]

[158] monitored the surface temperature of a high-power generator stator in operation at a hydroelectric power plant using FBGs. Six FBGs were evenly placed on the stator surface and embedded in the insulation material of a 175MW synchronous electric generator as shown in Figure2-17. Individual FBGs were packaged with stainless steel while the remaining fibre length was covered with high temperature teflon protective tubes. The FBGs were pre-calibrated using a peltier and a thermocouple. The generator was run for approximately 13 hours and all six sensors gave very similar thermal profiles with a maximum observed temperature difference between the sensors of less than 5^{o}C which is an indication of thermal equilibrium and mechanical balance.

Figure2-17: FBG sensor installation in the stator of a 175 MW electric generator [158]

In another work, [174] used five FBGs in conjunction with an optical rotating joint to perform temperature monitoring of the poles of a 310MVA, 56-pole, class B hydro generator which was experiencing outward insulation migration. The five FBG sensors were installed on four poles such that the four poles covered all possible positions between two consecutive spider arms of the machine. A single fibre was used to connect the FBG sensors to an optical rotating joint installed on the rotor axis to and from which light is transmitted as shown in Figure2-18. The use of the optical rotary joint offers a good option to varying the location of FBG sensors in situ an electric machine specifically on the rotor due to its rotating nature. Actual hotspot temperature measurements were obtained using FBG.

Figure2-18: FBG installation using a rotating optical joint [174]

[45], [46], [175] in separate but related investigations used FBGs to determine the quasi-distributed temperature measurements for stator bars in large generators. [175] embedded multiple FBGs packaged in stainless steel capillaries inside a stator to measure the temperature. [45] on the other hand, installed a multiplexed optical cable with 12 fibres around the circumference of the stator of a 370MVA generator. This was to investigate the influence of temperature on the FBGs when inserted in a package. Each of the 12 fibres had three FBGs to achieve distributed sensing as well as robustness with the packaging. Results revealed a steady state temperature difference between the FBGs of less than 3°C. The difference was due to the temperature gradients inside the box where the sensors were placed during the experiment. [46] investigated the simultaneous sensing of temperature and vibration using the same 370MVA generator. In the sensor, each FBG measured vibration and temperature independently. Three multiplexed FBGs were installed into six different winding slots to sense the stator bars, thus giving six transducers. The FBGs were encapsulated into a jelly tube and in turn protected with a semi-conductive package before installing them between the stator top and bottom bars. The generator was run experimentally at 60Hz for 23 hours with all FBGs detecting mechanical vibration at 2Hz and electromagnetic vibration at 120Hz. The machine experienced a shutdown due to failure during the test and all the FBGs were able to measure the temperature as well as vibration changes caused by the machine shutdown.

[165] reported a proof-of-principle where FBG was used as an electric field sensor. A prototype of voltage sensor based on an FBG was designed and tested with maximum reflectivity at 1577.5 nm. The application of a strong electric field caused a small variation of the optical path length of the waveguide due to electrostriction and thus, perturbed the grating peak reflectivity wavelength. The FBG sensor response yielded a signal at twice the original oscillation frequency showing an approximate quadratic dependence on the field amplitude. In [34], [37] a composite FBG/Terfenol-D sensor was used to sense main air gap flux in PM machines. The focus in [34] was to improve the understanding the impact of the positioning of the composite in-situ sensor when exposed to magnetic excitation. Monitoring the health of rotor magnets in PM machines through in-situ observation of the air-gap magnetic flux density was the focus in [37]. The FBG/Terfenol-D sensor was positioned in situ stator slots both axially aligned with, and perpendicular to the rotor axes of anisotropy of a PM motor as shown in Figure2-19.

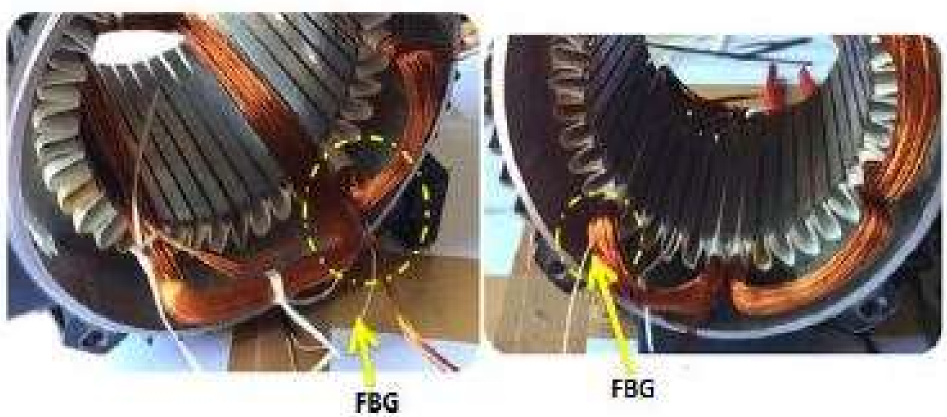

Figure2-19: Embedded FBG in stator slots of electric machines [37]

It was observed that whilst there was reduced sensor sensitivity of about 85% in the perpendicular axis compared to axial axis, diagnostic information on observed flux distribution were retained in both positions. Signal levels in both positions were also sufficient and usable for condition monitoring purposes. Demagnetisation of rotor was experimentally detected with varying degree of severity in [37]. FBG thermal sensing was recently reported in [26], [36], [43], [44], [176] with the first four works utilising FBG inherent multiplexing sensing capability. Distributed thermal sensing system for stator winding internal thermal condition monitoring in operating low voltage electric machines (LVEMs) was carried out in [26], [36], [43], [176]. A feasibility study on simultaneous extraction of thermal and mechanical information on machine bearings condition monitoring from the same optical sensing head was performed in [44]. By calibrating the FBG sensor behaviour under exclusively thermal excitation conditions, the differentiation of in-service signatures arising from thermal excitation from those produced by mechanical excitation was achieved [44]. Thus, the FBG sensor offered an advantage of being simultaneously utilised as both a thermal and mechanical sensor with a single in-situ sensing head. In other works, [26], [36], [43], [176] installed an array of FBGs (two per phase) on a rewound three phase IM. The FBGs were installed in a circumferential spatial distribution pattern to facilitate thermal monitoring of multiple hot spots due to open and short circuit faults on the stator winding. PEEK capillary and teflon tube were used as covering for the multiplexed fibre for protective purposes due to its brittleness. Results demonstrated that the multiplexed sensor array was effective in providing circumferential peak temperature distribution of the stator windings in operating machines, under normal and abnormal operating conditions.

The potential for using FBG strain sensing for health monitoring of an electric machine shaft and recognise shaft misalignment condition in generator drivetrains has been reported in [40]. FBG strain gauges were non-invasively installed on the test machine frame in axial, radial and circumferential orientation. The installation was done by bonding the respective sensing head to the surface of the frame drive-end cap using Kapton polyamide tape. It was reported that no observable detrimental effect due to thermo-mechanical cross sensitivity was identified when detecting angular misalignment. The three different orientation frame strain FBG measurements also revealed lower sensitivity for the FBG sensors that were radially placed in comparison to the axial and circumferential FBGs.

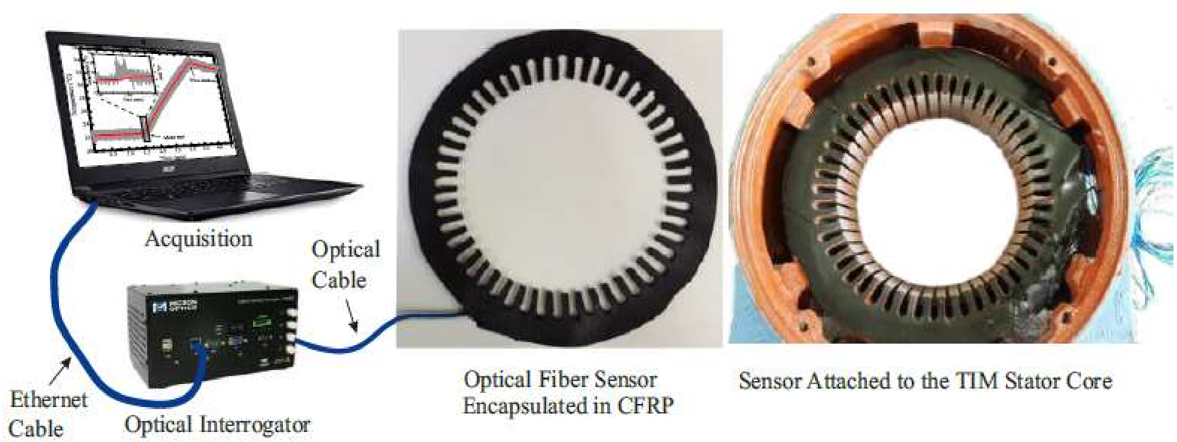

Figure2-20: Installing FBG in carbon fibre reinforced polymer [177]

Strain and temperature measurements in the stator of three phase IM were carried out using six FBGs which were integrated into a carbon fibre reinforced polymer (CFRP) encapsulation (see

Figure2-20). The encapsulation was said to have appropriate mechanical energy transfer to measure dynamic strain and temperature. Tests were performed with new healthy and defective bearings on a three phase IM operating at full load. Results showed that the main peaks of frequency caused by strain observed coincided with the electrical supply frequency (60 Hz) and mechanical bearing forces (30 Hz). Harmonic components at 120Hz, 180Hz and 240Hz were also present. For the damaged bearings frequencies of 89.8Hz, 116.5Hz, 146.4Hz, and 149.7Hz were identified.

2.3 Chapter Summary

This chapter has discussed the common types of faults that occur in electrical machines and the commonly used techniques in detecting them. The chapter has thoroughly reviewed current research in the use of FBG sensors in electrical machines applications.

Chapter 3

FBG as Electric Machine Sensors - Methodology

FBGs continue to find applications as electric machine sensors in the area of condition monitoring and fault detection. This chapter explains the underpinning principle of FBG and provides a step-by-step explanation of the methodology used in the non-invasive use of FBG for IM condition monitoring. It will lay out the foundation for broken rotor and inter-turn fault detection using FBG-T sensing technique for the subsequent chapters.

3.1 Basic Principle of FBG

One of the most commonly used optical fibre sensors for strain and temperature measurements is the FBG technology, thanks to its ease of manufacture as well as its relatively strong signal reflectivity [148] upon which its sensing principle depends. Light is known to travel in a straight line in air at an approximately constant speed, c = 3 x 10^8 metre per second (m/s). However, when it travels through a different medium it bends due to refraction, because air has a different refractive index from the medium through which the light now travels (Figure 3-1). Although the frequency of the light wave does not change, its wavelength changes [178]. The relationships between its speed in air (c), its speed in a different medium (v), the refractive index of the medium (n), its wavelength (λ) and its frequency (f) are given by:

$$c = f\lambda \tag{3-1}$$

$$n = \frac{c}{v} \tag{3-2}$$

Snell's law relates the angle of incidence θ_1, the angle of refraction θ_2, the refractive indices of the two mediums involved during the light travel n_1 and n_2 respectively, and the light's wavelengths in both mediums λ_1 and λ_2 as:

$$\frac{n_1}{n_2} = \frac{\lambda_2}{\lambda_1} = \frac{sin\theta_2}{sin\theta_1} \tag{3-3}$$

In order for some light to be reflected (bounce back away from the new medium) then the angle of incidence must equal the angle of refraction i.e., $\theta_1 = \theta_2$. The reflection of light at the interface between two different media is commonly known as Fresnel's reflection effect. According to [178], the refracted angle tends to get smaller than the incident angle when light is travelling from a fast medium to a slow one (for example, air to water). However, for the converse light travel (water to air), the incident angle tends to get larger but it cannot exceed 90° while remaining in the new medium. Hence this incident angle constraint suggests that the largest incident angle for refraction occurs when $n_2 < n_1$. However, beyond a certain incident angle known as critical angle, θ_c, provided $n_2 < n_1$ still exists, there will be no refraction at all. Instead, the light wave will be totally reflected away from the new medium through which the light was intended to travel. This is called total internal reflection which is the principle utilised by optical fibres [178].

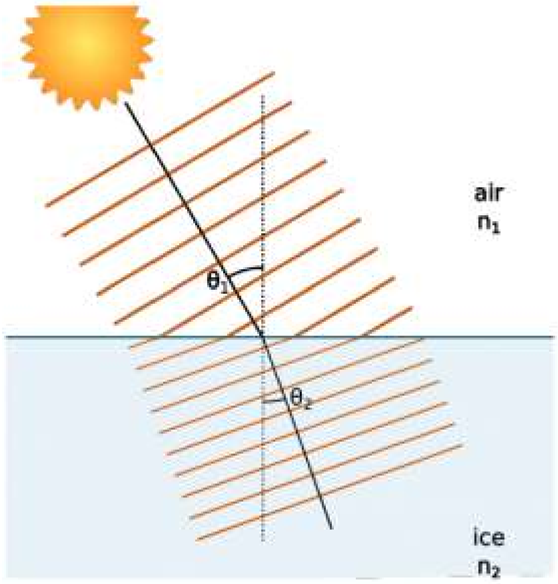

Figure 3-1: Basic concept of refraction of light [178]

Total internal reflection phenomenon reveals the possibility of confining light travel to a material with higher refractive index but not a lower one (i.e.$n_2 < n_1$). In a typical optical fibre silica cable, its core with a higher refractive index, n_1 is surrounded by a cladding whose refractive index, n_2 is only about 1% lower than that of the core. This is to satisfy the condition for total internal reflection [178]. For example, the core could have $n_1 \approx 1.4475$ and the cladding $n_2 = 1.444$ and provided the fibre cable is not excessively bent, the light will just bounce around in the cable with minimal loss [178]. When the light which is guided along the fibre core comes in contact with the inscription of the gratings, it is weakly reflected by each grating plane by Fresnel effect [148]. Figure 3-2 shows an incident radiation being reflected by the lattice of a crystal by Fresnel effect. Depending on incident angle and the reflected light from each grating plane, the light wave then recombines with other reflections in the backward direction in either a constructive or destructive interference pattern. The nature of interference of the resultant light wave, be it constructive or destructive is also dependent on whether the wavelength of the incoming light satisfies Bragg's law given by [148]:

$$2d\ sin\theta = \eta\lambda \tag{3-4}$$

According to Bragg's law, for constructive interference leading to higher peak(s) in the resultant wave, then η should be an integer; otherwise, destructive interference will occur leading to zero or a small amplitude in the resultant wave. With the light's incident angle θ = 90° and d, the distance between peaks of the interference pattern, then for vacuum with refractive index, $\eta = 1$; $\lambda = 2d$ is the approximate wavelength of the reflection peak which means that the fibre reflects part of the incoming spectrum [148].

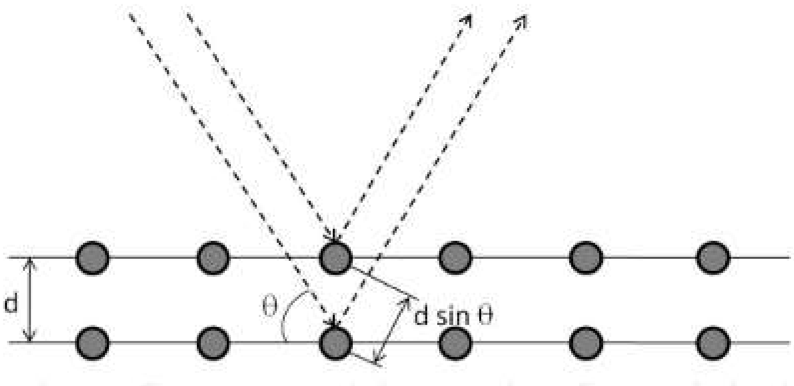

Figure 3-2: An incident radiation is reflected by the lattice structure of a crystal [148]

For silica material used to make optical fibre, the distance travelled by light, d is affected by the material's refractive index, η, thus equation (3.4) can be adapted for silica as:

$$2\eta_{eff}\Lambda = \lambda_B \tag{3-5}$$

where λ_B is the Bragg wavelength, η_{eff} is the effective refractive index of the fibre and Λ is the periodicity of the grating [148]. The η_{eff} is determined by the average of the refractive index of the fibre core and the refractive index of the fibre cladding. From equation (3.5), it is possible to change the Bragg wavelength also known as 'Bragg Shift' by either varying the fibre's effective refractive index or the grating periodicity or both. This is the fundamental principle of the FBG sensing. According to [148], by designing the proper interface, desired measurement can be made to impose some external force or disturbance on the grating which will result in a braggshift proportional to the perturbation applied. This makes the FBG useful as a sensor in a wide range of parameter measurements including temperature, vibration, pressure, and displacement.

Longitudinal deformation and temperature variation are two forms of perturbations that have been observed to change both η_{eff} and Λ [148]. Longitudinal deformation and temperature result in photo-elastic and thermo-optic effects respectively. This is where the change in the optical behaviour of the gratings due to their effective refractive index (η_{eff}), is proportional to the amount of strain and temperature difference applied to the fibre respectively. Longitudinal deformation and temperature also result in increase in the grating pitch and thermal expansion respectively, which affect the periodicity of the fibre gratings (Λ). The effect of temperature can be incorporated into equation (3.5) by differentiating λ_B with respect to temperature using product rule yields as follows [148]:

$$\frac{\Delta\lambda_B}{\Delta T} = 2\eta_{eff}\frac{\partial\Lambda}{\partial T} + 2\Lambda\frac{\partial\,\eta_{eff}}{\partial T} \tag{3-6}$$

If we substitute (3.5) into (3.6) for both expressions on the right-hand side of (3)

$$\frac{\Delta\lambda_B}{\Delta T} = \lambda_B\,\frac{\partial\Lambda}{\partial T}\frac{1}{\Lambda} + \lambda_B\frac{1}{\eta_{eff}}\frac{\partial\,\eta_{eff}}{\partial T} \tag{3-7}$$

Rearranging (3.7) we get

$$\frac{\Delta\lambda_B}{\lambda_B} = \frac{1}{\Lambda}\frac{\partial\Lambda}{\partial T}\Delta T + \frac{1}{\eta_{eff}}\frac{\partial\,\eta_{eff}}{\partial T}\Delta T \tag{3-8}$$

which can be rewritten simply as

$$\frac{\Delta\lambda_B}{\lambda_B} = (\alpha + \eta)\Delta T \tag{3-9}$$

The first term represents the thermal expansion of silica (**α**) while the second term represents the thermo-optic coefficient (η).

Similarly, the effect of longitudinal deformation or simply referred to as strain can be incorporated into equation (3.5) by differentiating λ_B with respect to length using product rule as follows [148]:

$$\frac{\Delta\lambda_B}{\Delta L} = 2\eta_{eff}\frac{\partial\Lambda}{\partial L} + 2\Lambda\frac{\partial\,\eta_{eff}}{\partial L} \tag{3-10}$$

If we substitute (3.5) into (3.10) for both expressions on the right-hand side of (3.10)

$$\frac{\Delta\lambda_B}{\Delta L} = \lambda_B\,\frac{\partial\Lambda}{\partial L}\frac{1}{\Lambda} + \lambda_B\frac{1}{\eta_{eff}}\frac{\partial\,\eta_{eff}}{\partial L} \tag{3-11}$$

Rearranging (3.11) we get

$$\frac{\Delta\lambda_B}{\lambda_B} = \frac{1}{\Lambda}\frac{\partial\Lambda}{\partial T}\Delta L + \frac{1}{\eta_{eff}}\frac{\partial\,\eta_{eff}}{\partial T}\Delta L \quad (3\text{-}12)$$

The first term on the right-hand side of (3.12) represent the strain of the grating period due to fibre extension while the second term is the photo-elastic coefficient (ρ_e) due to change in refractive index with strain. In optical fibre, both terms produce opposite effects when strain is applied to the fibre. This is such that while the distance between gratings tends to increase, thus increasing the Bragg wavelength, the photo-elastic effect results in a decrease in the effective refractive index. This is due to decrease in the density of the fibre (from cladding to core), thus decreasing the Bragg wavelength [148]. Hence in simplifying equation (3.12), second term carries a negative sign as follows:

$$\frac{\Delta\lambda_B}{\lambda_B} = (1 - \rho_e)\varepsilon_z \quad (3\text{-}13)$$

where ε_z is the longitudinal strain of the grating.

Therefore, the sensitivity of FBG to strain and temperature can be represented by combining (3.9) and (3.13) as follows:

$$\frac{\Delta\lambda_B}{\lambda_B} = (1 - \rho_e)\varepsilon_z + (\alpha + \eta)\Delta T \quad (3\text{-}14)$$

Theoretically, for the F-SM1500-4.2/125 single mode, all glass, highly bend-insensitive and photosensitive fibre used in this research @ 1550.1nm wavelength has:

$$\rho_e = 0.22, \alpha = 0.55\ x10^{-6}/^oC, and\ \eta = 8.6\ x\ 10^{-6}/^oC$$

Thus, sensitivities of the FBG fabricated on this fibre for temperature and strain will be:

$$\frac{\Delta\lambda_B}{\Delta T} = 14.18\ pm/^oC\ \ and\ \ \frac{\Delta\lambda_B}{\Delta\varepsilon} = 1.209\ pm/\mu\varepsilon$$

Optical fibre technology is known for low cost, although its interrogator is still currently expensive. Signal processing is not complex using the FBG technology and the option for multiparameter sensing which utilises multiplexing also available with FBG technology. The pyrophoric nature of the terfenol-D alloy means that the FBG-T should be adequately encapsulated to avoid self-combustion. Although self-combustion is rare, this can be easily avoided. Compared to the other techniques, FBG technology utilising a magnetostrictive transducer such as terfenol-D, can only be used in applications where the environment is void of unwanted magnetic fields. This is to avoid magnetostriction caused by noisy magnetic fields to interfere with the sensor reading. For example, in industrial areas where several large electric motors are running side by side, with each motor having its own stray flux. In such applications, each motor has to operate within a controlled enclosure such as a Faraday cage, so that only the stray flux of the machine being monitored reaches the sensor. Otherwise, the FBG-T sensor would be more appropriate for stand-alone electric machine applications.

3.1.1 Faraday Effect Principle

An alternative to the use of FBG for sensing applications is the Faraday's magneto-optic effect. In 1845, Michael Faraday discovered the magneto-optical effect which has been exploited to develop the only known commercial fibre optic current sensor (FOCS) for large DC system built by the manufacturing giant, ABB [179]. The Faraday Effect principle exploited by ABB is illustrated in Figure 3-3 and states thus:

"*If a linearly polarised light is decomposed into left and right circularly polarised components which are then coupled into an optical fibre that is exposed to a magnetic field (caused by the current to be measured); at the end of the fibre the two components are reflected, and their polarisation direction swapped as they retrace their optical path to the sensor electronics. This results in a phase difference which is proportional to the line integral of the magnetic field along the optical fibre, hence it is a direct and precise measure of the current producing such magnetic field"* [180].

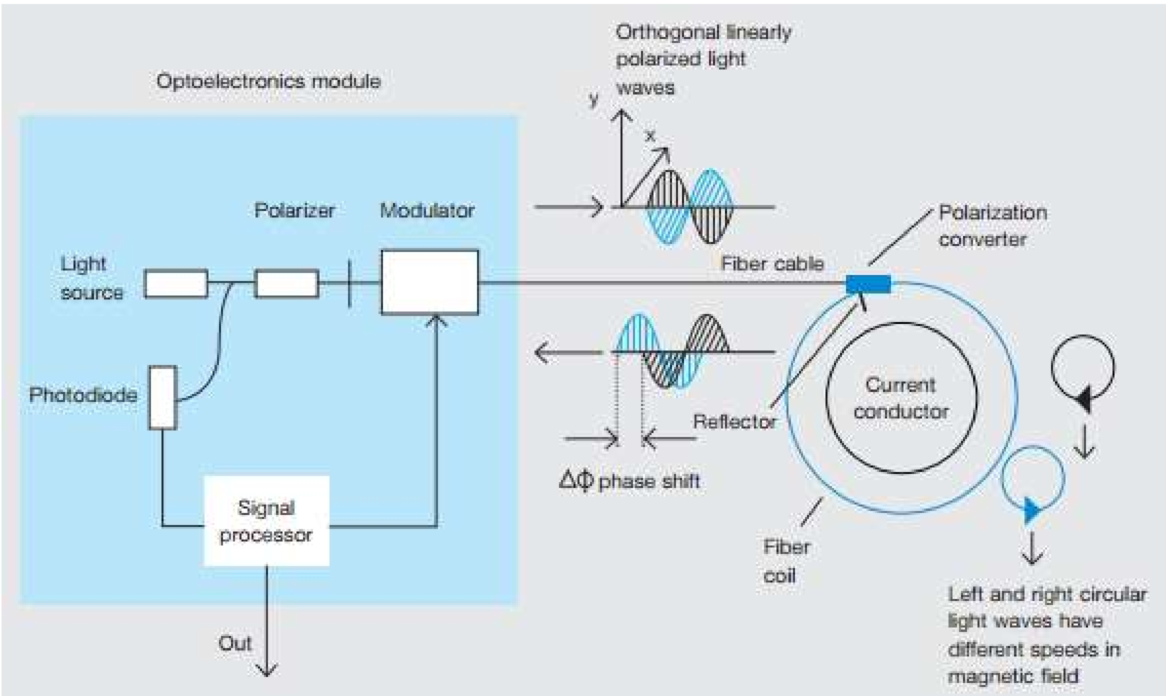

Figure 3-3: Faraday effect principle utilising magneto-optics [179]

During the research, the choice of using the FBG technology instead of Faraday effect was down to simplicity, cost, number of single point failures in the experimental set up and the intrusive requirement to gain access to the stator coil for measurements. With respect to the number of single point failures, this was based on the number of individual components that would be assembled. The Faraday effect required a greater number of components which were possible points of failure, affecting the reliability of the set up in terms of fault tolerance. Overall, the FBG technology in addition to its non-invasive advantage, also offered simplicity in its set up and lesser number of components.

3.2 Types of FBGs

3.2.1 Uniform FBG Sensor

FBGs are formed basically by a periodic modulation of the refractive index of a fibre core along its longitudinal plane and are produced using various techniques [148]. The choice of these gratings is based on their reflectivity response characteristics and perceived suitability for fault detection during spectral analysis. Uniform FBG is the standard FBG in which the gratings have equal and evenly spaced distance called the period, between them. They are fabricated usually using a phase mask technique [181] to expose a short length of photosensitive fibre to a periodic distribution of light, such that the fibre's refractive index is permanently varied in accordance with the exposure of the light intensity. Typical lengths of the FBG sensors are up to tens of millimetres with a period typically in the sub-micron region e.g., nanometre. FBGs act to couple light from the forward-propagating mode to a backward, counter-propagating mode of the optical fibre [182]. Figure 3-4 shows the uniform gratings (yellow) within the fibre core and surrounded by the fibre cladding.

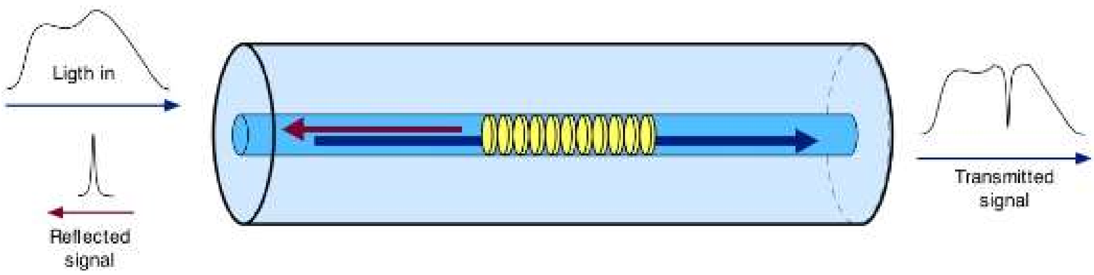

Figure 3-4: FBG - Fibre cladding with evenly spaced gratings within its core [183]

The principle of sensing with respect to braggshift is illustrated in **Error! Reference source not found.** which shows an incident light spectrum prior to its transmission through the FBG sensor. Upon incidence on the gratings, the light spectrum is observed to have a transmitted and a reflected spectra with different profiles. It is the reflected spectrum caused by the gratings that is used as a reference for FBG sensing where wavelength shift is observed due to strain on the gratings. The strain which causes the wavelength shift is caused by an external influence which is the parameter to be sensed, otherwise there will be no wavelength shift if the gratings do not experience any strain.

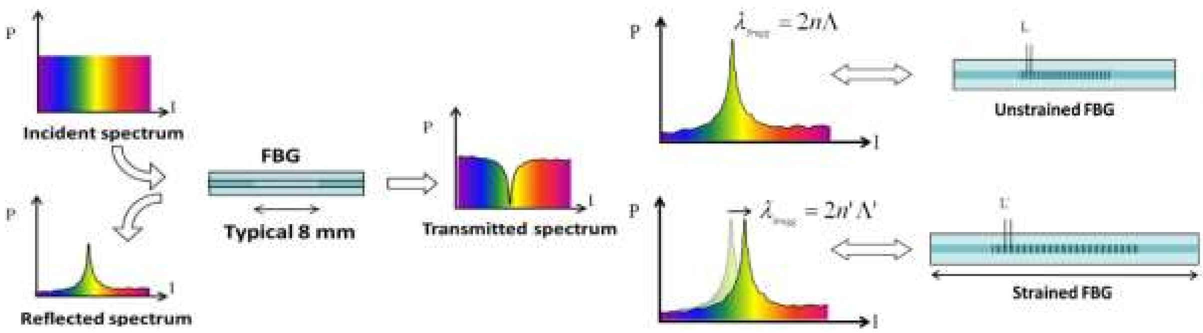

Figure 3-5: Bragg shift concept for light spectrum – incident, transmitted and reflected

3.2.2 Long Period Grating (LPG) Sensor

The LPG sensor is similar to the standard FBG sensor except that the period between the gratings is longer in the order of 100µm-500µm with typical fibre core lengths between 2 and 3cm (Figure 3-6). They are most conveniently fabricated by ultra violet exposure through a shadow mask [182]. LPG sensors depend on the coupling of light propagating in the core to the forward propagating cladding modes of an optical fibre [182], thus they do not produce any reflected signal, unlike the uniform FBG as shown in Figure 3-7. The LPG sensor was considered but due to loss of fabrication capability at Aston Institute of Photonics Technologies (AIPT), the research work could not experiment with these types to compare if they will offer any advantage over the uniform FBG sensors.

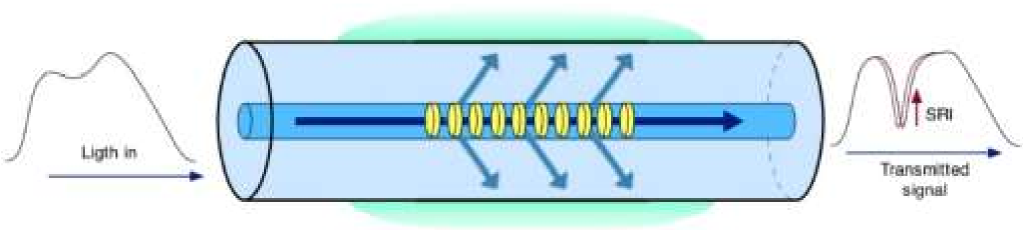

Figure 3-6: LPG - Fibre cladding with longer spaced gratings within its core [183]

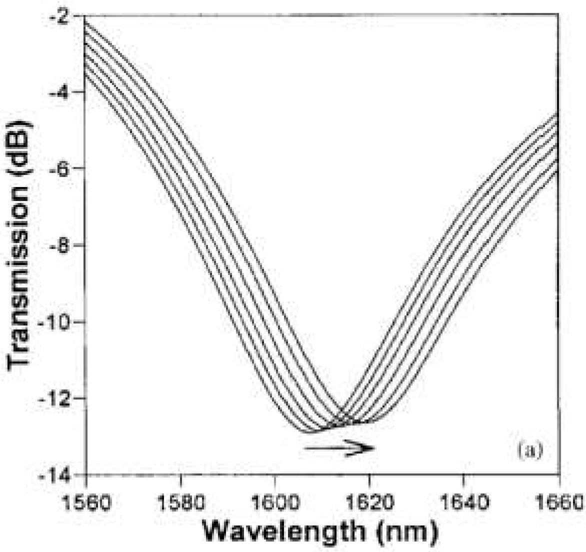

Figure 3-7: LPG spectrum of temperature-induced braggshifts [184]

3.2.3 Tilted FBG (TFBG) Sensor

TFBG also known as side-tap grating, has a period similar to the uniform FBG but the grating plane is not normal to the fibre axis. In other words, it is tilted at an angle, θ_g [182] (see **Error! Reference source not found.**). Because of the tilt angle, there are more mode couplings i.e. multiple numerous reflections, compared to the uniform FBG. Figure 3-9 shows the transmission spectrum of a TFBG with the core mode propagation (single peak on the right) clearly visible and can be distinguished from the multiple cladding modes. This standout single peak could be used as the reference wavelength in the same way as the uniform FBG when utilising the TFBG as a sensor. However, due to lack of expertise in the fabrication of the TFBG at AIPT, experimental investigation of the use of TFBG and how its performance compared with uniform FBG was not possible.

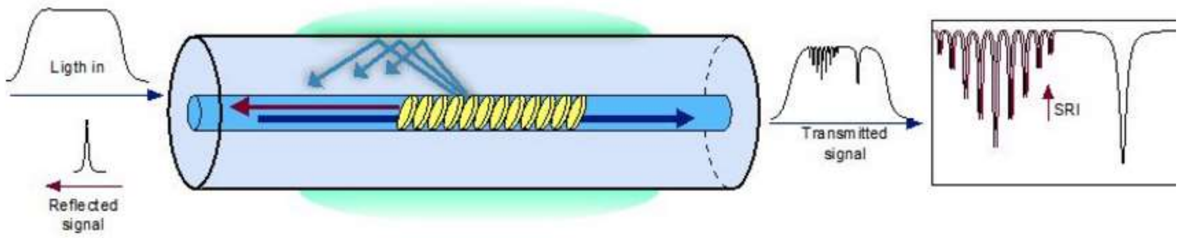

Figure 3-8: TFBG - Fibre cladding with tilted gratings within its core [183]

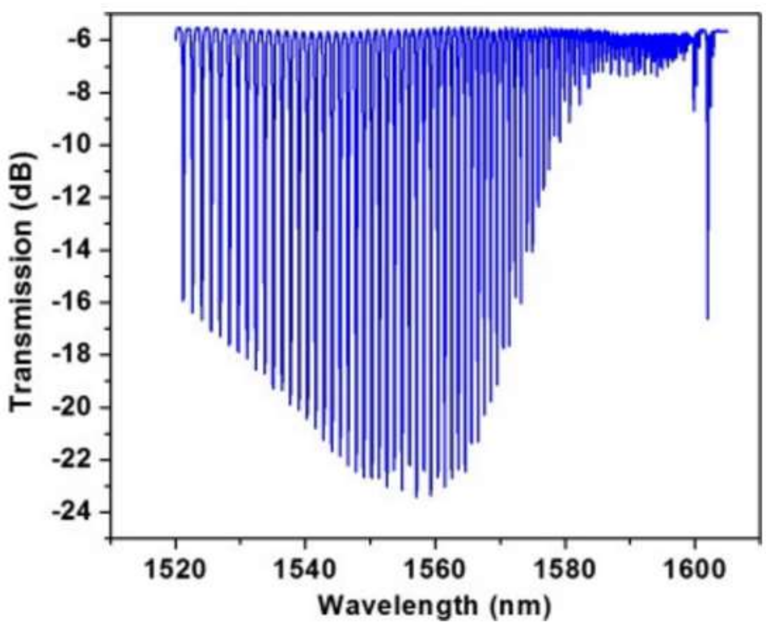

Figure 3-9: Transmission spectrum of a 10° TFBG measured in air using linearised input light [185]

3.3 Optical Magnetostrictive Sensing Using Terfenol-D

Apart from strain (vibration) and temperature sensing, fibre optic sensing has been successfully implemented in the sensing of current and magnetic field. In some sensing applications based solely on research, GMMs e.g., Terfenol-D and Monel-400 have been bonded to the FBG using a high strength and temperature glue such as Loctite [34], [186]–[191]. It is noteworthy that Terfenol-D is quite expensive with a dearth of suppliers globally. It is also pyrophoric as earlier mentioned, but this can be controlled by ensuring it is not exposed to oxygen-rich environment when using it for sensing. This can be easily achieved by inserting the alloy into some protective covering or tube. In this research, a 6mm diameter, 26mm long, cylindrical-shaped terfenol-D rod manufactured by Tdvib LLC, USA was used.

3.3.1 Theory of Magnetostriction

“Magnetostriction is the lattice deformation that accompanies magnetisation [192]”. It is the strain induced by a change in magnetisation [193]. Early magnetostrictive materials discovered exhibited their magnetostriction at very low temperatures with very little or no magnetostriction at zero room temperature. This led to the search for alloys with large magnetostriction at higher temperatures to allow for room temperature operations, which are now referred to as GMM [194]. Currently, applications where GMMs (mostly rare-earth based alloys) are used include nanoelectromechanical/microelectromechanical systems, energy harvesters, sensors, actuators and transducers [195]. More recently GMMs are being utilised in several mechatronics engineering and smart materials applications [196]. Terfenol-D is currently one of the strongest GMMs commercially available with excellent magnetostriction generating strains 100 times greater than traditional magnetostrictives. It is 2-5 times greater than traditional piezoceramics [195], [197]. It offers the advantage of a high Curie temperature (380°C), which enables magnetostrictive performance greater than 1000 ppm from room temperature to 200°C. With appropriate adjustments in its alloy composition, its operating range can extend down to cryogenic temperatures [197]. Challenges associated with the use of terfenol-D include its brittleness, its pyrophoric (self-combusting) nature, cost and dearth of manufacturers and suppliers. To put into context, within the global research community there appears to be only one known reliable supplier of terfenol-D materials and products which is TdVib, LLC in the USA and they have supplied the terfenol-D used in this research as well.

Unravelling the microscopic origin of this concept has over the years proved to be challenging even for great mathematicians and physicists such as Heisenberg as reported in [198], thus magnetostriction continues to be largely treated phenomenologically [193]. Although the functional properties of materials often depend on the detailed and subtle interplay of electronic, spin and lattice degrees of freedom, the actual understanding of the details of this electron–spin–lattice interplay remains one of the most challenging scientific problems in condensed matter physics [193]. The strain response – the physical movement of atoms in response to the external influence, in this case, magnetic field, is often complex in solids where macroscopic effects can constrain the motion [193]. For rare earth compounds such as terfenol-D, the strain is often associated with the highly anisotropic 4f electron distribution. This 4f distribution couples via the spin-orbit interaction to both the 4f magnetic moment and the surrounding atoms [199]. Magnetic anisotropy simply means the property of a material that allows it to change its characteristics depending on direction [200]. The resulting changes in size or orientation of the magnetic moment are reflected in a change of the 4f charge distribution, consequently forcing the surrounding atoms to attain new equilibrium positions. This leads to a large magnetostrictive strain [199]. The occurrence of magnetostriction is empirically evident. However, due to difficulty in accurately modelling its molecular behaviour, it is difficult to this day to fully fathom the hysteresis behaviour and sometimes, inconsistent strain response to magnetisation. As [200] puts it: “From the perspective of modelling and control, magnetostrictive materials exhibit nonlinear effects and hysteretic phenomena to a degree which other smart materials, for instance electro strictive compounds, do not.” Scientists continue to research new compositions of rare earth compounds that exhibit large magnetostriction with less magnetic anisotropy and less hysteresis characteristics at room temperature.

Two forms of changes in magnetisation exists in magnetostriction: reversible and irreversible. Reversible magnetisation changes occur when small magnetic fields are applied which allows the material to return to its initial magnetic state once the field is removed, hence it is conservative in nature. Irreversible magnetisation changes occur when large magnetic fields are applied, which would require external restoring forces to return the material back to its original magnetic state, hence it is dissipative in nature [200]. Figure 3-10 shows how magnetic dipoles of a magnetostrictive material respond to the presence of a magnetic field. Depending on whether the strength of such magnetic is small or large, reversible or irreversible magnetisation would occur. For the purpose of this research, external machine stray flux is to be used which is expected to be a magnetic field of small strength (in the μT range), thus it is expected that only reversible magnetisation will be evident.

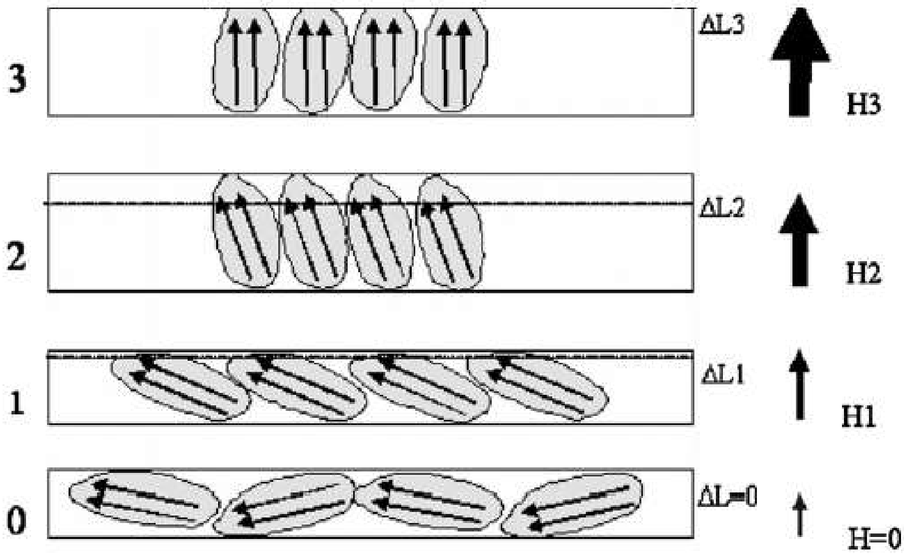

Figure 3-10: Behaviour of magnetic dipoles of GMMs when a magnetic field is present [189]

3.3.2 Terfenol-D Characteristics

Terfenol-D ($Tb_{0.3}Dy_{0.7}Fe_2$) as an alloy of iron (Fe), terbium (Tb) and dysprosium (Dy) has its name coined from the initial alloy – $TbFe_2$ (TERFE-), its place of origin – the Naval Ordnance Laboratory (NOL), and Dy (D) which was added later [201], [202]. NOL is now a defunct research arm of the US Military. Dysprosium was added to terfenol after research found that it lowered the amplitude of the required magnetic flux to produce the large magnetostriction already exhibited by $TbFe_2$ at room temperature [201], [202]. According to the IEEE standard on magnetostrictive materials [203] the piezomagnetic constant, permeability and elastic compliance coefficient of terfenol-D are respectively given by:

$$d_{33} = \left(\frac{\partial S_3}{\partial H_3}\right)_T = \left(\frac{\partial B_3}{\partial T_3}\right)_H \tag{3-15}$$

$$\mu^T{}_{33} = \left(\frac{\partial B_3}{\partial H_3}\right)_T \tag{3-16}$$

$$s^H{}_{33} = \left(\frac{\partial S_3}{\partial T_3}\right)_H \tag{3-17}$$

where S_3 is the strain, H_3 is the magnetic field strength (A/m), B_3 is the magnetic flux density (T), and T_3 is the stress (Pa) along the polarisation direction (i.e., x_3 axis). According to [204] the coupling factor (k_{33}) between strain, permeability and stress is given by:

$$k_{33} = \frac{d_{33}}{\sqrt{s_{33}^H \mu_{33}^T}} \tag{3-18}$$

To characterise terfenol-D, several experiments were carried out based on the above formulas at different mass loaded pre-stress conditions using varying amounts of pressure including elasticity and resonance measurements. These experiments were based on small-diameter (<10mm) rods with random grain orientations. [201], [202] admitted that because terfenol-D is now produced in various sizes with diameters now in cm range, magnetostrictive measurements taken from individual samples of small diameter, would not be representative of those from larger diameters. There would be sample-to-sample variations of the characteristics of the terfenol-D depending on the dimensions especially given that the results even for small-diameter terfenol-D revealed nonlinearity [12][205]. Unfortunately, there is no known model to accurately predict the specific characteristics of terfenol-d rods depending on their sizes; although there are generic expectations from all magnetostrictive materials to produce strain when subjected to a magnetic field. [206], [207] submitted the hypothesis that the relationship between strain and the magnetic field for an amorphous magnetic material is such that strain is given by:

$$\frac{\Delta L}{L} = \frac{3\sigma_s}{2}\left(\left(cos\theta_f\right)^2 - (cos\theta_i)^2\right) \tag{3-19}$$

where θ_f and θ_i are the final and initial angles between the magnetic domains and the applied field. σ_s is a constant representing the material constant obtained experimentally when the material in an initial hypothetical demagnetised state is magnetised to saturation. It was suggested [206], [207] that maximum strain occurred when all the magnetic moments rotate through 90° hence:

$$\frac{\Delta L}{L}(\max) = \frac{3\sigma_S}{2} \tag{3-20}$$

Terfenol-D has several times been classed as a ferromagnetic material, however its behaviour during this research work agrees with [208] who described it as a rare earth rich ferrimagnetic material. Since large magnetostrictions are due to the strong magneto-mechanical coupling that results from the dependence of magnetic moment orientation on inter-atomic spacing [200]; terfenol-D can be said to have such strong magneto-mechanical coupling at room temperature. As submitted by [199], the huge anisotropy of the 4f electron cloud observed in rare-earth transition-metal compounds such as Terfenol-D ($Tb_{0.3}Dy_{0.7}Fe_2$) is *thought* to be commonly associated with its giant magnetostrictive characteristic. At microscopic level using x-ray absorption spectroscopy, it has been experimentally analysed that the large strain observed in Terfenol-D is mostly due to the elongation of the Tb-Tb bond. This bond is of the order of 8 x 10^{-3}Å compared to the other atomic interactions (Fe-Tb, Fe-Fe, etc.) [199]. Due to the very large magnetic anisotropic characteristic of terfenol-D, there is the presence of magnetic moment jumping, also called Barkhausen jump when a sinusoidal magnetic field is applied to it. This jumps results in an un-smooth magnetisation curve as well as non-linearity in material behaviour [200], [205]. Magnetic moment jumping occurs because of magnetic dipoles whose magnetic moments cause them to abruptly enter or leave low energy directions [200].

Terfenol-D exhibits a unipolar magnetostrictive characteristic such that a positive strain is produced regardless of the polarity of the magnetic field [209], [210]. Thus, the alloy will show the same strain response to alternating magnetic flux as well as DC. This is crucial to understanding how to use the FBG-T sensor in this research for condition monitoring of electric machines. The external stray flux being used as a monitoring signature is a sinusoidal flux while a current-controlled DC magnetic flux will be used to calibrate the sensor. Given that the stray flux strength is usually small, it is expected that the reversible magnetisation of the terfenol-D in the magnetic field domain would translate into a reversible wavelength shift in the optical domain for the FBG-T sensor. [209], [210] confirmed the hysteresis nature of FBG-T as composite sensor where the start wavelength varied slightly from the return wavelength. This is a transferred characteristic from the terfenol-D onto the bragg grating spectral response. Due to hysteresis and non-linear behaviour of terfenol-D, a direct return to initial wavelength may not always occur, but the path should exhibit a reversible trend in theory based on the above submissions. [209], [210] specifically experimented on the impact of temperature in the use of FBG-T for sensing applications to see the impact of cross sensitivity where temperatures from 10°C up to 78.7°C were applied. Only small braggshifts of the order of 2.351pm/°C and 9.34pm/°C were observed for specimens with and without temperature compensation respectively. [211] performed a similar experiment on the FBG-T composite sensor between 20°C up to 80°C and observed a sensitivity of 11.4pm/°C without compensation. Temperature variation during this investigation will be kept to a minimum as much as possible. It is expected that temperature variation throughout the experiment would be lower than the 10°C used in these previous works, to minimise braggshifts due to external ambient temperature.

Though novel in the context of FBG sensing, the use of external flux has been proved to be reliable in wider context of electrical machine sensing. Provided the external flux can be sensed reliably and transduced into an optically measurable strain, then non-invasive condition monitoring of electric machines can be realised, which is what this experimental investigation has proved.

3.3.3 IM Stray Flux Characteristics

Stray flux as earlier stated is the attenuated main air gap flux. For three phase IM, it is as a result of the stator and rotor currents on the machine extremities in the stator or rotor coil ends (in WRIMs) and the end rings in squirrel cage rotors as defined and illustrated by [212] in Figure 3-11. However, accurately modelling its characteristics has been reported to be more difficult compared to the main air gap flux. This is because the stray flux is influenced by the geometric design of the machine yoke [122] which varies from one machine manufacturer to another.

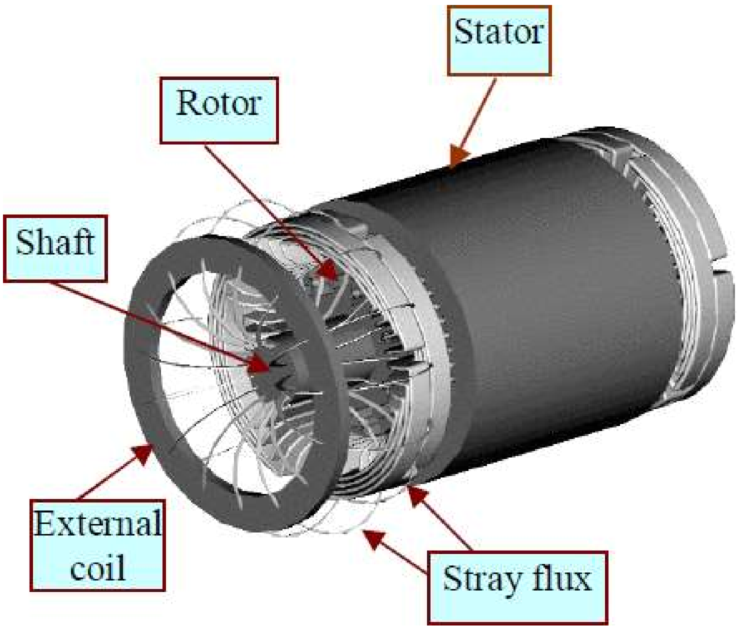

Figure 3-11: Illustration of IM stray flux characteristics [212]

It is also sinusoidal in nature, following the sinusoidal nature of the main air gap flux since it is induced by the stator and rotor currents [213]. However, as alluded to by [213]–[215], the stray flux contains rich harmonic components that have been successfully analysed for fault detection in IMs. In several literature such as [216]–[219], a rise in the magnitude at the side band frequency defined by $f_{BRB} = (1 \pm 2ks)f_s$ has been associated with the presence of BRB in IMs; where f_s is the supply frequency, k is an integer (1,2,3,…) and s is the slip of the IM. However, according to [213], the stray flux can contain varying degree of both stator and rotor magnetic fields depending on the physical location of the measurement point. This suggests that the stray flux characteristics, though a leaked copy of the main air gap flux, depends also on the sensor being used to measure it and its location.

3.4 Methodology

3.4.1 Main Laboratory Equipment and Functions

The main equipment used in this research as highlighted in Figure 3-12 are:

❖ Light Source & Optical Spectrum Analyser (OSA): performed a dual function as a source of broadband light spectrum which is transmitted through the optical fibre sensor; received and analysed the reflected light spectrum. OSA Settings were as shown in Table 3-1:

Table 3-1: OSA specification and settings

Parameter	Detail
Manufacturer	Hewlett-Packard
Centre wavelength	1550nm
Span	5nm
Reference	-50dB
Scale/Division	0.5dB
Resolution	0.06nm
Sweep time	76ms
Sensitivity	Auto
Mode type	single
Bandwidth @ 3dB	~3.99nm

❖ Terfenol-D Transducer: converted the stray flux of the IMs into strain. A 6mm diameter, 26mm long, cylindrical-shaped terfenol-D rod manufactured by Tdvib LLC, USA was used.

❖ Loctite Adhesive: acted as the transfer medium for transferring the strain produced by the terfenol-D onto the FBG for optical sensing and measurement. It was used to bond the terfenol-D to the FBG. Loctite 401 was used with the following characteristics as provided by the manufacturer in Table 3-2:

Table 3-2: Loctite adhesive specification

Parameter	Detail
Technology	cyanoacrylate
Chemical type	Ethyl cyanoacrylate
Uncured appearance	Colourless/transparent
Components	one-part
Viscosity	low
Cure	Humidity
Application	bonding
Key substrates	metals, plastics and elastomers

❖ Optical Fibre with FBG: specifications for the optical fibre are shown in Table 3-3.

Table 3-3: FBG specification

Parameter	Detail
Manufacturer/Model	Fibercore
Centre wavelength	1550nm
Grating length	10mm
Period	0.5µm
Cladding diameter	125µm
Core diameter	4.2µm
Full width at Half Maximum (FWHM)	~0.1nm
Reflectivity	41%
Mode type	single
Bandwidth @ 3dB	~3.99nm

❖ IMs: test machines to provide stray magnetic flux under different conditions. Three identical 3-phase IMs were used with the following specifications shown in Table 3-4:

Table 3-4: IM specification

Parameter	Detail
Power rating	2.2kW
Number of poles	4
Power factor	0.8
Efficiency	87%
Torque	14.6Nm @ 50Hz
Inverter Speed range	5Hz-90Hz
Shaft diameter	28mm D x 60mm L
Motor Housing	Cast iron

❖ DC Motors: acts as a load for the IMs

❖ Fibre Stripper: used to remove the cladding of the optical fibre to expose the fibre core to allow for correct termination of the fibre into bare fibre connectors which can then be directly connected to the OSA. It is also used to prepare the optical fibre for cleaving when two separate fibre cores are to be fused into one

❖ Fibre Cleaver: used to fuse two fibre cores into one using thermal radiation. It is useful when the FBG sensor is to be connected to a pig tail or patch cord to provide easy connection to the OSA

❖ Variable Frequency Drive (VFD): used to operate the IMs at different test frequencies with the aid of an external potentiometer for speed control. RS 510 2.2kW inverter with built in EMC filter, single phase input was used. Its specifications are provided in Table 3-5. The control mode for the inverter is Volts per frequency (V/F) control and Sensor-less Vector (SLV) control. The SLV is sometimes called Open Loop Vector (OLV) mode was preferred as it uses a vector algorithm to determine the optimum output voltage required to run the motor. Vector control accomplishes this by using current feedback from the motor [220]. Therefore, the use of such algorithm means that there will be a different output voltage when the motor is run at different frequencies.

Table 3-5: RS510 VFD specification

Parameter	Detail
Manufacturer/Model	RS Pro/RS510 series
Power Rating	2.2kW
Input	Single phase
Output	Three phase
Supply Voltage	200 – 240Vac
Current Rating	21A
External Potentiometer for Speed control	Available
Control Mode	V/F Control + SLV Control

❖ Flux meter: used to measure the stray flux. Two fluxmeters were used.

Initially a single axis RS Pro Magnetic Field meter was used with a sampling rate of 2.5 times per second, without auto data logging functionality. Its range was 20/200μT

Later, a data logging tri-axis Magnetic field meter, HHG1394 manufactured by Omega Engineering was used with sampling time capability of about 0.5 seconds, a resolution of 1μT and a range of 2/200 μT

❖ Thermometer: used for temperature measurement of the sensor. A digital temperature probe with a range of -50°C – 110°C and a resolution of 0.1°C was used. Please note that due to the brittleness of the bare fibre used in this research, the temperature probe was placed as close as possible (about 2-3cm away) to the FBG-T sensor without actual contact to avoid breakage. Where the FBG-T sensor is adequately protected, actual contact can be made during temperature measurement.

❖ PC with LabView Software: connected to the OSA to acquire numerical data of the optical spectra analysed by the OSA for further analysis in MATLAB

Figure 3-12: The main equipment used during this research

3.4.2 Fibre Preparation

Prior to entering the Photonics laboratory (clean room), a health and safety induction was carried out which included watching a laser safety video as well as undergoing an eye test at the Aston's Optometry clinic. Activities carried out during the training include:

Prior to connecting the fibre to any equipment, the following should be done:
i). strip the fibre coating using a stripper to expose the cladding especially around all areas where the gratings have been fabricated which will be in contact with the machine whose signatures are to be extracted

ii). thoroughly clean the stripped (exposed cladding) surface using medical wipes soaked in alcohol

iii). use the cleaver to cut the fibre tip before connecting it to the bare fibre (BF) connector in such a way that only a small portion shows at the tip of the BF connector.

The cut fibre may require further cleaning before connecting it to the bare fibre connector depending on the ease with which slides into the BF connector.

iv). the tip of the fibre on the BF connector is then connected to the fibre connector cleaner for further cleaning v). BF connector can then be connected to the connectors on the OSA and light source for light transmission via the fibre

3.4.2.1 Connection to Light Source and OSA

In order to avoid damage caused by repeated tightening and loosening of connectors to/from the OSA and light source equipment, a patch cord should be connected directly to both equipment such that parameter sensing fibres can be repeatedly connected to and disconnected from the patch cords. This is because the patch cords are quite cheap to replace when compared to the cost and downtime any damage to the built-in connectors on the optical equipment would have.

3.4.2.2 Bragg Gratings Fabrication

Initial set of FBGs have been fabricated in the clean room of AIPT, Aston University, Birmingham. The single mode fibre (SMF) was first hydrogenated for 4 days at 100 bar and 80^{o}C to enhance photosensitivity and the final profile was measured after annealing in an oven at 80^{o}C over 48 hours to remove any residual hydrogen in the fibre. A set up involving the use of an acoustic optical modulator (AOM) which modulates a laser beam generated by a 100mW, 244 nm frequency doubled argon ion laser, was used to fabricate the gratings. An interference pattern was first generated through the beam being incident on a phase mask. During the grating fabrication, the fibre is then placed within the interference pattern and scanned across the phase mask at a predetermined rate by a high precision linear motor stage. The beam is measured at the point of incidence on the fibre with a diameter of 270μm during fabrication and the beam profile was compensated for by the beam size during design [221]. The grating was measured with an OSA pre-annealing and with a LUNA optical vector analyser post annealing.

3.4.3 Experimental Set up Procedure

Figure 3-13, Figure 3-14 and Figure 3-15 show the test rig set up for this research. The various steps taken during the experimental rig set up have been explained in Table 3-6 below.

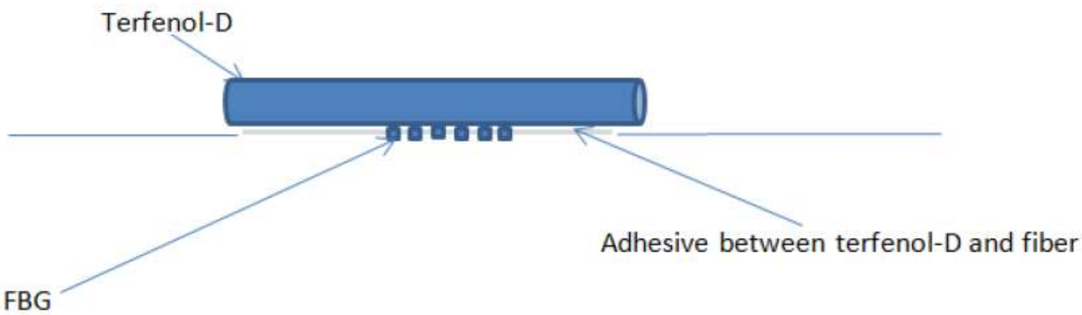

Figure 3-13: FBG-T sensor bonding arrangement

Table 3-6: Experimental rig set up procedure

Step	**Activity carried out**
Identifying the FBG sensor location	The location of the Bragg grating was first identified using a hot soldering iron. ***Step 1:*** The FBG optical fibre was connected to a broadband light source and OSA (in this case, dual function OSA) and the OSA tuned to desired settings to clearly show the sensor spectrum. ***Step 2:*** The soldering iron was carefully brought near the stripped section where the FBG is suspected to be inscribed. ***Step 3:*** The FBG spectrum responded to the high temperature of the hot soldering iron and the location of the grating was estimated
Bonding FBG to Terfenol-D	During bonding, it is crucial not to incorrectly bond the FBG as there are two ways this activity can be carried out: a) applying the adhesive over the FBG surface and then place the terfenol-D over the adhesive; OR b) placing the terfenol-D over the FBG surface before applying the adhesive over the alloy and the grating. The latter was preferred because it increases the contact surface area between the FBG and the alloy. Given that FBG sensing relies largely on the relative contact between the grating and the measurand, the former option would create an adhesive layer between the alloy and the grating, which could have an adverse effect on sensor performance. ***Step 4:*** The terfenol-D was placed over the FBG surface and Loctite 416 adhesive was gently applied across the alloy to bond it to the grating (see Figure 3-13). It was left to cure for several hours, although, it cured within minutes. The FBG spectrum was still visible on the OSA whilst the terfenol-D was being bonded onto the FBG.
Tubing FBG-T	***Step 5:*** the composite sensor (FBG-T) was then disconnected from the OSA and carefully inserted into an acrylic tube. Before the insertion, the acrylic tube was tested to confirm it is magnetically insensitive by measuring the external flux from one motor with and without the tube using the gaussmeter. Both readings were exactly the same.
IM-DC Machine Coupling	***Step 6:*** the test machines (IMs), each in turn, were coupled to a DC motor which acted as the driven load, using rotor shaft couplings of appropriate diameters.

VSD/IM Connection	***Step 7:*** The coupled IM is then connected to a VFD. The VFD has a three-phase input where the IM is connected to, and a single-phase output which is connected to 230V utility supply.
OSA/Light Source/PC Connection	***Step 8:*** The FBG-T was then connected to the dual function OSA/light source via pigtails. The OSA was thereafter connected to a PC via a GPIB adapter where LabView was used to export the numerical spectral data to MS Excel.
LabView/MATLAB Interface	***Step 9:*** The exported data was then imported into MATLAB for data analysis.

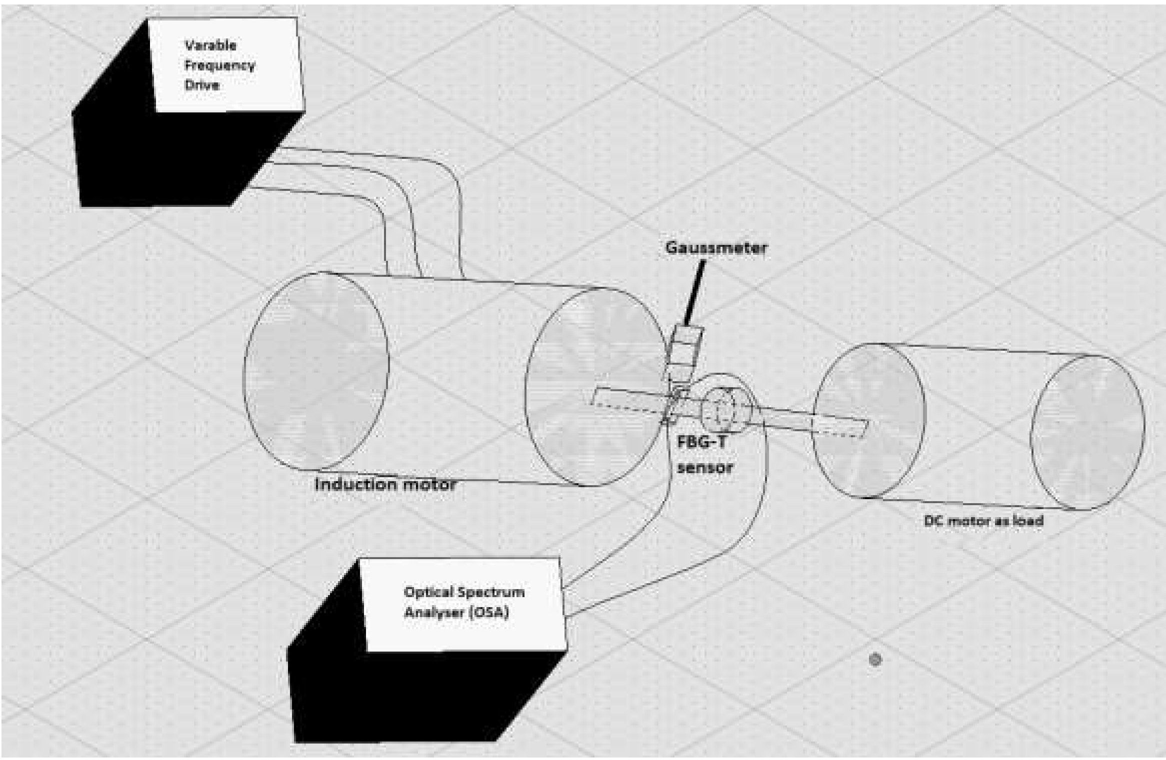

Figure 3-14: Schematic of experimental test rig

Figure 3-15: Complete experimental test rig

3.5 Grating Calibrations

3.5.1 Temperature Calibration

FBG sensors are sensitive to both strain and temperature (cross sensitivity) as stated in a previous chapter. Understanding the impact of temperature on the magnetostrictive transducer is crucial to interpreting experimental results obtained.

3.5.1.1 Operating Conditions Investigated

Ideally a step change thermal excitation would have been preferred, however, due to limited resources in the laboratory, an improvised heat source is used to generate different amount of heat for the FBG-T sensor temperature calibration. A standard WAHL hair dryer with varying temperature control levels was used together with a basic digital temperature probe to create hot air and measure the resulting heat applied to the FBG-T sensor whilst connected to the OSA. The schematic and actual set up are as shown in Figure 3-16 and Figure 3-17.

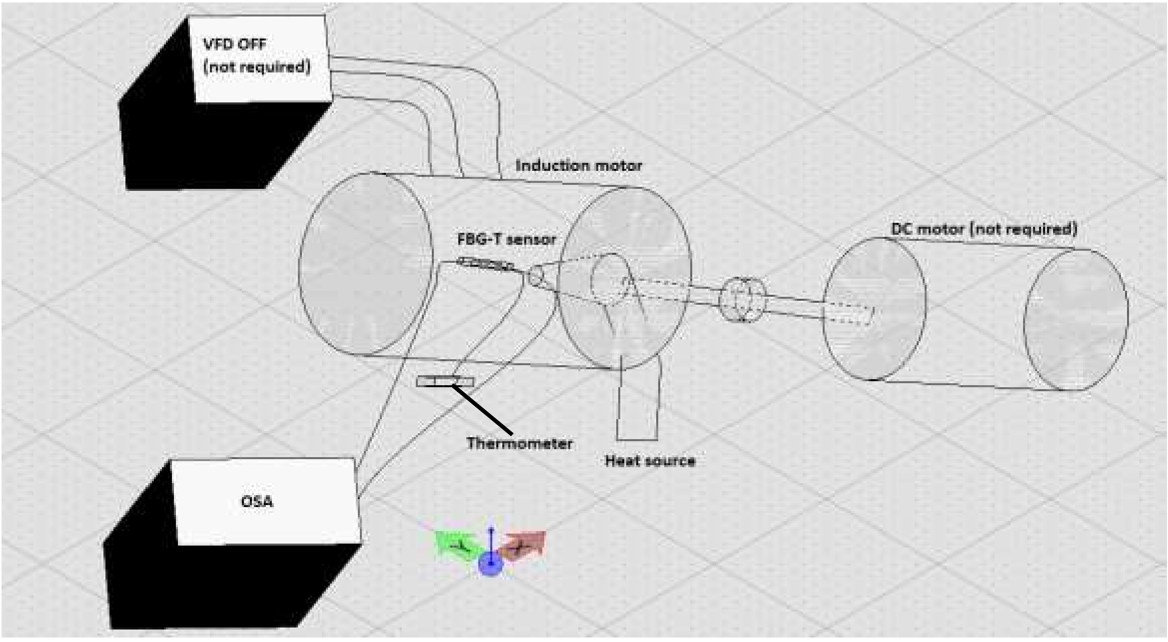

Figure 3-16: Schematic of temperature calibration set up

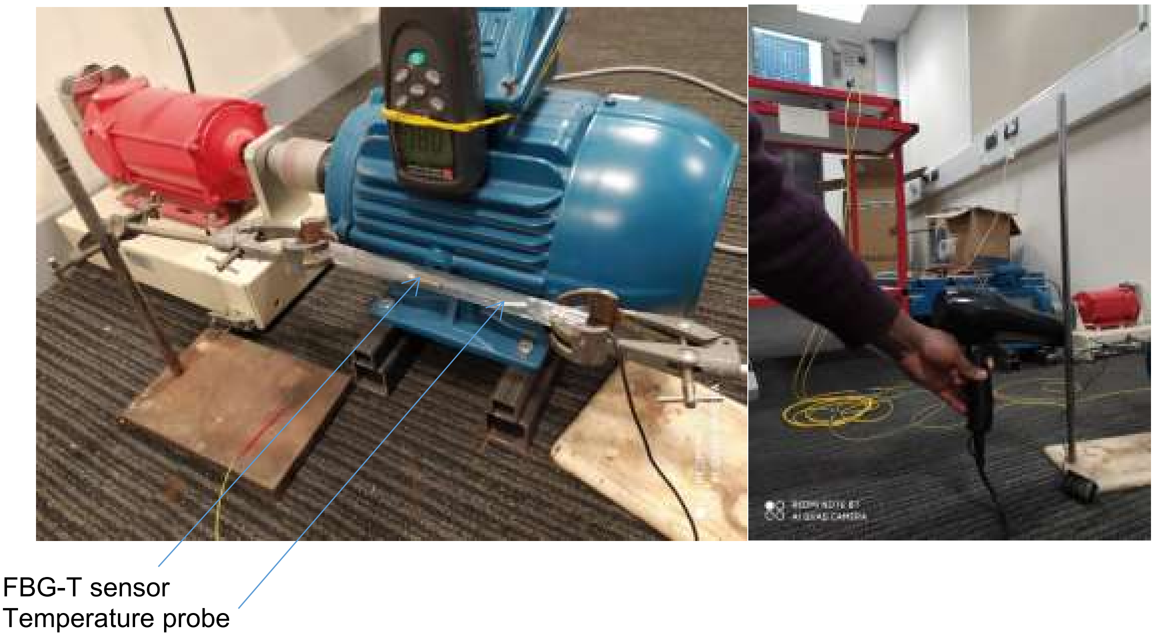

Figure 3-17: Heat application set up for FBG-T sensor

The specifications for both equipment and the procedure are as follows:

WAHL Hair dryer (heat source)

- 230V ac supply

Digital temperature probe

- Temp. range: -50°C – 110°C
- Resolution: 0.1°C
- Power supply: 2 x 1.5V
- Accuracy: ±1.5°C

Basic Procedure

- Heat was applied for 15mins
- Allowed to cool for 30mins

3.5.1.2 Result Analysis & Discussion

Table 3-7 shows data obtained from the temperature calibration.

Table 3-7: Temperature calibration of FBG-T sensor

Tempmax (°C)	20.9	25.3	31.1	36.1	42.6	51.2	71.1
Tempchg (°C)	0	3	10	13.3	19.4	25.1	48.4
Roomtemp (°C)	20.9						
Braggmax (pm)	0	90	230	355	540	680	1025

The FBG-T sensor was observed to respond to temperature in an instantaneous manner such that when temperature rises, the braggshift immediately increases rapidly to its maximum for the given temperature. Once the heat source is removed, the braggshift is lost very rapidly and the FBG-T returns to its initial wavelength *within several minutes* (Figure 3-18 – top plot). This is in contrast to the FBG-T sensor behaviour when the braggshift is due to a magnetic field where the change in wavelength is gradual up to some level and then stays constant until the magnetic field is removed. Upon field removal, the braggshift then resumes for a short time before it then starts returning to its initial wavelength which takes several hours as shown in Figure 3-18 – mid plot. The short-lived behaviour is due to the paramagnetic nature of the terfenol-D where its magnetic dipoles attempt to re-orientate to a new state of magnetic equilibrium. This causes the FBG to strain further, causing some further braggshifts which does not last once the weak residual magnetism is completely lost. After then, the commencement of the return journey. It should be mentioned that temperature does affect terfenol-d but the change in temperature has to be significant to cause a strain. According to the manufacturer [197], the coefficient of thermal expansion (CTE) for terfenol-d is 0.000011ε per degree (°C) rise in temperature (11ppm/°C). Given the measurements obtained, for the maximum change in temperature observed (48.4°C), the expected change in length would be 0.0005324mm which was insufficient to cause a transferable strain large enough for a braggshift. Even if such a strain occurred, it would have been negligible given the rapidness of the rise and fall of the braggshift to and from its original wavelength which was a consistent characteristic at each individual temperature. In addition to the near instantaneous response, the order of magnitude of the observed braggshifts as shown in Figure 3-18 (bottom plot) are much larger compared to the values observed when magnetic field is applied. There is a near linear relationship between temperature change and maximum braggshift which is expected given the sensitivity of FBG, in this case, 20.77pm/°C. Thus, it is reasonable to state that the observed braggshift is largely due to the high thermal sensitivity of FBG. A caveat here is that the FBG sensing is largely dependent on the state of the terfenol-d. However, in this case, the hot air was blasted directly at the FBG-T hence the quick response from the FBG. Should the temperature in the room change even by 2-5°C and the terfenol-d temperature does not increase by that amount, then the FBG may not respond as it is directly bonded to the terfenol-d. A significant increase in temperature is thus required to cause a braggshift solely due to temperature change.

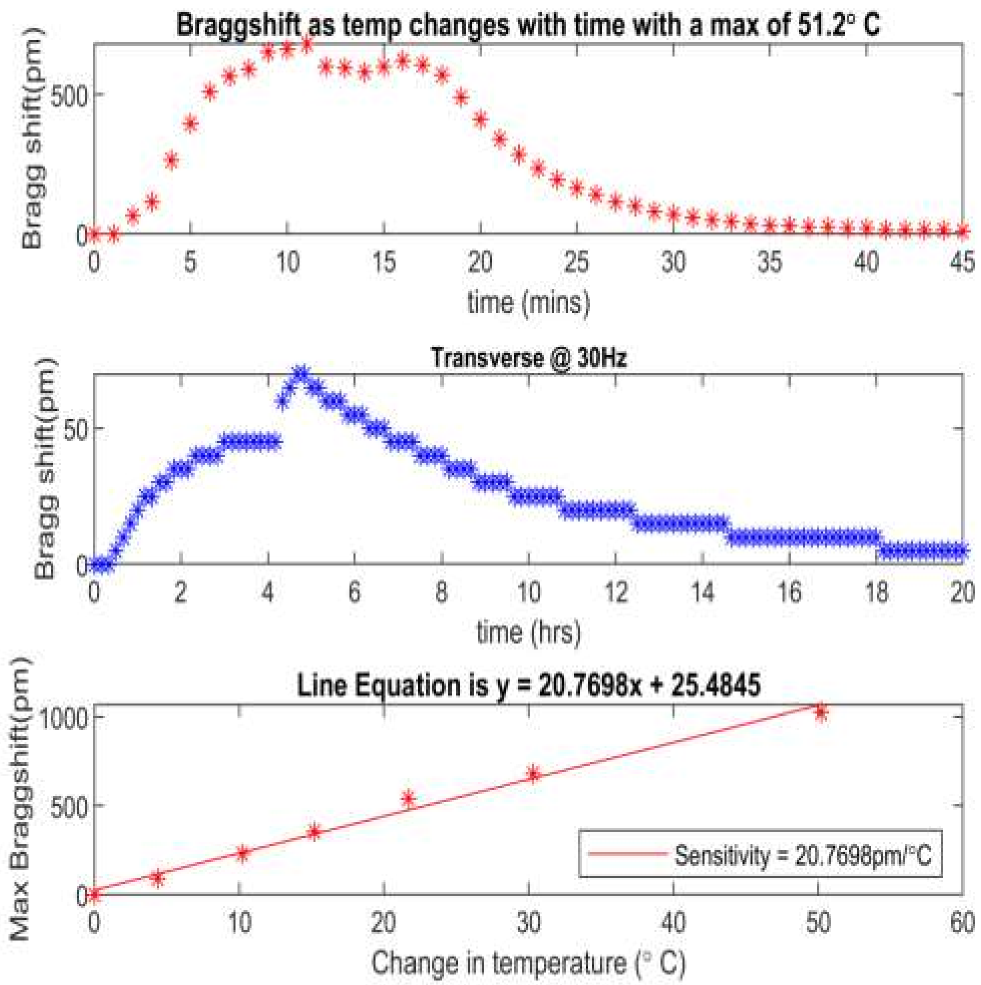

Figure 3-18: Characterisation of FBG-T sensor with respect to temperature

Plots in Figure 3-18 show how braggshift resulting from the application of a maximum temperature of 51.2°C to the FBG-T compares to the braggshift due to stray flux when test motor is run at 30Hz.

3.5.2 Magnetic Strength (Flux density) Calibration

To calibrate the FBG-T sensor a magnetic field source and a magnetic field sensor were needed. For the magnetic field source, an openly wound 4V DC motor whose windings were exposed was used with a DC power supply unit to provide the needed current for different magnetic field strengths. A tri-axial auto data logger magnetic flux meter was used to measure the magnetic flux density for each applied current.

3.5.2.1 Procedure & Results

The complete set up is shown in Figure 3-19 and Figure3-20 where different amount of currents were applied generate magnetic field of different strengths measured by the auto data logger. Plots showing the optical spectra and time variation of braggshifts for each test current and corresponding magnetic flux density are shown in Figure 3-21, Figure 3-22 and Figure 3-23. Table 3-8 shows the readings obtained and the gradient of Figure 3-24 confirms the sensitivity of the FBG-T sensor. A directly proportional relationship between the current and the magnetic flux, and as a result, the braggshift was observed. The optical spectra visibly showed the increase in the braggshift with current given that the magnetic flux in this case was DC in nature. As earlier mentioned, the unipolar nature of terfenol-D magnetostriction was evident in the time varying plots of braggshifts where there was a steady increase in the braggshift with time until the maximum braggshift was attained. The rate at which the braggshifts occurred for each current value appeared to be faster than the rate observed for earlier tests performed with stray flux which is sinusoidal in nature.

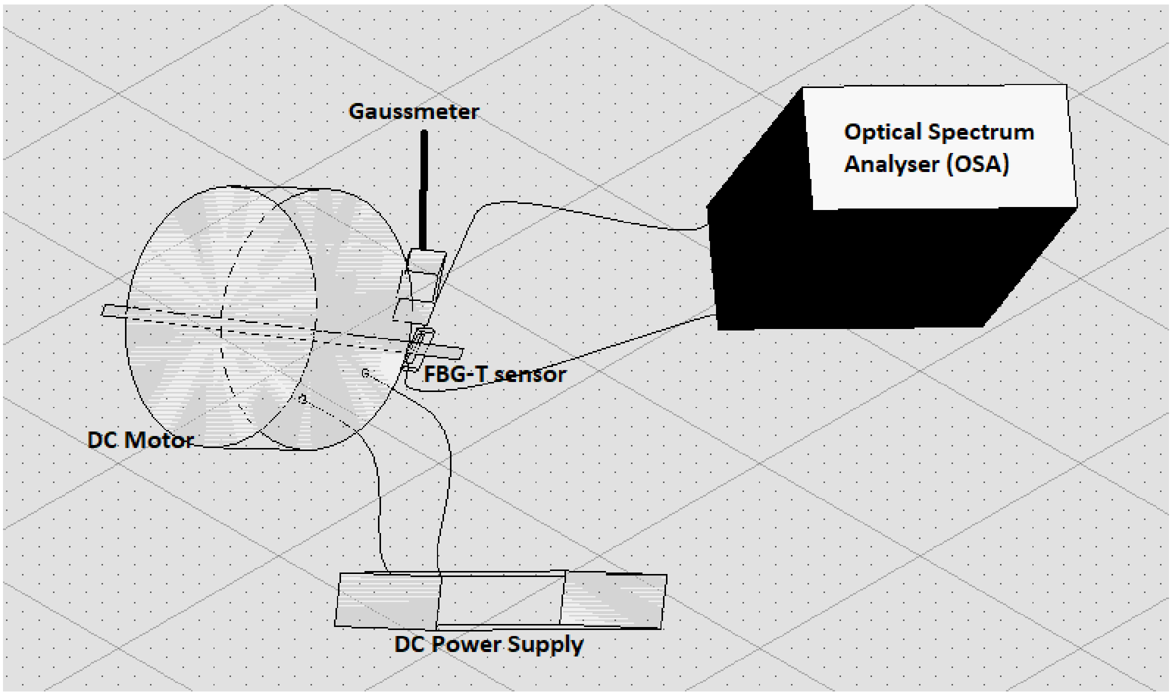

Figure 3-19: Schematic of magnetic flux calibration set up

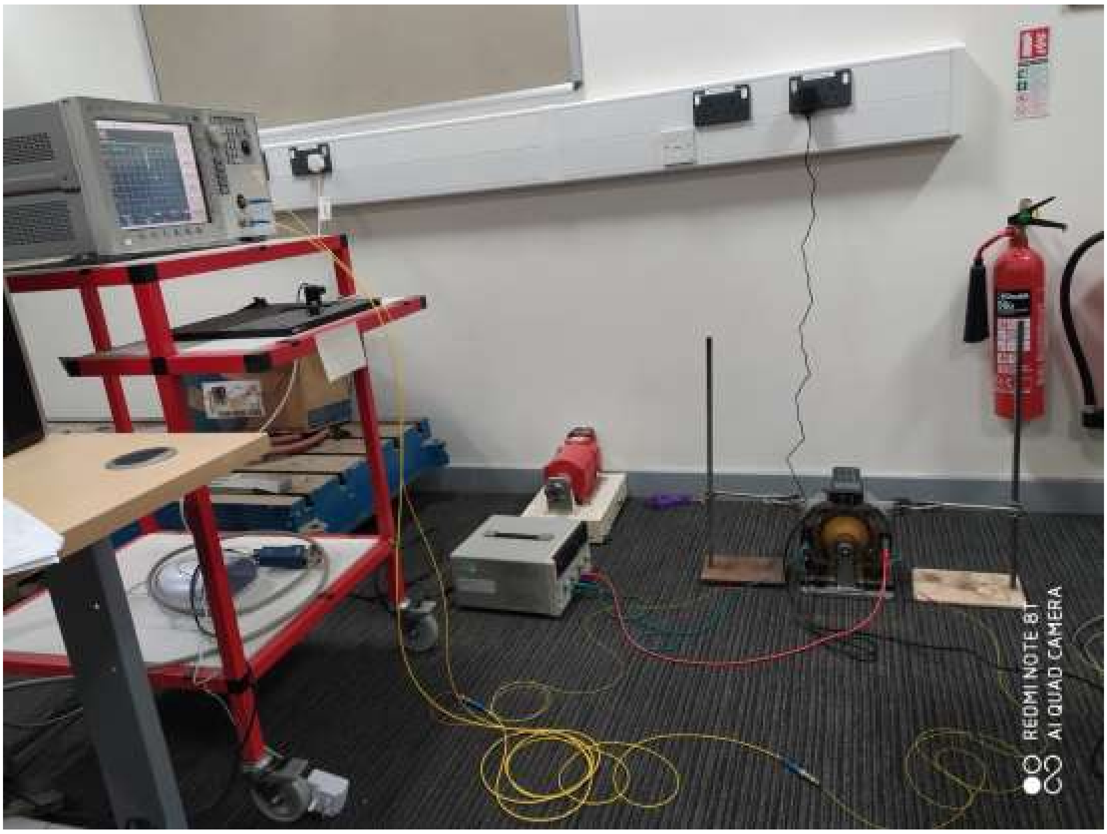

Figure3-20: Actual Magnetic flux FBG-T sensor calibration set up

This suggests that although the magnetostrictive transduction process is unipolar, the rate at which the transduction process occurred was affected by the very nature of the magnetic flux causing the strain. This can be explained by the oscillatory nature of ac waveform which will slow down the movement of the magnetic dipoles in moving to a new state of equilibrium whilst attempting to align to the direction of the magnetic field. There is, however, less perturbation and oscillatory motion when DC magnetic flux is the driving influence on the magnetic dipoles. The same difference in rates could not be observed in the reversible magnetisation process when the terfenol-D returned to its initial length. For each applied current, the FBG-T sensor was yet to return to its initial wavelength even though it responded as soon as the field was back on. It appeared to have settled down at a new wavelength which is very likely due to the hysteretic nature of the magnetostrictive transducer in the FBG-T sensor. It is noteworthy that this did not affect the results obtained as the reference was based on the current initial wavelength at the start of the test. Temperature changes were minimal for each test current with the maximum change of less than 0.13°C, hence temperature did not significantly impact on the braggshifts observed. The sensitivity of the FBG-T sensor obtained was 19.3810pm/µT as shown in Figure 3-24.

Table 3-8: FBG-T magnetic flux calibration data

Supply voltage (V)	Current (A)	Magnetic flux density (μT)	Max. Braggshift (pm)	Max Temp. change during 4 hours (°C)
0	0	0.121999	0	0
2.4	1.15	1.626061	30	0.064632
3.2	1.45	1.986906	35	0.088701
4.7	2.15	2.902456	55	0.111912
5.4	2.45	4.064479	80	0.082357
7.2	3.12	6.377667	120	0.127088
Duration of applied current (hours)	2 (ON) & 2 (OFF)			

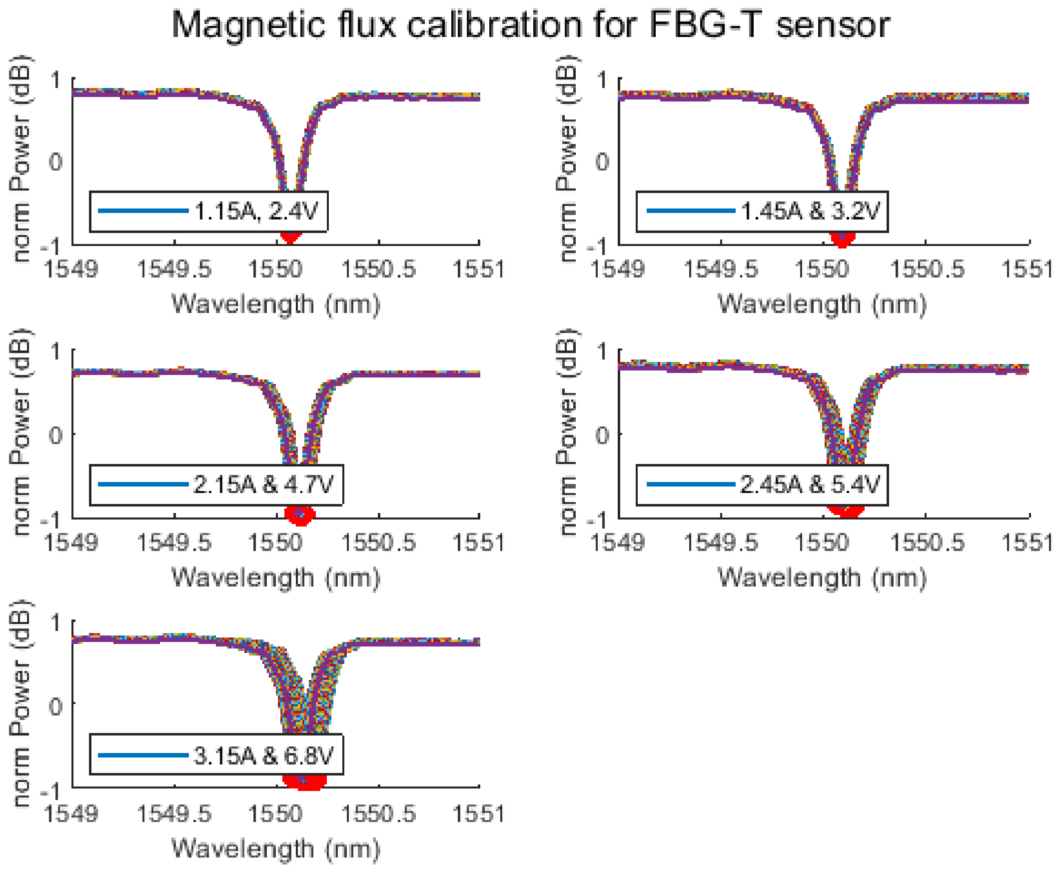

Figure 3-21: Optical spectra at different current and magnetic flux densities

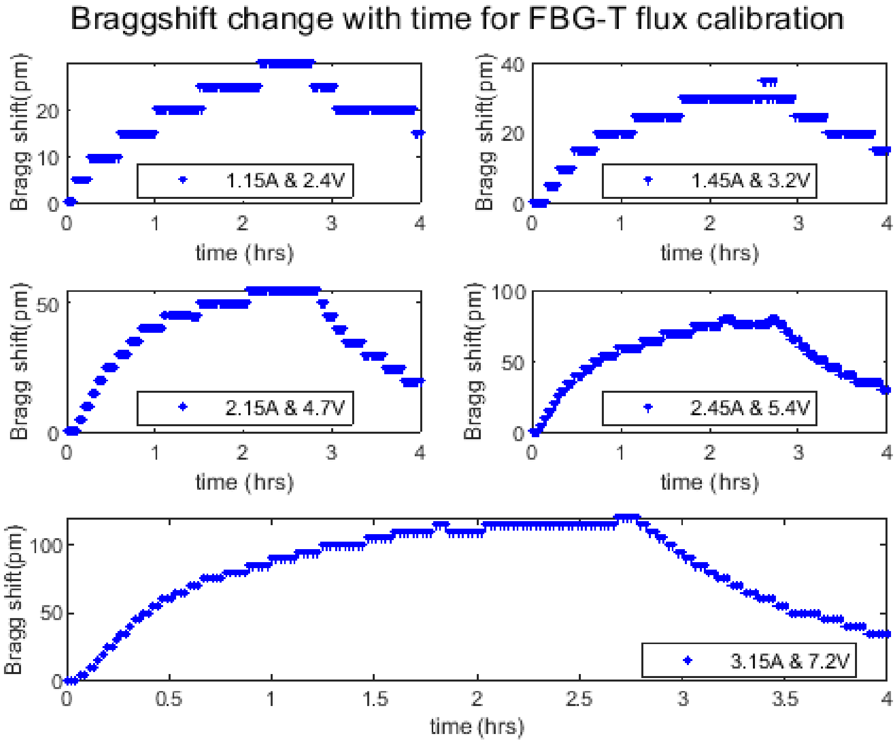

Figure 3-22: Time varying braggshifts at different currents and magnetic flux densities

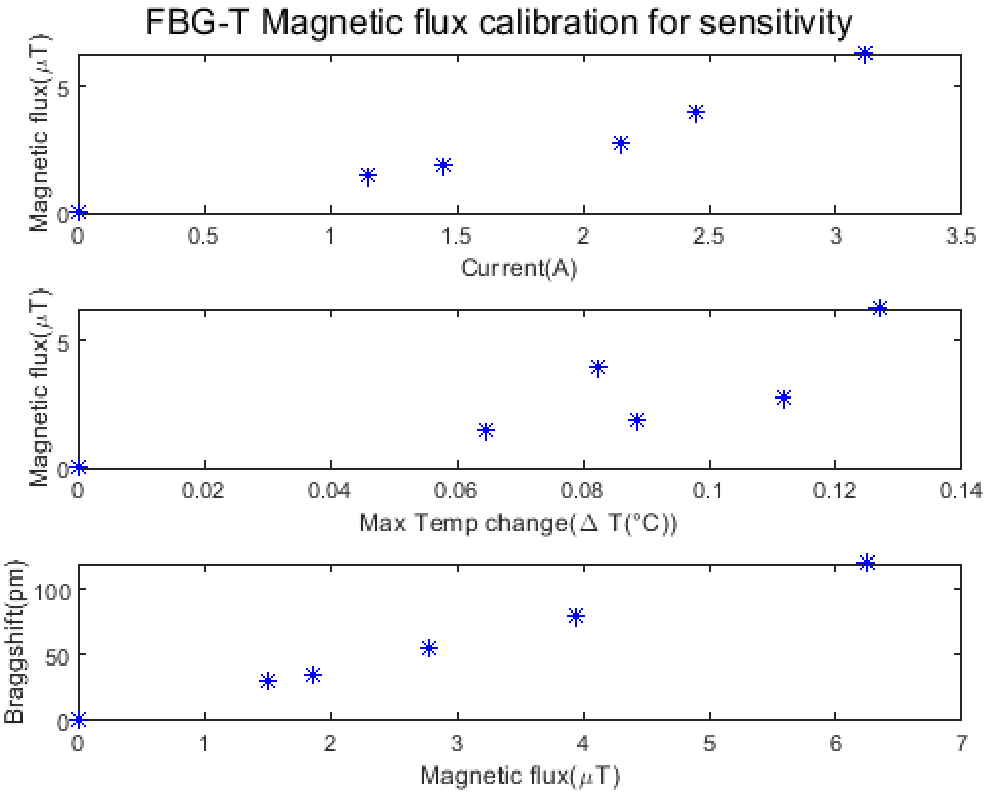

Figure 3-23: Plots of the changes of magnetic flux with current, braggshift and temperature

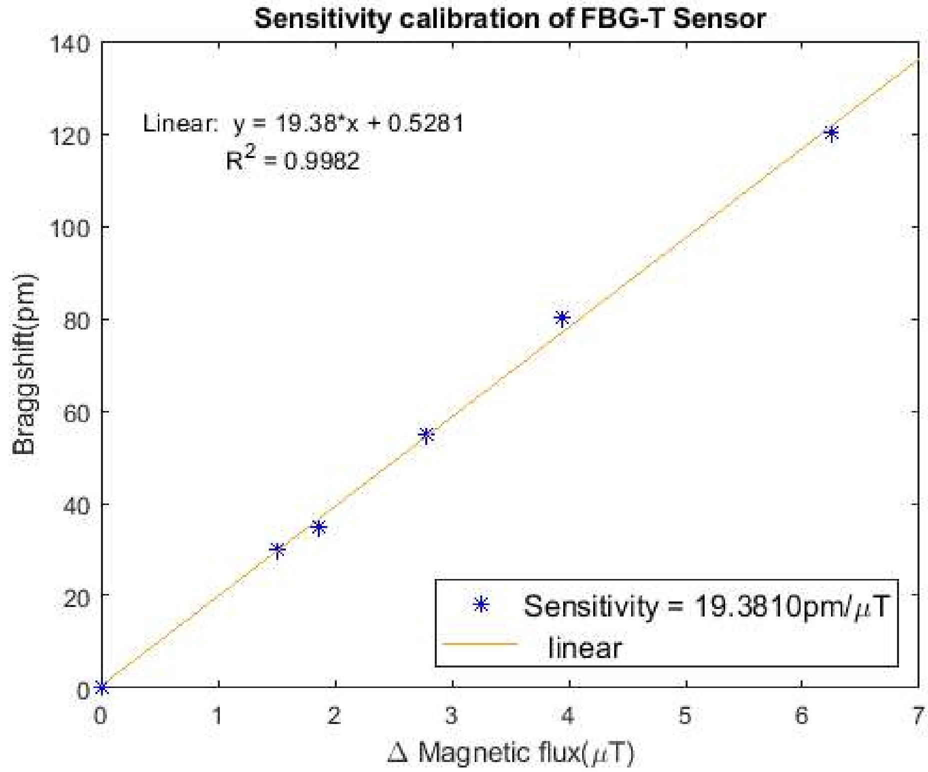

Figure 3-24: FBG-T magnetic flux sensitivity

3.6 Positioning FBG-T Sensor

The test rig for the experimental investigation was set up with the goal of testing different machine conditions. Due to the cross-disciplinary nature of the experiment, the work involved collaboration with research colleagues from AIPT. The FBG sensors were fabricated in-house in the AIPT laboratory by a post-doctoral colleague using phase-mask technique. The IMs used throughout this research are of the conventional radial flux geometry design. Two major factors were taken into consideration in positioning the FBG-T: proximity to the main air gap flux and sensor surface area exposed to the external flux. The closest part of the machine to the main air gap flux is the flange coupling at the DE of the machine. Hence, this was one of the positions considered. Three possible axes to position the sensor at the DE are:

- transverse (perpendicular to rotor shaft)
- inclined (intermediate between parallel and perpendicular to rotor shaft) or
- axial or longitudinal (parallel to rotor shaft)

The second option was very quickly discarded because magnetic fields are well known to be either at their maximum field strength or zero depending on whether the flux lines are cutting across a surface either perpendicularly or in parallel to the surface respectively. Transverse and longitudinal positions were later empirically tested to identify the optimal sensor position.

3.6.1 Axial (Longitudinal) Positioning

The schematic for axial positioning of the FBG-T is shown in Figure 3-25. Figure 3-26 shows the actual test rig for the axial (longitudinal) set up with the FBG-T sensor connected to the OSA. Two retort stands were used to clamp the tubed-FBG-T sensor, which is positioned axially. Prior to the start of the experiment, the machine flux was measured with and without the acrylic test tube to confirm that it did not affect the magnetic flux density being measured. A flux meter was positioned directly over the yoke just above the FBG-T sensor in order to measure the external magnetic flux cutting across the sensor; while the FBG-T sensor was centrally placed about 4cm away from yoke due to the limitation of the retort stands.

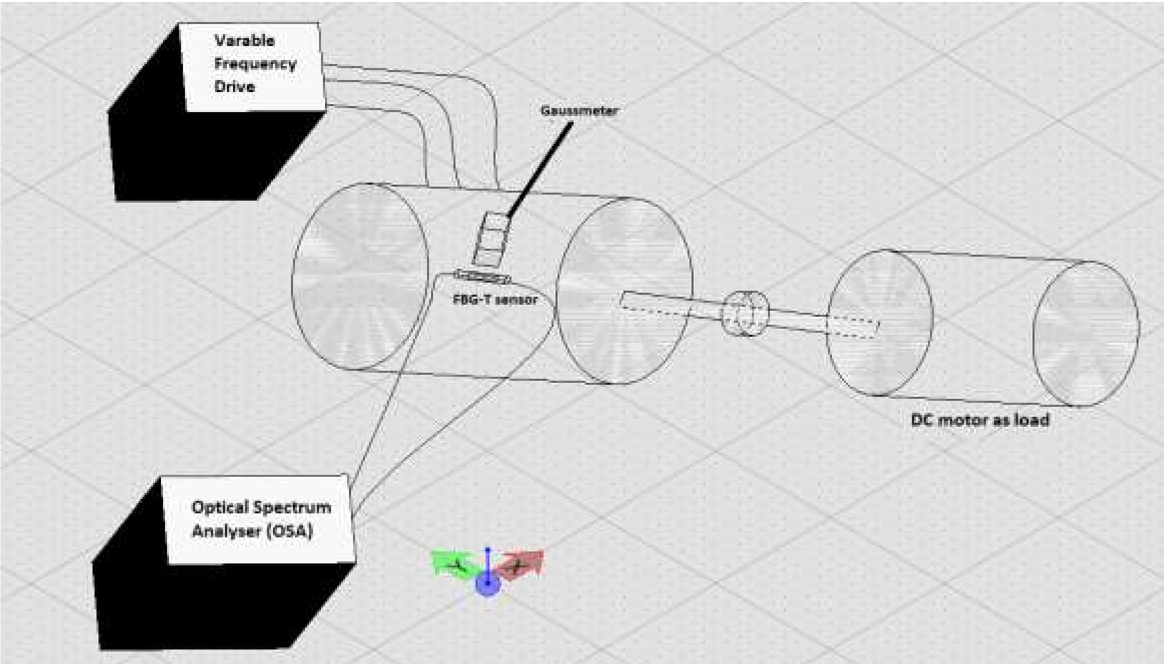

Figure 3-25: Schematic of FBG-T sensor in axial position

Figure 3-26: Axial positioning of FBG-T sensor for stray flux monitoring

3.6.1.1 Operating Conditions Investigated

The machine was run at different operating frequencies using a VFD ranging from 5Hz – 30Hz in steps of five. For each frequency, the machine was initially run for two hours then turned off for 18 hours to allow the FBG-T sensor to return to its initial or close to its initial wavelength. Pre-stress levels are known to affect terfenol-D magnetostrictive response [201], [202]. As a result, to mitigate the effects of pre-stress on the terfenol-D performance for each test, hence the 18 hours between tests so that only one test is run per day. This does not mean that the sensor requires 18 hours to reset before it is used. Provided the initial wavelength is known as the reference, the braggshifts can be computed without waiting for 18 hours to reuse the terfenol-D alloy. For example, the DC calibration test at five different currents and magnetic field strengths, was carried out within minutes apart. The magnetic behaviour of the terfenol-d transducer is such that its magnetic dipoles orientate in a certain way when magnetic field is applied to it. When the field is subsequently removed, the magnetic dipoles tend to seek a new state of rest. Despite field removal, the search for a new state of rest initially increases its entropy, thus causing the FBG to strain and experience more braggshifts. The magnetic moment of the dipoles then gradually decreases which then further reduces the amount of braggshift observed until they finally come to rest with zero entropy.

Parameters measured during this test are stray flux density, temperature and braggshift. Table 3-9 highlights the results obtained at the various frequencies. A maximum braggshift of 35pm was observed at 25Hz. Temperature was relatively constant with a maximum change of about 1.95 °C hence will have negligible effect on the FBG-T performance. The flux at maximum frequency (30Hz) was 1.7784µT which is quite small. This will be compared with the transverse position result.

Table 3-9: Data for axial positioning of FBG-T sensor

Frequency (Hz)	5	10	15	20	25	30
RMS Flux density (µT)	0.5671	1.0716	1.2873	1.5617	1.7142	1.7784
Max Braggshift (pm) during operation	5	20	10	20	30	30
Max Braggshift (pm) during 20 hours	10	20	15	25	35	30
Mean Temperature (°C) during operation	19.8846	21.56	20.5692	20.9077	19.6077	20.0538
Duration of operation	2 hours per frequency					

3.6.1.2 Result Analysis & Discussion

The increase in magnetic flux density with frequency was approximately linear as expected because the VFD also increased the voltage amplitude with frequency (see Figure 3-27). However, the magnitude of the maximum flux was quite small due to the severe attenuation of the main air gap flux which is one of the main functions of the yoke of any machine. Braggshifts were observed for all individual operating frequencies as shown in Figure 3-28 and Figure 3-29 which confirms the FBG-T is sensing the stray flux from the machine at different frequencies whilst in the longitudinal position. Due to the innate hysteresis nature of the terfenol-d transducer and the expected changing nature of the magnetic flux (since it is produced by an ac voltage), the *maximum* braggshift during the period of observation was of interest as well as the *change in wavelengths over time.* Another crucial parameter under consideration was the magnitude of the stray flux. This is particularly important given that the stray flux is already a severely attenuated version of the main air gap flux, its magnitude must be sufficient to cause a strain in the FBG-T sensor.

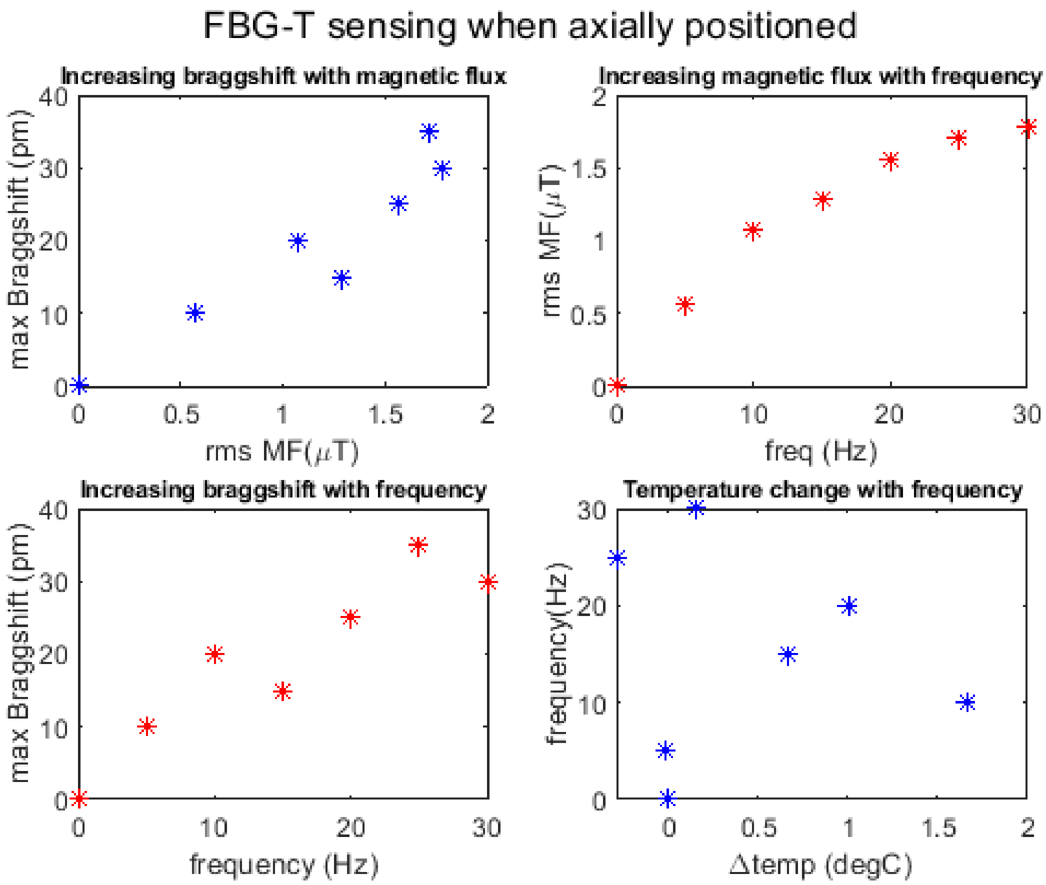

Figure 3-27: Results for FBG-T sensing in axial position

From Figure 3-27, owing to the severely attenuated magnetic flux lines, the corresponding braggshift per frequency is understandably small. This is not a problem but rather it is strong evidence of the performance characteristic of the FBG-T sensor and its ability to detect even very small flux changes due to high sensitivity. Indeed, a large amount of flux is not required as a pre-requisite for FBG-T sensing technology. Another observation was the slight increase in braggshift after the machine is turned off (loss of magnetic field after two hours). The increase was observed at 5Hz, 15Hz, 20Hz and 25Hz but not at 10Hz and 30Hz. There is no evidence of a link between the frequency and the behaviour of the magnetic dipoles within the magnetostrictive transducer. However, there is known theory as to the entropic behaviour of the magnetic dipoles in the terfenol-d alloy due to its quasi-ferromagnetic nature which decays over time. This behaviour is responsible for the further increase in braggshift shortly after the field is removed and given that it is random, the degree of randomness determines whether there will be some significant increase in braggshift or not. This was continuously monitored as the experiment progressed to observe any consistency in the sensor characteristic in this regard.

Figure 3-27 also shows that the temperature change was less than 2°C across all operating frequencies during the test, which is negligible. This is particularly important for the FBG-T sensor performance as both terfenol-D and FBG are sensitive to significant temperature changes.

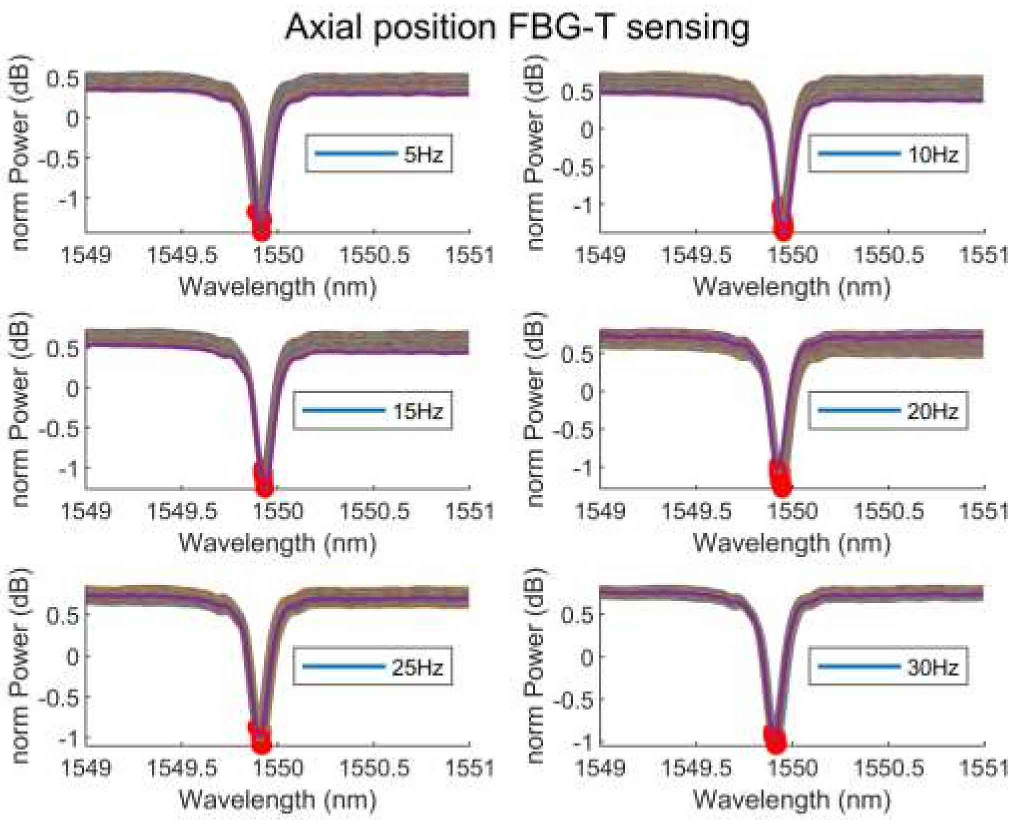

Figure 3-28: FBG-T optical spectra with FBG-T sensor in axial position

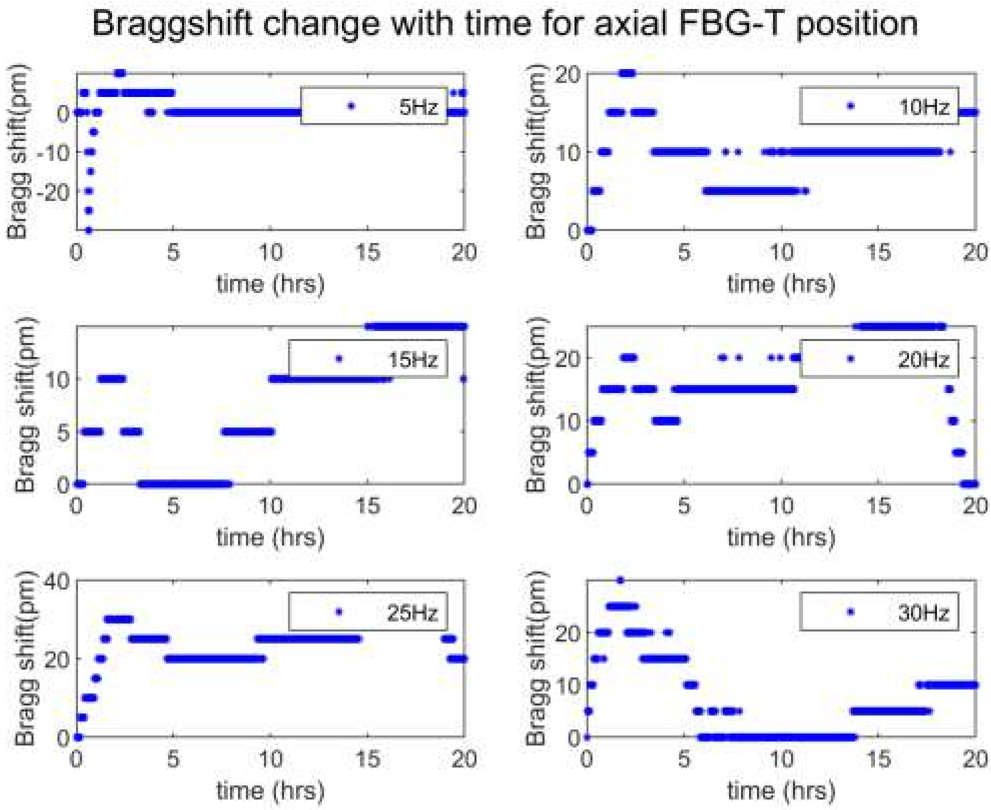

Figure 3-29: Braggshift variation with time with FBG-T in axial position

3.6.2 Transverse (Lateral) Positioning

The FBG-T sensor was then placed just above the flange coupling at the DE of the IM. The rotor shaft centre was used as a reference point for the sensor position as shown in Figure 3-30 with the flux meter directly above the sensor. The setup schematic is as shown in Figure 3-31.

Figure 3-30: Transverse positioning of FBG-T sensor for stray flux monitoring

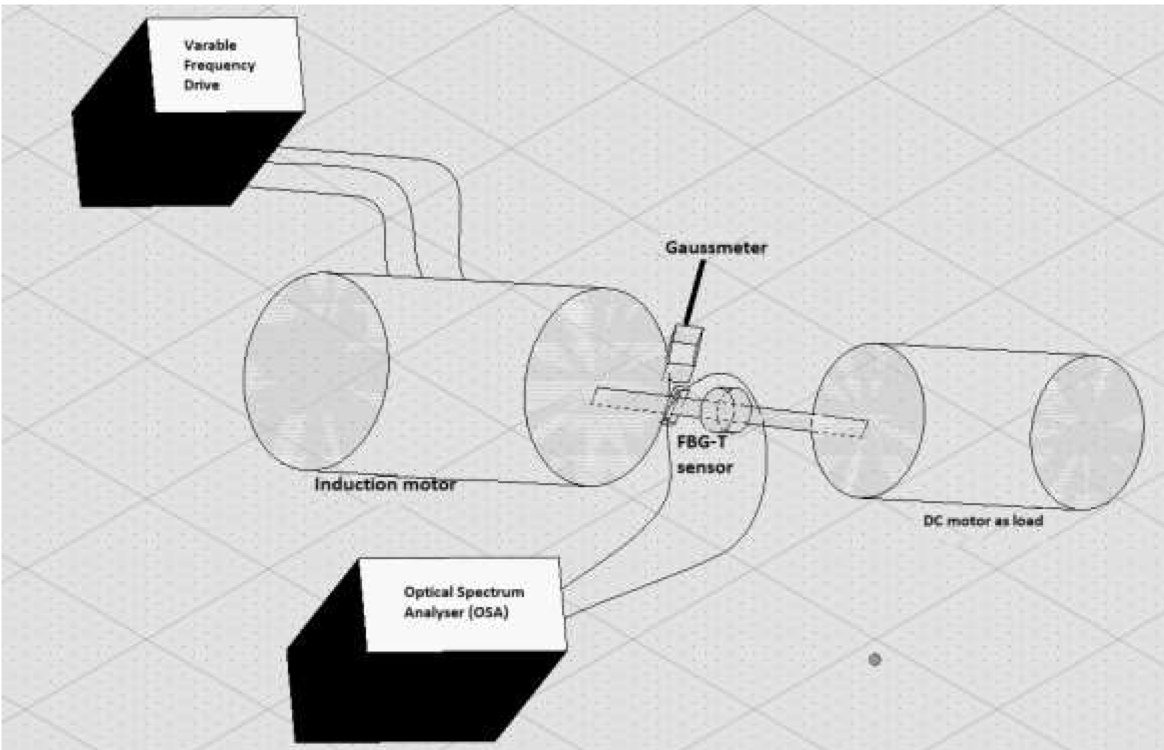

Figure 3-31: Schematic of FBG-T sensor in transverse position

3.6.2.1 Operating Conditions Investigated

The machine was also run at different operating frequencies using a VFD ranging from 5Hz – 30Hz in steps of five. For each frequency, the machine was initially run for two hours then turned off for 18 hours to reduce pre-stress levels and allow the FBG-T sensor to return to its initial or close to its initial wavelength. Stray flux density, temperature and braggshift were again measured at the six different frequencies (Table 3-10). A maximum braggshift of 55pm was observed at 20Hz. Temperature was again relatively constant with a maximum change of about 1.52°C hence will have negligible effect on the FBG-T performance. The flux at maximum frequency (30Hz) was 12.1654μT.

Table 3-10: Data for transverse positioning of FBG-T sensor

Frequency (Hz)	5	10	15	20	25	30
RMS Flux density (μT)	1.1410	4.1770	7.1228	9.5393	11.1127	12.1654
Max Braggshift (pm) during operation	30	50	45	55	45	45
Max Braggshift (pm) for 20 hours	35	55	55	65	65	70
Mean Temperature (°C) during operation	24.1615	23.96	24.8692	25.4154	25.1	25.6846
Duration of operation	2 hours per frequency					

3.6.2.2 Result Analysis & Discussion

As expected braggshifts were observed for all individual operating frequencies as shown in Figure 3-32, Figure 3-33 and Figure 3-34 which confirms the FBG-T is sensing the stray flux from the machine at different frequencies whilst in the transverse position. The magnitude of the flux density was observed to be higher with a more consistent behaviour of change in wavelength with time over all frequencies. This confirms the earlier suggestions that the yoke do have some significant attenuating impact on the stray flux. The increased flux densities and corresponding increase in braggshifts for each individual operating frequency is attributed to the reduced surface area of the yoke in the transverse sensor position including the absence of any yoke corrugations. In the transverse position there was also consistency in the behaviour of the sensor, with a gradual increase in braggshift as the machine is turned on. A further increase in braggshift as soon as the machine is turned off then occurs; and finally a descent towards its initial wavelength over time. This behaviour was observed in each of the six frequencies as shown in Figure 3-33. It will be observed the FBG-T may not end up at exactly its initial wavelength, this is primarily due to the inherent hysteresis feature of the terfenol-d. Each time, the new wavelength is taken as the initial wavelength behaviour when a magnetic field is applied to the sensor, as part of computing the braggshift. The increase in magnetic flux density with frequency was also approximately linear as expected because of the VFD and this time, with a higher flux density due to less attenuation of the main air gap flux when sensor is placed in the transverse position.

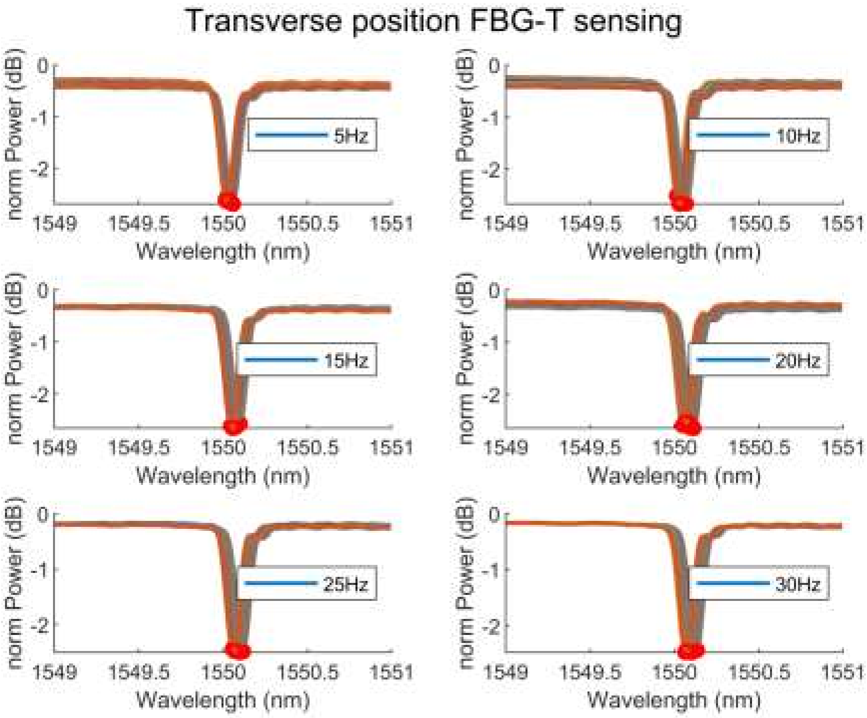

Figure 3-32: Optical spectra with FBG-T in transverse position

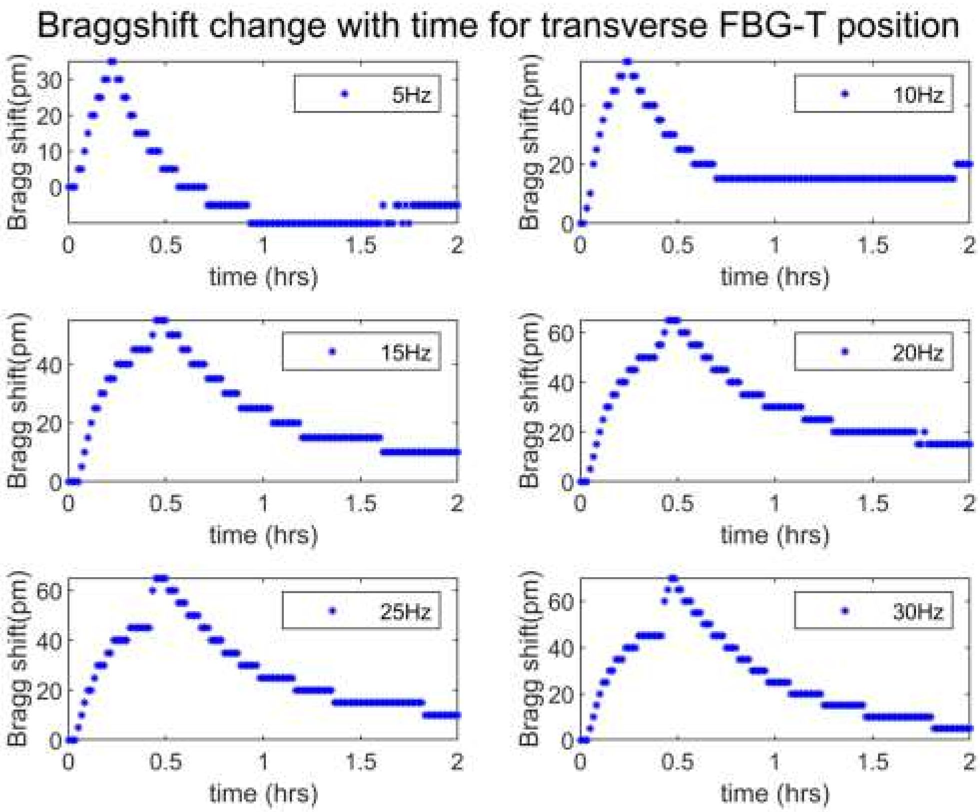

Figure 3-33: Braggshifts variation with time with FBG-T in transverse position

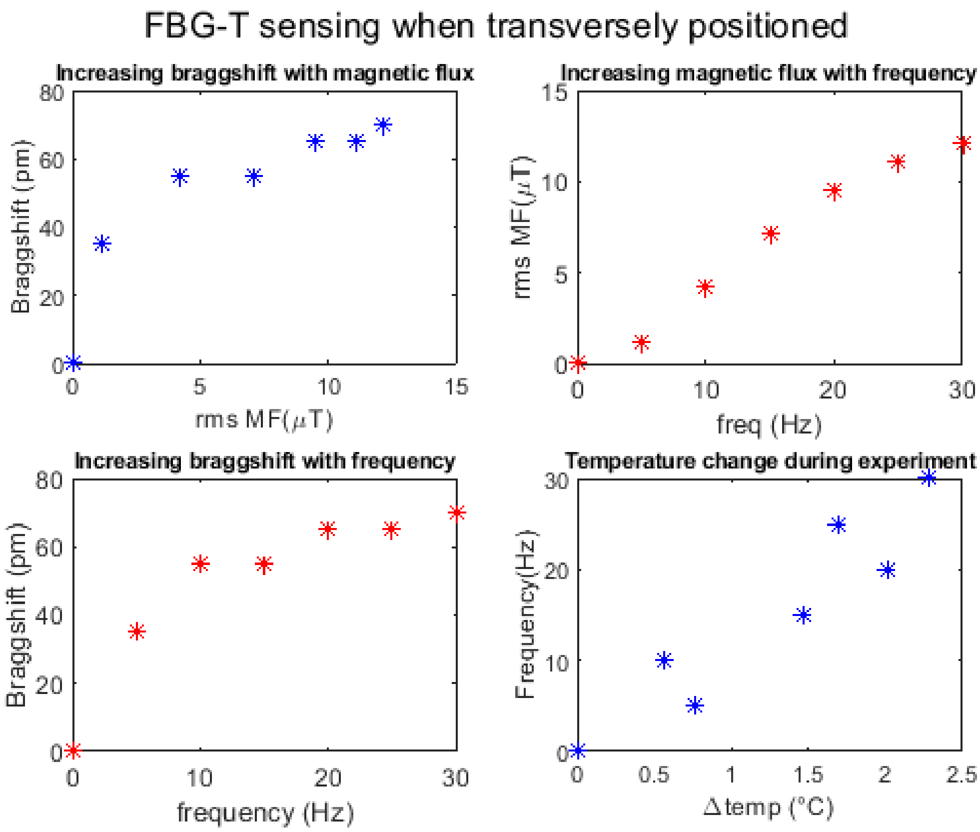

Figure 3-34: FBG-T sensing in transverse position

Figure 3-34 confirms an increase in braggshift with magnetic field strength at all frequencies although there appear to be an equal amount of braggshift at 10Hz and 15Hz, as well as 25Hz and 30Hz. This is very likely caused by the hysteresis behaviour of the terfenol-D, hence there will be an RT later as part of this investigation to further understand this behaviour. There was a consistent increase in braggshift after the machine is turned off (loss of magnetic field) for each individual frequency. This in theory, is due to the magnetic moment caused by entropy of the dipoles whilst moving to their final state of rest just before the temporary weakly-retained magnetic flux is completely lost (quasi-ferromagnetic behaviour). Figure 3-34 shows that the temperature change was negligible with a maximum change of less than 2.5°C across all operating frequencies during the test, hence will not impact on the FBG-T sensor performance.

3.6.3 Axial vs Transverse (Radial) Comparison

3.6.3.1 FBG-T Curve Characteristics Behaviour

Given the result analyses from both sensor positions, it is apparent that the transverse position offers more consistency in sensor behaviour which is in line with expectation in the presence and removal of magnetic field (see Figure 3-35). Axial positioning of the FBG-T offers erraticism and given the already inherent hysteresis property of the terfenol-d alloy; the introduction of additional unpredictability will cast doubts about the realisation of the reliable condition monitoring sensor for machines. It is noteworthy that the transverse sensor positioning does have some resetting to do each time the sensor is to be re-used as it may or may not return to its exact initial wavelength. Thus, it is experimentally justifiable to submit that the preferred positioning of the FBG-T sensor based on behavioural characteristic is the transverse position.

3.6.3.2 Magnitude of Observable External Stray Flux

Figure 3-35 also shows the variation of observable stray flux with frequency for both transverse and axial sensor positions. It is obvious that more flux will cut across the sensor when placed in the transverse position at the DE of the machine. Although this has been attributed to reduced surface area of the flux-attenuating and corrugated yoke, one can argue that the transverse position is closer to the source of the magnetic flux which is in the air gap within the machine. This is because the air gap is between the rotor and the stator whose windings are wrapped internally close to the flanges of the machine. Given that the stray flux is already mitigated, a detectable magnitude is required to cause magnetostriction in the FBG-T sensor. Hence, the preferred position based on observable magnetic flux will be the transverse position. Compared to literature, a similar work recently done by [51] reports similar results. Axial and radial (transverse) FBG sensor positions were examined for a surface permanent magnet rotor. The radial (transverse) positioning of the composite sensor (FBG with terfenol-

D) gave higher amplitudes of flux when compared to the axial position. This agrees with observations in this research. From both the behavioural characteristic and observable magnetic flux density viewpoints, the transverse position became the experimental choice and thus was utilised throughout the rest of the investigation.

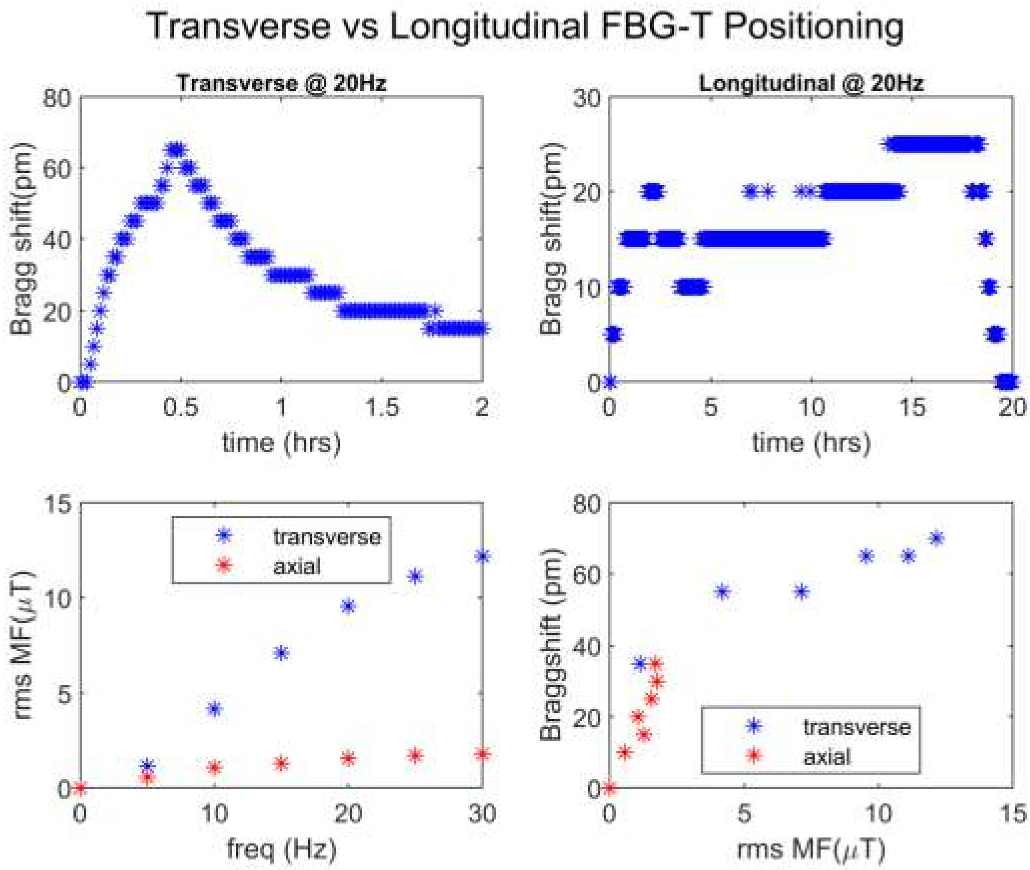

Figure 3-35: Comparison between FBG-T in transverse and axial sensor positions

3.7 Machine Operating Conditions Investigated

Three conditions were investigated: healthy motor, broken rotor fault (Chapter 4) and short circuit inter-turn fault (Chapter 5). The motor was run under two sets of frequency intervals for two hours continuously and four hours continuously: 5-30 Hz with a 5 Hz step interval and 10-50Hz with a 10Hz interval. In some cases, the machine was run for an extended period and intermittently depending on specific objectives such as evidence of the FBG-T sensor response to the presence and absence of stray flux. Table 3-11 summarise the investigation carried out and reported during this research.

Table 3-11: Investigations carried out during FBG-T condition monitoring

Frequency (Hz)		ON-time (hrs)		OFF-Time (hrs)		Healthy	5H		1H		Inter-turn	
5	10	2	4	18	16	✓	✓	✓	✓	x	✓	x
10	20	2	4	18	16	✓	✓	✓	✓	x	✓	x
15	30	2	4	18	16	✓	✓	✓	✓	x	✓	x
20	40	2	4	18	16	✓	✓	x	✓	x	✓	x
25	50	2	4	18	16	✓	✓	x	✓	x	✓	x
30	-	2	4	18	-	✓	✓	x	✓	x	✓	x
102030 on off		1 per freq (1hr on 1hr off)		14		✓	-		-		-	
102030 on		10Hz-1hr on 20Hz-1hr on 30Hz-18hr on		20		✓	-		-		-	
20 on off		3		17		✓	-		-		-	

It is crucial to state that the frequency interval for interrogation in LabView was every 60 seconds. This is because of the large amount of data per test, the limitation of the computer's processing capability where the data capture program was run and the very low resolution of the OSA available. The implication of this limitation is that the data analysed in this thesis are based on what has been observed using available equipment. However, with an equipment capable of higher rate time measurements of the braggshifts and having a higher resolution, more information about the characteristics of the braggshifts in relation to the FBG-T sensor behaviour can be obtained. For the purpose of providing empirical evidence that the concept of non-intrusive FBG-T sensing is practicable, results from this research are sufficient. However, in order to further analyse the measured parameters and further understand the concept, then higher resolution and at higher rates of measurements will be required. Also, the choice of 5-30Hz was completely based on the risk assessment carried out for the test rig prior to the start of the experiment. Exceeding 50Hz caused serious vibrations because of the platform on which the IM was installed. As a result, safety was prioritised and given that the motors were run via the VFD, it typifies variable speed applications which are now very common in many industrial machine applications.

3.8 Effect of Bonding Points on Metal-Surface Mount FBG Sensors

During the early part of the research prior to setting up the machine test rig, a separate work was carried out to study the effect of bonding points on metal-surface mount FBG sensors. A crucial aspect of the use of FBG for sensing application is its dependence on bonding in order to transduce sensed strain or temperature into optical braggshifts. It was observed that as the number of bonding points increased when the FBG is bonded to another material, the signal-to-noise ratio of the FBG spectrum deteriorated. An optimal number of bonding points for a given resolution of the OSA is thus, required to optimally utilise the FBG for sensing applications. The effect of increasing the number of bonding points on metal-surface mount

FBG sensors have been covered in the author's journal publication in [222].

3.9 Chapter Summary

This chapter has covered the underpinning principle of FBG sensing technology and how magnetostriction and optics have been merged to form a composite FBG-T sensor. Characteristics of the magnetostrictive transducer, terfenol-D have been discussed including the phenomenon of magnetostriction and some theories behind the microscopic behaviour of the magnetic dipoles of this material when subjected to a magnetic field. The step-by-step methodology for the investigation of the use of the FBG-T sensor for condition monitoring and fault detection of electric machines, IMs in this case, has been stated. Temperature and magnetic flux calibrations of the FBG-T sensor were then performed where sensitivities of 20.77pm/°C and 19.3810pm/μT were respectively obtained. Preliminary investigation on the optimal positioning of the FBG-T sensor either in axial or in transverse position was carried out. The latter position was found to generate comparatively better results with improved repeatability and sensitivity. From preliminary investigation in this chapter, the novel non-invasive sensing of stray flux using FBG-T has been demonstrated. The next chapters will investigate the capability of the FBG-T in discriminating between two different machine fault conditions.

Chapter 4

Broken Rotor Bar Fault Detection

BRB fault is classed as one of the common faults which can occur in the most widely used machine type, the squirrel cage IMs. This Chapter investigates the use of the FBG-T sensor in detecting broken rotor fault condition under various experimental test conditions. It will describe how each broken rotor condition is emulated, how the test rigs are set up, and the results analysed for healthy and two forms of the same BRB faults.

IM Broken Rotor Fault Detection Using FBG-T Sensor

The braggshift technique is the underpinning sensing principle for FBG sensing, however, most reviewed literature on the use of FBG in electrical machines applications have not directly utilise this principle (see Chapter 3). This principle as earlier explained makes FBG sensing simple and user friendly. However, in this analysis braggshift would be complemented with signature aberration to produce evident changes in machine conditions which is the basis for normalisation of the braggshift. To use the braggshift principle, a reference FBG-T spectrum with a specific wavelength is required to be tracked over time to detect the amount of change caused by the external flux. For the optical spectrum when the IM is under a healthy condition, a **spline** function in MATLAB has been used to recreate the spectrum to allow for a more accurate tracking of the coordinates of the minimum turning point along the Gaussian spectral curve. The spline is a mathematical function that allows the shapes of continuous and discontinuous curves to be captured with the piecewise polynomial (pp) function, extensively used in many applications to realise the Bezier or B-spline curve [223].

4.1 IM Conditions

Prior to monitoring any machine condition, a reference spectrum is required which will be tracked in order to account for any braggshifts caused by magnetostriction of the FBG-T sensor. In their work on FBG fabrication, [224], [225] demonstrated that for a multi-channel Gaussian shaped FBG, the reflected spectrum is given by:

$$|r(\lambda)| = \sqrt{R_f} \sum_{f=1}^{N} \exp\left(-\left(\frac{\lambda-\lambda_f}{b}\right)^4\right) \times \exp\left(i2\pi n_{eff}\left(\frac{1}{\lambda}-\frac{1}{\lambda_f}\right)d_f\right) \tag{4.1}$$

where N is the number of channels, b = 0.15 nm is the bandwidth of each channel, n_{eff} the effective refractive index, R_f is the desired reflectivity, λ_f (in nm) is the central wavelength, and d_j is a group delay parameter of the j-th channel. However, for this work a single channel FBG was used with centre wavelength of 1550.1nm i.e., N=1.

Given that the reflected broadband signal after introducing the FBG plus any noise is signal A(λ) and the broadband light source signal alone is signal B(λ), then there is need for normalisation of the spectrum to extract the reflected FBG spectrum only, C(λ). Initial measurement of B(λ) was obtained from the OSA as shown in Figure 4-1 (top); followed by measurements of the reflected broadband signal after introducing the FBG plus any noise, which is signal A(λ) shown in Figure 4-1 (middle). With the OSA already in logarithmic (dB) scale, normalisation of the FBG spectrum was carried out via software in MATLAB by logarithmically subtracting the light source from the reflected broadband signal after introducing the FBG plus any noise. The resulting signal after extracting the actual sensor spectrum (Figure 4-1 - bottom) is as follows:

$$C(\lambda) = A(\lambda) - B(\lambda) \tag{4.2}$$

4.1.1 Healthy machine

Three identical motors have been utilised as the devices-under-test (DUT) in this research with one used as a benchmarking design and the other two subjected to damage to emulate faulty conditions. The key properties of the specification are given in Table 4-1. The motor is driven by a VFD. Figure 4-2 shows its parts before assembly and commissioning when disassembled and as seen, they are all parts are in new and healthy state.

Table 4-1: Specification of the IM used

Specification	Induction Motor	VFD
Manufacturer	WEG	RS Pro
kW/hp rating	2.2/3	2.2/3
No. of phases	3	1 (in)/3(out)
Input voltage (V)	230/400	200-240
Rated Current (A)	7.93/4.58	21
No. of poles	4	-
RPM	1450rpm	0.01 - 599 Hz
Rated Torque (Nm)	14.49	-
Power factor	0.80	-

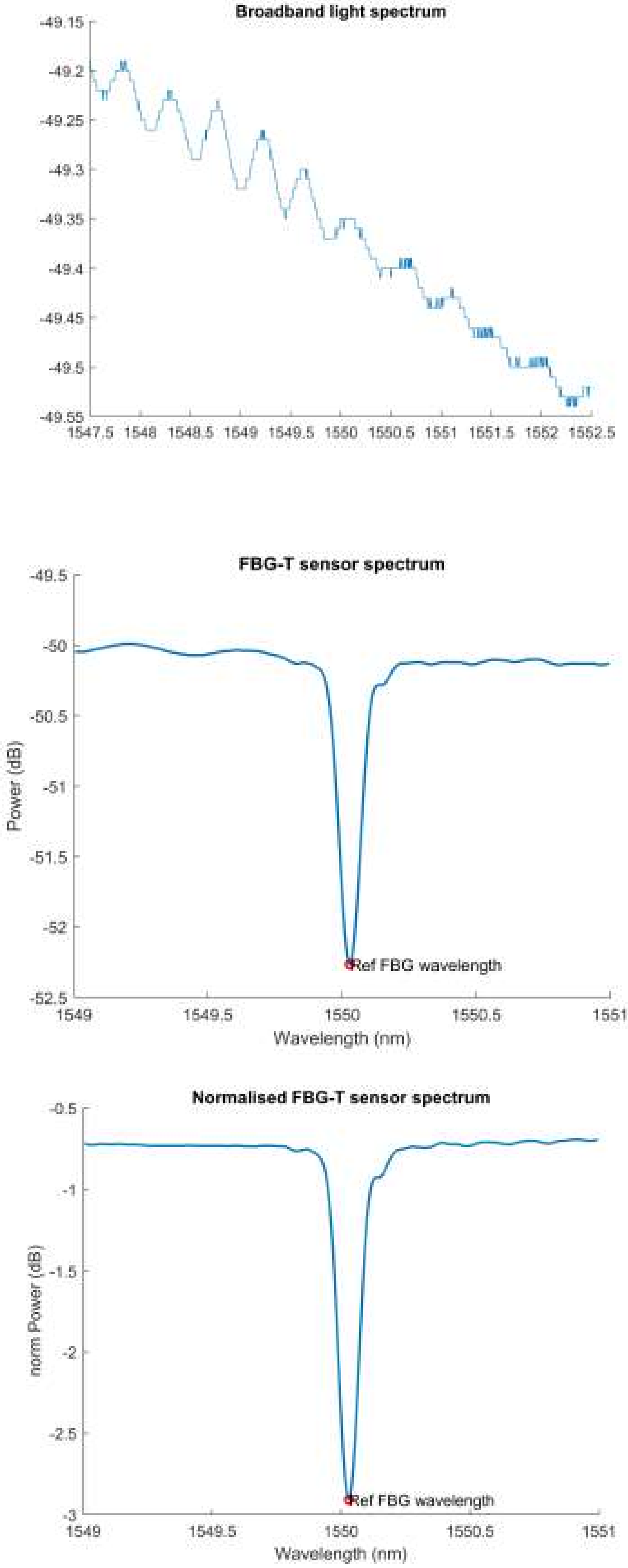

Figure 4-1: Normalisation of optical spectral responses for light source and FBG-T sensor

Figure 4-2: Disassembled healthy motor confirming its state

4.1.2 Emulation of Rotor Damage

A second IM was first subjected to a drill through its rotor squirrel cage to emulate a broken rotor. Figure 4-3 shows the rotor being broken in the in-house workshop. In order to investigate the FBG-T sensor capability to distinguish between faulty and healthy motor conditions. It should be mentioned that though the two BRB conditions appear different from the figure, they are the same single bar BRB as only one rotor bar was damaged.

Figure 4-3: Boring holes on rotor to emulate one single bar BRB condition

4.2 FBG-T Sensing Data Analysis & Discussion

The overview and actual test rig set ups for both healthy and broken rotor are shown in Figure 4-4. Each of the motors is used to drive a DC motor as load with the FBG-T transversely positioned at the DE of the IM using the rotor shaft centre as its reference. The sensor is then connected to the bi-functional broadband light source and OSA which serially connected to a PC via National Instrument GPIB cable. This is to allow the use of LabView software to collect and store numerical spectral data that can be retrieved and analysed in MATLAB. The motor was driven by a VFD.

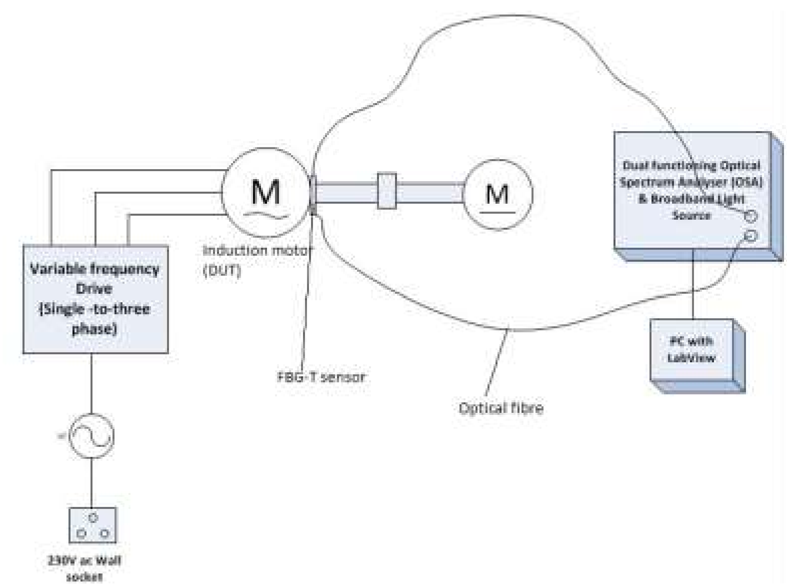

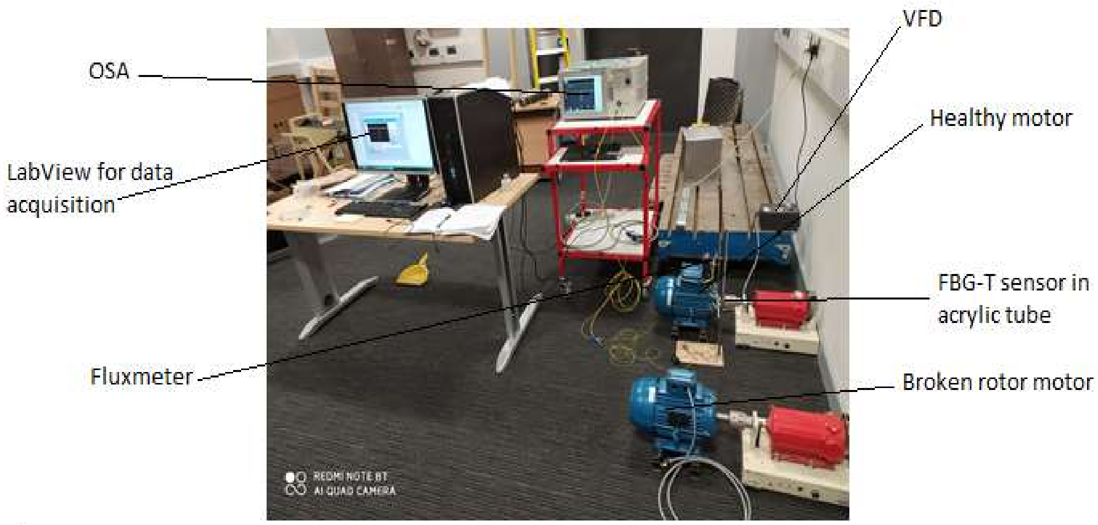

Figure 4-4: Schematic and actual experimental test rig set up

4.2.1 Normal Healthy rotor

4.2.1.1 Single Frequency Operation

Table 4-2 shows the measurements obtained under healthy rotor condition at the various operating frequencies. The IM was run for two hours per frequency then turned off for at least 18 hours to minimise pre-stress levels of the terfenol-D alloy, before the motor was re-run at the next frequency. Whilst the motor is running, instantaneous temperature and magnetic flux density readings were manually taken every 10 minutes, initially due to unavailability of a data logger.

Table 4-2: Healthy motor condition data for single frequency operation

Frequency (Hz)	5	10	15	20	25	30
RMS Flux density (μT)	1.141014	4.176973	7.122785	9.539344	11.11269	12.16544
Max Braggshift (pm) during operation	30	50	45	55	45	45
Max Braggshift (pm) during 20 hours	35	55	55	65	65	70
Max Temp. change (°C) during operation	1.4	1.6	1.4	1.8	1.5	1.4
Duration of operation	2 hours per frequency					

The optical spectra showing the braggshifts at various frequencies (Figure 4-5) do not provide any obvious information apart from corroborating the actual working of the FBG-T sensor whereas the sensor behaviour with time showed consistency. From the time varying plots of braggshifts in Figure 4-6, there is clear evidence of a reversible magnetisation where the magnetostrictive element returns to its original wavelength after the stray flux is removed across all test frequencies. However, before embarking on the return journey, the terfenol-D is observed to strain just immediately after the stray flux is lost. This is due to its paramagnetic nature where its magnetic dipoles attempt to re-orientate to a new state of magnetic equilibrium. This causes the FBG to strain as well causing some further braggshifts (more conspicuous in Figure 4-6 braggshift plots for 15Hz, 20Hz, 25Hz and 30Hz) which does not last once the weak residual magnetism is completely lost. Immediately after this occurrence, the return journey commences. Another important observation from the time varying braggshift plots was the irregular hysteresis property of terfenol-D as the sensor did not make it to its initial wavelength by the time the terfenol-D returned to its initial length. Apart from the hysteresis nature of terfenol-D, it is possible that as the rate at which the magnetostriction reduces with time, the observable micro-strain near the end of the sensing process could become smaller than the sensitivity of the grating. This can lead to failure of the FBG to respond especially given that it largely depends on the adhesive between the terfenol-D and itself for micro-strain sensing. The order of magnitude for the strain is already in pm wavelength which means the FBG is already proving its micro-strain capability. For condition monitoring purposes, the focus is on the braggshift due to machine operation. Figure 4-7 depicts the observed relationship between braggshifts, frequency and magnetic flux density. Increase in frequency was accompanied by a corresponding increase in the magnetic flux but the braggshifts observed appear to be less linear and even disproportionate. However, across the entire frequency range, the order of magnitude of the braggshifts was consistent between 30pm and 70pm. Maximum observed temperature change was less than 2°C across the entire operating frequency range as there was a non-linear relationship between the temperature changes observed and frequency. The importance of temperature measurement is to ascertain that the braggshifts observed are largely due to stray flux rather than temperature.

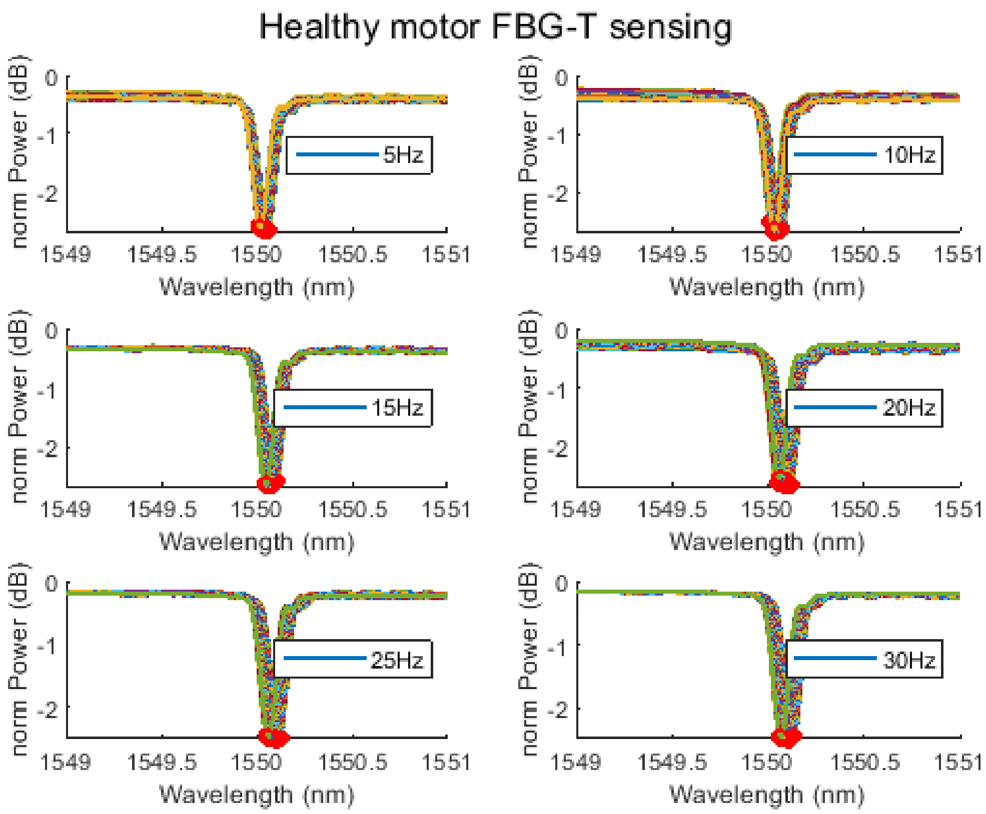

Figure 4-5: Optical spectra of motor under healthy condition

4.2.1.2 Multi-Frequency Operation

The purpose of this multi-frequency test is to corroborate the reliability of the FBG-T sensor in responding to the *presence or absence* of stray flux. In order to further verify that the stray flux is responsible for the braggshifts, the motor was operated under several different conditions such as intermittently turning the machine on and off to emulate presence and absence of stray flux respectively. First, the motor was run for 20 hours at 10Hz, 20Hz and 30Hz non-stop as shown in Figure 4-8.

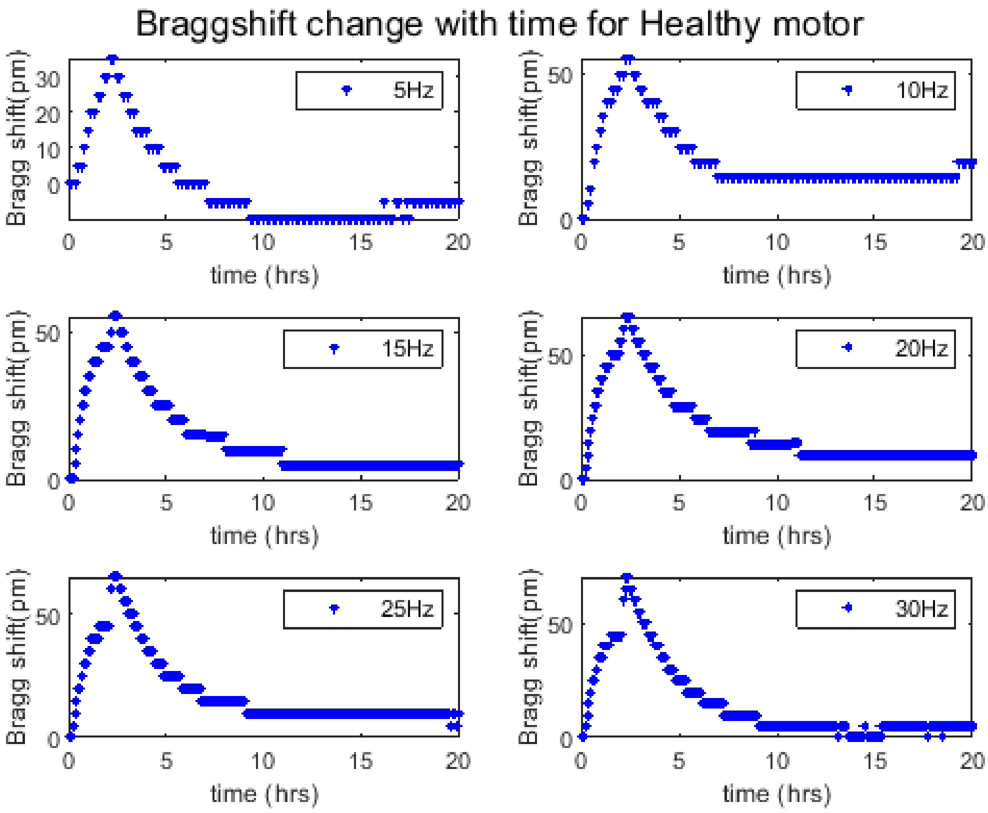

Figure 4-6: Braggshift under healthy condition

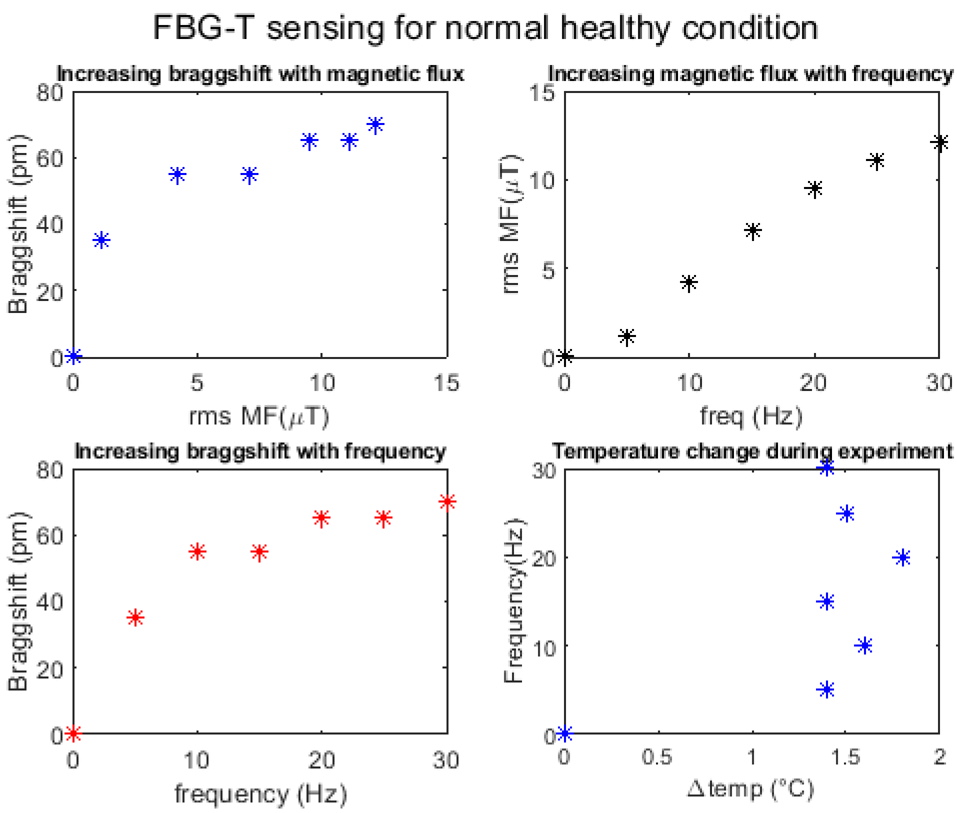

Figure 4-7: Variation of magnetic flux density with frequency, braggshifts and temperature for a healthy IM

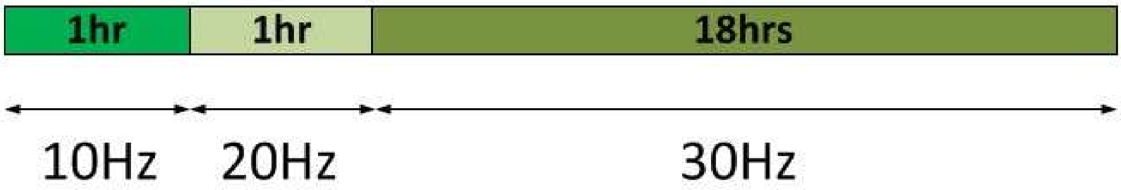

Figure 4-8: Time pattern showing 20-Hour continuous operation of motor

Figure 4-9 and Table 4-3 show the results of the first multi-frequency test. Initially at 10Hz the maximum braggshift observed was 30pm until when the motor frequency was changed to 20Hz during the next hour. The maximum braggshift remained at 30pm for most of the time before increasing to 35pm. A similar response was observed with no initial significant change in braggshift with a further increase in frequency to 30Hz until later, when the maximum braggshift finally settled at 40pm for the remaining 18-hour period. The FBG-T sensor began its reversible magnetism behaviour as soon as the machine was switched off. Owing to the hysteresis nature of terfenol-D, the sensor made it to a slightly different wavelength compared to its initial wavelength. This reset aberration is not particularly important for the application of the use of FBG-T sensing in machine condition monitoring; because the initial wavelength can be changed and braggshift is relative to any chosen initial wavelength not an absolute value.

Table 4-3: Data for multi-frequency first test operation

Test number	Frequency range (Hz)	RMS Flux density (μT)	Max Braggshift (pm) during ON operation	Pattern of operation (non-stop)		Key observations
				ON	OFF	
1	10	4.075036	30	1	-	Braggshift increased with increase in the motor frequency during operation in a non-linear manner
	20	9.35003	35	1		There was a steady but disproportionate rise in the magnitude of the stray flux as the frequency was increased
	30	12.20455	40	18		FBG-T sensor mainly responded to the presence of the stray flux - not necessarily its magnitude but to its nature or spectral content

Overall, provided the stray flux was continuously present and not interrupted, there was a 5pm braggshift increase with increase in the motor frequency during operation. This observation suggests that the frequency of the stray flux does influence the FBG-T response whether in a linear or nonlinear manner; this will be explored in more tests to be reported. Another factor that can cause the further increase in braggshift is the amplitude of the stray flux. There was a steady but disproportionate rise in the magnitude of the stray flux when the frequency was increased. How much of the FBG-T response is due to the amplitude of the stray flux is not yet known. However, given that disproportionate increase in the amplitude resulted in the same amount of braggshift each time the motor frequency was changed raises doubts as to whether the amplitude is solely responsible for such response. Hitherto, the goal is to establish that the FBG-T sensor can respond accurately to the presence and absence of stray flux. From the initial observation, it means that the magnetostrictive transducer in the FBG-T sensor mainly responds to the presence of the stray flux - not necessarily its magnitude only, but also to its frequency components - as its magnetic dipoles orientate to find a new quasi-equilibrium state whilst the stray flux is still present.

The above submission of the FBG-T sensor response to the presence of magnetic flux was corroborated in two other experiments where the stray flux was intermittently removed.

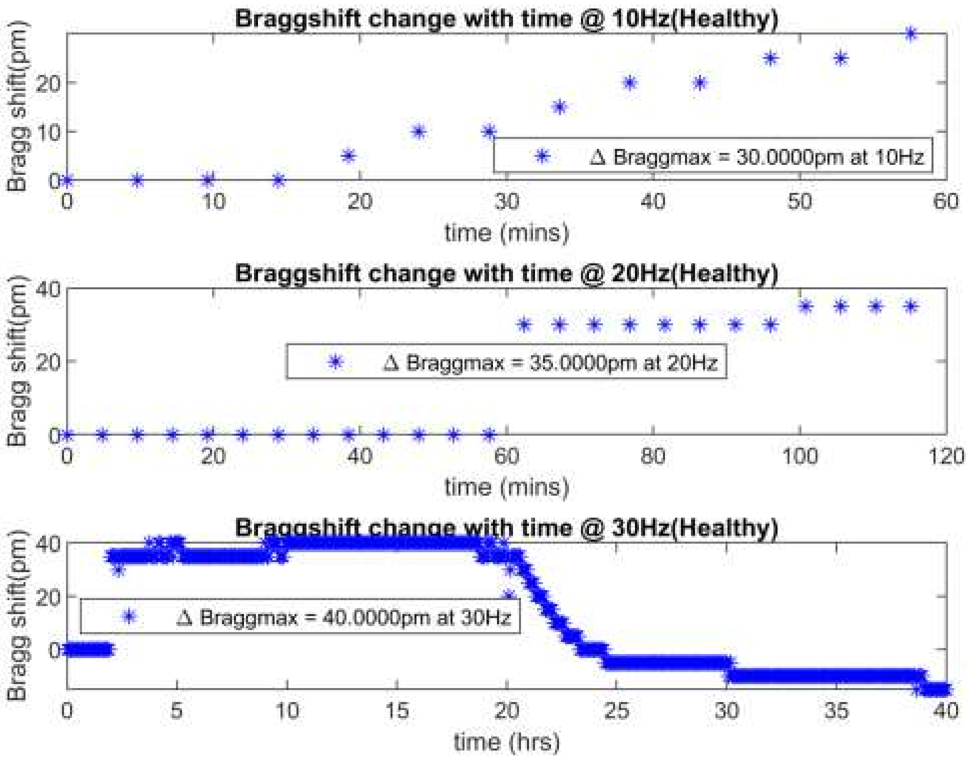

Figure 4-9: Braggshift response when machine was run continuously at three different frequencies

Next, the motor was run at three different frequencies with intermittent switching off and on prior to changing the frequency in a pattern as shown in Figure 4-10.

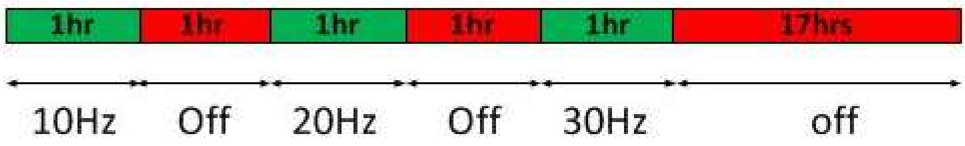

Figure 4-10: Intermittent switching pattern for the second multi-frequency test

The motor was initially run at 10Hz for one hour then turned off for one hour. Then it was run at 20Hz for another one hour before being turned off for yet another one hour and finally run at 30Hz for an hour, before finally turning it off for 17 hours to reduce the pre-stress level of the FBG-T sensor. In the third multi-frequency test, the motor was run at the same frequency of 20Hz for one hour, turned off for the next hour before being turned back on, and so on. This was done such that the motor was turned on for three hours cumulatively and turned off for 17 hours to allow the FBG-T sensor pre-stress level to be minimal as illustrated in Figure 4-11.

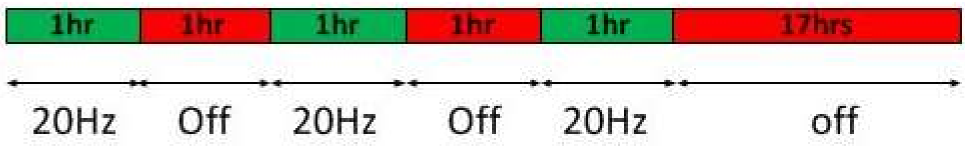

Figure 4-11: Intermittent switching pattern for the third multi-frequency test

In both second and third multi-frequency test scenarios, the FBG-T sensor behaved in the same way in response to the presence and loss of the stray flux as shown in Figure 4-12 and Figure 4-13; although with different amounts of maximum braggshifts during each test. During the second test, the FBG-T sensor at 10Hz initially experienced a strain equivalent to 50pm when the motor was in operation. However, soon after the motor was switched off and the stray flux was lost, the sensor slowly began its reversible magnetisation behaviour back to its initial wavelength. After an hour, with the motor turned back on at 20Hz, the FBG-T sensor immediately responded to the presence of stray flux by increasing its braggshift once again and recorded a higher braggshift of about 75pm relative to its initial wavelength. The reason for the higher braggshift is due to its new initial state which was about 25pm before the stray flux was re-introduced as shown in Figure 4-12. If we add the new initial state with 25pm to the previous maximum of 50pm, the new maximum braggshift should be 75pm in theory which corresponds to the newly observed maximum braggshift. This result thus suggests that the FBG-T sensor responds to the presence of the stray flux rather than the difference in operating frequency even though the magnitude of the stray flux was higher at 10Hz than at 20Hz. A consistent sensor response was observed once again when the motor was turned off. The FBG-T suddenly responded to the loss of stray flux which is responsible for the gradual reduction in the observed braggshift between 3-4 hours of the tests (see Figure 4-12). As soon as the motor was turned back on at 30Hz on the 4th hour, the FBG-T sensor immediately responded as before to the presence of the stray flux by halting the gradual decline of braggshift. It then increased up to 90pm maximum (relative to its initial wavelength) after the motor was turned off following operation at 30Hz for one hour. Table 4-4 summarises results from second multi-frequency test.

Table 4-4: Data for multi-frequency second test operation

Test number	Frequency range (Hz)	RMS Flux density (µT)	Max Braggshift (pm) during ON operation	Pattern of operation (non-stop) ON	Key observations
2	10	4.151741	50	1	Braggshift increased with increase in the motor frequency during operation in a non-linear manner
	OFF				There was a steady but disproportionate rise in the magnitude of the stray flux as the frequency was increased.
	20	9.423407	75	1	Stray flux magnitude was very identical to previous values
	OFF				FBG-T sensor reliably detected the presence and absence of stray flux (See **Error! Reference source not found.**)
	30	12.5504	90	1	
	OFF				

Relative to the previous maximum braggshift of 75pm, there is a further 15pm braggshift. This means an initial 50pm maximum braggshift was observed at 10Hz during the first one hour of operation, followed by a further 25pm braggshift at 20Hz after the stray flux was re-introduced and finally another additional 15pm braggshift at 30Hz when the stray flux was again re-introduced. There is evidence of an increase in braggshift whenever the stray flux is re-introduced at a higher frequency, but the braggshift appear to be nonlinear for the same change in frequency. It is known that the terfenol-D element of the FBG-T sensor is non-linear and has hysteresis which is responsible for the non-linearity in the amount of braggshift observed, but there is no doubt in the FBG-T response to the presence and absence of stray flux. To further substantiate this evidence, the third test of operating the motor at the same frequency of 20Hz whilst switching the motor on and off showed identical behaviour as shown in Figure 4-13.

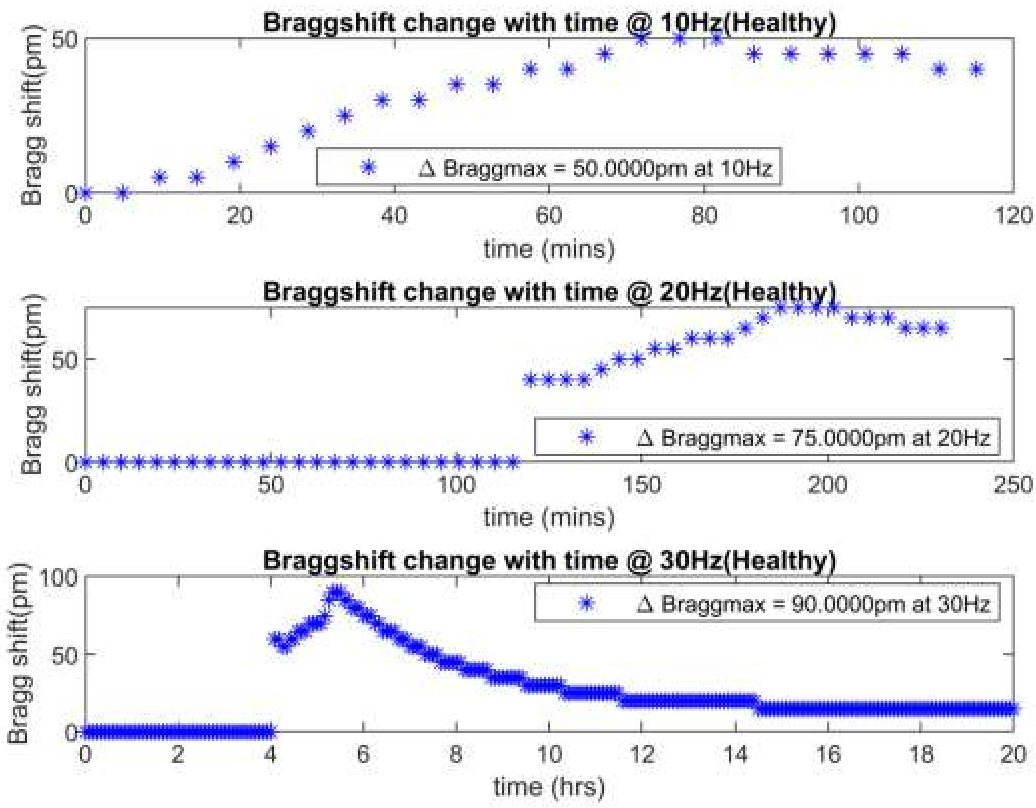

Figure 4-12: Braggshift response when machine was switched on and off intermittently

An initial maximum braggshift of 40pm was observed during the first hour of operation when the stray flux was present. Immediately after the stray flux was lost in the next hour, the FBG-T response was a gradual decline of observed braggshifts until about 35pm when the motor was switched back on. The FBG-T response to the re-introduction of the stray flux was again an increase in braggshift up to a maximum of 50pm relative to the initial wavelength. In other words, an increase of 10pm compared to the previous maximum braggshift. As earlier explained, this is due to the non-linear and hysteresis behaviour of terfenol-D as the magnitude of the stray flux remained within the same range as shown in Table 4-5.

Table 4-5: Data for multi-frequency third test operation

Test number	Frequency range (Hz)	RMS Flux density (μT)	Max Braggshift (pm) during ON operation	Pattern of operation (non-stop) ON	Key observations
3	20	9.351728	40	1	Braggshift decreased each time stray flux was lost and then increased each time stray flux was re-introduced
	OFF				Stray flux magnitude was reasonably constant each time at 20Hz
	20	9.44335	50	1	
	OFF				FBG-T sensor reliably detected the presence and absence of stray flux (See Figure 4-14)
	20	9.50511	60	1	
	OFF				

The non-uniform oscillatory behaviour between presence and absence of stray flux was further observed when the motor was turned off for the following hour and then switched back on for another hour (between 4th and 5th hour). A maximum braggshift of 60pm was reached relative to the initial wavelength which accounts for a further 10pm braggshift compared to the previous maximum braggshift. Although the magnitude and frequency of the stray flux remained reasonably constant, further braggshifts were observed each time the stray flux was re-introduced. When the flux was finally removed after the motor was switched off; the reversible characteristic of the FBG-T sensor became evident as shown in Figure 4-14. There is now clear evidence that the FBG-T sensor responds to stray flux. Based on the theory of magnetostriction, the above sensor behaviour is understandable because magnetostriction lies in the non-uniform motion of the magnetic dipoles within the given material, which is primarily caused by the presence or absence of a magnetic field.

The test operations above do disrupt the motion of these magnetic dipoles causing them to move in a certain way to align themselves with the direction of the field and then suddenly forces them to go back to another non-aligned state of rest. Whilst this phenomenon is taking place, the motion being transferred to the FBG as strain does not take the direction of the magnetic dipoles into consideration as strain is a scalar quantity not a vector, hence the braggshift regardless of whether the magnetic field is lost or re-introduced. As earlier explained by several physicists [193] the reason why these magnetic dipoles move unpredictably and unevenly is still not known. Hence magnetostriction continues to be treated as a phenomenon with no known mathematical model. For using FBG-T as a reliable condition monitoring and fault detection sensor, the clear evidence of an accurate and consistent response of the sensor to the presence of stray flux offers the opportunity to further explore its use and understanding its limitations. Table 4-6 summarises the observation for the multi-frequency tests for the healthy IM. Next is to test the FBG-T sensor against different machine conditions for the purpose of fault detection during condition monitoring.

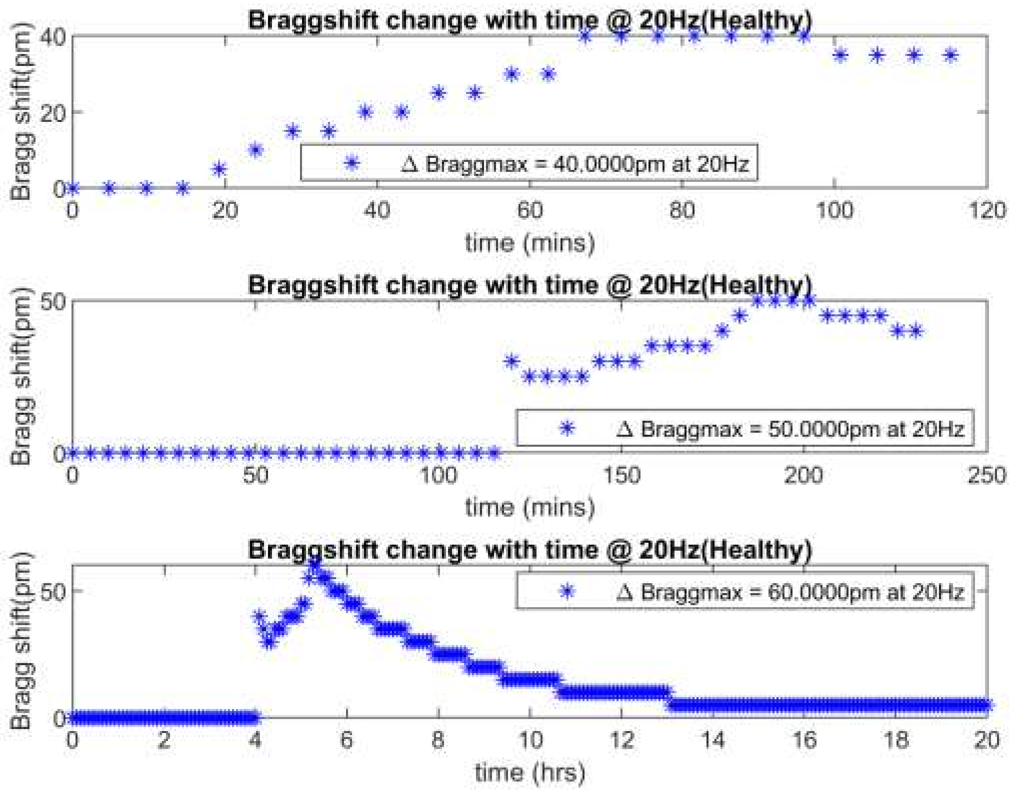

Figure 4-13: Braggshift response when machine was switched on and off intermittently

Table 4-6: Healthy motor condition data for multi-frequency operation

Test number	Frequency range (Hz)	RMS Flux density (μT)	Max Braggshift (pm) during ON operation	Max Braggshift (pm) during ON&OFF hours	Max Temp. change (°C) during operation	Duration of operation (hours)	
						ON	OFF
1	10	4.075036	40	40	1.1	1	20
	20	9.35003				1	
	30	12.20455				18	
2	10	4.151741	-	90	2.5	1	1
	20	9.423407				1	1
	30	12.5504				1	15
3	20	9.351728	-	60	1.8	1-0-1-0-1-0	
		9.44335					
		9.50511					

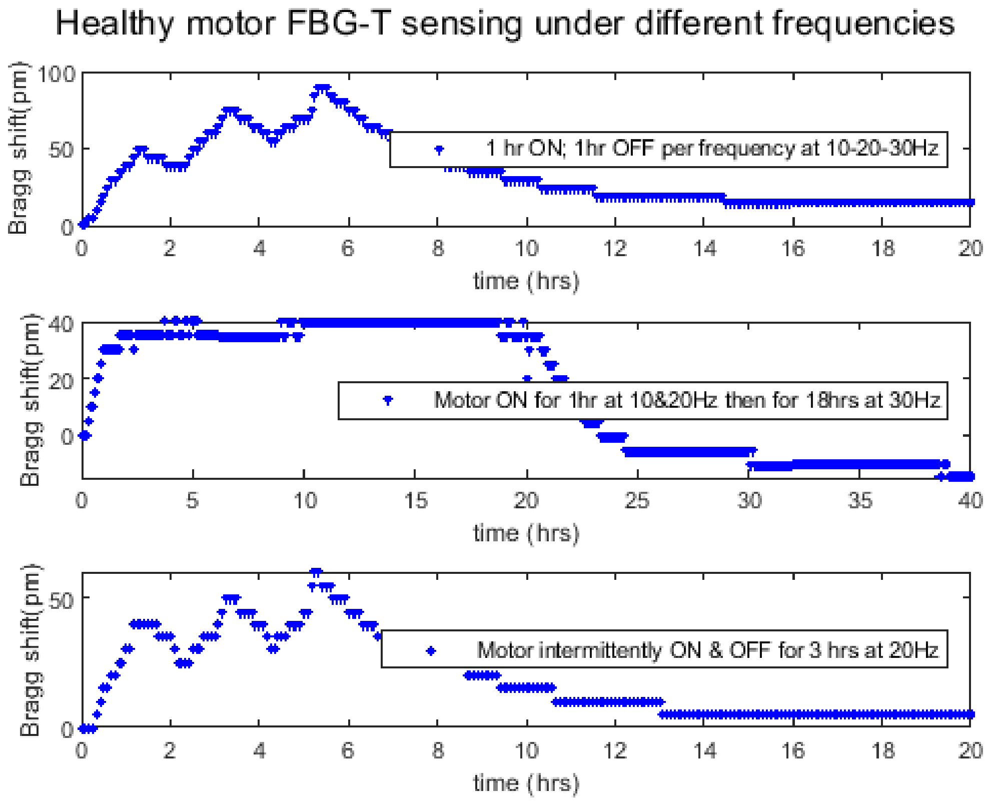

Figure 4-14: Braggshifts observed under various operating conditions for a healthy motor

4.2.2 Broken Rotor Conditions

FBG-T sensor spectral response when machine was run under the single bar BRB conditions as shown in Figure 4-15 did not provide any obvious observation regarding the specific rotor condition but rather confirmed the occurrence of braggshift which is evidence of the sensor responding to the presence of stray flux. The time varying braggshift response for BRB in Figure 4-16 did show that the FBG-T sensor does sense further strain immediately after the stray flux is lost. This is consistent with earlier observations owing to the paramagnetic nature of terfenol-D. The magnitude of maximum braggshift was again inconsistent with change in frequency under the single bar BRB conditions. However, what was consistent was the order of magnitude of the braggshifts. Generally, under the broken rotor condition they were largely above the mid-50s and closer to the 100pm mark. Temperature change during tests of both conditions was reasonably minimal with a maximum change of 2.2°C during the 10Hz frequency one-hole single bar BRB test. For the five-hole single bar BRB test, the maximum temperature change was 1.2°C. In theory both one-holed and five-holed single bar BRB are the same fault as only one single rotor bar is broken. There was direct relationship between the frequency and amplitude of the stray flux as expected but this apparently did not result in a similar directly proportional braggshift as summarised in Table 4-7, Figure 4-16 and Figure 4-17. Because both faults are one and the same even though looked different, the FBG-T response was identical as shown in Figure 4-15, Figure 4-16 and Figure 4-17. The FBG-T sensor thus is able to detect two different forms of the same BRB fault with identical braggshifts.

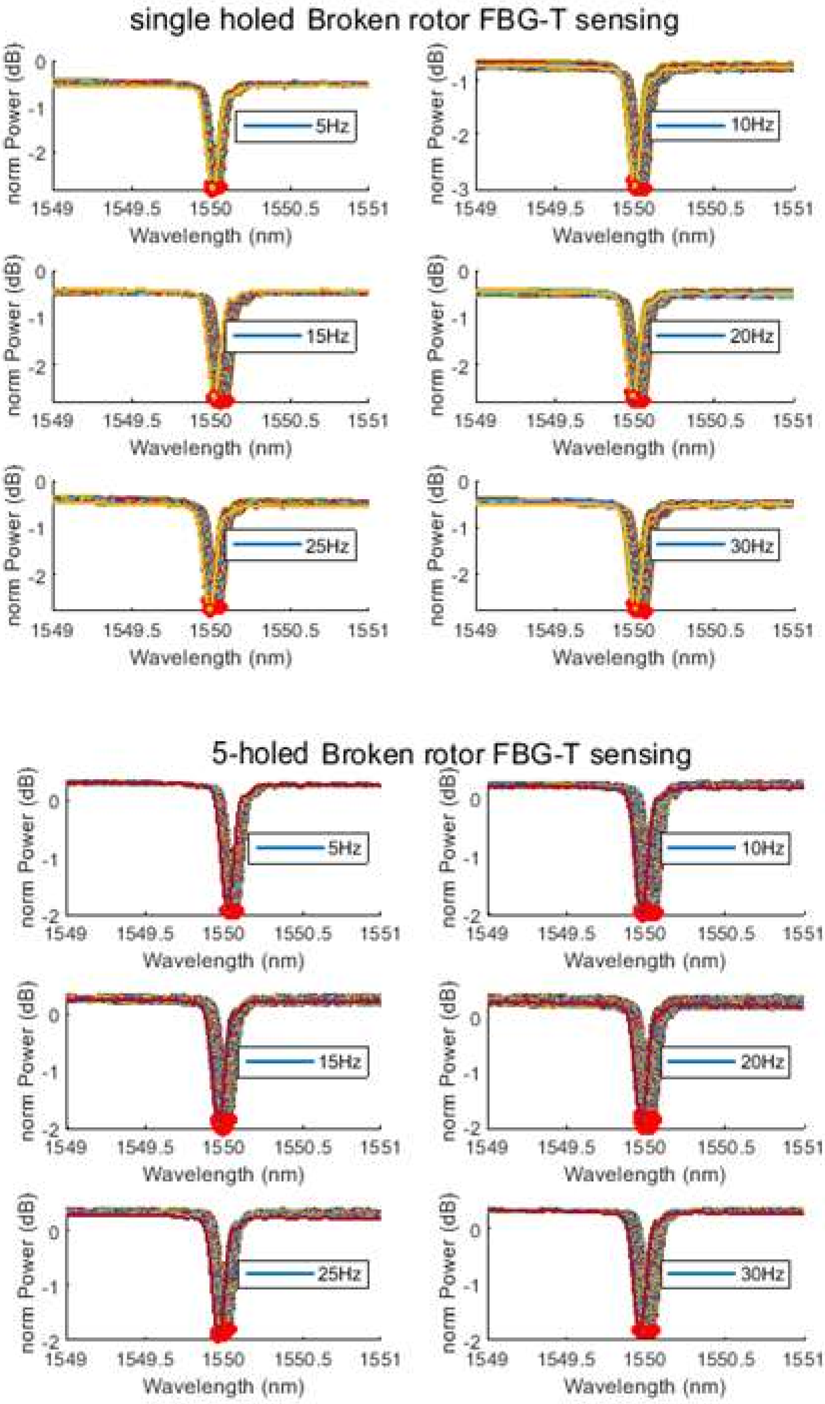

Figure 4-15: Optical spectra response of FBG-T sensor single broken bar condition

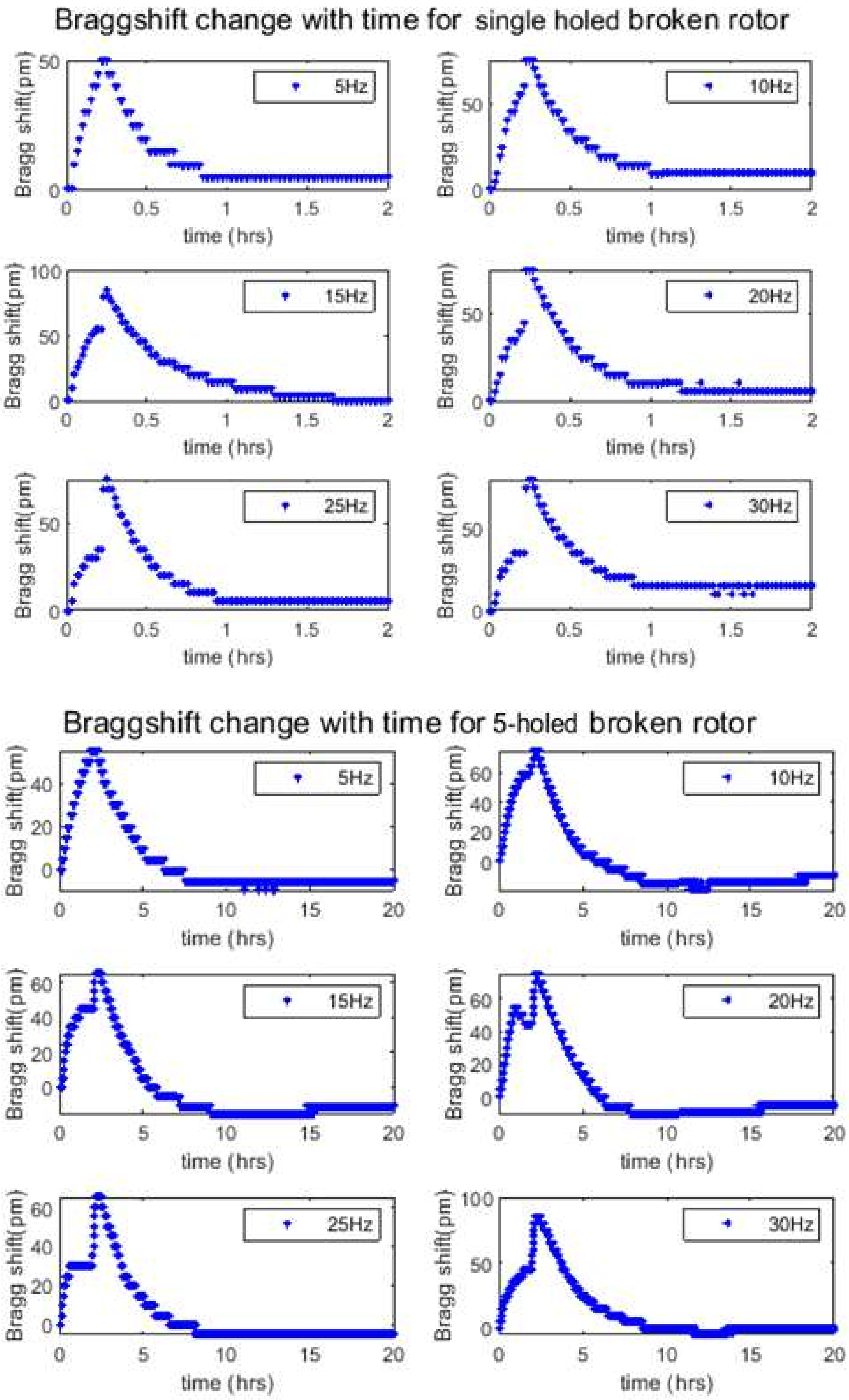

Figure 4-16: Time varying braggshift response of FBG-T sensor for single broken bar condition

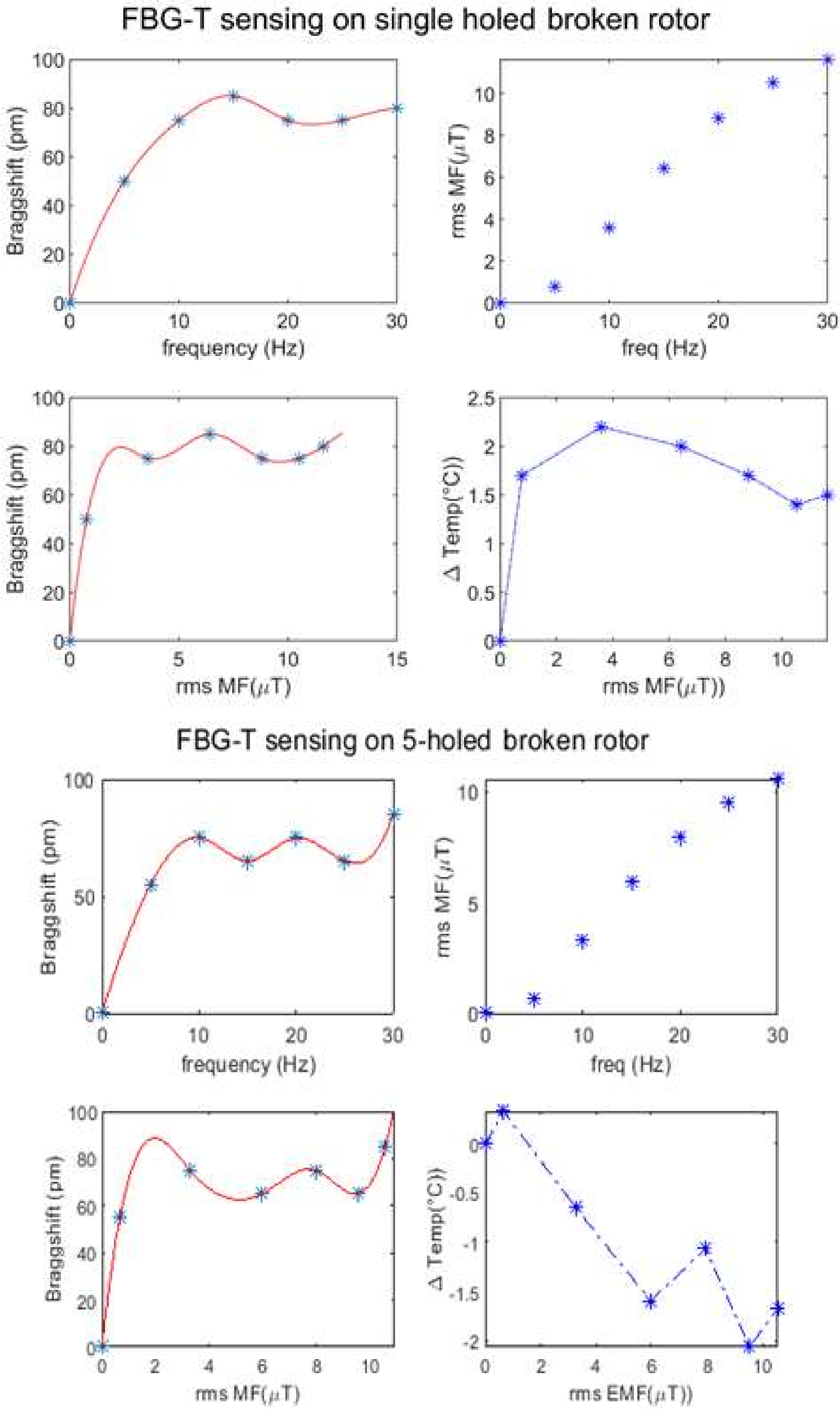

Figure 4-17: Variation of magnetic flux density with frequency, braggshifts and temperature for BRB

Table 4-7: Data for broken rotor motor condition

Frequency (Hz)	5	10	15	20	25	30
One-hole single bar broken rotor						
RMS Flux density (μT)	0.767813	3.584254	6.428448	8.824229	10.51763	11.62513
Max Braggshift (pm) during operation	45	55	55	40	35	35
Max Braggshift (pm) during 20 hours	50	75	85	75	75	80
Max Temp. change (°C) during operation	1.7	2.2	2.0	1.7	1.4	1.5
Five-hole single bar broken rotor						
RMS Flux density (μT)	0.665395	3.269313	5.970382	7.948426	9.530926	10.552626
Max Braggshift (pm) during operation	55	65	45	55	30	50
Max Braggshift (pm) during 20 hours	55	75	65	75	65	85
Max Temp. change (°C) during operation	0.8	0.2	1.2	1.2	1.1	0.5
Duration of operation	2 hours per frequency					

4.3 FBG-T Response to Two Forms of Single Broken Bar

4.3.1 Single-Holed Broken Rotor

Figure 4-18 compares the single hole broken rotor to the healthy rotor condition. Braggshifts under both conditions appear to be consistent in the order of magnitude of tens of pm. However, there were consistently higher values of braggshifts under the faulty machine condition compared to the healthy condition although in both cases, the braggshifts were nonlinear. Given that the amplitude of the stray flux increased with frequency in a near linear manner under both healthy and faulty condition, the difference in the amplitudes when compared was small. From Physics, the force (F) on a current-carrying conductor with N number of turns is given by:

$$F = N(BIl) \tag{4.3}$$

where I is the current flowing through the conductor in amps, and l is the length of the conductor in metres. B is the magnetic flux density or strength measured in Tesla. One way to increase the magnetic field strength, B is to either increase the number of turns (N) or increase the current through the turns. Provided resistance stays constant, current can be increased by raising the voltage supplied to the conductor. In this work, number of turns has been reduced in the rotor by boring holes and extracting the aluminium bores in that area. Hence for the healthy motor, the VFD used increases the voltage applied to the stator windings as frequency is increased, thus increasing the magnetic field strength, B measured. On the other hand, for the BRB, although the magnetic field strength, B measured did increase with frequency due to the increased voltage from the VFD, the amplitudes were slightly less than those of the healthy motor. This is because of the reduced number of turns (N) resulting from the emulation of broken rotor damage.

The magnitudes of the stray flux produced under healthy condition were slightly but consistently greater than those produced under the broken rotor condition for the entire frequency range of operation. This is because the healthy rotor had slightly more turns than the broken rotor where some rotor turns had been removed. A crucial observation is that this is the first evidence that the braggshifts are not largely due to the amplitudes of the magnetic flux otherwise, the healthy rotor should have produced larger braggshifts across all frequencies but rather the reverse was the case. The spectral content of the stray flux plays a key role in influencing the unpredictable motion of the magnetic dipoles of the transducer during magnetostriction. This will be investigated later where an auto data logger will help acquire the time varying stray flux signal for further analysis. Temperature change did not significantly impact on the braggshifts because if this was the case, then the healthy rotor did experience although small, but a higher maximum temperature change than the broken rotor. This should have resulted in larger braggshifts. This explains why for the last three frequencies the braggshifts for healthy condition was a just a little higher than for the other frequencies as the maximum temperature changes which were observed during those frequencies as well. However, this was not high enough to affect the FBG-T’s ability to distinguish between the healthy and the broken rotor conditions. From the investigation so far, there is evidence that the optical spectra on its own cannot be relied upon to detect the broken rotor condition. Rather the time varying braggshift plot provides a distinct characteristic based on the order of magnitude of the braggshifts observed, that the FBG-T sensor can detect the machine’s faulty condition.

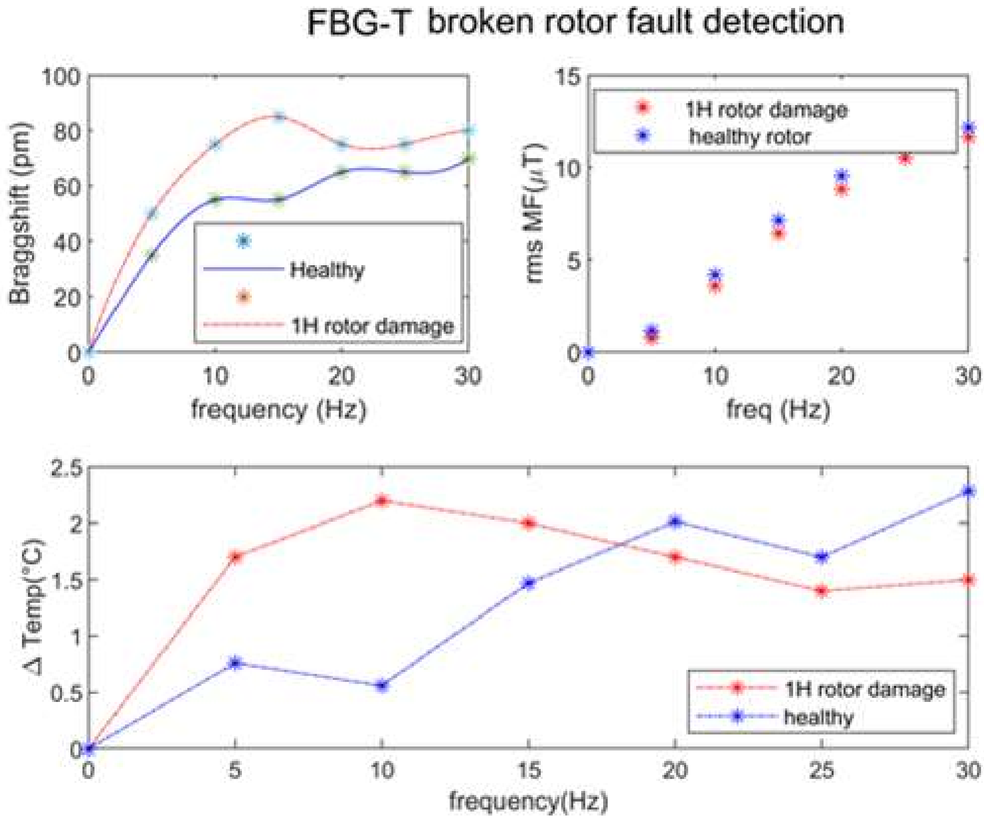

Figure 4-18: FBG-T sensor response in its use for one-hole BRB fault detection

4.3.2 5-Holed Broken Rotor

This does not make a difference in theory when compared with the single hole BRB as only one rotor bar is broken in both scenarios. Thus it is expected that the FBG-T should give similar response. The FBG-T did not give a clear-cut distinct response between the one-hole and the five-hole conditions as shown in Figure 4-19. However, the sensor was consistent in distinguishing between the healthy and the broken rotor conditions (one-hole and five-hole). As shown in Figure 4-19, there was linearity between stray flux produced and the motor frequency of operation. As expected, the 5-holed broken rotor produced less amplitudes of stray flux as it had the less number of turns compared to the stray flux produced by the healthy rotor with more number of turns. Braggshifts for one-hole and five-hole conditions were in the same order of magnitudes and identical values, which proves that the FBG-T sensor is detecting them as the same fault condition. Temperature change during the tests was minimal with the lower temperature change occurring in the five-hole BRB fault condition compared to the healthy condition. This is because the former has the lower number of turns and as a result will produce the lower amount of heat loss as well. In the next chapter, FBG-T sensor reliability in detecting a more severe electrical fault such as short circuit - which can be quite dangerous for any machine - will be investigated. Compared to the healthy machine condition, this analysis provides more confidence in the capability of the FBG-T sensor to succinctly distinguish between the healthy and broken rotor conditions.

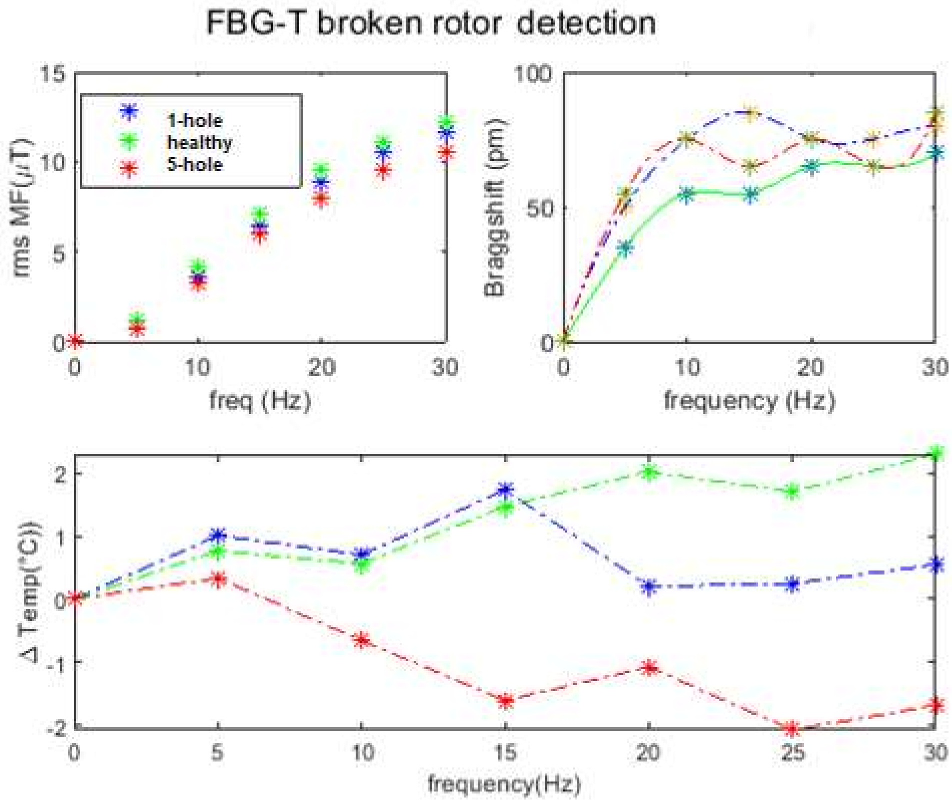

Figure 4-19: FBG-T sensor identical response to single broken bar condition compared to healthy rotor

4.4 FBG-T Stray Flux Sensing with Auto Data logger

In previous tests, the external (stray) magnetic field being extracted for the condition monitoring of the IMs have been manually obtained. Instantaneous readings were taken within a given time interval (every 10 minutes) from the flux meter and the temperature sensor. This limitation means that the time varying behaviour of the stray magnetic field cannot be observed. Albeit this does not affect the performance of the FBG-T sensor, it does ensure confidence in this research to automatically observe the stray flux. The HHG1394 Gauss meter seen in Figure 4-20 was used to realise auto data logging capability for the stray flux. The HHG1394 was manufactured by Omega Engineering UK with a proprietary software and a tri-axial sensing functionality. This makes it suitable for low and extremely low frequency magnetic fields independent of measurement angle. Table 4-8 shows the specification of the HHG1394 data logging gauss meter.

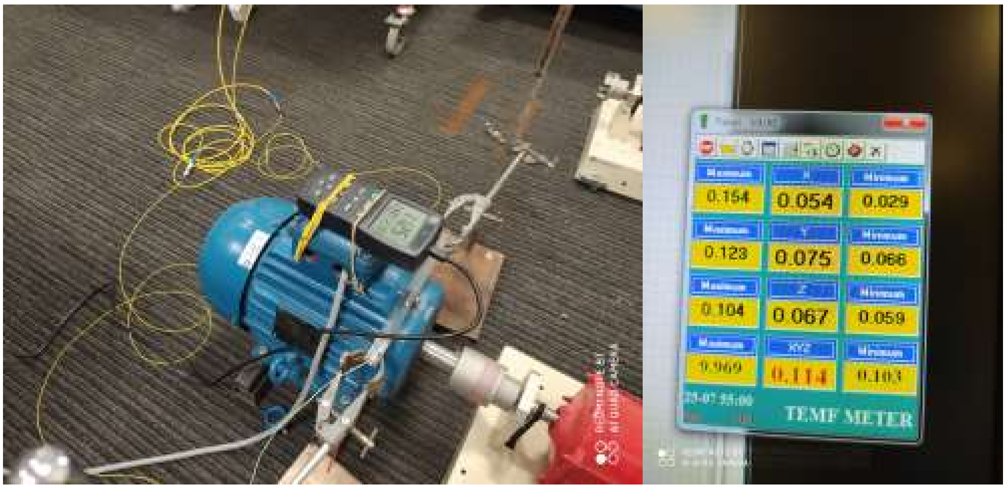

Figure 4-20: HHG1394 auto data logger and software used during tests

Table 4-8: HHG1394 Data logger flux meter specification

Parameter	Specification
Range	20/20/200µT
Resolution	0.001/0.01/0.1 µT
Sampling time	60secs
Memory capacity	2000 data sets
Measurement axis	X, Y, Z
PC connection mode	USB

Although ambient room temperature was relatively constant throughout the experiment with very little variation, both room and FBG-T sensor temperatures were continuously monitored automatically. National Instrument NI 8-slot USB CompactDAQ (cDAQ-9172) chassis together with the NI-9122 4-channel temperature input module were used with two thermocouples connected – one each for the sensor and the room. The cDAQ was connected to a PC where data was acquired and displayed in LabVIEW as shown in Figure 4-21.

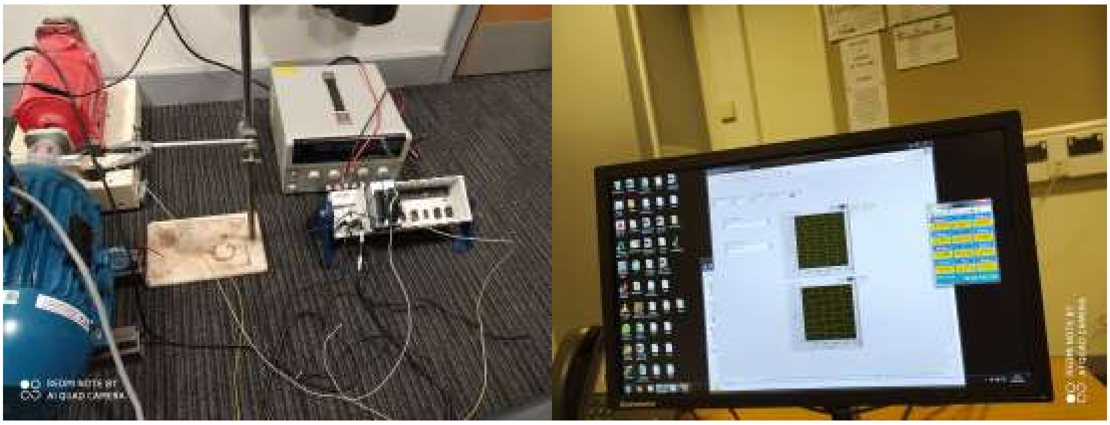

Figure 4-21: NI cDAQ-9172 chassis connected to LabVIEW for temperature data monitoring

4.5 Healthy IM

4.5.1 Test Conditions

Identical experimental set up as explained in previous chapters was used, with the main difference being the auto data logging for both stray magnetic flux and temperature. The machine was run at similar frequency range as before i.e., 5 – 30Hz with 5Hz interval but in addition, the machine was also run at slightly higher frequency range of 10-50Hz with 10Hz interval. For the auto data logging phase, the motor was run for longer hours (four instead of two as previously) to observe if there will be discrepancies in the FBG-T sensing characteristics. This part of the experiment inherently embeds a *reproducibility test* for the use of the FBG-T sensor in the condition monitoring and fault detection of IMs under slightly different operational scenarios. Prior to running the healthy motor, it was disassembled and observed to confirm its healthy state as depicted in Figure 4-22 before reassembly.

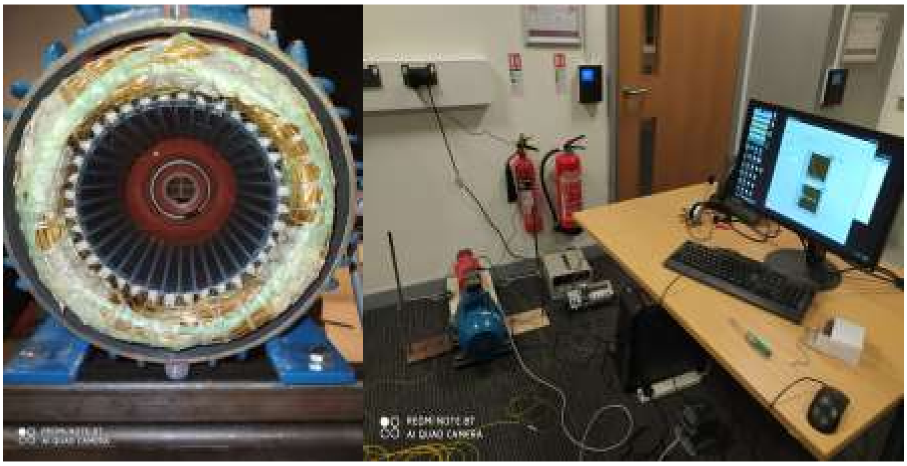

Figure 4-22: Healthy stator winding prior to assembly (left) and during test (right)

4.5.2 Results & Discussion

4.5.2.1 5Hz Frequency interval

Table 4-9 summarises the observations from running the IM at various frequencies in a step interval of 5Hz. There was consistency in the response of the FBG-T to the stray flux produced under a healthy condition with the maximum braggshifts in the same order of magnitude as before i.e., tens of pm oscillating around the mid-100pm range. The optical spectra at various frequencies again prove not to be useful in providing any insight into the machine condition except confirming the FBG-T sensor response to stray flux. The time varying braggshift plots once again showed consistency in the residual and reversible magnetic characteristics of the magnetostrictive transducer (terfenol-D). As earlier explained, these are respectively responsible for the further increase in braggshifts just immediately after the loss of stray flux; and the return path taken by the FBG-T sensor back to its initial wavelength due to the terfenol-D returning to its original length.

Table 4-9: Data for healthy motor condition at 5Hz step interval

Frequency (Hz)	0	5	10	15	20	25	30
RMS Flux density (μT)	0.147933	0.468905	1.186085	2.61452	5.280447	6.922083	7.423125
Max Braggshift (pm) during operation	0	65	45	45	30	35	30
Max Braggshift (pm) during 20 hours	0	70	55	60	50	55	55
Max ∆Temp during operation (°C)	0	1.6910	1.2730	1.2300	1.1910	1.3080	1.4910
Duration of operation	4 hours per frequency						

Both optical spectra and the time varying braggshifts are depicted in Figure 4-23. Machine was operated in a relatively constant ambient room temperature with less than 2°C maximum temperature change over the entire test period across all frequencies. A nonlinear but direct relationship between increased frequency and increased magnitude of stray flux was again observed which is consistent with the earlier results conducted without an auto data logger. At 5Hz the braggshift notably was observed to be unusually high (70pm), although still within range but still high enough to trigger some curiosity as to why (see Figure 4-24). This was analysed later in this chapter.

4.5.2.2 10Hz Frequency interval

Table 4-10 summarises key observations which are consistent with the initially observed features of the FBG-T sensor. Braggshifts due to the stray flux were in their tens of pm readings and the maximum braggshift per frequency during the motor's operational periods were consistently lower than the maximum braggshifts observed during the 20 hours of observation. As explained previously, this is due to the magnetic moment of the dipoles within the terfenol-D as they exhibit paramagnetic behaviour when they undergo reversible magnetisation upon application of small magnetic field which is lost once the field is removed.

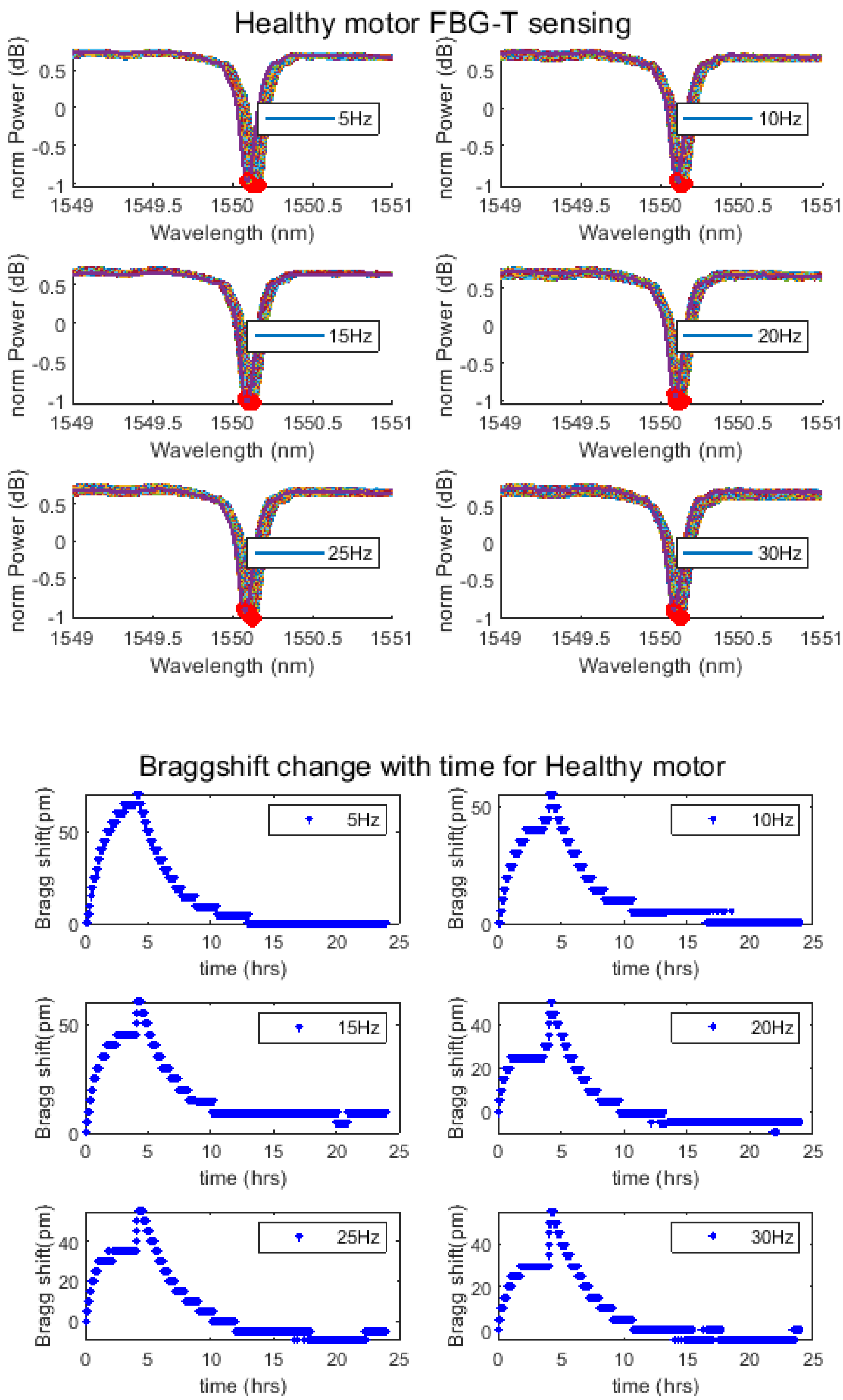

Figure 4-23: Optical spectral (top) and time varying (bottom) braggshift response for healthy condition at 5Hz step interval

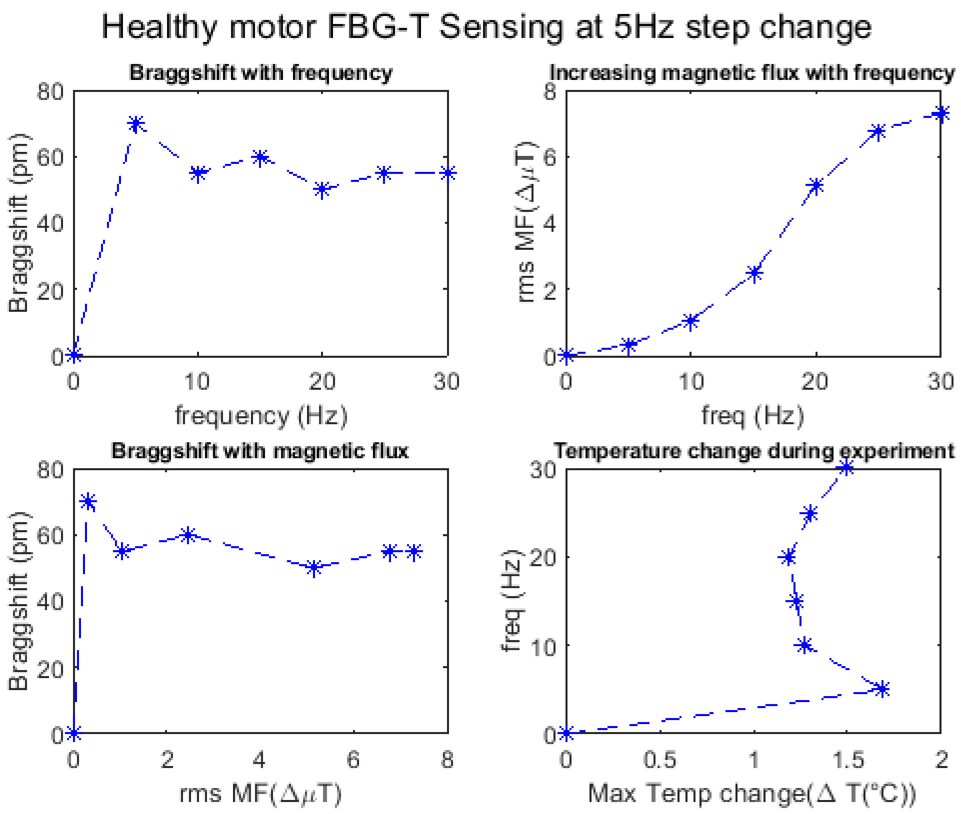

Figure 4-24: Variation of magnetic flux density with frequency, braggshifts and temperature for healthy condition

Table 4-10: Data for healthy motor condition at 10Hz step interval

Frequency (Hz)	0	10	20	30	40	50
RMS Flux density (μT)	0.13934 8	1.061366	4.684803	6.8177	7.132834	7.319245
Max Braggshift (pm) during operation	0	40	30	25	40	35
Max Braggshift (pm) during 20 hours	0	55	55	50	65	65
Max ΔTemp during operation (°C)	0	1.5930	1.6080	1.8060	1.8560	1.9030
Duration of operation	4 hours per frequency					

The magnetic dipoles would orientate and realign to a new state of rest once the field is lost and this causes a strain on the magnetostrictive material (terfenol-D) hence the further increase in braggshift until the residual magnetisation is lost completely. At this point, the magnetostrictive material returns to its original length which translates into a wavelength shift back to the initial wavelength. Figure 4-25 shows the braggshifts with time at both 10Hz and 50Hz and their corresponding optical spectra respectively. A similar pattern was observed at 20Hz, 30Hz and 40Hz where the FBG-T sensor senses the stray flux and responds until a certain state when it plateaus, typically within less than the 4 hours of operation.

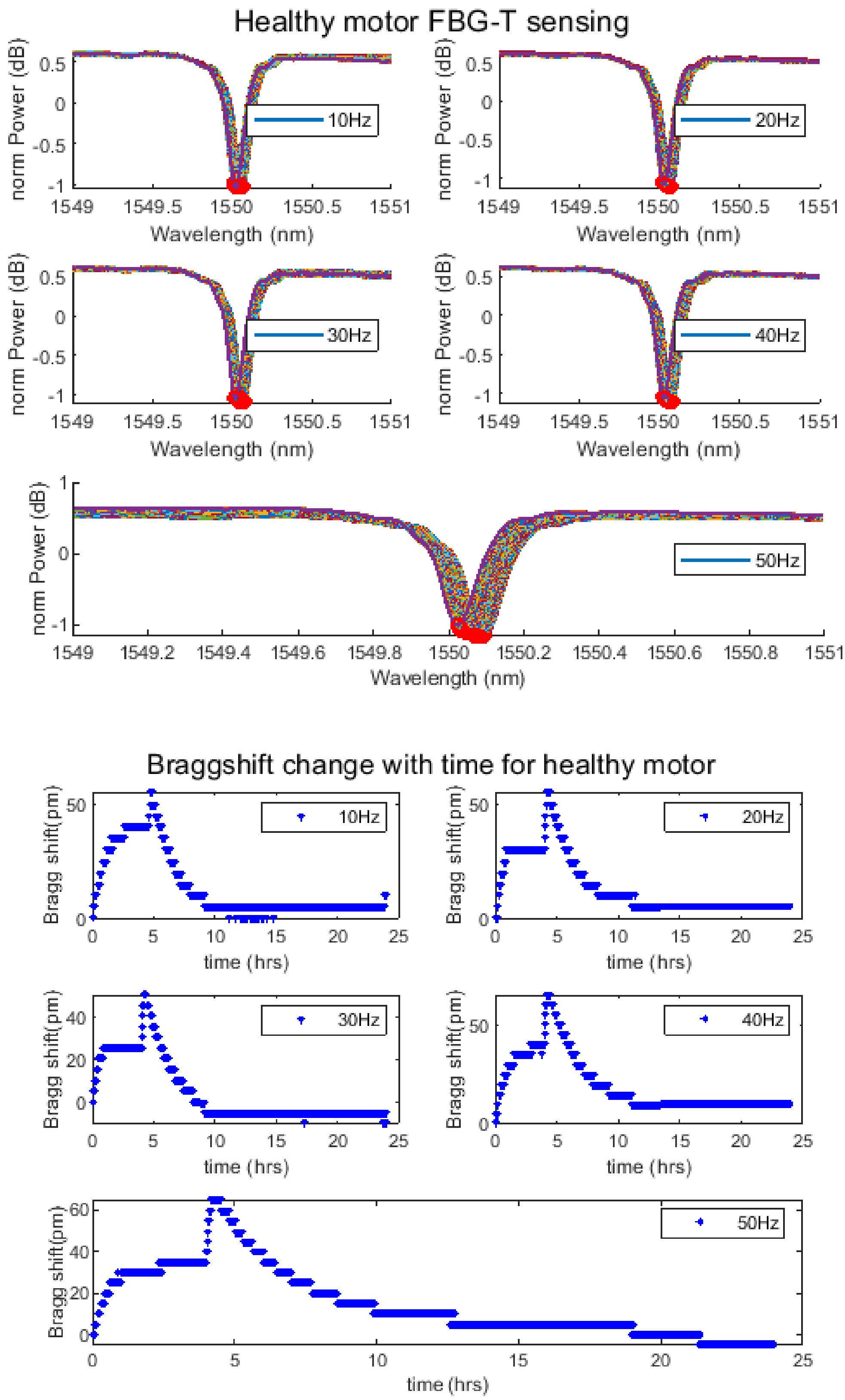

Figure 4-25: Optical spectral (top) and time varying braggshift (bottom) response of FBG-T sensor for healthy condition at 10Hz step interval

As soon as the machine is turned off and magnetic field lost, further braggshifts are observed for a short period owing to the paramagnetic behaviour of terfenol-D as previously explained. Once the residual magnetisation is completely lost, the return path journey begins, and the FBG-T sensor attempts to return to its initial state. Due to the huge hysteresis nature of terfenol-D, the FBG-T oftentimes, makes it close to its initial wavelength but usually not exactly, as shown in the figures.

With the aid of the data logger, time varying plots of the stray magnetic field were obtained as shown in Figure 4-26. The plots show the presence of noise when the motor is turned off after four hours and these noise amplitudes were excluded when computing the mean magnetic field in Table 4-10. At all frequencies, the stray flux was present, and its mean value increased with frequency in the μT range. It was observed that there was consistency in the nature of the magnetic field signal with its mean amplitude value increasing with frequency. This is expected as the VFD increased the voltage amplitude with frequency. However, the increase in magnetic field strength did not translate into a *proportionate* increase in braggshifts (Figure 4-27). There is now evidence that although there is a direct relationship between increasing frequency and observed stray magnetic flux, there is no direct relationship between maximum braggshift observed and frequency under healthy motor condition. For example, maximum braggshifts observed at 10Hz and 20Hz were both 55pm, while at 40Hz and 50Hz maximum braggshifts of 65pm were observed. But at 30Hz a maximum braggshift of 50pm was observed. Looking at the corresponding mean magnetic flux densities, the field strength at 40Hz and 50Hz are the only close values, thus, could be responsible for the same maximum braggshift. However, same could not be said for the other frequencies such as 10Hz and 40Hz where the mean magnetic flux densities are around 1.1μT and 4.7μT respectively. At 30Hz the mean magnetic flux density is about 6.8μT which suggests that the magnetostrictive behaviour of the terfenol-D is nonlinear. While this does not in any way discredit the reliability of the use of the FBG-T for machine condition monitoring, understanding the sensor characteristics will provide evidence of how to optimise the use of this sensor in machine monitoring applications. Therefore, this observation will be further experimented with repeated tests to ascertain the non-linearity relationship between braggshifts, magnetic flux and frequency both under healthy and faulty conditions.

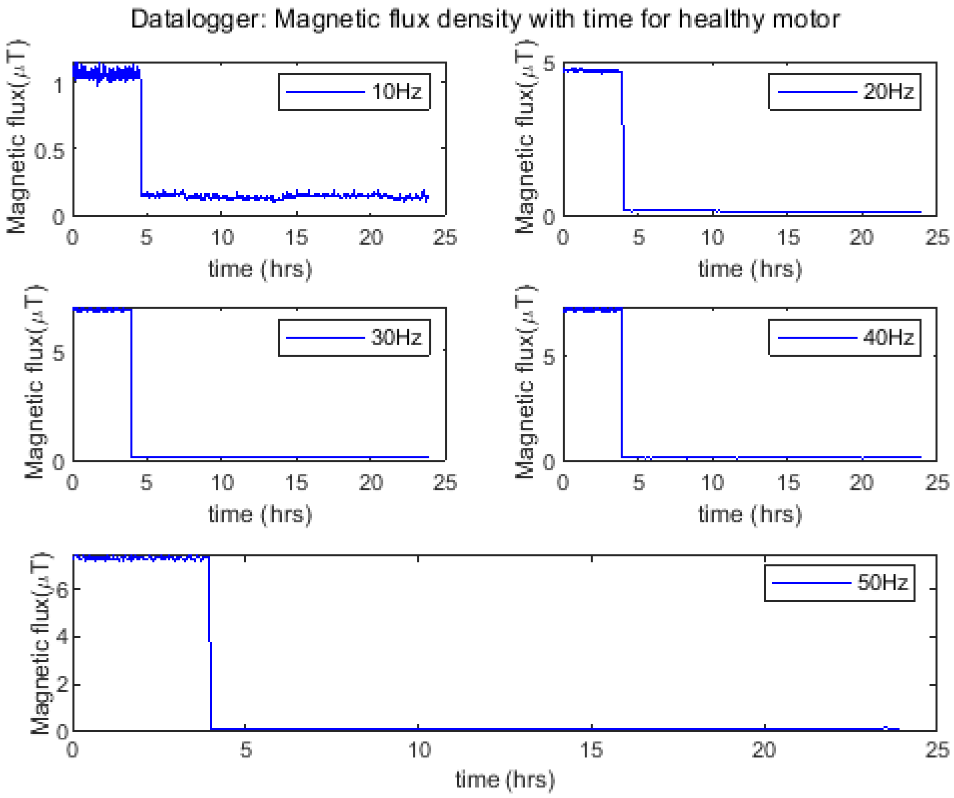

Figure 4-26: Time varying stray flux for healthy motor condition at 10Hz step interval

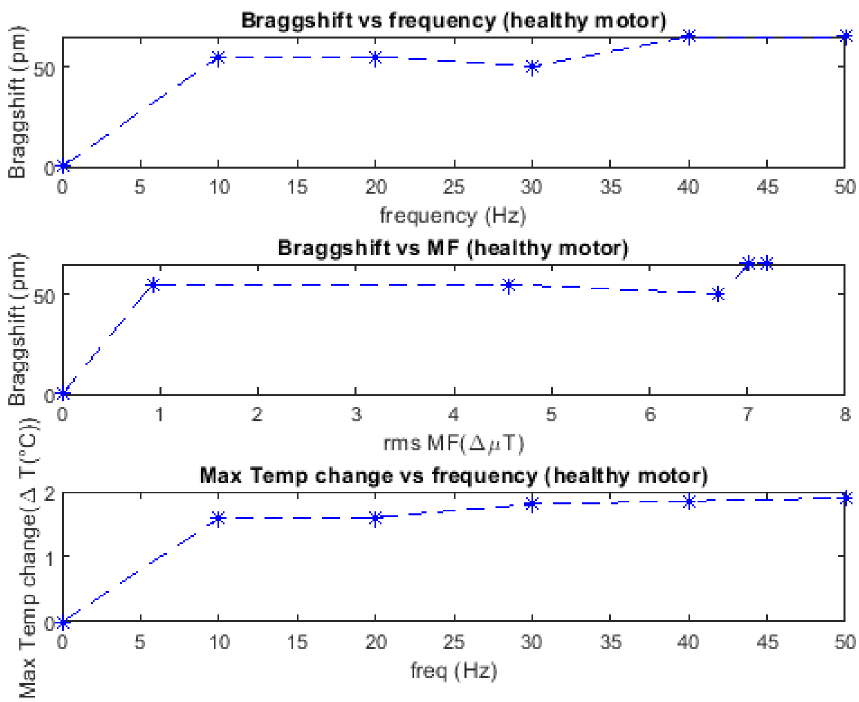

Figure 4-27: Variation of braggshift with frequency, stray flux and temperature for healthy condition at 10Hz step interval

To eliminate the influence of temperature, Figure 4-28 shows that the maximum temperature change was less than 2°C for all frequencies over the 20 hours of each test. Mean temperature change during the four hours of operating the motor was about 0.13°C, which is not significant knowing that terfenol-D has a much higher operating temperature range with a coefficient of thermal expansion of 0.000011ε per °C at 25°C ambient [197]. The temperature plots are consistent with expectations in that at all frequencies, temperature initially rose as the motor got warmed up and then plateaued for the duration of operation. All subsequent variations in temperature after the motor was turned off were largely due to ambient room temperature.

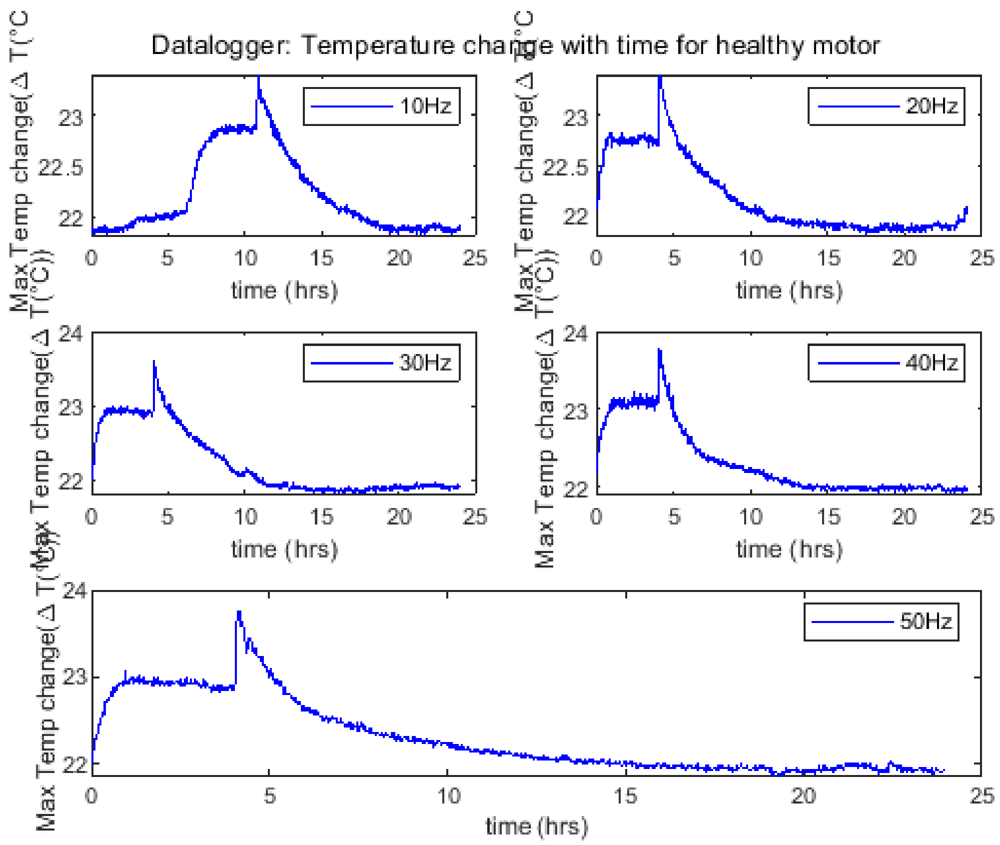

Figure 4-28: Temperature variation during healthy machine operation at 10Hz step interval

4.6 Broken Rotor IM

4.6.1 Test Conditions

Figure 4-29 shows the test conditions to emulate the BRB fault which was also used earlier in this chapter. The IM was run under similar operating conditions as the healthy motor at 5 – 30Hz with 5Hz interval as well as 10-50Hz with 10Hz interval. Due to the amount of vibration observed above 30Hz for the BRB test, the experiment was halted for health and safety reasons. Under extreme operating environment, the vibration would result in a significant and fast increase in the braggshifts which will be a very good indicator within the context of fault severity, however, health and safety comes first in this case. The laboratory test rig is also not robust enough to allow such vibrations without a potential damage to the FBG-T sensor.

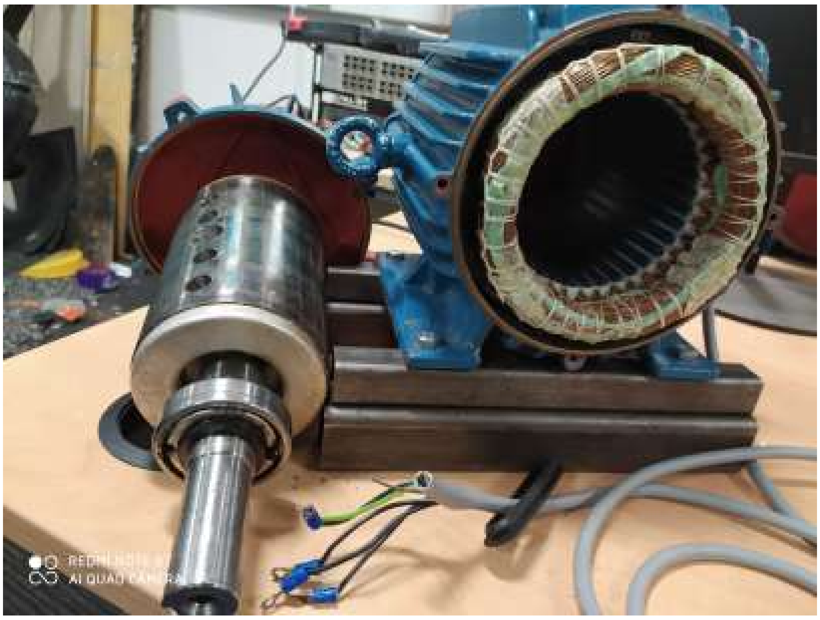

Figure 4-29: Emulation of broken rotor fault condition prior to assembly

4.6.2 Results & Discussion

4.6.2.1 5Hz Frequency interval

Table 4-11 once again confirms the consistency in the paramagnetic behaviour of the FBG-T sensor. Magnetic flux density was again observed to increase with frequency without a corresponding proportional increase in braggshifts. However, within the 5Hz interval the braggshifts were mostly within the tens of pm range similar to the healthy condition but generally slightly higher.

Table 4-11: Data for BRB Condition with Auto Data Logger

Frequency (Hz)	0	5	10	15	20	25	30
RMS Flux density (μT)	0.1394	0.2284	0.7428	2.1804	4.4652	5.7436	6.0265
Max Braggshift (pm) during operation	0	125	80	65	60	75	55
Max Braggshift (pm) during 20 hours	0	125	90	90	90	105	90
Max ∆Temp during operation (°C)	0	0.5340	0.4170	0.3400	0.3240	0.5380	0.5340
Duration of operation	4 hours per frequency						

Figure 4-30 shows the consistency in the FBG-T sensor's reversible magnetisation response and hysteresis. Generally, the stray flux causes the FBG-T sensor wavelength to shift increasingly until a maximum whilst the magnetic field is still present. This braggshift peak was attained before the elapse of the four hours of operation for each frequency. Once the magnetic field was lost (motor turned off), the braggshift further increased due to residual magnetism as previously explained. This continued until when the sensor was completely void of magnetism, then it attempts to return to its initial state. This was observed at each of the six frequencies under the broken rotor condition. FBG-T optical spectra in Figure 4-30 show the shifts in wavelength and the non-linear braggshift response to both frequency and magnetic flux density. The slightly higher braggshift observed at 5Hz is likely due to the inertial and excited pre-stress state of the terfenol-D transducer in the FBG-T sensor. The test at 5Hz was conducted after the sensor had been left for a longer period compared to the other frequencies. This could have increased its sensitivity, whereas for the other readings, the sensor had been left for at least 16 hours before the motor is run at another frequency. On average the braggshifts is of similar order of magnitude but slightly higher values of braggshifts than the healthy condition. Alternatively, this could be due to the harmonic component of the stray flux. This was later investigated using FFT spectral analysis.

Figure 4-31 shows the maximum braggshift at each frequency for the mean magnetic flux density. It is clear to see that though the magnetic flux density does increase, there is no proportionate increase in braggshift. This can only be explained by the atomic behaviour of the magnetic dipoles of the terfenol-D which hitherto, even physicists have failed to convincingly explain. These braggshifts unarguably are because of the stray flux as mean variation in temperature over the entire test frequencies was again less than 1°C as shown in Figure 4-31.

Figure 4-32 shows the time varying magnetic field which increased with frequency. At 5Hz the magnetic flux density was quite low under the broken rotor condition, hence was affected by the noise floor as shown. As the magnetic flux density increased with frequency, it became less impacted by noise. The time varying temperature profiles in Figure 4-33 shows that the maximum temperature change during each test was less than 1°C for the entire 20-hour period per frequency.

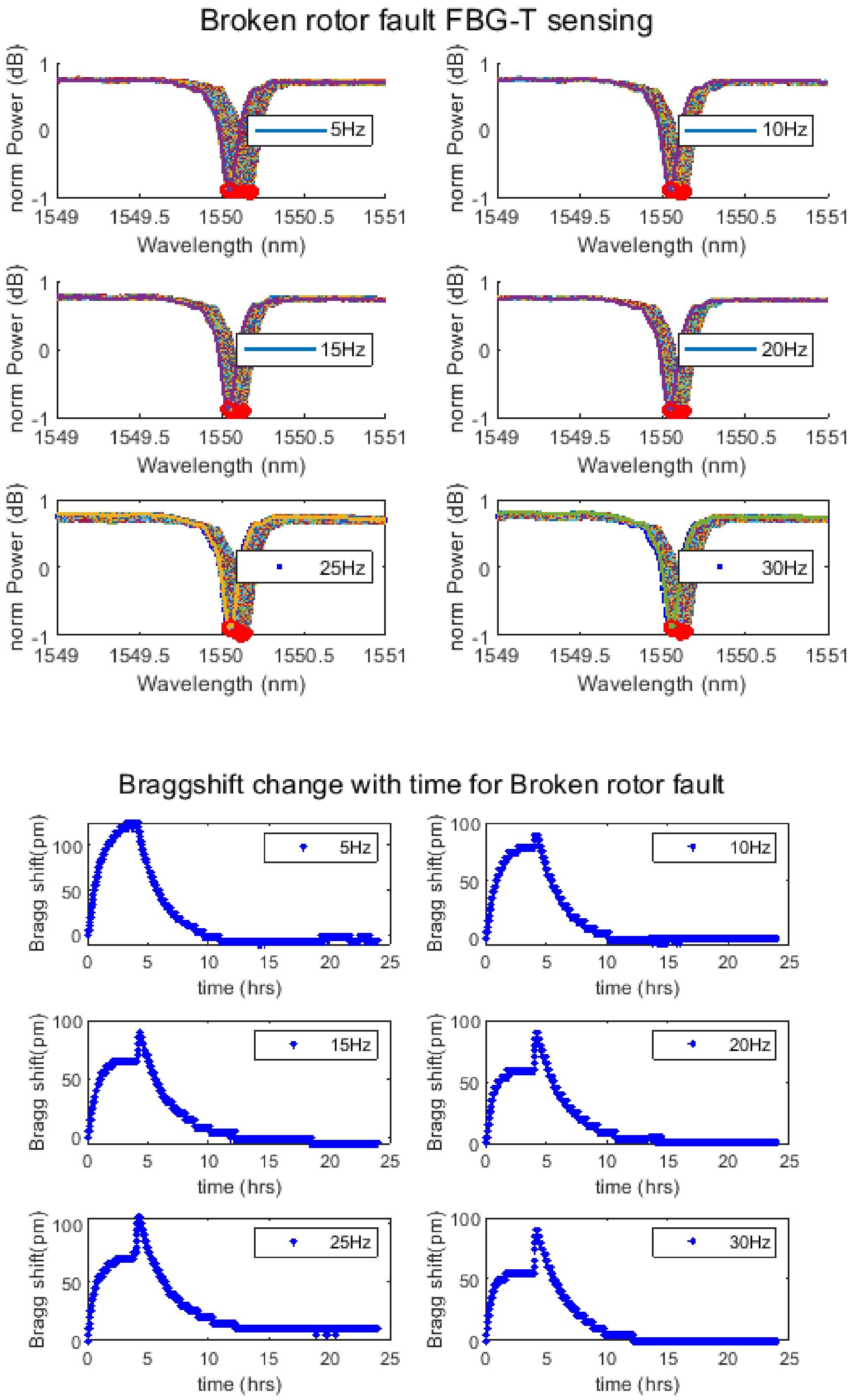

Figure 4-30: Optical spectral (top) and time varying braggshift (bottom) response of FBG-T sensor for BRB condition at 5Hz step interval

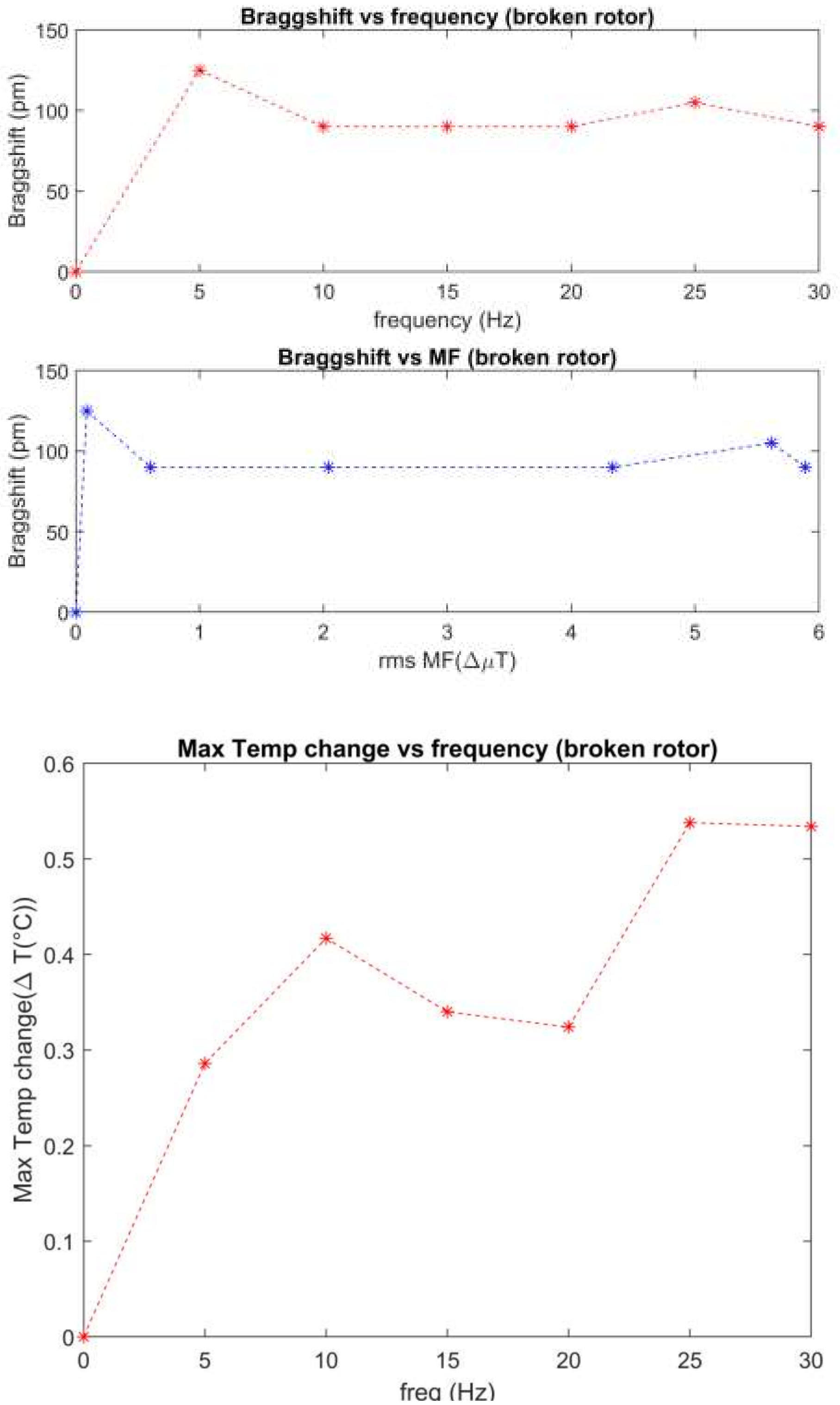

Figure 4-31: Variation of braggshift with frequency, stray flux, and temperature under BRB condition

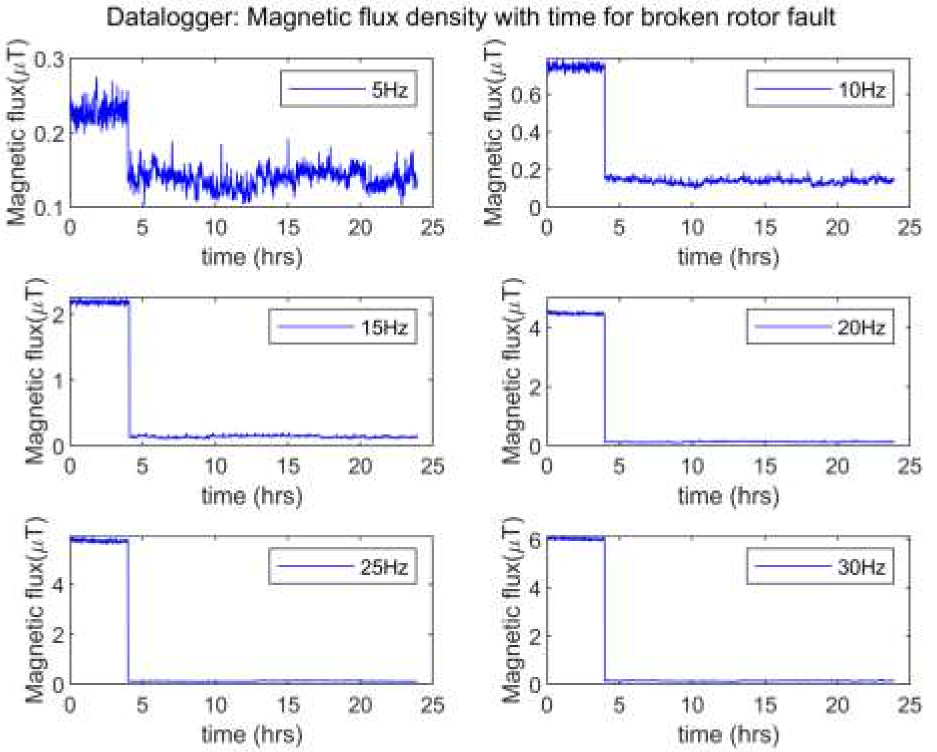

Figure 4-32: Auto data logger capture of stray flux under BRB condition

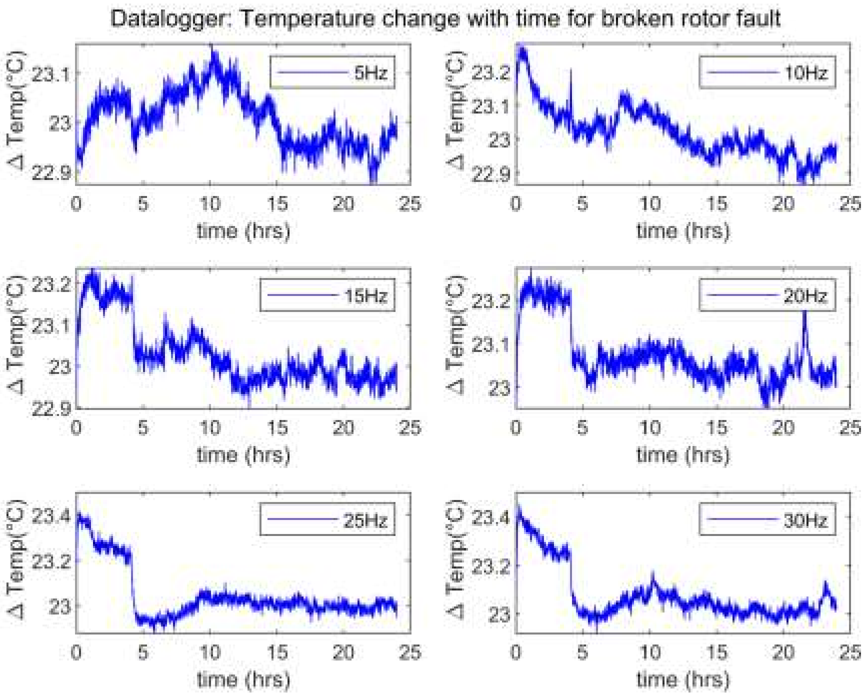

Figure 4-33: Auto data logger capture of temperature variation under BRB condition

4.6.2.2 10Hz Frequency interval

Table 4-12 summarises key observations of the broken rotor test under 10Hz interval. In terms of sensor behaviour, there was consistency under a reasonably identical ambient room temperature condition compared to the healthy machine state. Relationship between magnetic flux and frequency was again observed to be direct with corresponding disproportionate braggshifts.

Table 4-12: Data for BRB Condition with Auto Data Logger – 10Hz interval

Frequency (Hz)	0	10	20	30	40	50
RMS Flux density (μT)	0.1272	0.7777	4.6306	6.2335	-	-
Max Braggshift (pm) during operation	0	70	55	65	-	-
Max Braggshift (pm) during 20 hours	0	85	85	105	-	-
Max ΔTemp during operation (°C)	0	0.5210	0.6430	0.7050	-	-
Duration of operation	4 hours per frequency					

The braggshifts with respect to time as well as observed optical spectra shown in Figure 4-34 were consistent in behaviour as well at each frequency confirming the result of residual and reversible magnetisation experienced by the FBG-T sensor as well as hysteresis.

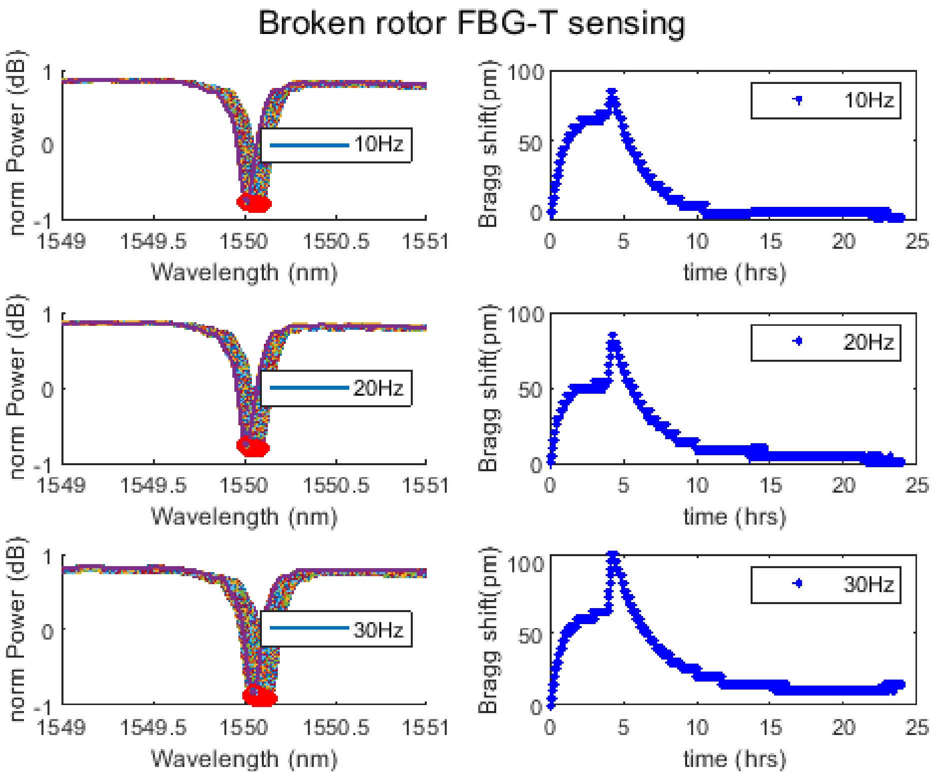

Figure 4-34: Optical spectral (left) and time varying braggshift (right) response of FBG-T sensor for BRB condition at 10Hz step interval

Time varying profile of stray magnetic field with braggshifts is like previous observations for each frequency (Figure 4-35) though non-linear, but within the tens of pm range as observed in the 5Hz interval. Temperature variation during each test was again insignificant with mean temperature change less than 1°C as before (Figure 4-36), thus did not have any significant impact on the FBG-T sensor performance.

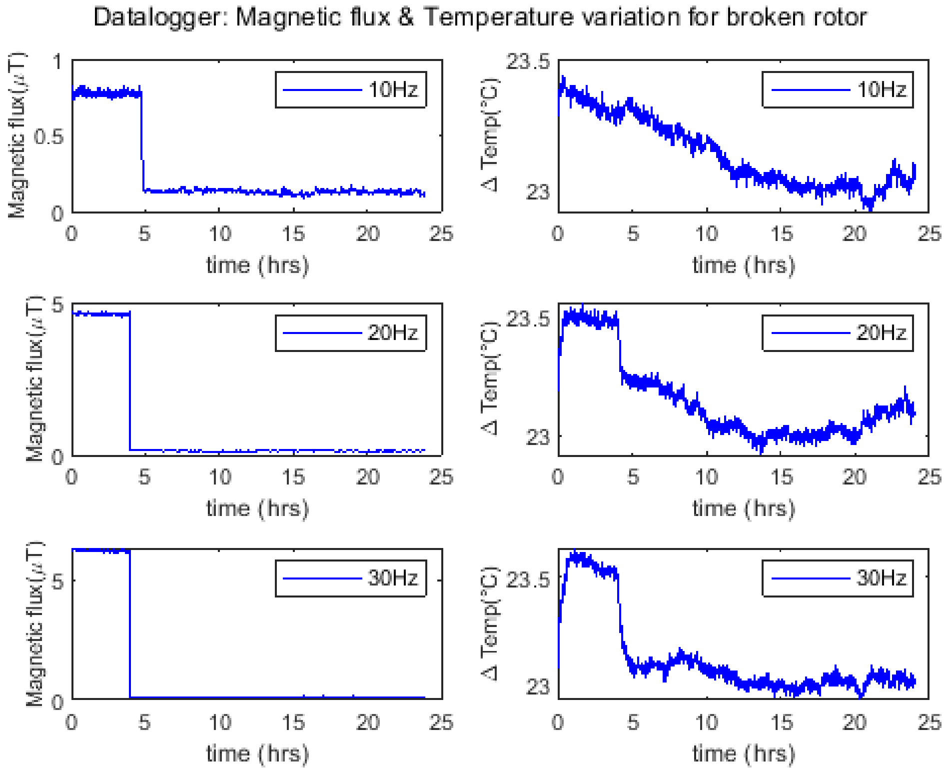

Figure 4-35: Time varying stray flux and temperature changes at three frequencies under BRB condition

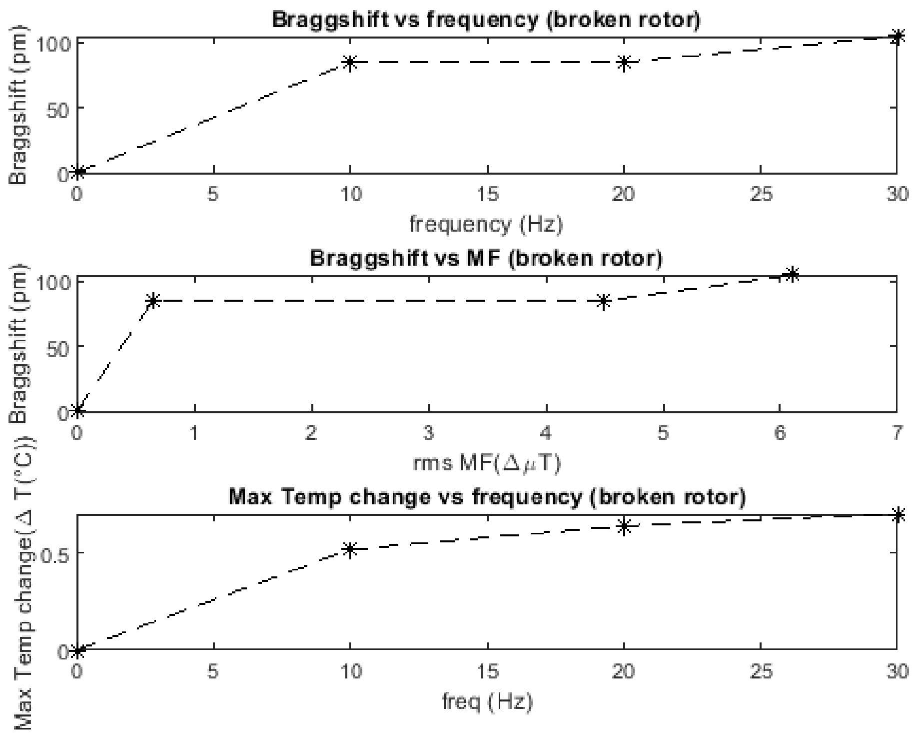

Figure 4-36: Variation of Braggshift with stray flux, frequency and temperature for BRB condition with 10Hz step interval

4.7 Faulty Severity Analysis

4.7.1 Healthy vs Broken Rotor

4.7.1.1 5Hz Frequency interval

Figure 4-37 provides confidence on the reproducibility characteristic of the FBG-T sensor in distinctly detecting a broken rotor fault condition. There is once again evidence from this investigation that for healthy motor condition the stray flux produced results in braggshifts around the mid-100pm range, whereas for broken rotor the range is around the 100pm mark. The magnitude of the stray flux produced corroborates with previous results where higher amplitudes were observed in the healthy motor compared to the broken rotor due to a greater number of turns in the former. As with previous observations, no apparent relationship was observed between the amplitude of the stray flux and braggshift because, under both healthy and faulty conditions, braggshifts remained within the same range regardless of the steady increase in the amplitude of the stray flux. Temperature changes were small with maximum values of about 1.7°C and 0.7°C recorded for healthy and broken rotor conditions respectively – which agrees with theoretical expectation based on the number of turns in each machine condition. There is now substantive evidence that FBG-T sensor can detect a broken rotor fault during condition monitoring. An interesting observation was the similarity in behaviour of the FBG-T sensor at 5Hz under both healthy and broken rotor conditions where the highest braggshifts were again recorded. As earlier mentioned, given that the amplitude of the stray flux is minimum at 5Hz under both conditions and there is no significant change in temperature, further spectral analysis of the stray flux was performed in the next chapter. This investigated that it is the difference in the harmonic spectrum of the stray flux at each frequency that influenced how the magnetic dipoles of the magnetostrictive material moved, resulting in the nonlinear proportionate braggshifts observed.

4.7.1.2 10Hz Frequency interval

Despite the safety limitation of the 10Hz step interval investigation, results obtained for the three safe frequencies under BRB condition further substantiated the evidence of reliability and reproducibility of the sensing capability of the FBG-T sensor in detecting BRB fault condition. As shown in Figure 4-38, the braggshifts observed are in the same order of magnitude as before with a slight but constant increase at higher frequencies of 40 Hz and 50Hz. Regardless of the increase from 40Hz to 50Hz no further braggshift was observed under healthy condition, hence the order of magnitude remained within the expected range. Similarly for the three frequencies tested under broken rotor, the order of magnitude of the braggshifts was consistent in the higher tens of pm range closer to 100pm than the 50pm for healthy machine condition. This gives a clear and distinct fault detection signature as observed previously in separate experiments.

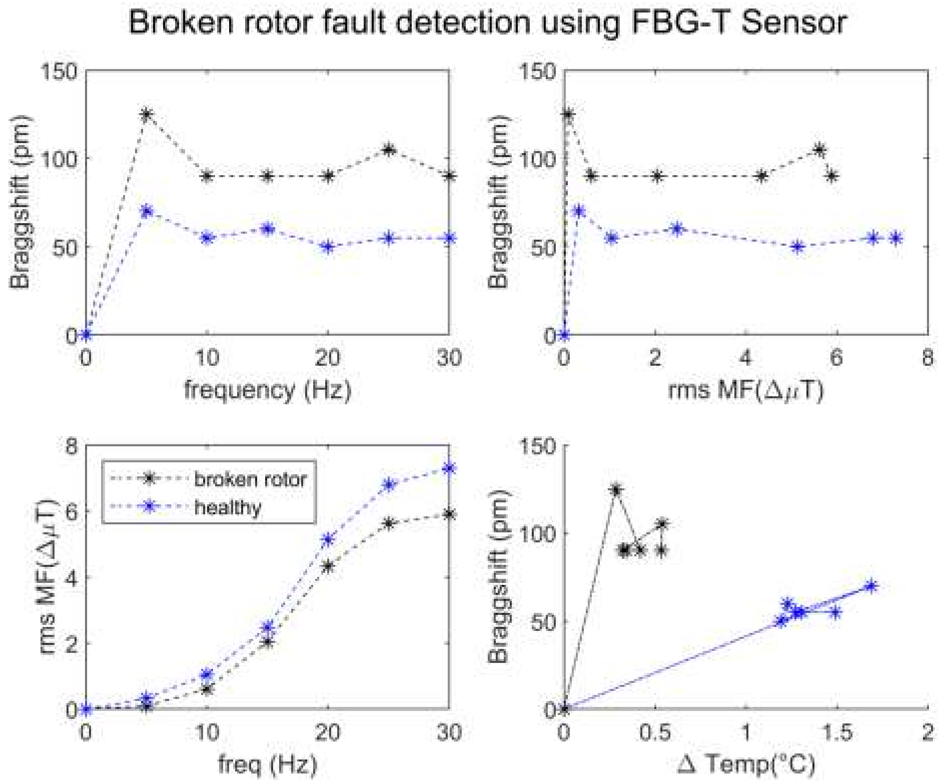

Figure 4-37: BRB fault detection capability of FBG-T sensor – RT at 5Hz step interval

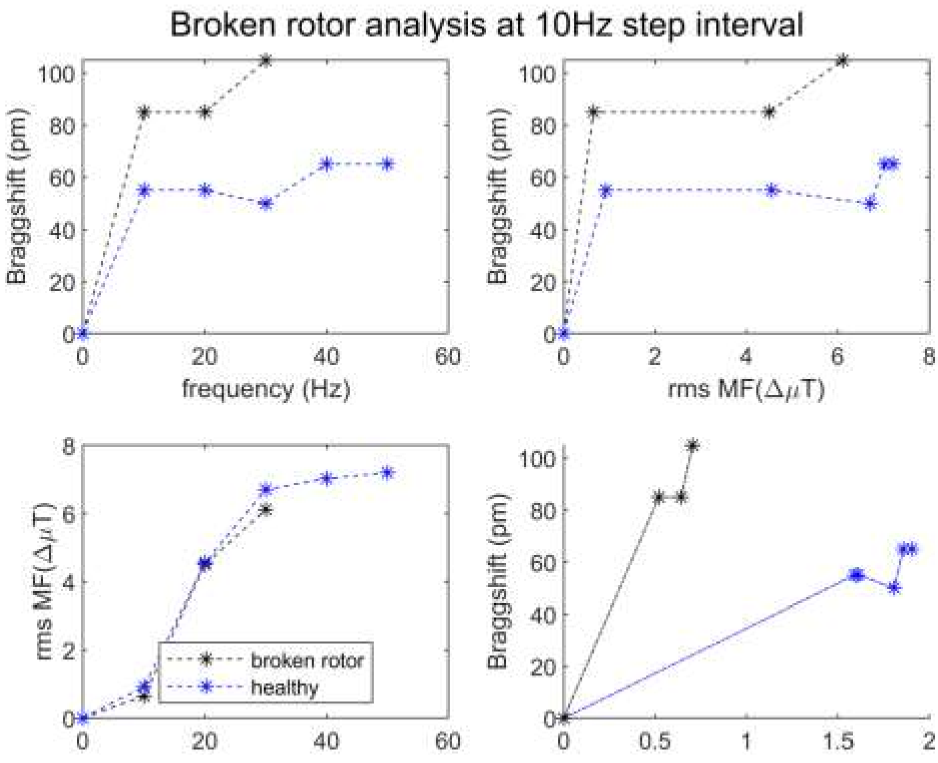

Figure 4-38: BRB fault detection capability of FBG-T sensor – RT at 10Hz step interval

Magnitude of stray flux appeared to plateau as frequency increased hence at 40Hz and 50Hz mean stray flux amplitudes were very close with a difference of about 0.3μT. With lesser amplitudes of stray flux due to reduced number of turns, the braggshifts observed under broken rotor were still consistent within previously observed ranges. This builds confidence in the evidence that braggshifts are not solely due to the amplitudes of the stray flux but that their spectral harmonic content is also responsible for the FBG-T nonlinear response, in terms of precision in the values of braggshifts observed. Upon data capture of the stray flux using the auto data logger, the data was exported into MATLAB where FFT spectral analysis to convert the data from time domain into frequency domain, was performed (see Figure 4-39). Figure 4-39 confirms that although the harmonic spectra for both healthy and broken rotor conditions were identical for each of the frequency of operation, there was a different and unique harmonic component within the spectrum for each machine condition. For example, at 10Hz motor frequency the unique harmonic component for healthy condition was around 260Hz (26^{th} harmonic) whereas under broken rotor it was 180Hz (18^{th} harmonic). As the motor frequency increased, the harmonic spectra for both machines conditions also increased such that at 20Hz the unique harmonic components for healthy and broken rotor conditions were 1.14kHz (38^{th} harmonic) and 1.11kHz (37^{th} harmonic) respectively. At 30Hz the unique harmonic components were respectively 1.65kHz (55^{th} harmonic) and 1.5kHz (50^{th} harmonic) for healthy and broken rotor conditions. This shows that although the spectral harmonic bandwidth for the stray flux is the same regardless of machine condition, there exists a third factor – a unique frequency component – which is different for the different machine operating conditions. Based on all other considerations investigated viz: amplitude of stray flux and impact of ambient temperature, there is strong evidence that a third factor is contributing to the braggshifts and especially the nonlinearity in its specific value. That third factor is the unique harmonic component which explains such unpredictable motion behaviour of the magnetic dipoles of terfenol-D given the test parameters and constraints. Thus, it is more appropriate at this stage to use order of magnitude rather than specific braggshift values to accurately detect BRB fault condition.

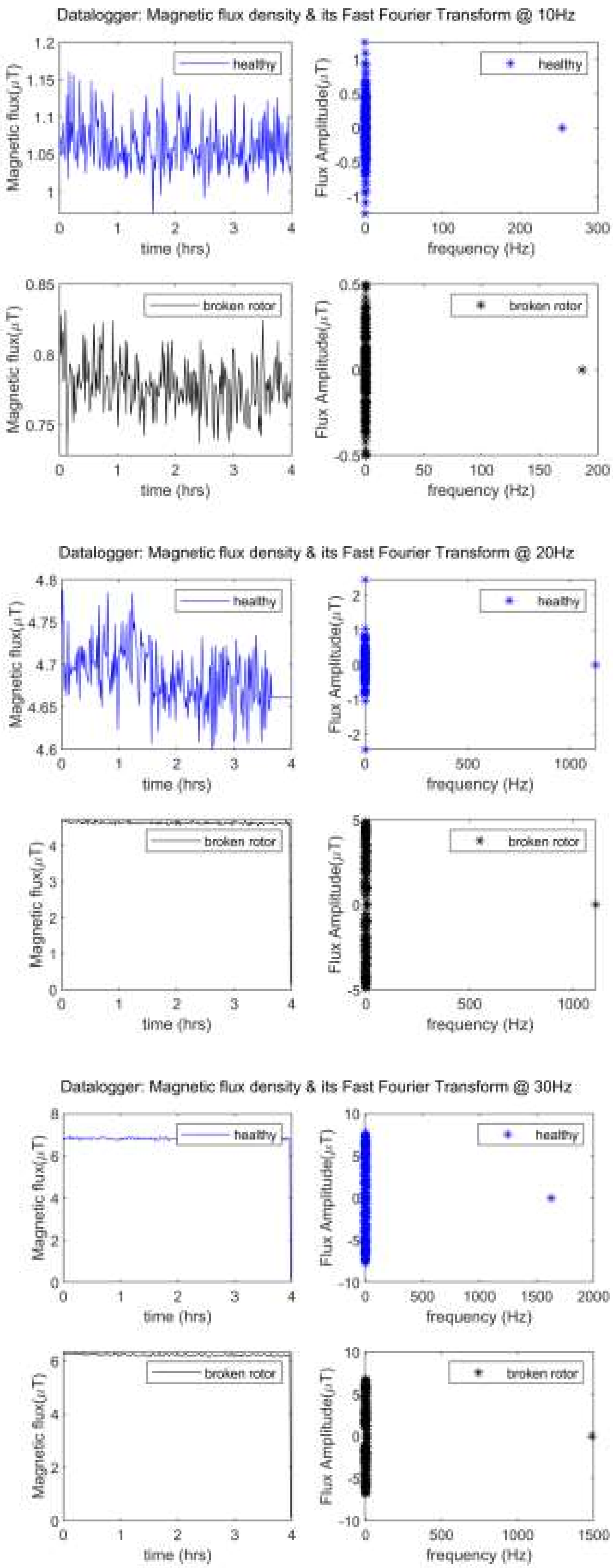

Figure 4-39: FFT harmonic analysis performed on the stray flux produced by both healthy and broken rotor

4.8 Broken Rotor Fault Results Compared with other Theoretical and Analytical Derivations

In their work, [226] developed a mathematical model for BRB fault in a three phase IM which was simulated in MATLAB. Simulation results did show that for a constant load, there was a significant difference in stator current between healthy and the BRB condition. However, as the severity of the BRB increased, the stator current only reduced by a small amount. In their own words: *"If a bar broken is increased then fault will be severe and stator current will be further decreased".* With reduced stator current, comes reduced magnetic flux in both the air gap and in turn, the stray flux. This agrees with experimental observations in this research as summarised in Table 4-7 where less magnitude of stray flux was repeatedly observed in the 5-hole broken rotor when compared to the healthy rotor under similar operating speed and load conditions. [227] simulated and analysed the BRB fault in D-q reference frame with results as summarised in Table 4-13. There was an increase in total resistance as the number of broken bars increased which means current flow in the rotor bar would decrease, leading to a decrease in magnetic flux too. Though the analysis was carried out separately from this research, experimental outcomes in this work validate the submission. Magnetic flux for broken rotor when compared to healthy machine condition did record less magnitude (Figure 4-37).

Table 4-13: Calculated rotor resistance per case of broken rotor [227]

Case	Number of broken bars	%	ΔRr	Total Rr
1	1 of 28	3.7	0.049Ω	1.389Ω
2	2 of 28	7.7	0.1032Ω	1.4432Ω
3	3 of 28	12	0.161Ω	1.501Ω
4	4 of 28	17	0.2278Ω	1.5678Ω
5	23 of 28	75	1.005Ω	2.345Ω

Lastly, [228] performed an FEM analysis of magnetic field distribution in two IMs with two different core materials each having BRBs. In agreement with other researchers, the results showed that the magnetic field line distribution was distorted in the case of broken bars for both IMs. This was attributed to the increased current flowing from the broken bars into the adjacent bars. The breakage of the rotor bars resulted in high saturation around them and around the stator teeth, therefore a high magnetic flux asymmetry. However, when results of the magnetic flux density in the stator teeth were analysed for both motors with two broken bar (2BB) and five broken bar (5BB) compared to no broken bar (NBB), there was consistent reduction in the magnetic flux density as the number of broken bars increased despite the difference in core materials (see Table III and Table IV of [228] for data). Once again, the result from this research validates these analyses previously carried out with magnetic flux density recorded for healthy being the higher and the single bar broken rotor having the magnetic flux of lower magnitude when compared as summarised in Table 4-7.

4.9 Chapter Summary

This chapter investigates the use of FBG-T sensor to reliably detect BRB fault condition. The FBG-T sensor has reliably detected the broken rotor condition when compared to the healthy condition, even after RTs. Despite the single broken bar fault emulated in two different forms, the FBG-T was consistent in performance when detecting the BRB condition. The ability of the FBG-T sensor to reliably detect the BRB condition offers huge and sufficient reliability index for its use in non-intrusive machine condition monitoring. Several mathematical, theoretical, and experimental derivations on broken rotor bar fault from previous published research outcomes have been used to validate results obtained from this research.

Chapter 5

Inter-Turn Fault Detection

ITSF is one of the widely known severe faults which can occur in any electric machine. To further deepen the understanding of the FBG-T sensing technique and its limitations, it is important to investigate its response under undesired dangerous machine conditions. This Chapter will investigate the use of the FBG-T sensor in detecting ITSF under various experimental test conditions and safety precautions. It will describe how the short circuit condition is emulated and how the test rig is set up. The FBG-T sensor performance will be analysed first between healthy and short circuit conditions, then for fault severity detection for the three different machine conditions viz: healthy, broken rotor and inter-turn short circuit.

Stator Short Circuit Fault Detection Using FBG-T Sensor

In this chapter FBG-T sensing performance in detecting a stator short circuit fault is investigated. It is particularly important to investigate the performance of the FBG-T sensor under ITSF condition because of how severe and dangerous such fault is in real life applications. ITSF can lead to malfunction of motors and even fire outbreak in some situations. Although similar experiments have been performed where FBG was intrusively and successfully used to detect short circuit faults (see Chapter 2), it is still novel to investigate non-intrusive technique using stray flux. Hence, it is relevant to test if the FBG-T would reproduce similar results. An understanding of whether the FBG-T sensor can detect such severe faults also boosts confidence in end user reliability as well as help researchers know the sensor limitations and consequently, how best to deploy these optical sensors.

5.1 IM Conditions

In this study, two distinctive machine conditions were emulated: the healthy condition and faulty condition with the latter providing ITSF. The ITSF was preferred to the inter-phase alternative due to the severity of the latter. A dedicated laboratory risk assessment was carried out to ensure that the faulty condition was emulated in a safely controlled manner and in a controlled environment. To allow for a near replica of a typical machine operating environment, the motor current rating on the VFD was intentionally increased and the overheat protection was disabled to avoid any trips. These settings were done in hindsight after the VFD had tripped on overcurrent and over-temperature during the initial test phase.

5.1.1 Healthy & Inter-turn Faulty Machines

In order to emulate ITSF, some short strands of copper conductors were tightly inserted to make electrical connections between the turns within the same phase in different parts of the stator windings as shown in Figure 5-1 and Figure 5-2. The latter figure shows the healthy IM identical in size and ratings to the ones in the previous chapter. For a healthy IM, the total loss is given by:

$$P_{tot} = P_{1cu} + P_{2cu} + P_{core} + P_{mech} + P_{stray} \tag{5.1}$$

where P_{1cu} and P_{2cu} are the copper winding losses in the stator and rotor respectively, P_{core} is the combined iron core loss due to eddy currents and magnetic hysteresis present in the core, P_{mech} is the mechanical loss mainly due to friction, and P_{stray} is the stray load loss. All these losses combine to generate heat physically within the motor. The copper winding losses are very much dependent on current flowing through the copper windings and the resistance of the winding and are given by:

$$P_{xcu} = I_{xcu}^2 R \tag{5.2}$$

where x denotes the location of the copper winding, for example, 1 for stator and 2 for rotor.

With the addition of a third set of strands between turns of each phase to emulate the short circuit condition, there will thus be additional copper winding loss, P_{3cu}. Thus, for the faulty IM with ITSF, the total loss is given by:

$$P_{tot} = P_{1cu} + P_{2cu} + P_{3cu} + P_{core} + P_{mech} + P_{stray} \tag{5.3}$$

where

$$P_{3cu} = I_{3cu}^2 R \tag{5.4}$$

Due to increased amount of current flow because of more copper windings, it is expected that the inter-turn fault condition will generate more I^2R losses in the form of heat. Depending on the quantity of heat within the machine, this should increase the heat on the periphery of the yoke which will be measured by the FBG-T sensor.

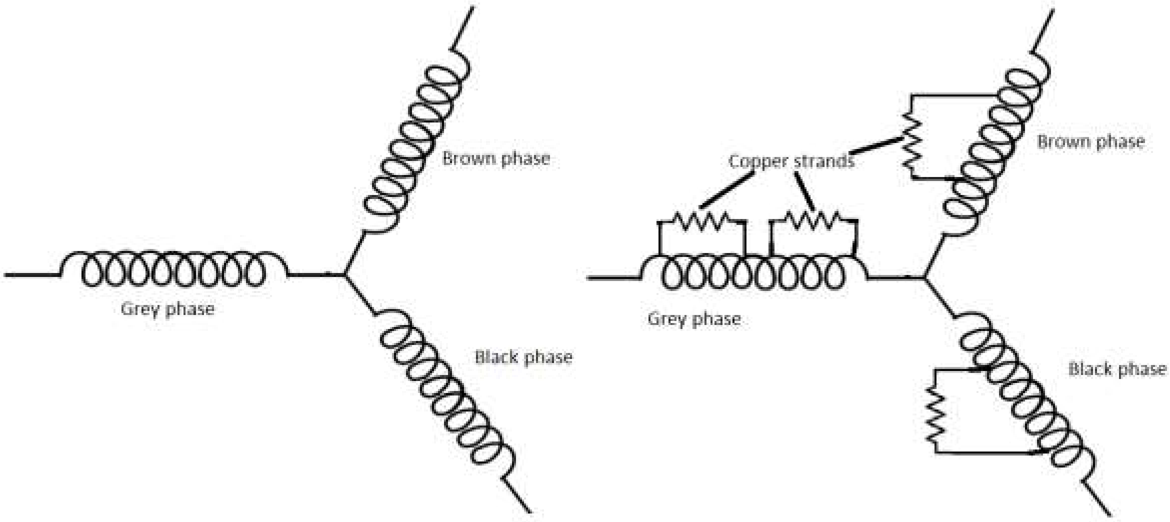

Figure 5-1: Illustration of healthy (left) and ITSF stator windings (right)

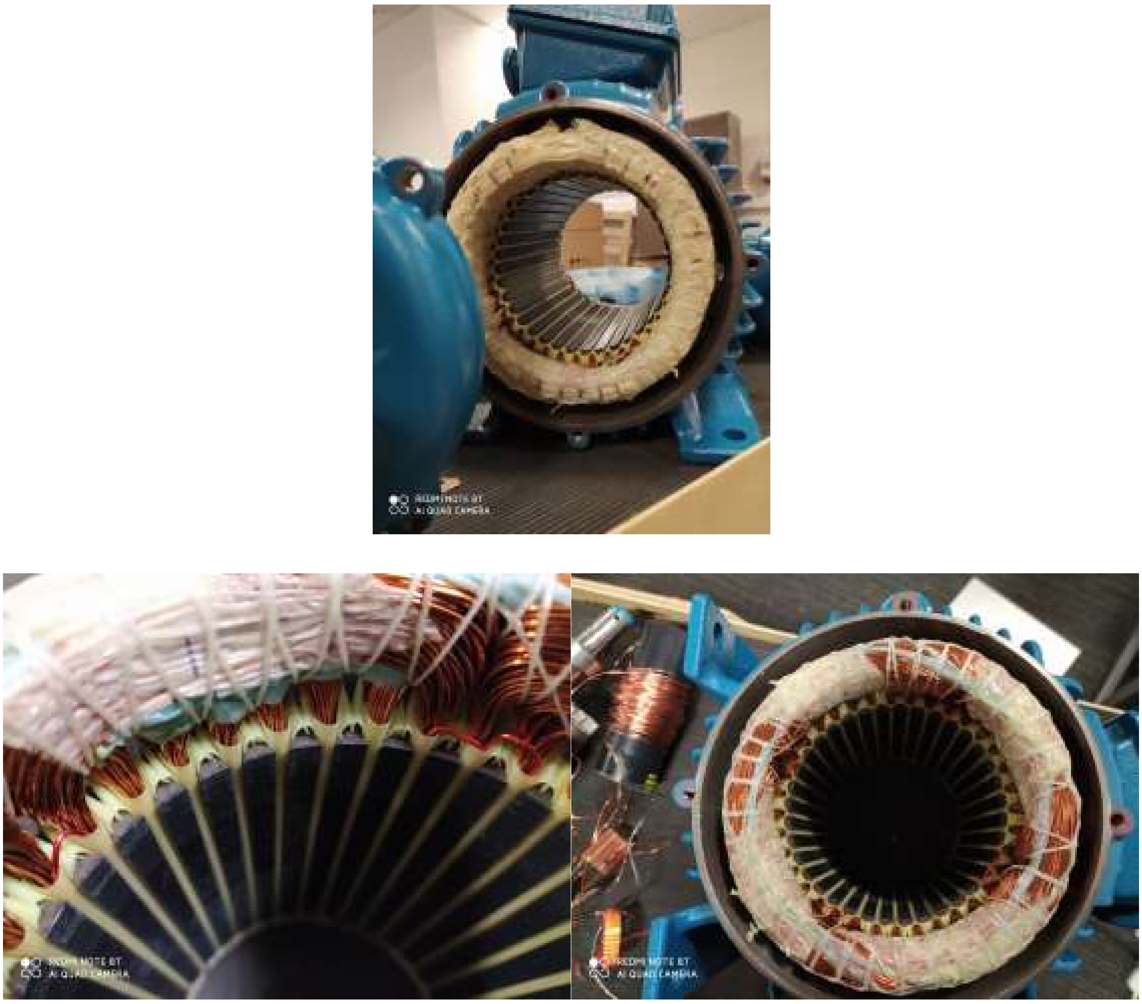

Figure 5-2: Emulating ITSF by inserting copper strands into stator winding

5.1.2 Set up and Results

The test rig setup is identical to the one in the previous chapter for broken rotor condition except that the machine conditions are now different. The short circuit faulty IM is connected to the VFD and then coupled to the DC motor as load. The FBG-T sensor is in the transverse position at the DE of the motor with the centre of the rotor shaft acting as a reference. The FBG-T is then connected to the OSA, which is in turn connected to the PC with LabView where numerical data are collected and stored. Figure 5-3 shows the circuit schematic and test rig set up.

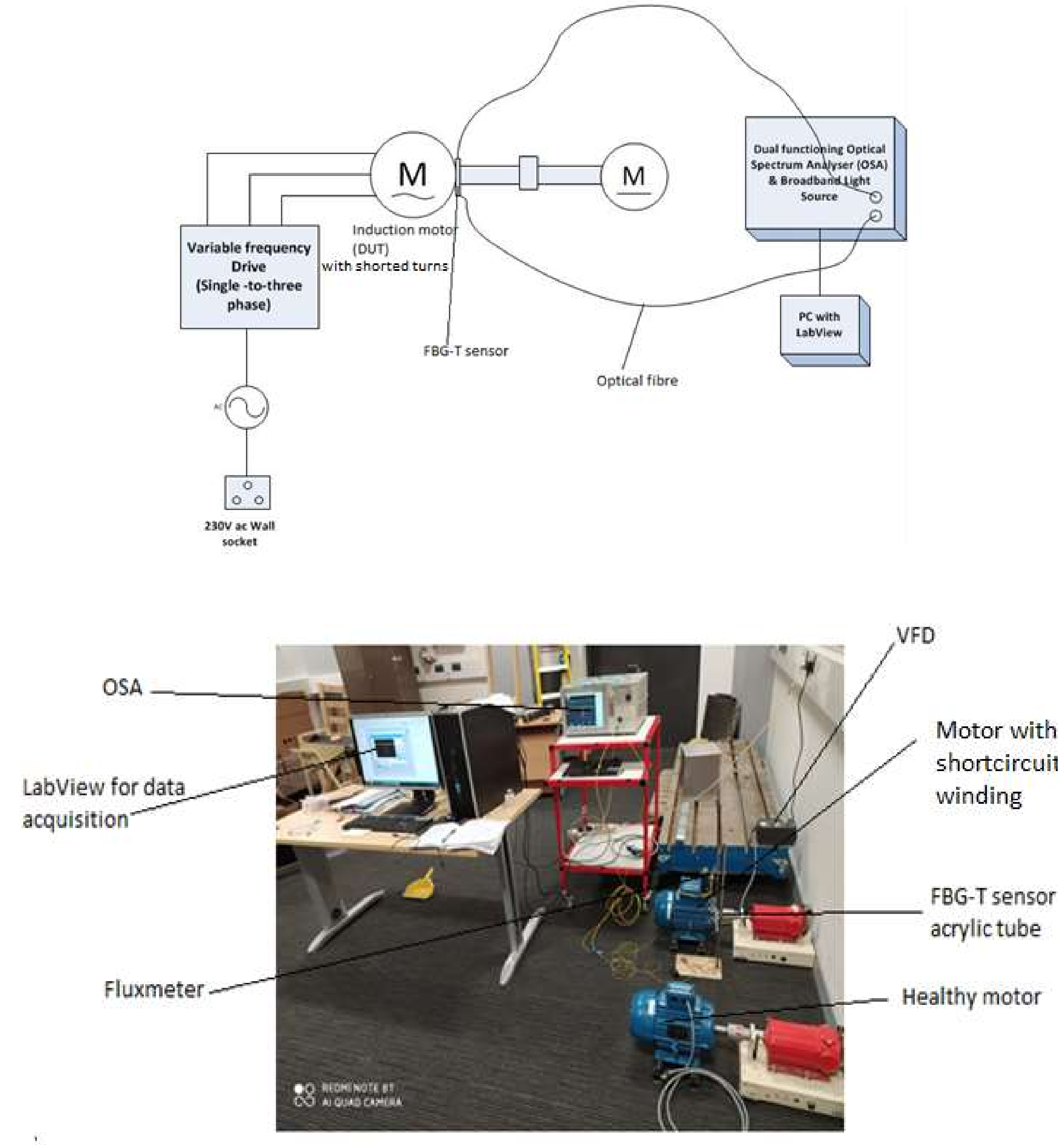

Figure 5-3: Schematic and actual test rig set up for ITSF condition

The test was conducted at the same frequencies as the healthy motor in the previous chapter (5Hz-30Hz). Observations confirmed significant temperature rise in the case of the ITSF and a dramatic increase in braggshift accompanied by a set of rather near-normal magnetic flux readings for frequency between 5Hz and 15Hz. By 20Hz it was observed that both the temperature and magnetic flux had reduced unexpectedly developing some curiosity as to why. Table 5-1 summarises the result.

Table 5-1: Data obtained for inter-turn short circuit machine condition

Frequency (Hz)	5	10	15	20 Burnt windings	25	30
RMS Flux density (μT)	1.63129	5.207296	9.335977	8.229172	-	-
Max Braggshift (pm) during operation	290	530	645	40	-	-
Max Braggshift (pm) during 20 hours	295	595	850	70	-	-
Mean Temperature (°C) during operation	23.853846	24.77	26.069231	23.03077	-	-
Duration of operation	2 hours per frequency					

5.2 FBG-T Short Circuit Sensing Data Analysis & Discussion

Large amounts of braggshifts are observed for the initial frequencies tested, which are 295pm, 595pm and 850pm respectively as depicted in Figure 5-4, Figure 5-6 and Figure 5-7 for the initial 5Hz, 10Hz and 15Hz frequencies tested. As can be seen, the noticeable large wavelength shifts are identical to the ones observed during the temperature calibrations (hundreds of pm) as shown in Figure 5-4. This initially suggests that they are largely due to the overtemperature caused by the increased I^2R losses because of the ITSF. However, a more detailed analysis in section 5.3.2 showed that this was not the case. Particularly of interest, is the time it took for the FBG-T sensor to return to its initial wavelength as well as the magnitude of the change in temperature causing such large braggshifts. Unlike the case of the temperature calibration, these large braggshifts required several hours to return to their initial wavelength converse to the several minutes it took during the temperature calibration. This clearly justifies the presence of a magnetic field and its effect on the braggshift. It thus confirms that the braggshift is due to both the magnetic flux and the overtemperature caused by the ITSF condition as the result was consistent at all three frequencies, 5Hz, 10Hz and 15Hz.

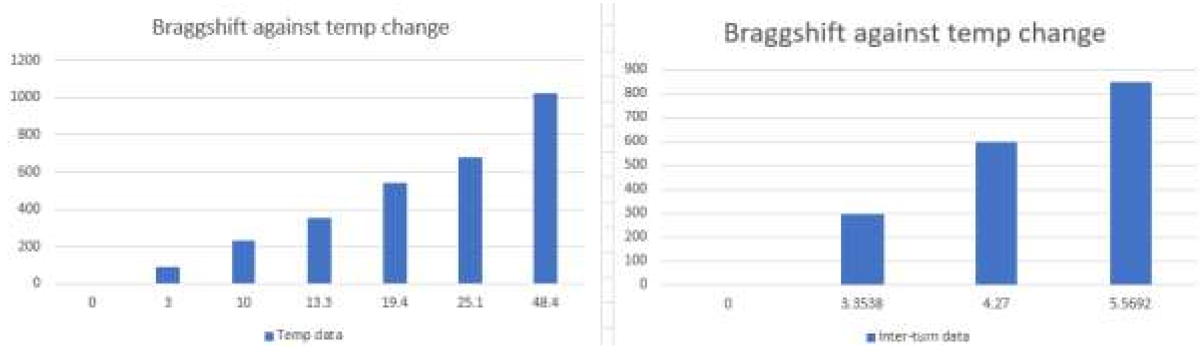

Figure 5-4: Comparison between braggshifts due to temperature only and ITSF

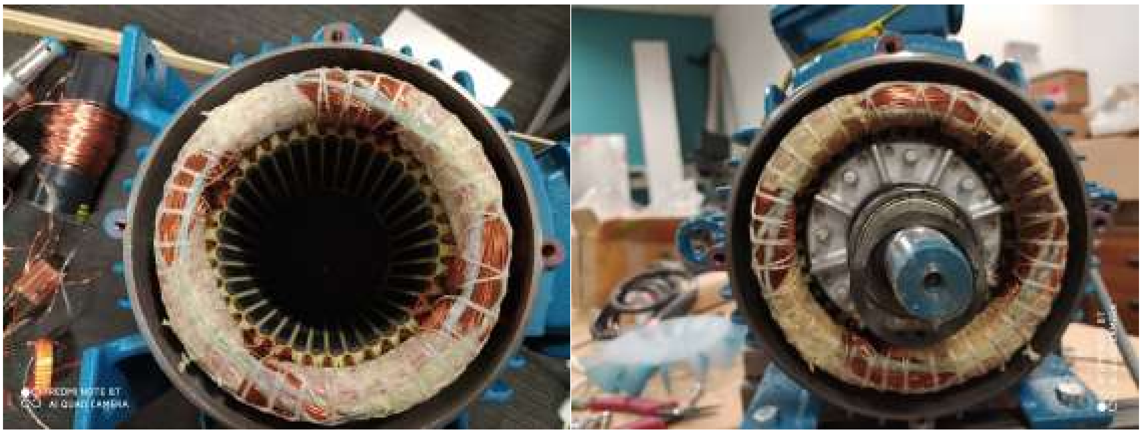

Figure 5-5: Stator windings before (healthy) and after ITSF (burnt)

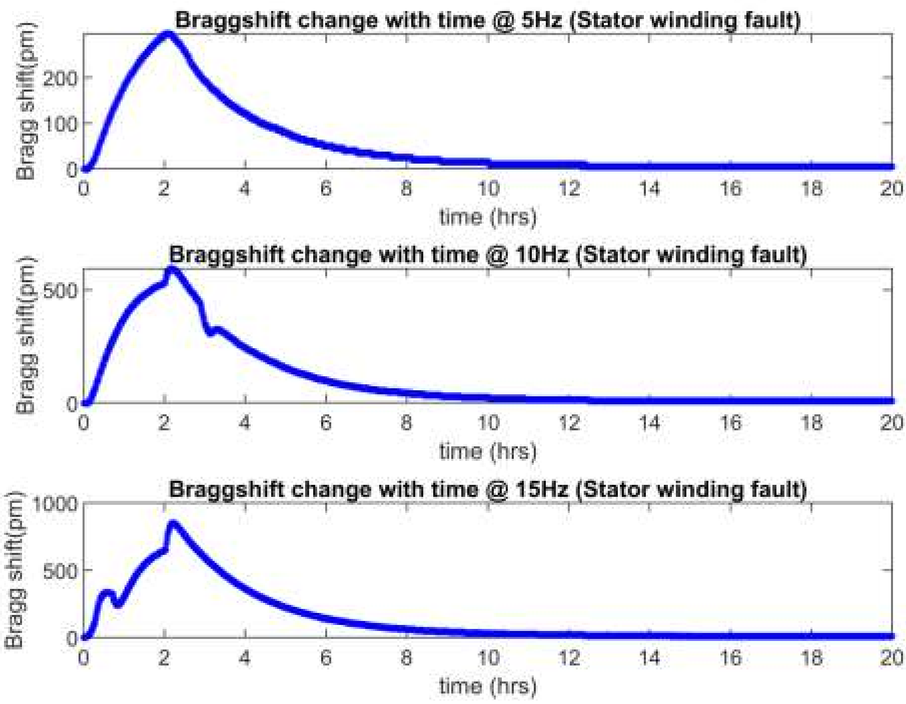

Figure 5-6: FBG-T response to ITSF - Reversible magnetisation trend with large braggshifts

The unexpected reduction in temperature and magnetic field strength necessitated the need to confirm whether the copper conductor strands were still in place, and whether the ITSF condition had been compromised. According to Faraday's law of electromagnetic induction with which the IM works, induced electromotive force, e is proportional to the rate of change of flux given by:

$$e = -N\frac{d\varphi}{dt} \tag{5.5}$$

where N is the number of turns and the magnetic flux, φ is a product of the magnetic field strength, B (in Tesla) and the cross-sectional area, A of the conductors. Thus, Equation 5.5 can be rewritten as:

$$e = -N\frac{d(BA)}{dt} \tag{5.6}$$

The thickness of the stator winding and thus its cross-sectional area, A is constant for this motor, thus it can be stated that the effective area contributing to the magnetic field strength is actually:

$$A_{eff} = NA \tag{5.7}$$

Rate of change of magnetic flux, dφ, thus can be written as:

$$\frac{d\varphi}{dt} = A_{eff}\frac{dB}{dt} \tag{5.8}$$

This means then that for a change in magnetic flux, dφ to result in a corresponding change in magnetic flux density or magnetic field strength, dB, there must be a change in the effective cross-sectional area of the stator windings. In other words, although there are N number of turns, each turn in the winding must contribute to the overall magnetic field strength. Here, the rotor is a squirrel cage and the number of turns, N in the stator winding has not changed. To reduce the magnetic field strength, either the number of turns (N) must be reduced, or the effective cross-sectional area (A_{eff}) must be reduced. During the experiment, neither of these parameters have been intentionally reduced, instead, as the motor frequency was increased to 20Hz, the rate of change of magnetic flux should have increased as well. As earlier mentioned, it was observed that both the temperature and magnetic field strength had reduced unexpectedly. With a fixed number of turns, the only explanation would be a change in the effective cross-sectional area of the stator windings. This means that there has been a reduction in the number of windings that are contributing to the magnetic flux generated within the motor. This reduction is possible if some of the windings have burned out which means they are having infinite resistance like an open circuit and thus, have become non-conducting and ineffective.

This is possible because the resistance of the copper winding increases with temperature given by:

$$R_T = R_{rm}(1 + \alpha \Delta T) \tag{5.9}$$

where R_T and R_{rm} are the resistances of the winding at a new temperature and at room temperature respectively; ΔT is the change in temperature; and α is the thermal coefficient of resistance which is constant for each type of conductor (in this case, α = 0.004Ω/°C for copper). Having established earlier that the inter-turn would result in higher temperature in form of heat, it is not unexpected that the increase in temperature has led to an increase in the stator winding resistance. This has possibly resulted in a burn out of some parts of the winding leading to an overall reduction in the effective cross-sectional area of the stator winding. Thus, has led to a reduction in the magnetic field strength.

After the motor was disassembled, it was observed that part of the stator winding had burnt out as suspected (Figure 5-5) which was the reason for the reduced temperature and magnetic flux as only a smaller number of conductors were carrying current (i.e., reduced A_{eff}). Therefore, the investigation was halted at this stage as the FBG-T sensor has proved to be very reliable in detecting such serious fault condition non-intrusively using stray flux. A repeat test was performed later with a smaller number of shorted copper strands, to avoid burning the stator windings on an identical machine and further substantiate this crucial observation. A plot of braggshift against frequency and magnetic flux (Figure 5-8) shows the large magnitude of the wavelength changes that has occurred due to the inter-turn fault as earlier explained. The figures also show the drastic increase in temperature with magnetic flux and the less drastic increase in magnetic flux with frequency. It is a well-known electrical principle that heat is the major outcome from a short circuit fault due to increased current flow and the slight increase in magnetic flux is owing to the slight increase in the number of conductors generating the flux.

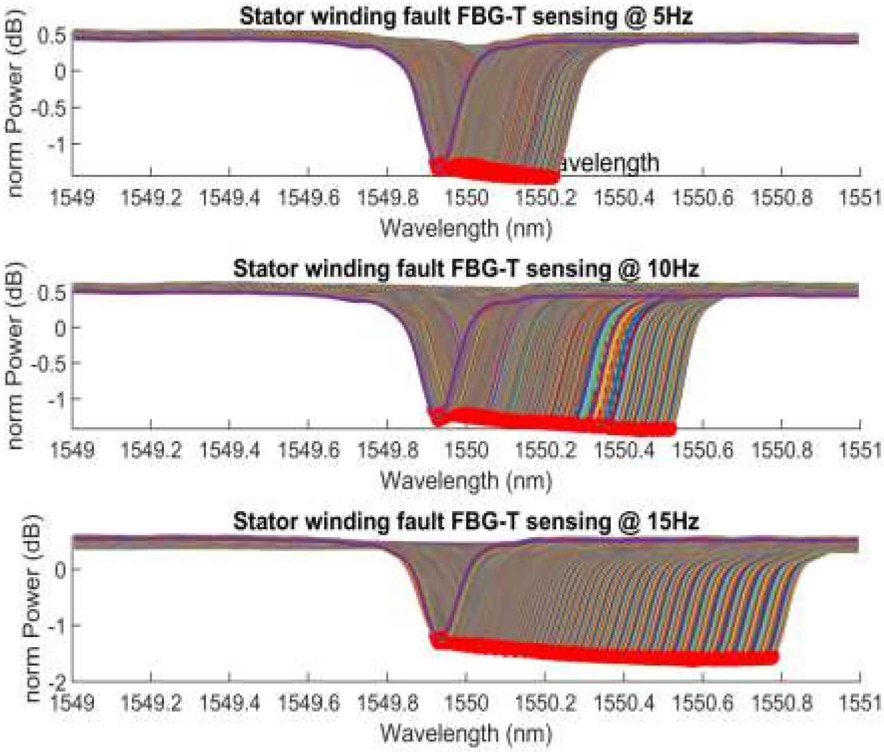

Figure 5-7: Optical spectral response of FBG-T sensor under ITSF condition

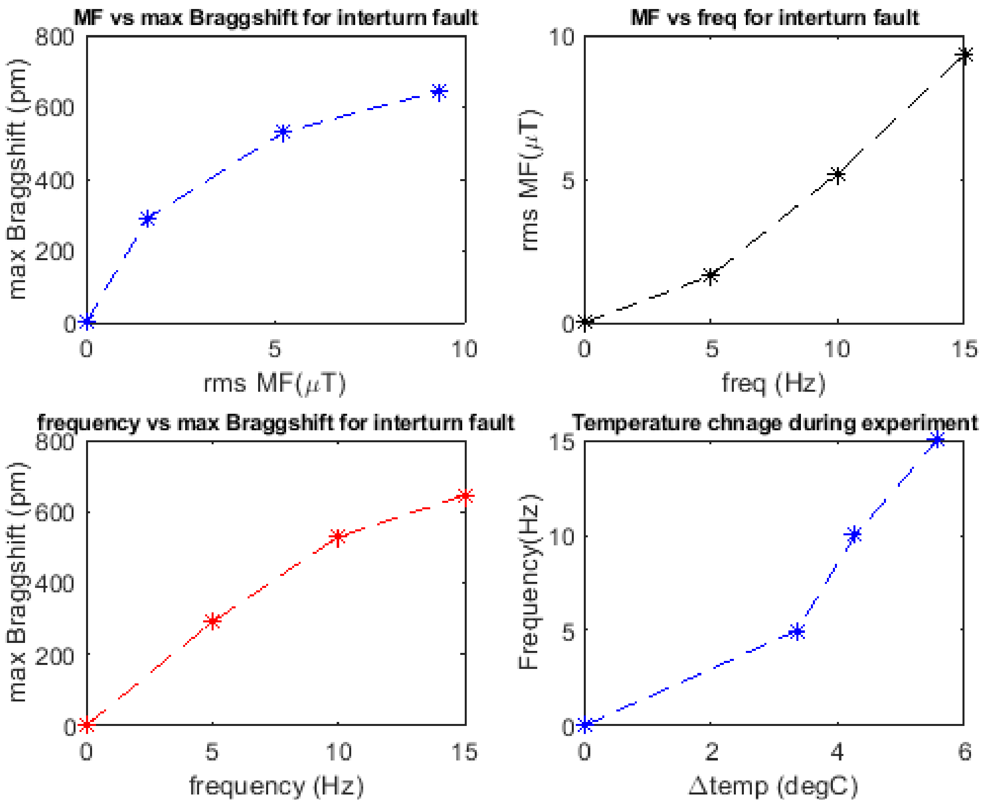

Figure 5-8: Variation of external magnetic flux density with frequency, temperature and braggshift under ITSF

5.3 Fault Severity Analysis without Auto data logger

5.3.1 Healthy vs Inter-turn

To detect the aberration from the healthy motor condition, data from both conditions were analysed in Table 5-2. Braggshifts observed with increase in frequency, and in turn magnetic flux, clearly showed a stark path between both motor conditions due to the severity of the inter-turn fault. Whilst braggshifts were in the tens of pm for the healthy condition, they were in the hundreds of pm for the short circuit condition (Figure 5-9) which is a succinct feature fundamental to the use of FBG-T sensor in fault detection. The disparity between the intensity of the stray magnetic flux was not large as only a few turns of extra copper conductor strands were added to emulate the fault condition. Figure 5-9 shows a slight increase in the magnetic flux for the faulty condition compared to the healthy state, due to a slightly higher current producing the magnetic flux. However, the temperature difference was significant.

Table 5-2: Comparison of braggshifts changes with temperature at different frequencies

Frequency (Hz)	Healthy	Inter-turn	Healthy	Inter-turn
	Braggshifts (pm)		ΔTemp. (°C)	
5	30	290	0.7615	3.3538
10	50	530	0.5600	4.2700
15	45	645	1.4692	5.5692

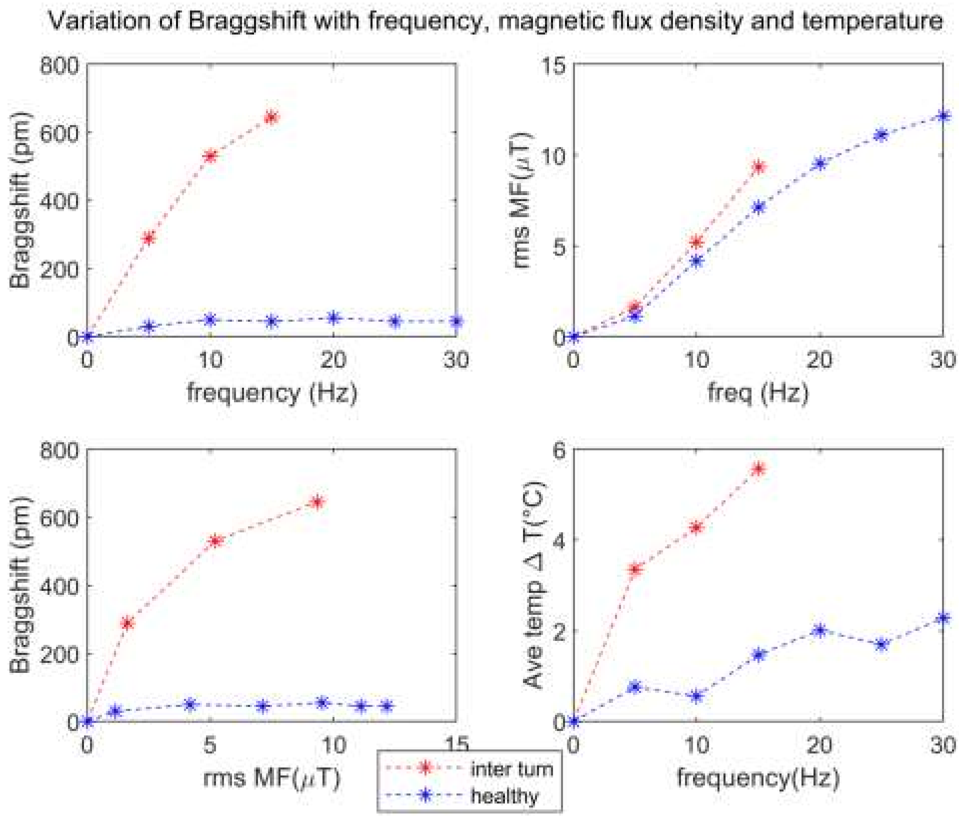

Figure 5-9: Variation of frequency with braggshifts, external magnetic flux density and temperature under ITSF

5.3.2 Temperature calibration vs ITSF

As earlier stated, there were similarities in the FBG-T sensor response to increase in temperature in terms the order of magnitude of braggshift in both the application of heat without the presence of a magnetic field during calibration, and the ITSF condition. Unlike the case of the temperature calibration, these large braggshifts required several hours to return to their initial wavelength converse to the several minutes it took during the temperature calibration as shown in Figure 5-10. A unique spectral observation when both data were analysed on the same plot is shown in Figure 5-11.

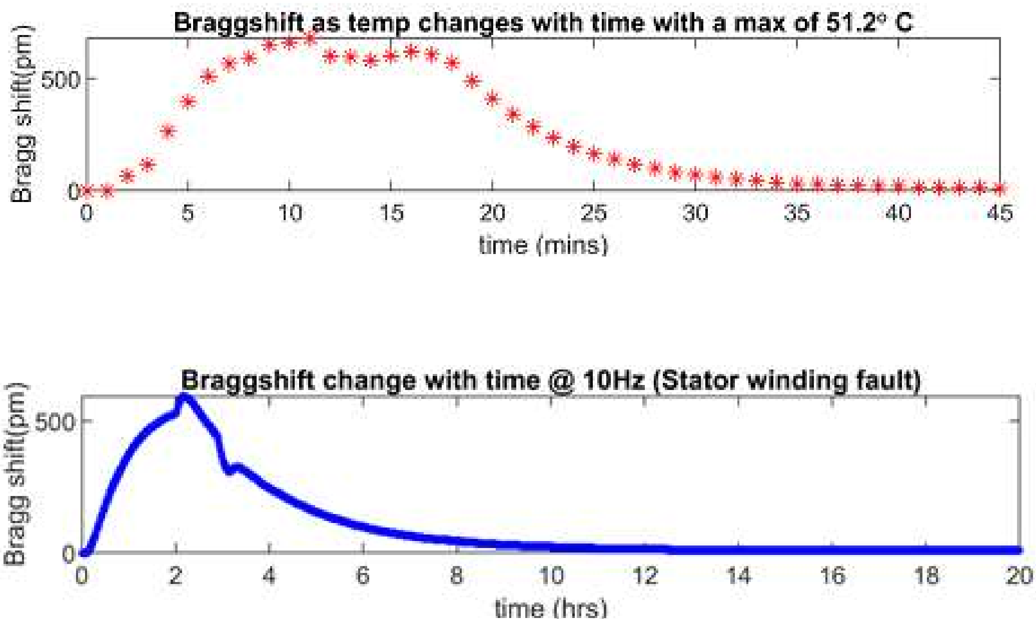

Figure 5-10 Braggshifts during temperature calibration versus ITSF condition

Although the temperature change for the absence of magnetic field was around 25.1°C before the FBG-T response could achieve a braggshift of 680pm; it took a temperature change of about 5.6°C to attain a braggshift of 645pm. This means that the inter-turn fault has caused some distortion in the magnetic flux property. This has significantly affected the behaviour of the magnetic dipoles, and hence the magnetostrictive behaviour of the terfenol-D which has been transferred to the FBG. This is important as it is not just the consequence of overtemperature that has been detected here, but much more than that. It is the combination of overtemperature and the distortion in the magnetic flux produced under a short circuit condition which has triggered an unambiguous and distinct response from the FBG-T sensor. This behaviour was consistent at all frequencies confirming that the large wavelength shifts detected are due to the ITSF and how it has distorted the magnetic flux.

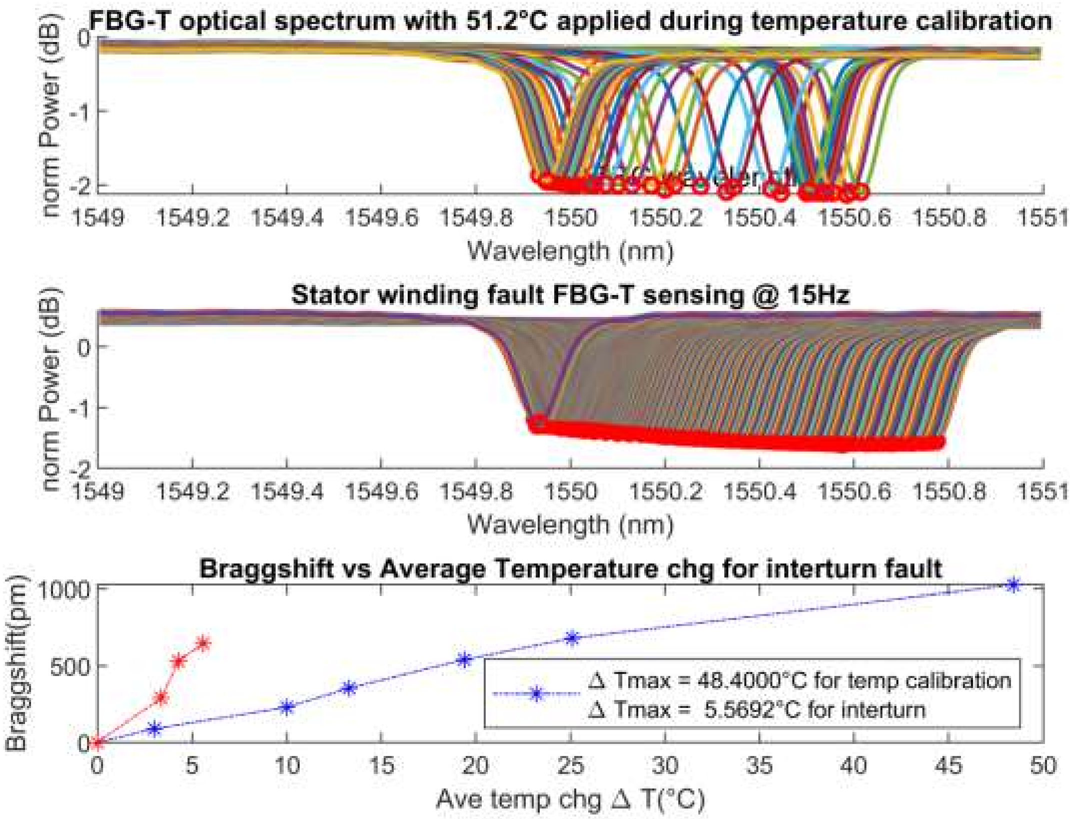

Figure 5-11: FBG-T response comparison between temperature calibration and ITSF condition

The way the braggshift occurred spectrally also shows a distinct pattern at all temperature and frequencies as shown in Figure 5-11. Wavelength changes exclusively due to temperature were more dispersed compared to the gradual and more sustaining shifts due to magnetic flux distortion caused by the short circuit fault. It is indeed very interesting to note that such distortion in the past has been analysed by researchers using various techniques as highlighted in Chapter 2. However, this investigation does prove two crucial points. Firstly, that FBG-T optical sensor can detect magnetic field distortions caused by short circuit faults not just intrusively, but *non-intrusively using stray flux* in a very reliable manner. Recent research findings by [31], [43], [229] did submit that in-situ measurements obtained using FBGs contained simultaneous information on the examined rotor's thermal and mechanical operating conditions. This in their opinion, provides a step forward in understanding the potential of FBG based rotor condition monitoring applications. Thus, the second crucial point here is that this experiment further confirms that FBG-T sensor does contain simultaneous information on *thermal and electromagnetic* operating conditions of the IM. Whilst the first point is novel, the second has been researched and corroborated in other experiments. This clearly justifies the presence of a magnetic field and its effect on the braggshift. It thus confirms that the braggshift is due to both the magnetic flux and the overtemperature caused by the ITSF condition as the result was consistent at all three frequencies.

5.3.3 Healthy vs Inter-turn vs Broken rotor damage

Figure 5-12 corroborate the capability of the FBG-T sensor to reliably detect machine conditions and their severity. A BRB faulted motor yields a slightly higher braggshift compared to the healthy motor condition using FBG-T. When compared to the short circuit condition, the FBG-T produces a significantly higher braggshift which suggests that the latter condition is a more severe fault condition. This is an established understanding of machine faults (see Chapter 2). This is very reassuring as depending on application, industrial control systems can rely on such feature extraction as a fault detection signature to know when to plan maintenance activities or when to immediately take a machine out of service. This is to avoid further damage or even fire outbreak as is the case with most short circuit faults if no protection schemes are in place. Another feature extraction is the use of temperature as a fault signature. In this case, the temperature change for both rotor damage and healthy conditions were almost within the same range of less than 3°C when the motor was run at all the six frequencies. Temperature variations, though small, are mainly due to the surroundings rather than the machine condition. Therefore, the braggshifts recorded for both conditions were less than 100pm and were mainly because of the magnetic flux rather than temperature. It should be said that every motor will heat up normally but once running the change in temperature is reasonably constant provided the load on the motor stays the same which was the case during this investigation.

On the other hand, inter-turn faults are known to result in overtemperature as earlier mentioned but in this case a temperature change of about 3.4°C and 5.6°C already produce braggshifts of about 290pm and 645pm at 5Hz and 15Hz respectively. These braggshifts were obtained at different times and days. It is clearly the case that temperature alone could not have caused such large braggshifts, given that the mean temperatures during the experiments were around 23.9°C at 5Hz, 24.8°C at 10Hz and 26.1°C at 15Hz. The initial mean room temperature was 20.7°C prior to starting the experiments. Though higher than the temperature under healthy condition which were 24.2°C, 23.96°C and 24.9°C at 5Hz, 10Hz and 15Hz respectively with an initial mean room temperature of 23.4°C; it is obvious that such massive braggshifts could not be attributed solely to temperature. Hence the FBG-T can be said to respond strongly to distortions in magnetic field behaviour even with stray flux.

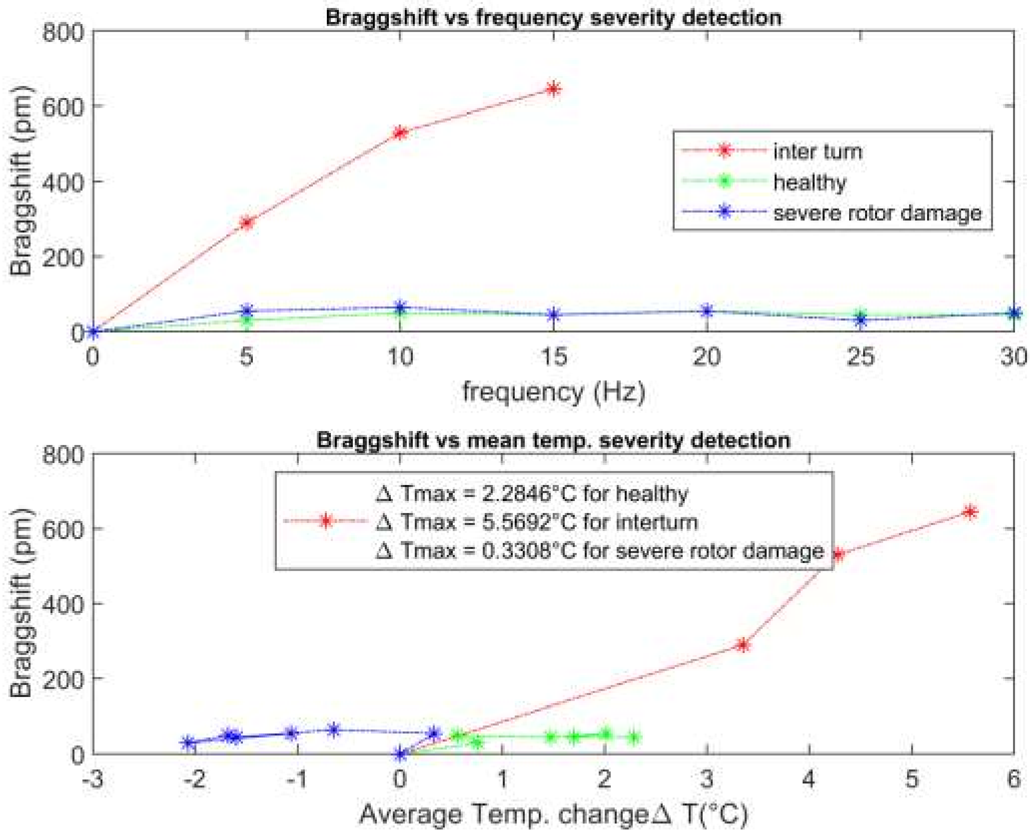

Figure 5-12: Braggshifts with changes in frequency and temperature for fault severity detection

5.4 Short Circuit Condition Monitoring with Auto Data Logger

5.4.1 Test Conditions

Figure 5-13 shows the three copper conductor strands that were used to emulate a short circuit fault in the IM. Earlier a similar test was performed but with more copper conductor strands which resulted in burnt stator windings following the over-riding of the built-in overcurrent protection in the VFD. In order to avoid a repeat of such damage, a smaller number of conductor strands was used to allow for testing over the entire test frequency range as this was not achievable previously, due to the damage to the motor. Motor was run from 5-30Hz with 5Hz interval as before but this time for the duration of four hours and turned off for 16 hours per frequency to reduce sensor pre-stress levels.

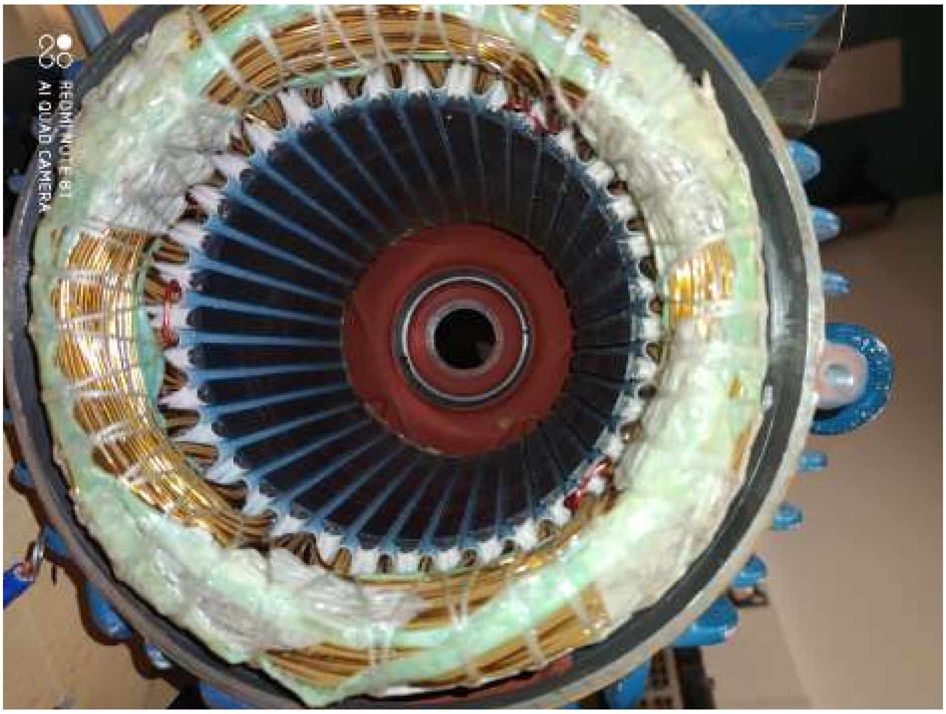

Figure 5-13: Three copper strands used to emulate a short circuit fault condition

5.4.2 Results & Discussion

5.4.2.1 5Hz Frequency interval

With a longer duration of operation, there was consistency in the behaviour of the FBG-T sensor with respect to braggshifts. The shift in wavelengths appear to rise and plateau within the four hours, and once the machine was turned off, further braggshifts were observed. The reason for this as explained earlier, is due to the paramagnetic characteristics of the terfenol-D transducer. This further braggshifts tend to last for only several minutes as shown in Figure 5-14 before a clear descent path back to the initial wavelength. The FBG-T behaviour described was observed when the motor was run at the different frequencies. Another key observation was that throughout the short circuit condition test, the FBG-T was observed to show less hysteresis when returning to its initial wavelength. This may be due to the spectral content of the stray magnetic flux as the other external factor (ambient temperature) which could affect the sensor was reasonably constant with minimal variation. It is worthy of mention that while this reduced hysteresis may be desired, it does not affect the use of the FBG-T sensor for fault detection because the underpinning principle of FBG sensing in general depends on the magnitude of braggshift.

Table 5-3: Data for ITSF using Auto Data Logger

Frequency (Hz)	0	5	10	15	20	25	30
RMS Flux density (µT)	0.1417	0.3414	1.3313	3.9901	8.4094	10.8951	11.5808
Max Braggshift (pm) during operation	0	160	165	205	230	240	250
Max Braggshift (pm) during 20 hours	0	165	205	270	330	385	430
∆Temp during operation (°C)	0	3.1280	2.9520	3.9530	4.2340	4.9440	6.8460
Duration of operation	4 hours per frequency						

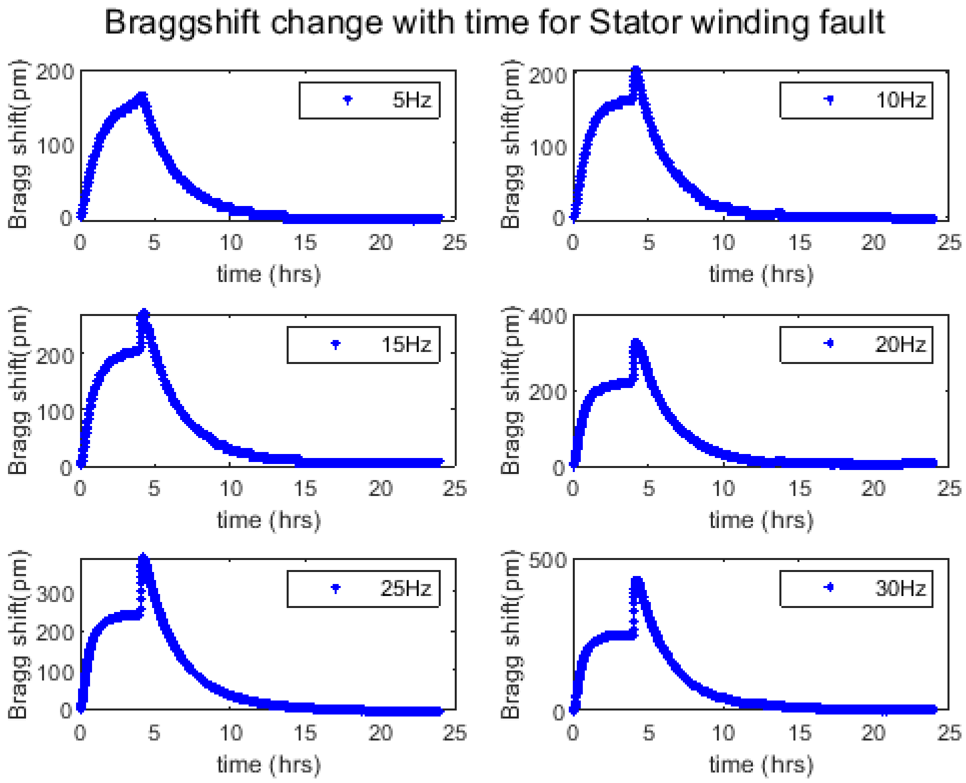

Figure 5-14: Braggshifts with time for entire frequency range at 5Hz interval under ITSF

Figure 5-14 and Table 5-3 show that the order of magnitude of braggshift observed during ITSF condition are in hundreds of pm which is clearly very high. These large braggshifts were succinct in the optical spectra at different frequencies where the wavelength shifts increased with frequency as depicted in Figure 5-15. In theory it would be easy to associate the large braggshifts to the increase in magnetic flux density or temperature or a combination of both factors. From Table 5-3, Figure 5-14 and Figure 5-15 there is a direct but non-proportional increase in braggshift with magnetic flux density as well as with maximum temperature change as frequency increased, which agrees with theory. However, when compared to corresponding values of magnetic flux density (Figure 5-16), the temperature changes in other machine conditions, and temperatures during sensor calibration in Chapter 3; it is difficult to convincingly suggest that only the *amplitudes* of these two measurands are responsible for such a large magnitude of braggshift. With the aid of the auto datalogger, the magnetic field obtained was later subjected to spectral analysis to further analyse its content.

Temperature increase as a natural result of ITSF was observed with the maximum observable change at higher frequencies (Figure 5-17). When compared to the results obtained during temperature calibration of the FBG-T sensor where similar order of magnitude of braggshifts were observed, these maximum temperature changes are much smaller to be largely responsible for such wavelength shifts.

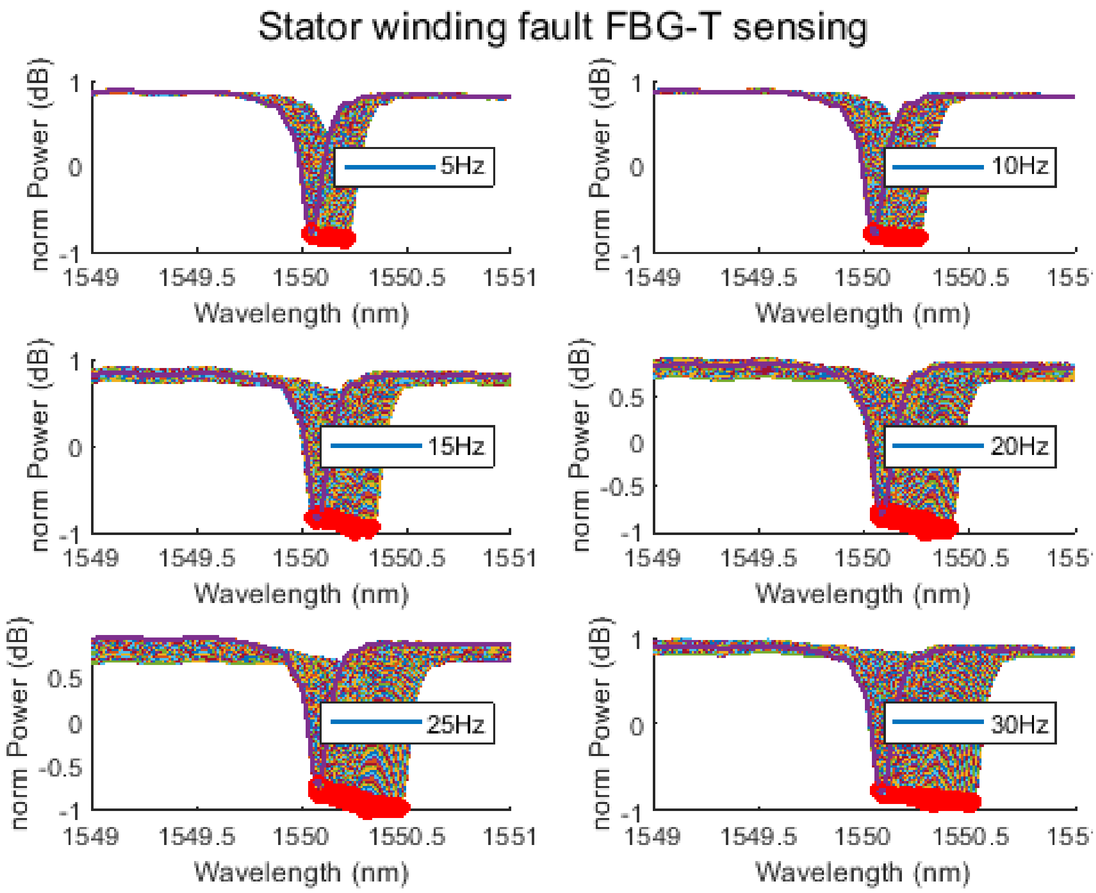

Figure 5-15: FBG-T optical spectra for entire frequency range at 5Hz interval under ITSF

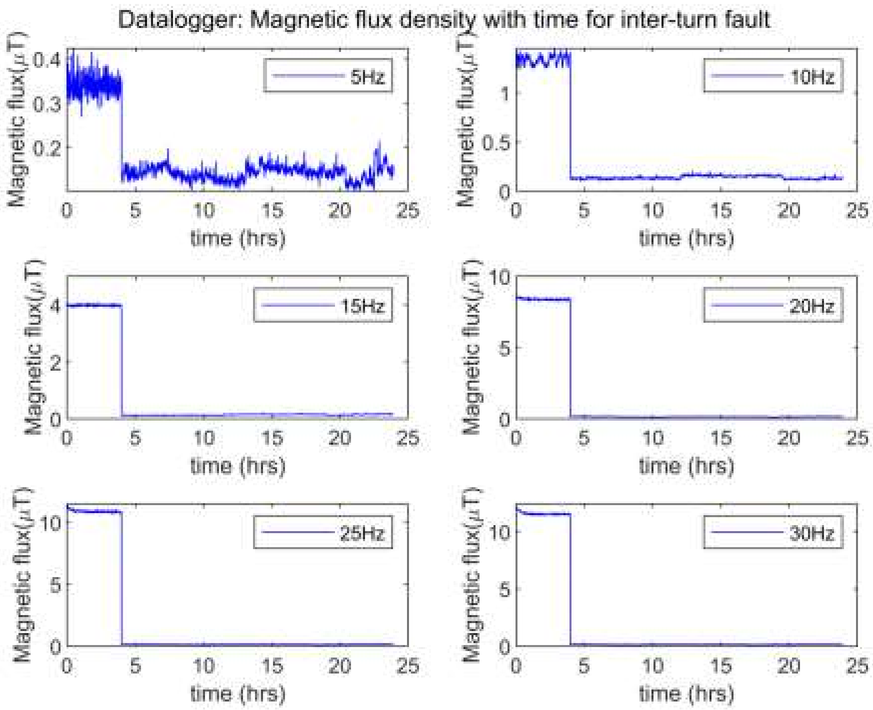

Figure 5-16: Variation of magnetic flux density with time for entire frequency range at 5Hz interval under ITSF

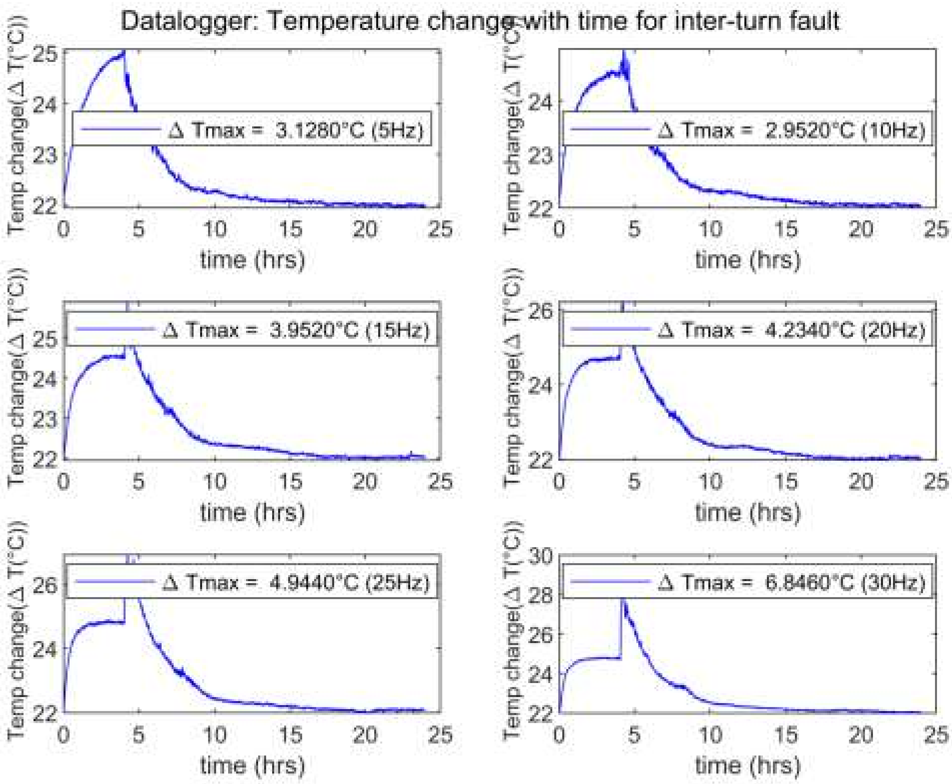

Figure 5-17: Temperature variation with time for entire frequency range at 5Hz interval under ITSF

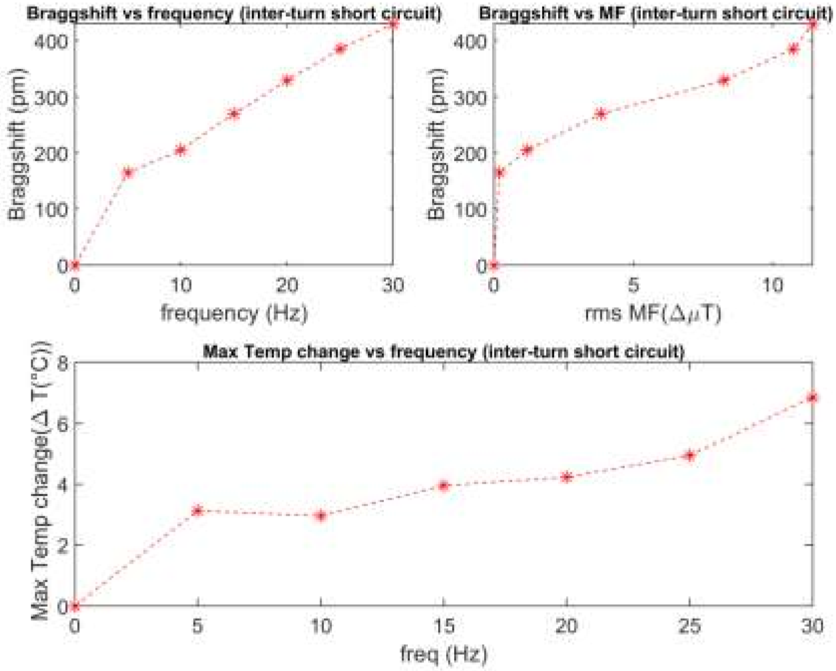

Figure 5-18: Variation of magnetic flux density and temperature with motor test frequencies

Figure 5-18 summarises the observations from the ITSF FBG-T condition monitoring test with large braggshifts in hundreds of pm which increased in magnitude as frequency of the motor was increased. At higher frequencies, the motor was made to do more work leading to higher temperature changes in addition to the shorted stator turns. The magnetic flux density though higher for larger braggshifts in terms of amplitude; its spectral content is partly responsible for the drastic and obvious FBG-T response to the ITSF condition. This will be further explained during severity analysis later in this chapter.

5.5 Faulty Severity Analysis with Data logger

5.5.1 Healthy vs Inter-turn

5.5.1.1 5Hz Frequency interval

Figure 5-19 results serve two purposes: first, to help explain observations from the test in relation to specifically identifying ITSF; and secondly to prove experimental reproducible evidence of the reliability of the use of FBG-T sensor for ITSF detection using stray flux. Compared to the healthy condition where braggshifts were barely just over 50pm irrespective of the frequency at which the motor is run; under ITSF condition, the braggshifts are well over 100pm even up to over 400pm. In fact, the braggshift directly responded to the change in the motor frequency. This was identical to the earlier observed results in Figure 5-8 when there were a greater number of shorted turns that burnt the stator winding initially. Though the experiment was halted after the motor damage incident, the trajectory for the both the healthy and the inter-turn conditions in the two tests are identical and clear in the accuracy of the FBG-T sensor to detect the short circuit faulty condition.

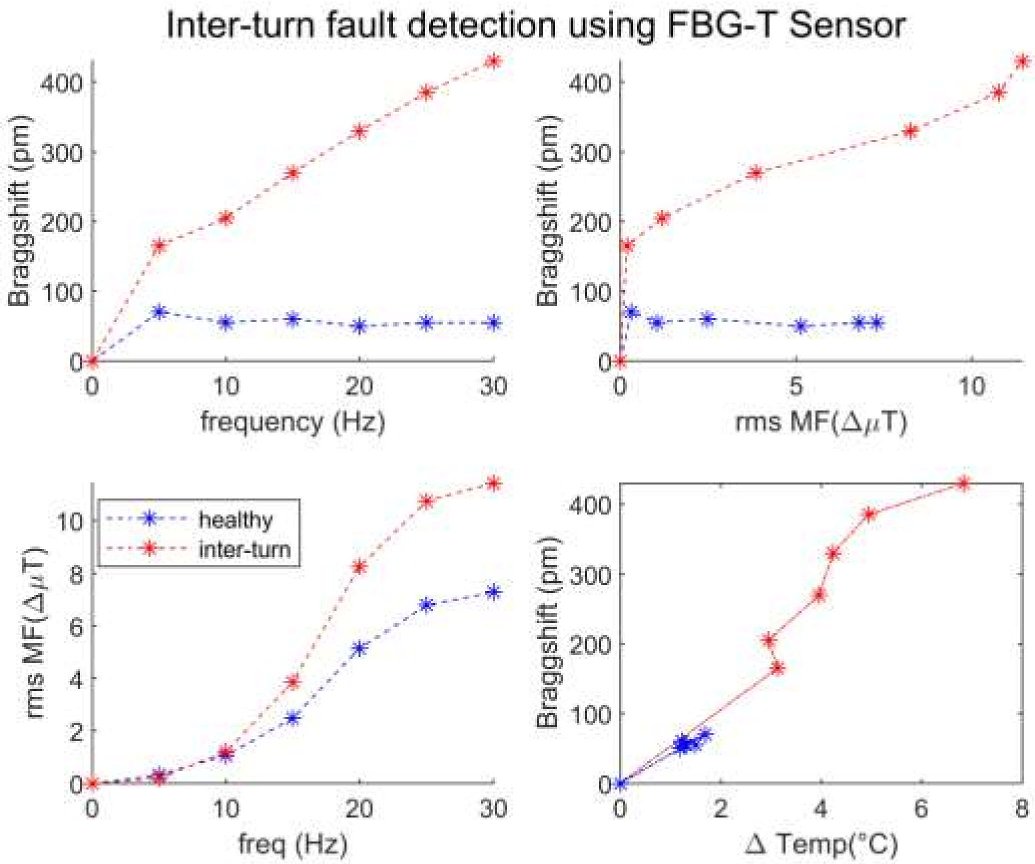

Figure 5-19: Braggshifts with changes in frequency and temperature for ITSF detection

The magnetic flux densities measured in both tests were of similar range as well and when compared with the frequency range, showed an increase in amplitude as motor frequency increased (see Figure 5-19 and Figure 5-9). Considering the magnitude of the stray flux is in μT range, the difference in flux densities between successive frequencies was less than 5μT which is small to cause such large braggshifts. When compared to the healthy condition, the magnitude of the flux density of both healthy and inter-turn fault conditions where in the same range with increasing difference between corresponding values as frequency increased. For example, at 10Hz the difference in magnetic flux density between healthy and inter-turn conditions was about 0.145μT whereas at 20Hz and 30Hz, the same difference was about 3.13μT and 4.16μT respectively. Same observation was made previously with a greater number of shorted turns and less operating time. With respect to the maximum temperature change observed in both reduced and higher number of turns, the results were identical. As expected, due to the short circuit the maximum observed temperature changes increased as frequency increased as the motor is made to do more work. Due to the difference in the number of turns in both tests, the temperature changes were slightly different. For instance, at 15Hz a maximum temperature change of 3.953°C was observed for the test with a smaller number of turns compared to 5.5692°C for the greater number of turns. This is expected due to more I^2R losses in the latter test. When compared to the healthy machine state, identical results in both tests showed that the maximum temperature change was always less than 1.7°C across all the individual motor frequency of operation. This is still lower than the lowest temperature change observed under short circuit condition for both tests in Figure 5-19 and Figure 5-9. Another observation was that unlike in healthy state where there was no evidence of a direct relationship between temperature variation across operating frequencies; there was a clear and direct proportionality for the short circuit condition. As the motor frequency increased, the temperature also increased again due to the additional short circuit I^2R losses which increased with loading on a motor.

5.5.2 Healthy vs Broken Rotor vs Inter-turn

5.5.2.1 5Hz Frequency interval

To analyse FBG-T performance in discriminating fault and identifying fault severity level, Table 5-4 combines the results from each test condition and Figure 5-20 pictorially analyses the results in the table.

Table 5-4: Comparison of braggshifts changes with temperature and magnetic flux density at different frequencies

Frequency (Hz)	**Healthy**	**Broken rotor**	**Inter-turn**	**Healthy**	**Broken rotor**	**Inter-turn**
		Braggshifts (pm)			**ΔTemp. (°C)**	
5	70	125	165	1.6910	0.5340	3.1280
10	55	90	205	1.2730	0.4170	2.9520
15	60	90	270	1.2300	0.3400	3.9530
20	50	90	330	1.1910	0.3240	4.2340
25	55	105	385	1.3080	0.5380	4.9440
30	55	90	430	1.4910	0.5340	6.8460
			Magnetic flux density			
5	0.468905	0.2284	0.3414			
10	1.186085	0.7428	1.3313			
15	2.614542	2.1804	3.9901			
20	5.280447	4.4652	8.4094		(μT)	
25	6.922083	5.7436	10.8951			
30	7.423125	6.0265	11.5808			

The FBG-T sensor reliably and accurately detected the different faults despite the hysteresis nature of the magnetostrictive element of the sensor. The order of magnitude for each machine condition was different and consistent. Healthy machine and broken rotor conditions both have braggshifts in the tens of pm range. However, the latter has consistently higher values closer to the 100pm marks compared to the healthy which has consistently mid-hundred range. The slight but consistent increase in braggshift for broken rotor compared to healthy condition was observed across each individual motor frequency. The more severe inter-turn fault has braggshifts in a different and higher order of magnitude than both broken rotor and healthy conditions which can reliably serve as a crucial fault indicator for operations and maintenance of electric machines. With respect to the magnetic flux densities, there was a general increase in magnitude with the increase in the effective number of turns contributing to the generation of the flux inside the machine. This is in line with theory, as increase in the number of turns leads to increase in the generated magnetic flux. Thus, the broken rotor condition was observed to have the lowest magnitudes since it had the least number of turns compared to the healthy state. The inter-turn condition had more turns than the healthy state, and hence higher magnitudes of stray magnetic flux. Temperature within any machine will also increase with increase in the number of turns due to I^2R losses. As expected across the different motor frequency range, the broken rotor condition having the lowest number of turns experienced the least amount of temperature change. The BRB condition recorded a maximum of just over 0.5°C compared to healthy state with a maximum temperature change of less than 1.7°C. The short circuit condition experienced the highest temperature change of just below 7°C as expected but when compared to higher values temperature values obtained during temperature calibration of the sensor, it begs the questions: could there be a different factor responsible for such large braggshifts other than temperature?

Since the stray magnetic field and temperature are the two dominant factors that could be responsible for braggshifts in this experiment and their magnitudes have been observed; then the other factor left to be considered is the nature of the magnetic field itself i.e., its spectral content. In Chapter 3 during magnetic flux calibration, it was observed that the FBG-T response to DC magnetic field was straightforward in that, it did not exhibit any further braggshift once the field was removed, and it returned to its initial wavelength within minutes. This difference in sensor response is clearly due to the nature of the magnetic flux in this case, AC or DC. Thus, it is justifiable to consider analysing the frequency content of the AC stray flux as this is the remaining factor yet to be analysed, which can confirm the significant difference in response for inter-turn fault compared to broken rotor and healthy conditions.

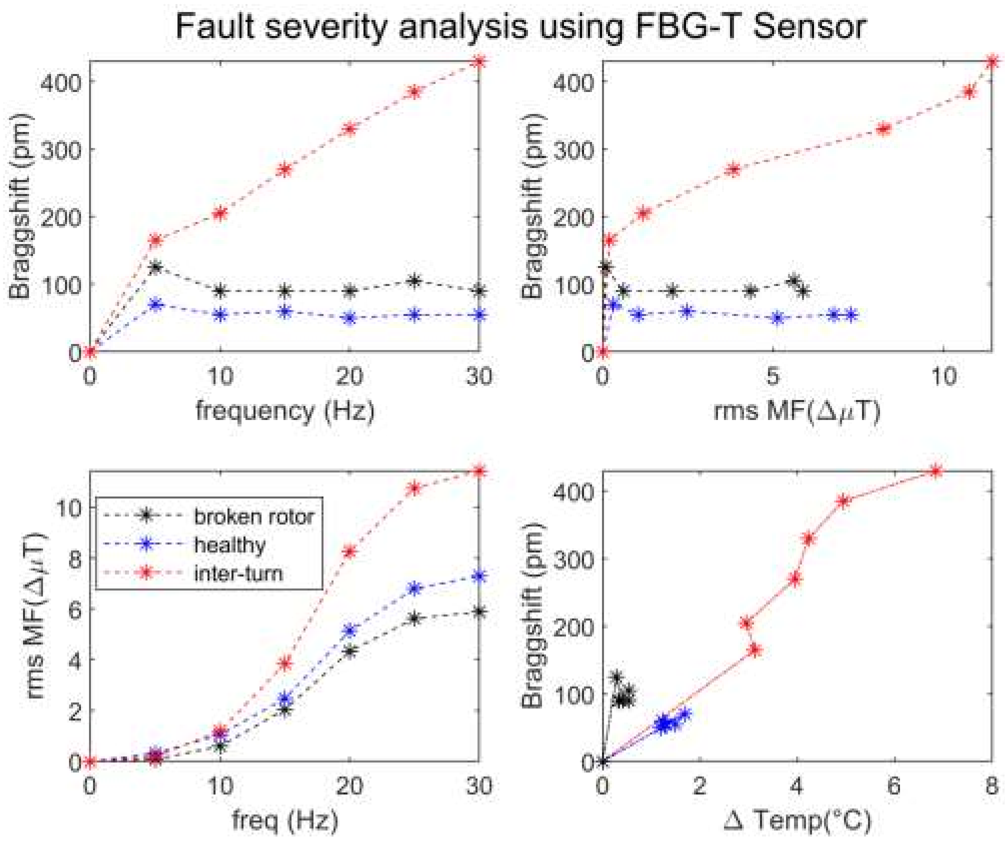

Figure 5-20: Variation of magnetic flux, frequency and maximum temperature with braggshifts for fault severity detection (5Hz interval)

Figure 5-21 shows the spectral content of the stray magnetic flux at each motor frequency under healthy, broken rotor and short circuit conditions. Data obtained from the auto data logger was again exported to MATLAB to perform FFT spectral analysis. FFT on the stray flux revealed a significant difference in spectral content but consistency in such differences as well. For instance, when the motor is run at odd frequencies (5Hz, 15Hz and 25Hz), the stray flux under broken rotor condition consistently showed significant variation in its time varying amplitude compared to variations observed when motor was run at even frequencies (10, 20 and 30Hz). This behaviour may be due to forced vibration characteristics of the motor at odd frequencies compared to even frequencies which would require vibration analysis which is beyond the scope of this work. Despite this observation, there is no evidence that this time varying amplitude characteristic influenced the FBG-T sensor capability to distinguish between the machine conditions. The harmonic spectrum of the stray magnetic flux further revealed that as the motor was run at a higher frequency, the bandwidth of its frequency spectrum increased. For each motor frequency, there appear to be a specific harmonic component that was unique compared to the other harmonic components and this unique frequency was different for each motor condition even at the same operating frequency.

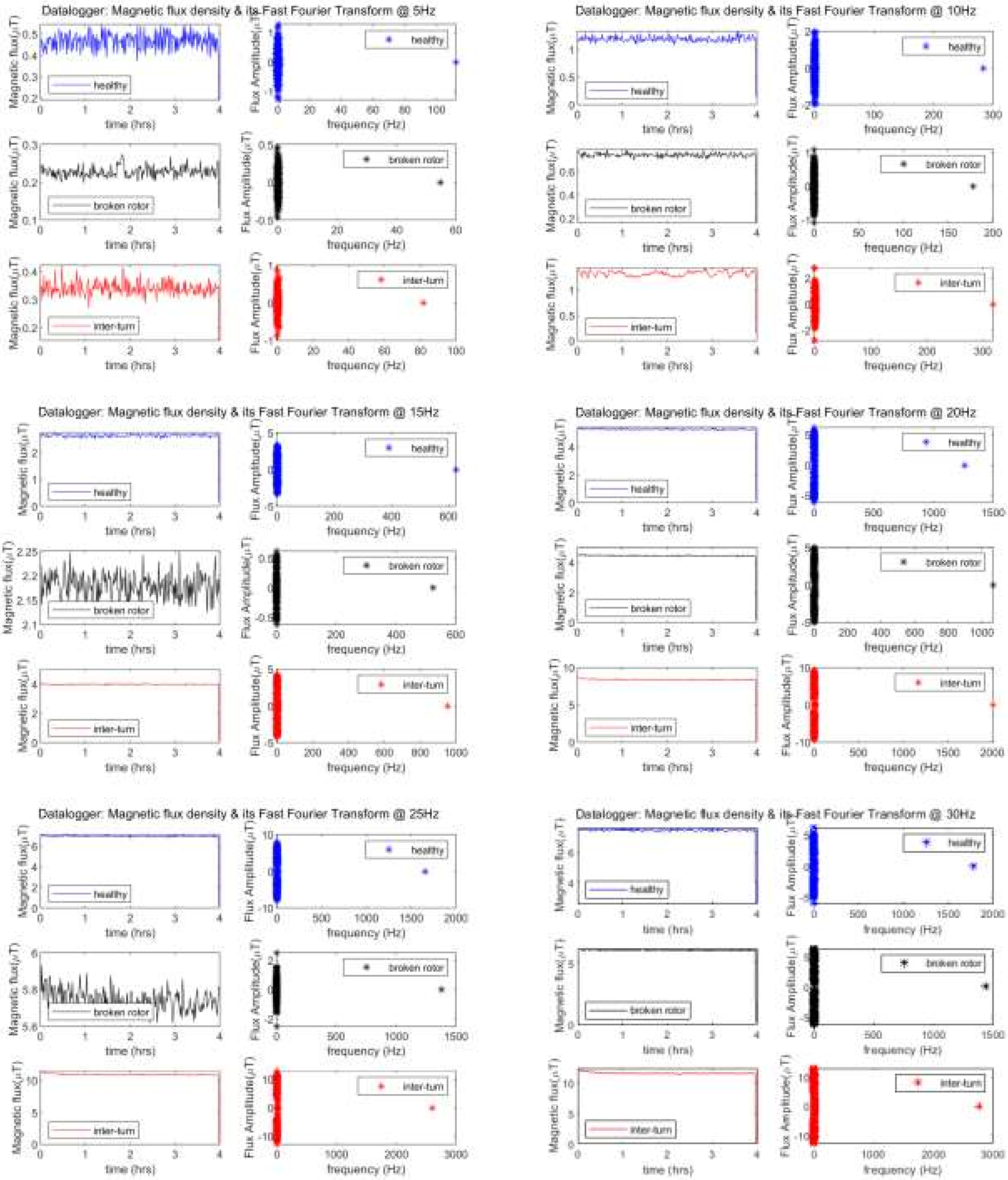

Figure 5-21: FFT Spectral analyses on the stray magnetic field under various machine conditions

For instance, at 20Hz the unique harmonic component for the healthy condition was 1.3kHz, whereas for broken rotor and inter-turn conditions, the unique harmonic components were 1.05kHz and 2kHz respectively. At 30Hz the unique harmonic component for healthy, broken rotor and inter-turn conditions were 1.8kHz, 1.45kHz and 2.7kHz. Although the unique harmonic component did vary under the different machine conditions, there was consistency in the pattern of such variations across each of the entire motor operating frequency range. It was observed that the unique harmonic components for healthy condition was always higher than the corresponding values for broken rotor condition, while the highest values of harmonic components were consistently observed to be under the ITSF condition. The only exception to this observation was at 5Hz where the unique harmonic component was highest for the healthy condition followed by the inter-turn and then the broken rotor. This is particularly significant as it helps explain the unusually high braggshift observed at 5Hz, despite the magnetic flux density amplitude and maximum temperature change remaining within the expected ranges of 0.468905μT and 0.5340°C respectively. For healthy motor condition with such values, the expected braggshift based on other observed responses should be mid-50s or lower but unusually, a 70pm braggshift was observed without any corresponding increase in the magnetic flux amplitude or temperature change. There is clear evidence that the unique harmonic component plays a role in addition to amplitude of the stray magnetic flux in explaining the magnetostrictive behaviour of the terfenol-D. This thus, explains the very large braggshifts for inter-turn fault condition in addition to the effects of higher amplitudes of magnetic flux and temperature changes.

5.5 ITSF Results Compared with other Theoretical and Analytical Derivations

Most of the machine faults that have been previously studied focussed on main air gap flux and very little research is based on the stray flux. As earlier described in Chapter 2, the magnitude of the stray flux is directly proportional to the magnitude of the main air gap flux, with an attenuation proportionality constant. Experimental results from previous works show that the addition of extra turns of windings to emulate short circuit within the stator does result in an increase in current. An increase in current clearly implies an increase in the amount of main air gap flux which is in turn proportional to the stray flux. In [230], varying amount of extra windings were added to a 4kW, three phase PMSM to create ITSFs. To explore the influence of fault intensity on the short circuit current, the PMSM was short-circuited by 1 to 5 turns, and the fault intensity σ was graded from 3.33% to 16.67% correspondingly for different fault resistances. Both simulation and calculation results obtained for the short circuit current with different fault intensities as shown in Table 5-5 and Table 5-6 where R_1turn is the resistance of one turn.

Table 5-5: Amplitude of Short Circuit Current with Different Fault Intensities, with extra turns $R_F=100R_{1TURN}$ [230]

Fault intensities (%)	Simulation result(A)	Calculation result(A)
3.33	20.52	19.68
6.66	31.3	29.61
9.99	41.67	39.29
13.33	51.55	48.62
16.65	60.82	57.5

Table 5-6: Amplitude of Short Circuit Current with Different Fault Intensities, No extra turns $R_F=R_{1TURN}$ [230]

Fault intensities (%)	Simulation result(A)	Calculation result(A)
3.33	546.8	512.5
6.66	595.4	568.6
9.99	519.6	498.9
13.33	436.6	418.3
16.65	368.2	352.3

As was reported, results here confirmed increase in current with increase in shorted turns which consequently results in increase in the magnetic flux. With no extra turns $R_F=R_{1TURN}$, there was a decrease in current for both simulation and calculation (Table 5-6). [230] did agree from experimental and analytical evidence that short circuit current, Is affects magnetic field distribution in stator and makes impacts on performance of the machine. This validates similar results obtained during the same ITSF experiments conducted during this research as shown in Table 5-1and Table 5-3 with and without the auto datalogger. The magnitude of the stray flux increased with increase in number of turns between both tests as well as with increase in frequency during each test. Heat rise due to fault winding resistances was also observed though not adequately studied in their report [230]. In a similar FEM study of inter-turn short circuits in IMs by [231], an increase in the rms value of the magnetic flux density of the machine with ITSF compared to the healthy motor was observed. The increase or variation in the magnetic flux density was attributed to increase in the machine's supply current due to increasing amplitude of the third harmonic in this case. Harmonics of hundreds of Hz were observed and conclusions were made that actual motor and simulations confirmed that harmonics affected the behaviour of the magnetic flux and current, in the presence of an inter-turn fault. This again confirms the outcomes of this research as results agree with those obtained from [231].

In a more closely related work, [232] sensed the external stray magnetic field outside the motor stator yoke under ITSF condition using proprietary TMR sensors for a surface-mounted PMSM (SPMSM). What makes this work interesting is that the motor was run at different speed (in revolution per minutes, rpm) and load conditions. Results confirmed that the higher the motor speed (rpm) the higher the rms fault current the motor produces. Motor was run at 150rpm and 300rpm with and without load and results showed that the fault currents produced by the inter-turn short circuit at 300rpm with and without load were higher than those produced by 150rpm with and without load. This is really significant because the research in this work involves running the motors at different speeds and the results obtained in [232] agree with the experimental results in this research. Increase in speed results in higher fault currents, which in turn results in higher magnitudes of both air gap flux and stray flux as shown in Table 5-1and Table 5-3.

[233] reported that there was good agreement with simulations results from their models with other studies, and when compared with experiment carried out on a specially wound 2 hp IM with taps to allow different number of turns to be shorted. Using various analytical models, results obtained summarised in Table 5-7 confirms that an increase in the number of shorted turns will cause an increase fault current. This as earlier explained, will increase the air gap flux and in turn the stray flux. This in in agreement with the experimental results obtained in this work as mentioned previously, especially when the number of turns was reduced, and the test repeated at the same frequencies. From Table 5-1and Table 5-3, with more number of shorted turns at 5Hz, 10Hz and 15Hz, the resulting stray flux were respectively 1.63129μT, 5.207296μT and 9.335977μT; compared to 0.3414μT, 1.3313μT and 3.9901μT respectively at the same frequencies with less number of shorted turns. Thus, it is evident that results obtained in this work agree with those from previous research where analytical, theoretical, and experimental derivations have been used to prove the consistent behaviour of ITSF conditions in various electrical motors.

Table 5-7: Experimental and simulation results for different numbers of shorted turns with short circuit current limited externally [233]

n	Experimental result		Simulation result	
	I_n (mA)	$I_{r,ext}$ (A)	I_n (mA)	$I_{r,ext}$ (A)
1	4	2.7	5.6	2.9
2	15	5.3	16	5.6
3	30	8.98	31.4	8.1
4	54	10	48.5	10.2

5.6 Chapter Summary

FBG-T sensing reliability and accuracy has been tested under healthy, broken rotor and short circuit machine conditions. It is evident that the FBG-T sensor can reliably and accurately monitor the condition of the machines. It unambiguously detected the short circuit fault condition with succinct braggshifts observable via the pre-analysed sensor's optical spectra as well as post-analysed plots of braggshifts variation with time, frequency, and temperature. For broken rotor conditions, braggshifts tend to be within the same order of magnitude although with higher values across most frequencies compared to values observed when machine is under healthy condition. The difference in magnitude between observed external magnetic flux density for all conditions agrees with theoretical expectations with higher flux densities under short circuit fault condition due to a greater number of turns.; Lower flux values observed for broken rotor conditions were due to reduced rotor windings relative to the values obtained when the motor is healthy. However, the magnitude of these flux densities is not enormously large to cause such significant braggshifts especially for the short circuit condition. Through FFT spectral analyses of the stray magnetic flux at each operating frequency, there was evidence that a unique harmonic component identifiable under different machine conditions, contributed to the magnetostrictive behaviour of the terfenol-D transducer responsible for the braggshifts observed. Particularly for ITSF, there were higher amplitudes of stray flux and temperature changes which were not convincingly sufficient to solely cause such large braggshifts. However, after spectral analyses of the stray flux, there is now evidence that three factors contribute to such large braggshifts viz: amplitude and harmonic spectrum of the stray flux as well as temperature. Several mathematical, theoretical and experimental derivations on ITSF from previous published research outcomes have been used to validate results obtained from this research.

Chapter 6
Conclusion

Terfenol-D is widely known to exhibit large hysteresis behaviour, but this has not prevented its use in many sensor applications. Understanding the impact of hysteresis on the FBG-T sensor due to its terfenol-D part is important for optimising sensor performance. This Chapter will discuss the impact of hysteresis on FBG-T sensor performance and briefly analyse results from RTs carried out to further understand any limitations that the FBG-T may inherently possess. The research work is then summarised with discussions regarding what could have been done and what further work can be done in future.

6.1 Hysteresis Effect on FBG-T Stray Flux Sensing

Throughout this experimental investigation, results obtained have consistently showed hysteresis and non-linearity as two characteristics of the FBG-T sensor that can affect its performance like any other conventional sensor. Within the scope of condition monitoring and fault detection, both characteristics have not affected the FBG-T accuracy and reliability in distinguishing between different kinds of faults even with repeated tests using manual and auto data logging instruments. In cases such as discriminating between fault types: broken rotor versus inter-turn faults, a complementary feature extraction is said to be optimal. This is because the optical spectra provided a vivid picture of large amounts of braggshifts with a confirmatory time varying braggshift plots of the ITSF condition. Several other plots have been used to provide and further analyse results with the FBG-T sensor performing as expected each time during the investigation except for the varying degree of hysteresis each time the sensor resets. To investigate whether the different degrees of hysteresis would change the order of magnitude of the expected braggshifts, three RTs have been performed for the condition monitoring of the healthy IM.

6.2 Reproducibility Tests (RT)

From **Error! Reference source not found.** and Figure 6-1 the FBG-T sensor shows significant levels of nonlinearity in the braggshifts observed across all three tests. The temperature changes during each test were less than 2^{o}C, thus such small variations in temperature would not have significantly contributed to the nonlinear results obtained. The negligible impact of temperature is confirmed because the tests which recorded the highest temperature change did not actually record the highest braggshift. For example, during RT1, the highest temperature change of 1.46°C was recorded at 25Hz with a maximum braggshift of 65pm; whereas the maximum braggshift of 90pm during RT1 occurred at 5Hz where the highest temperature change of 1.37°C was observed. During RT2 a similar observation was made where at 30Hz with a maximum temperature change of 1.02°C a 70pm braggshift was observed; whereas at 5Hz a higher maximum braggshift of 75pm was observed despite the highest temperature change being 0.05°C which is small. During RT3, for a maximum temperature change of 1.57°C, a maximum braggshift of 50pm was recorded at 15Hz, whereas for a temperature change of 0.32°C a maximum braggshift of 65pm was recorded. There appear to be no evident correlation of the maximum temperature changes during the test and the FBG-T braggshift response. The other reason for such nonlinearity is due to hysteresis as the FBG-T sensor did not always return fully to its initial wavelength. This suggests that the terfenol-D may not have been in the same initial magnetisation state as the previous test frequency before a new test is carried out. This means at the end of each test the magnetic dipoles may have different magnetisation status or orientation before they are exposed to a different stray flux with different characteristics due to change in frequency, and thus would not produce the same braggshifts.

Table 6-1: RT1 (-), RT2 (-) and RT3 (-) for healthy induction motor

Frequency (Hz)	5	10	15	20	25	30
Max Braggshift (pm) during 4hr ON operation	90	65	40	45	45	25
	70	60	50	35	40	45
	55	50	50	70	70	40
Max Braggshift (pm) during 20 hours OFF	90	75	55	65	65	50
	75	75	65	55	60	70
	55	55	50	85	80	65
Mean FBG-T Temp (°C)	22.41803	22.35181	22.30601	22.31958	22.24995	22.22310
	22.47015	22.35674	22.39681	22.31017	22.24732	22.27890
	22.44053	22.36041	22.29699	22.32481	22.27951	22.31825
Mean Room Temp (°C)	23.78461	23.75217	23.73075	23.73334	23.71194	22.69940
	22.52319	22.55988	22.59024	23.13965	23.23244	23.30260
	23.72038	23.66973	23.86870	23.68685	23.63166	21.99553
Max temp Change ΔT (°C)	1.36658	1.40036	1.42474	1.41376	1.46199	0.4763
	0.05304	0.20314	0.19343	0.82948	0.98512	1.0237
	1.27985	1.30932	1.57171	1.36204	1.35215	0.32272
Complete Duration	24 hours					

Figure 6-2 mostly show consistent sensor behaviour in terms of gradual increase in braggshifts up to some maximum and plateau until the stray flux is removed.

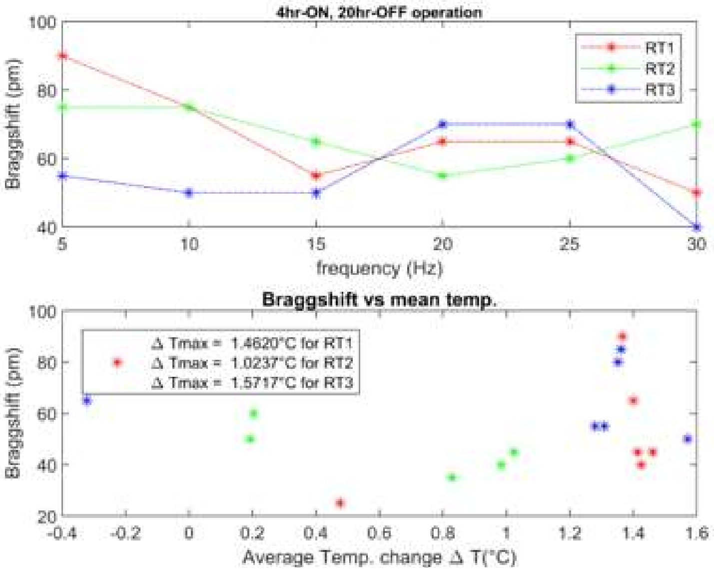

Figure 6-1: Comparison of braggshifts with frequency and maximum temperature change during FBG-T RTs

Then a small further increase in braggshift owing to residual magnetisation before the downward journey back to its original wavelength due to reversible magnetisation experienced by terfenol-D. The inability for the FBG-T response to make it to the initial wavelength has been explained earlier in previous chapters and referenced sources, as mainly due to the hysteresis behaviour of terfenol-D which is transferred to the FBG. During RT1, the FBG-T only made it to its initial wavelength and rested there at 15Hz motor frequency. During RT2, the FBG-T successfully reset to its initial wavelength at 15Hz, 20Hz and 30Hz; while during RT3 complete return to initial wavelength only occurred at 30Hz with large anomalies observed 25Hz signifying a large degree of hysteresis. As a sensor, while such characteristics is not desirable, terfenol-D continues to be used as a magnetostrictive sensor in industrial applications despite its nonlinear and large hysteresis features. This is because it is the understanding of its limitations and operating characteristics that allows its use in a reliable and accurate manner. One factor that have played a role in revealing significant levels of nonlinearity and hysteresis in certain time more than others is the time gap between tests. The sensor was used continuously for two years at different intervals – in most cases between consecutive days, whereas in other cases several days or even weeks between tests during which the pre-stress magnetisation level of the terfenol-D is different. For example, when tests were conducted after several days or weeks the FBG-T sensor was observed to react more slowly which could be due to the inertial magnetic states of the magnetic dipoles, compared to when a test is performed the next day. The optical spectra for RT1, RT2 and RT3 looked very similar to those obtained in pervious chapters and did not provide any additional information except the confirmation of the braggshifts due to the FBG-T response to the presence of stray flux.

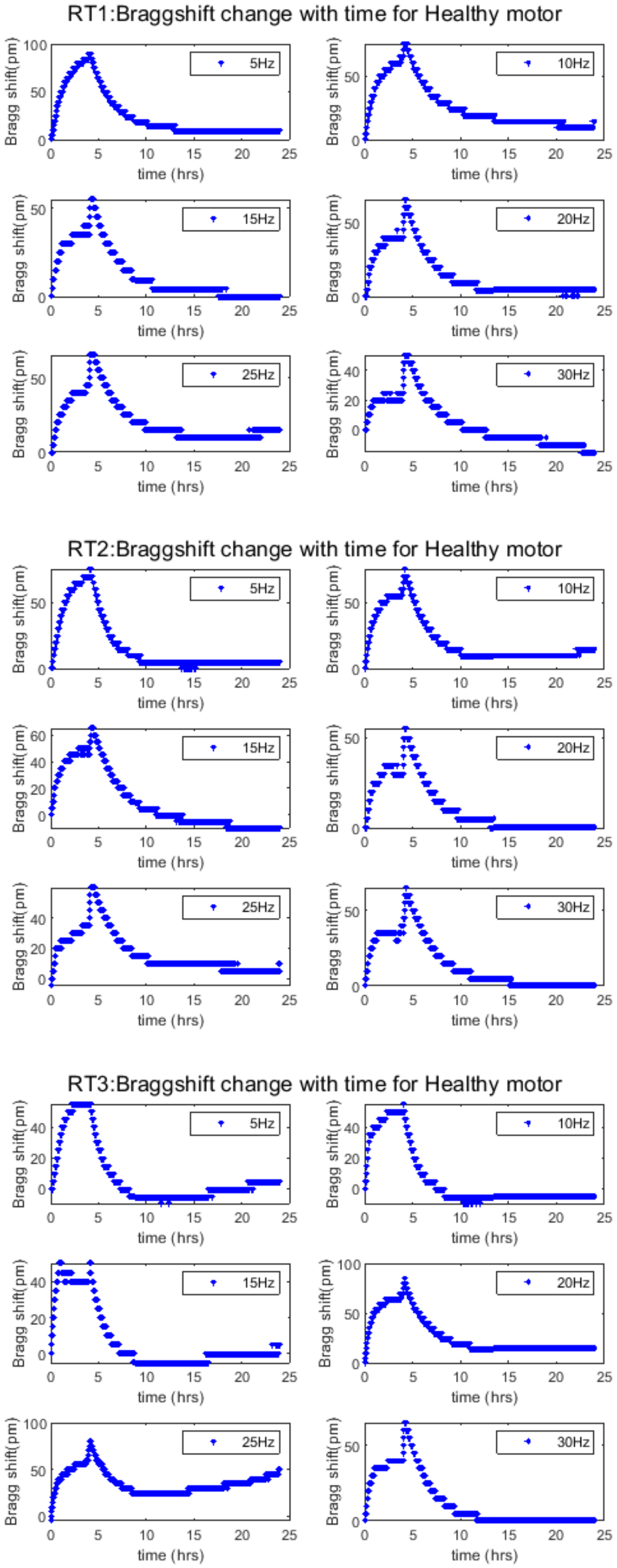

Figure 6-2: Time varying braggshifts observed during RT1, RT2 and RT3

6.3 Summary and Recommendations for future work

6.3.1 Summary

This thesis was aimed at investigating whether a composite sensor made from terfenol-D bonded to FBG could non-invasively utilise externally available stray flux (µT range) from an IM to monitor its condition and detect fault(s). An introduction of the entire work and its research significance have been provided in Chapter 1 including the aim, objectives and key achievements of this research. A detailed and critical review of common electric machines faults and existing fault detection techniques including an in-depth review of optical fibre fault detection technique have been covered in Chapter 2. Chapter 3 comprehensively described the underpinning principle of FBGs and explains the phenomenon of magnetostriction as well as the characteristics of terfenol-D. This chapter also presents the methodology of the entire research including step-by-step procedure for experimental test rig(s) set up, calibrations and optimal sensor positioning. In Chapter 4 and 5, the use of the FBG-T sensor in monitoring and detecting different machines conditions have been demonstrated. Whilst Chapter 4 analysed the BRB fault condition, Chapter 5 did analyse a more dangerous ITSF condition under safe and risk assessed laboratory environment. Each chapter in turn described how each condition was emulated and FBG-T sensor performance was comparatively analysed between and amongst all fault conditions. The effect of hysteresis on the performance of the FBG-T sensor was finally analysed via RTs detailed in Chapter 6 with recommendations for future work provided.

6.3.2 Conclusion

This research set out to achieve some six main objectives which have all been satisfactorily achieved. A thorough and comprehensive review of the different faults that commonly occur in electric machines, their causes and fault detection techniques has been undertaken. As part of this review process, it was found out that based on the current state of the art, optical sensors especially FBGs have only been applied intrusively in electric machine condition monitoring and fault detection research. This made this research even more significant as stray flux was yet to be used with FBG technology hitherto. This research has shown through several experiments, the proof-of-concept that the FBG-T sensor can capture stray flux in the µT range and respond to it reliably and accurately. A composite sensor has been successfully fabricated using a cyanoacrylate adhesive to bond a magnetostrictive transducer, terfenol-D on to an FBG on a standard optical fibre. Following the FBG-T fabrication, successful investigation into understanding how such a sensor can be best used to sense stray flux from an IM and whether the amplitude of the stray flux is strong enough has been carried out. Not only has the FBG-T sensor detected the stray flux, but it has also utilised this measurand to determine various machine conditions. During this investigative research, the optimal sensor positioning was empirically determined to be the transverse position just above the DE of the IM relative to the rotor shaft.

Non-invasive condition monitoring was achieved in this experiment-based research where the FBG-T sensor utilised stray flux to monitor and output different machine conditions with distinct spectral observations for different kinds of faults. Amongst the machine conditions tested were healthy, BRB and ITSF conditions. The sensor provided more information about each condition of the machine with the most unambiguous being the ITSF condition. When compared to the healthy condition, the FBG-T showed reliable and accurate pre-processed optical braggshift spectral response as well as post-processed time varying braggshift response. This was evident in all repeated tests with and without the auto data logger. The auto data logger was later used to acquire the stray flux signal for harmonic analysis to further understand how the sensor was able to do this. For broken rotor condition, the FBG-T sensor was again accurate and reliable in detecting this condition when compared to the healthy state. By analysing and further investigating initial results, the research revealed substantial evidence that the factors responsible for braggshifts were beyond the magnitude of the stray flux as expected based on theory. The research showed that the spectral components of the stray flux (i.e., its harmonic content) affected how the magnetic dipoles of the magnetostrictive material responded, which resulted in the micro-strains that were observed as braggshifts on the optical spectrum(s). In conclusion, the FBG-T sensor response to the stray flux produced under each machine condition depended largely on the movement of the magnetic dipoles of the terfenol-D transducer. Such movement was consistently observed to be reversible i.e., reversible magnetisation which is because of the small amplitudes of the stray flux. Although physicists have not been able to explain this movement which can be unpredictable, it was evident from experimental results that the nature of the magnetic flux causing the magnetostriction played a significant role in the motion of these dipoles. Having analysed the amplitudes of the stray flux under different test conditions, there was no doubt that the amplitude on its own was not responsible for the motion of the magnetic dipoles of the terfenol-D. This led to further investigation of the harmonic content of the stray flux which showed that each machine condition did indeed produce a stray flux of unique spectral content responsible in part for the motion of the magnetic dipoles of the terfenol-D. This translated into corresponding braggshifts that were also analysed for each test.

Finally, the research was able to show that the FBG-T sensor was able to detect two forms of the same single broken rotor fault by giving similar responses for both single holed single BRB and five-holed single BRB. The FBG-T was also able to distinguish healthy, broken rotor and short circuit conditions. It is worthy of mention that despite the large hysteresis and non-linearity that characterise terfenol-D as an alloy, these characteristics have not compromised the reliability and accuracy of the composite FBG-T sensor for this machine condition monitoring application. It is important to highlight that there was no degradation of the sensor characteristics during the entire two years of installation and testing repeatedly carried out.

6.3.3 Future work

In this work, two major fault conditions have been experimented with FBG-T. More machine fault conditions can be tested in future to analyse how the FBG-T would respond. Tests can be extended to different machine types and sizes as well such as PMSMs, various reluctance machine types, etc - to investigate whether increased or reduced amplitudes of stray flux would have significant impact on the braggshifts. These investigations will also further determine how big a role the harmonic spectral content plays in the FBG-T response when distinguishing various machine conditions. Will changing the type of FBG affect the sensor performance and how? Testing the FBG-T with other non-uniform gratings such as long period gratings with terfenol-D (LPG-T) to investigate whether different grating types would respond better to different machine conditions or even identical conditions with different severity levels. This has the potential of developing an integrated FBG-T sensor whose response takes advantage of the multiplexing capability of the optical fibre. One of the limitations of this work is the available resources to perform experiments as due to lack of a controlled temperature chamber, an improvised heat source was used which could have introduced some error in the temperature sensitivity obtained. Over the course of the experiment, results repeatedly showed that temperature changes were not large enough to cause error in the results. However, it will be useful to perform a temperature calibration using a controlled temperature chamber to further minimise any errors and compensate better in future.

Another difficulty was the unavailability of finite element models (FEM) for FBG-T sensor as there is very little work done in this area and only experimental research has been carried out even for the intrusive monitoring. Efforts were made to work with Photonics experts to develop a model but there seem to be little or no expertise in cross-modelling FBG in Photonics with terfenol-D in Material Science fields which will be very useful for future work. As part of the future work, a severity level experiment can be conducted for BRB fault, where different number of rotor bars are damaged. The same should be separately performed for ITSF using different number of turns to cause the short circuit. The FBG-T sensor response to BRB and ITSF severity levels will show its accuracy and reliability in detecting faults of the same type with different severity levels. Despite any limitations of the FBG-T sensor, its unique and succinct response to ITSF was undoubtedly evident with high repeatability index both spectrally and its time varying braggshift response.

Another future work would be to investigate the spectral content of the stray flux using higher resolution equipment with smaller sampling time (0.01 – 0.1s) as this was a limitation of the auto datalogger. The auto data logger had a minimum sampling time of 0.5 seconds and thus finer details of the harmonic spectrum of the stray flux at each frequency was not possible. With a much higher sampling time, the amplitudes of each harmonic can be more thoroughly analysed to further understand the role of the unique harmonic content in the magnetostrictive behaviour of the terfenol-D transducer. This can also help in the multi-physical modelling of the FBG-T sensor since magnetostriction continues to be a challenge for physicists to accurately model and predict, given that the phenomenon is of microscopic particle origin occurring within the magnetic domain of materials. Although optical fibre on its own is immune to EMI, its dependence on the magnetostrictive transducer in the composite FBG-T sensor makes the sensor susceptible to EMI. Thus, when using it, this should be borne in mind to minimise error. However, this is particularly to avoid inaccuracies for less severe machine conditions such as broken rotor, whereas for short circuit, the FBG-T can be relied upon to quickly detect such serious faults within the machine as this research as proved.

References

[1] C S Gallinat and D K Weyl, “Motors are everywhere and efficient – but they can be even better,” *CLEANENERGY MINISTERIAL*, 2014. [Online]. Available: http://www.cleanenergyministerial.org/Blog/motors-are-everywhere-and-efficient-but-they-can-be-even-better-414.

[2] Jim Plourde, “Monitoring induction motors for energy savings,” 2011. [Online]. Available: http://www.controleng.com/single-article/monitoring-induction-motors-for-energy-savings/5bfaa5385d8bab73100e37d54caec817.html.

[3] Schneider Electric, “Monitoring Induction Motors for Energy Savings (Part 2),” *PowerLogic Solut.*, vol. 8, no. 2, 2006.

[4] United Nations, “Climatic change affects everyone,” *Sustainable Development Goals.*, 2015. [Online]. Available: http://www.un.org/sustainabledevelopment/climatechange/.

[5] P J Zhang, Y Du, T G Habetler, and B Lu, “A Survey of Condition Monitoring and Protection Methods for Medium-Voltage Induction Motors,” *Ieee Trans. Ind. Appl.*, vol. 47, no. 1, pp. 34–46, 2011.

[6] Yuri Merizalde Luis Hernandez-Callejo and Oscar Duque-Perez, “State of the Art and Trends in the Monitoring, Detection and Diagnosis of Failures in Electric Induction Motors,” *energies 2017*, vol. 10, 2017.

[7] S Grubic, J M Aller, B Lu, and T G Habetler, “A survey of testing and monitoring methods for stator insulation systems in induction machines,” in *2008 International Conference on Condition Monitoring and Diagnosis*, 2008, pp. 196–203.

[8] “Main generator on line monitoring and diagnostics,” *EPRI*, 1996.

[9] Anees Mohammed, Borong Hu, Zedong Hu, Siniša Djurović, Li Ran, Mike Barnes, and Philip A. Mawby, “Distributed Thermal Monitoring of Wind Turbine Power Electronic Modules Using FBG Sensing Technology,” *IEEE Sens. J.*, 2020.

[10] Joao Batista Rosolem, Rivael Strobel Penze, Claudio Floridia, Fabio Renato Bassan, Rodrigo Peres, Eduardo Ferreira Da Costa, Artur De Araujo Silva, Antonio Donizete Coral, Joao Roberto Nogueira Junior, Deleon Vasconcelos, and Marcelo Agra Ramos Junior, “Dynamic Effects of Temperature on FBG Pressure Sensors Used in Combustion Engines,” *IEEE Sens. J.*, 2021.

[11] Bruno Rente, Matthias Fabian, Miodrag Vidakovic, Jerry Sunarho, Heriberto Bustamante, Tong Sun, and Kenneth T.V. Grattan, “A Fiber Bragg Grating (FBG)-Based Sensor System for Anaerobic Biodigester Humidity Monitoring,” *IEEE Sens. J.*, 2021.

[12] Bruno Rente, Matthias Fabian, Miodrag Vidakovic, Xuan Liu, Xiang Li, Kang Li, Tong Sun, and Kenneth T.V. Grattan, “Lithium-Ion Battery State-of-Charge Estimator Based on FBG-Based Strain Sensor and Employing Machine Learning,” *IEEE Sens. J.*, 2021.

[13] Jitendra Kumar, Gitender Singh, Manoj K. Saxena, Om Prakash, Sudhir K. Dixit, and Shankar V. Nakhe, “Development and Studies on FBG Temperature Sensor for Applications in Nuclear Fuel Cycle Facilities,” *IEEE Sens. J.*, 2021.

[14] Hongli Li, Gang Xu, Xin Gui, Lei Liang, and Zhengying Li, “An FBG Displacement Sensor in Deformation Monitoring of Subway Floating Slab,” *IEEE Sens. J.*, 2021.

[15] Shahriar Sefati, Rachel Hegeman, Farshid Alambeigi, Iulian Iordachita, Peter Kazanzides, Harpal Khanuja, Russell H. Taylor, and Mehran Armand, “A Surgical Robotic System for Treatment of Pelvic Osteolysis Using an FBG-Equipped Continuum Manipulator and Flexible Instruments,” *IEEE/ASME Trans. Mechatronics*, 2021.

[16] Chaoyang Shi, Zhongxin Tang, and Shuxin Wang, “Design and Experimental Validation of a Fiber Bragg Grating-Enabled Force Sensor With an Ortho-Planar Spring-Based Flexure for Surgical Needle Insertion,” *IEEE Trans. Med. Robot. Bionics*, 2021.

[17] Tianci Zhang, Baojun Chen, and Siyang Zuo, “A Novel 3-DOF Force Sensing

Microneedle with Integrated Fiber Bragg Grating for Microsurgery," *IEEE Trans. Ind. Electron.*, 2021.

[18] Ali Ebrahimi, Muller Urias, Niravkumar Patel, Russell H. Taylor, Peter L. Gehlbach, and Iulian Iordachita, "Adaptive Control Improves Sclera Force Safety in Robot-Assisted Eye Surgery: A Clinical Study," *IEEE Trans. Biomed. Eng.*, 2021.

[19] F. De Tommasi, C. Massaroni, A. Carnevale, D. Lo Presti, E. De Vita, A. Iadicicco, E. Faiella, R. F. Grasso, U. G. Longo, S. Campopiano, M. Carassiti, and E. Schena, "Fiber Bragg Grating Sensors for Temperature Monitoring During Thermal Ablation Procedure: Experimental Assessment of Artefact Caused by Respiratory Movements," *IEEE Sens. J.*, 2021.

[20] Jun Peng, Shuhai Jia, Hongqiang Yu, Xilong Kang, Shuming Yang, and Shouping Xu, "Design and Experiment of FBG Sensors for Temperature Monitoring on External Electrode of Lithium-Ion Batteries," *IEEE Sens. J.*, 2021.

[21] Hongbo Zou, and Mi Lu, "Developing High-Frequency Fiber Bragg Grating Acceleration Sensors to Monitor Transmission Line Galloping," *IEEE Access*, 2021.

[22] Mudabbir Badar, Ping Lu, Qirui Wang, Thomas Boyer, Kevin P. Chen, and Paul R. Ohodnicki, "Real-Time Optical Fiber-Based Distributed Temperature Monitoring of Insulation Oil-Immersed Commercial Distribution Power Transformer," *IEEE Sens. J.*, 2021.

[23] Sanjib Sarkar, Devasena Inupakutika, Mandrita Banerjee, Mehdi Tarhani, and Mehdi Shadaram, "Machine Learning Methods for Discriminating Strain and Temperature Effects on FBG-based Sensors," *IEEE Photonics Technol. Lett.*, 2021.

[24] Manasa Perikala, V. V.Lakshmi Pathi, Lekshmi S. Rajan, and Praveen Chandra Pandey, "Cantilever Supported Fiber Bragg Grating Flow Sensor for Space Applications," *IEEE Sens. J.*, 2021.

[25] Ya Li Wang, Yun Tu, and Shan Tung Tu, "Development of Highly-Sensitive and Reliable Fiber Bragg Grating Temperature Sensors with Gradient Metallic Coatings for Cryogenic Temperature Applications," *IEEE Sens. J.*, 2021.

[26] Anees Mohammed, and Siniša Durović, "Design, instrumentation and usage protocols for distributed in situ thermal hot spots monitoring in electric coils using FBG sensor multiplexing," *J. Vis. Exp.*, 2020.

[27] A. Mohammed, S. Djurovic, A. C. Smith, and K. Tshiloz, "FBG sensing for hot spot thermal monitoring in electric machinery random wound components," *Proc. - 2016 22nd Int. Conf. Electr. Mach. ICEM 2016*, pp. 2266–2272, 2016.

[28] Anees Mohammed, Juan I. Melecio, and Šinisa Djurović, "Open-Circuit Fault Detection in Stranded PMSM Windings Using Embedded FBG Thermal Sensors," *IEEE Sens. J.*, 2019.

[29] Anees Mohammad, and Sinisa Djurovic, "Evaluation of fiber-optic sensing performance for embedded thermal monitoring of electric machinery wound components," in *2016 5th Mediterranean Conference on Embedded Computing (MECO)*, 2016, pp. 72–76.

[30] A Mohammed, and S Djurović, "Rotor Condition Monitoring Using Fibre Optic Sensing Technology," *Iet*, no. January, pp. 1–6, 2020.

[31] Anees Mohammed, and Sinisa Djurovic, "Electric Machine Bearing Health Monitoring and Ball Fault Detection by Simultaneous Thermo-Mechanical Fibre Optic Sensing," *IEEE Trans. Energy Convers.*, 2021.

[32] Jonathan Hunte, Anees Mohammed, and Sinisa Djurovic, "Response Time Characterisation of a Fibre Bragg Grating Humidity Sensor for Power Conversion Device Applications," in *2020 9th Mediterranean Conference on Embedded Computing, MECO 2020*, 2020.

[33] A Mohammed, N Sarma, and S Djurovic, "Fibre Optic Monitoring of Induction Machine Frame Strain as a Diagnostic Tool," *Ieee Iemdc*, no. May, p. 7, 2017.

[34] Juan I. Melecio, Anees Mohammed, and Sinisa Djurovic, "Characterisation of FBG

based Magnetic Field Sensor Response Sensitivity to Excitation Orientation for Rotating Electric Machine Applications," in *2019 8th Mediterranean Conference on Embedded Computing, MECO 2019 - Proceedings*, 2019.

[35] D.S. Vilchis-Rodriguez, S. Djurovic, P. Kung, M. I. Comanici, and A. C. Smith, "Investigation of induction generator wide band vibration monitoring using fibre Bragg grating accelerometers," in *2014 International Conference on Electrical Machines (ICEM)*, 2014, pp. 1772–1778.

[36] Anees Mohammed, Juan I. Melecio, and Sinisa Djurovic, "Stator winding fault thermal signature monitoring and analysis by in Situ FBG sensors," *IEEE Trans. Ind. Electron.*, 2019.

[37] Anees Mohammed, Juan I. Melecio, and Sinisa Durovic, "Electrical Machine Permanent Magnets Health Monitoring and Diagnosis Using an Air-Gap Magnetic Sensor," *IEEE Sens. J.*, 2020.

[38] Anees Mohammed, and Sinisa Djurovic, "FBG Thermal Sensing Features for Hot Spot Monitoring in Random Wound Electric Machine Coils," *IEEE Sens. J.*, vol. 17, no. 10, pp. 3058–3067, 2017.

[39] G. Hulme, S. Djurovic, A.C. Smith, and D.S. Vilchis-Rodriguez, "Detectability of Cage Rotor Induction Machine Stator Fault Using Current Analysis," in *7th IET International Conference on Power Electronics, Machines and Drives (PEMD 2014)*, 2014, pp. 2.11.02-2.11.02.

[40] Yingzhao Wang, Anees Mohammed, Nur Sarma, and Sinisa Djurovic, "Double Fed Induction Generator Shaft Misalignment Monitoring by FBG Frame Strain Sensing," *IEEE Sens. J.*, 2020.

[41] C J Crabtree S. Djurovic P.J. Tavner and A.C. Smith, "Condition monitoring of wind turbine induction generators with rotor electrical asymmetry," *IET Renew. Power Gener.*, vol. 6, no. 4, pp. 207–216, 2012.

[42] Anees Mohammed, and Sinisa Djurovic, "Stator Winding Internal Thermal Stress Monitoring and Analysis Using in-situ FBG Sensing Technology," *IEEE Trans. Energy Convers.*, pp. 1–1, 2018.

[43] Anees Mohammed, and Sinisa Djurovic, "In-situ thermal and mechanical fibre optic sensing for in-service electric machinery bearing condition monitoring," in *2019 IEEE International Electric Machines and Drives Conference, IEMDC 2019*, 2019.

[44] A. Mohammed, and S. Djurovic, "Multiplexing FBG Thermal Sensing for Uniform/Uneven Thermal Variation Monitoring in In-service Electric Machines," in *Proceedings of the 2019 IEEE 12th International Symposium on Diagnostics for Electrical Machines, Power Electronics and Drives, SDEMPED 2019*, 2019.

[45] Uilian J. Dreyer, Erlon V. da Silva, André Biffe Di Renzo, Cicero Martelli, and Jean Carlos Cardozo da Silva, "Quasi-distributed fiber Bragg grating temperature sensors for stator bars monitoring of large electric generators," p. 991607, 2016.

[46] Uilian Jose Dreyer, Felipe Mezzadri, Guilherme Dutra, Thiago da Silva, Carlos Alberto Bavastri, Erlon Vagner da Silva, Cicero Martelli, and Jean Carlos Cardozo da Silva, "Quasi-Distributed Optical Fiber Transducer for Simultaneous Temperature and Vibration Sensing in High-Power Generators," *IEEE Sens. J.*, vol. 18, no. 4, pp. 1547–1554, Feb. 2018.

[47] Geraldo Bieler, and Marcelo M. Werneck, "A magnetostrictive-fiber Bragg grating sensor for induction motor health monitoring," *Meas. J. Int. Meas. Confed.*, 2018.

[48] S Chen, D Vilchis-Rodriguez, S Djurović, M Barnes, P Mckeever, and C Jia, "Direct on Chip Thermal Measurement in IGBT Modules Using FBG Technology—Sensing Head Interfacing," *IEEE Sens. J.*, vol. 22, no. 2, pp. 1309–1320, 2022.

[49] Anees Mohammed, and Siniša Djurović, "A study of distributed embedded thermal monitoring in electric coils based on FBG sensor multiplexing," *Microprocess. Microsyst.*, vol. 62, pp. 102–109, 2018.

[50] Anees Mohammed, and Sini\vsa Djurović, "Feasibility study of embedded FBG thermal sensing use for monitoring electrical fault-induced thermal excitation in random wound coils," *J. Eng.*, 2019.

[51] A A Suryandi, I E Damian, and S Djurović, "FBG Magnetostrictive Composite Flux Sensor Response Characterisation for Surface Permanent Magnet Rotor Flux Monitoring," in *2021 10th Mediterranean Conference on Embedded Computing (MECO)*, 2021, pp. 1–6.

[52] H Ren, L Ran, X Liu, L Liu, S Djurović, H Jiang, M Barnes, and P Mawby, "Quasi-distributed Temperature Detection of Press Pack IGBT Power Module Using FBG Sensing," *IEEE J. Emerg. Sel. Top. Power Electron.*, p. 1, 2021.

[53] A Mohammed, and S Djurović, "FBG array sensor use for distributed internal thermal monitoring in low voltage random wound coils," in *2017 6th Mediterranean Conference on Embedded Computing (MECO)*, 2017, pp. 1–4.

[54] A Mohammed, and S Djurović, "FBG Thermal Sensing Ring Scheme for Stator Winding Condition Monitoring in PMSMs," *IEEE Trans. Transp. Electrif.*, vol. 5, no. 4, pp. 1370–1382, 2019.

[55] Zafar J Khan Gulamfaruk N. Surya Makarand S. Ballal and Hiralal M. Suryawanshi, "A Simplified Frequency-Domain Detection of Stator Turn Fault in Squirrel-Cage Induction Motors Using an Observer Coil Technique," *IEEE Trans. Ind. Electron.*, vol. 64, no. 2, pp. 1495–1506, 2017.

[56] Institute of Electrical and Electronics Engineers (IEEE), "IEEE Guide for Induction Machinery Maintenance Testing and Failure Analysis. IEEE Standards." .

[57] P O'Donnel, "Report of large motor reliability survey of industrial and commercial installations, Part I," *IEEE Trans. Ind. Appl.*, vol. 1A-21, pp. 853–864, 1985.

[58] A Bellini Filippetti, F, Tassoni, C, Capolino, G, "Advances in diagnostic techniques for induction machines," *IEEE Ind. Electron.*, vol. 55, pp. 4109–4126, 2008.

[59] A Garcia-Perez Romero-Troncoso, R, Cabal-Yepez, E, Osornio-Rios, R, "The application of high-resolution spectral analysis for identifying multiple combined faults in induction motors.," *IEEE Trans. Ind. Electron.*, vol. 58, pp. 2002–2010, 2011.

[60] F Bianchini Monteiro, P, Pederiva, R, Diniz, V., "An empirical demodulation for electrical fault detection in induction motors," *IEEE Trans. Instrum. Meas.*, vol. 65, pp. 559–569, 2016.

[61] A Bonnett, "Root cause AC motor failure analysis with a focus on shaft failures," *IEEE Trans. Ind. Appl.*, vol. 36, pp. 1435–1448, 2000.

[62] A Costa, "Investigación de Nuevas Técnicas de Mantenimiento de Parques Eólicos. Ph.D. Thesis," Coruña University, Coruña, Spain, 2012.

[63] M Haji Toliyat, H, "Pattern recognition—A technique for induction machines rotor broken bar detection," *IEEE Trans. Energy Cpnversions*, vol. 16, pp. 312–317, 2001.

[64] A Soualhi Medjaher, K, Zerhouni, N, "Bearing health monitoring based on Hilbert—Huang transform, support vector machine, and regression," *IEEE Trans. Instrum. Meas.*, vol. 64, pp. 52–62, 2015.

[65] Enrique C Quispe and Rosaura C Mendoza Alvaro J. Bazurto, "Causes and Failures Classification of Industrial Electric Motor," *ANDESCON, 2016 IEEE*. IEEE, 2016.

[66] S Nandi Toliyat, H.A, Li, X., "Condition monitoring and fault diagnosis of electrical motors - A review," *IEEE Trans. Energy Cpnversions*, vol. 20, no. 4, pp. 719–729, 2005.

[67] Bindu S and Vinod V Thomas, "Diagnoses of Internal Faults of Three Phase Squirrel Cage Induction Motor - A Review," *IEEE*, 2014.

[68] S Pradhan P.S. Bhowmik and M. Prakash, "Fault Diagnostic and Monitoring Methods of Induction Motor : A Review," *Int. J. Appl. Control. Electr. Electron. Eng.*, vol. 1, no. 1, pp. 1–18, 2013.

[69] A H Bonnett and C Yung, "Increased efficiency versus increased reliability," *IEEE Ind.*

Appl. Mag., vol. 14, no. 1, pp. 29–36, 2008.

[70] A Lebaroud and G Clerc, “Classification of induction machine faults by optimal time-frequency representations,” *IEEE Trans. Ind. Electron.*, vol. 55, no. 12, pp. 4290–4298, 2008.

[71] Baskar Venkata Ramana and S, “Diverse Fault Detection Techniques of Three- phase Induction Motor- A Review,” *2016 International Conference on Emerging Technological Trends [ICETT]*. IEEE, Kollam, India, 2016.

[72] A A Jimoh and Y Hamam O. Imoru, “Origin and Manifestation of Electrical Machine Faults–A review,” *The 2nd IEEE Conference on Power Engineering and Renewable Energy (ICPERE)*. Bali-Indonesia, 2014.

[73] Xiaodong Shi and Mahesh Krishnamurthy Yao Da, “Health Monitoring, Fault Diagnosis and Failure Prognosis Techniques for Brushless Permanent Magnet Machines,” *Vehicle Power and Propulsion Conference (VPPC), 2011 IEEE*. IEEE, Chicago, IL, USA, 2011.

[74] Sang Bin Lee Rangarajan M. Tallam Greg C. Stone, Gerald B. Kliman, Jiyoon Yoo, Thomas G. Habetler and Ronald G. Harley, “A Survey of Methods for Detection of Stator-Related Faults in Induction Machines,” *Ieee Trans. Ind. Appl.*, vol. 43, no. 4, pp. 920–933, 2007.

[75] Nathaniel Taylor, “Dielectric response and partial discharge measurements on stator insulation at varied low frequency,” KTH Royal Institute of Technology, Stockholm, Sweden, 2010.

[76] K H Kim, “Simple online fault detecting scheme for short-circuited turn in a PMSM through current harmonic monitoring,” *IEEE Trans. Ind. Electron.*, vol. 58, no. 6, pp. 2565–2568, 2011.

[77] H Nejadi-Koti J. Faiz and Z. Valipour, “Comprehensive review on inter-turn fault indexes in permanent magnet motors,” *Iet Electr. Power Appl.*, vol. 11, no. 1, pp. 142–156, 2017.

[78] Wenping Cao Zheng Liu Po-Hsu Huang, Gui Yun Tian and James L. Kirtley, “Non-Invasive Winding Fault Detection for Induction Machines Based on Stray Flux Magnetic Sensors,” in *Power and Energy Society General Meeting (PESGM), 2016*, 2016.

[79] Aller Grubic. S. J.M., Lu, B., Habetler, T.G., “A survey on testing and monitoring methods for stator insulation systems of low-voltage induction machines focusing on turn insulation problems,” *IEEE Trans. Ind. Electron.*, vol. 55, no. 12, pp. 4127–4135, 2008.

[80] M Moallem M. Eftekhari S. Sadri, and A. Shojaei, “Review of Induction Motor Testing and Monitoring Methods for Inter-turn Stator Winding Faults ,” *2013 21st Iranian Conference on Electrical Engineering (ICEE)*. IEEE, Mashhad, Iran, 2013.

[81] M Moallem M. Eftekhari S. Sadri, and M. Hsieh, “Online Detection of Induction Motor’s Stator Winding Short-Circuit Faults,” *Ieee Syst. J.*, vol. 8, no. 4, pp. 1272–1281, 2014.

[82] Mahmoud Zaggout, Li Ran, Peter Tavner, and Christopher Crabtree, “Detection of rotor electrical asymmetry in wind turbine doubly-fed induction generators,” *IET Renew. Power Gener.*, vol. 8, no. 8, pp. 878–886, 2014.

[83] Galina Mirzaeva, Khalid Imtiaz Saad, and Mohsen Ghaffarpour Jahromi, “Comprehensive Diagnostics of Induction Motor Faults Based on Measurement of Space and Time Dependencies of Air Gap Flux,” *IEEE Trans. Ind. Appl.*, vol. 53, no. 3, pp. 2657–2666, May 2017.

[84] Rudra Narayan Dash, Sangeeta Sahu, Chinmoy Ku. Panigrahi, and Bidyadhar Subudhi, “Condition monitoring of induction motors: — A review,” in *2016 International Conference on Signal Processing, Communication, Power and Embedded System (SCOPES)*, 2016, pp. 2006–2011.

[85] Taner Goktas, Muslum Arkan, M. Salih Mamis, and Bilal Akin, “Broken rotor bar fault monitoring based on fluxgate sensor measurement of leakage flux,” in *2017 IEEE*

International Electric Machines and Drives Conference (IEMDC)*, 2017, pp. 1–6.

[86] Konstantinos Gyftakis, Jose Antonino-Daviu, Raul Garcia-Hernandez, Malcolm McCulloch, David Howey, and Antonio Cardoso, “Comparative Experimental Investigation of the Broken Bar Fault Detectability in Induction Motors,” *IEEE Trans. Ind. Appl.*, pp. 1–1, 2015.

[87] William T Thomson, and Ronald J Gilmore, “Motor Current Signature Analysis to Detect Faults in Induction Motor Drives - Fundamentals, Data Interpretation and Industrial Case Histories,” in *Proceedings of the 32nd Turbomachinery Symposium*, 2003, pp. 145–156.

[88] Attiq Ur Rehman, Yu Chen, Lulu Wang, Yihan Zhao, Yonghong Yin, Yonghong Cheng, and Toshikatsu Tanaka, “Experimental research and analysis on rotor winding inter-turn short circuit fault in DFIG,” in *2016 International Conference on Condition Monitoring and Diagnosis (CMD)*, 2016, pp. 164–167.

[89] Ilias Ouachtouk, Soumia El Hani, Said Guedira, Khalid Dahi, and Hamza Mediouni, “Broken rotor bar fault detection based on stator current envelopes analysis in squirrel cage induction machine,” in *2017 IEEE International Electric Machines and Drives Conference (IEMDC)*, 2017, pp. 1–6.

[90] Hongzhong Ma, Yuanyuan Ding, P. Ju, and Limin Zhang, “The application of ANN in fault diagnosis for generator rotor winding turn-to-turn faults,” in *2008 IEEE Power and Energy Society General Meeting - Conversion and Delivery of Electrical Energy in the 21st Century*, 2008, pp. 1–4.

[91] Yao Duan, “A review of condition monitoring and fault diagnosis for permanent magnet machines,” in *2012 IEEE Power and Energy Society General Meeting*, 2012, pp. 1–4.

[92] Gilsu Choi, Yichao Zhang, and T. M. Jahns, “Experimental Verification of Rotor Demagnetization in a Fractional-Slot Concentrated-Winding PM Synchronous Machine Under Drive Fault Conditions,” *IEEE Trans. Ind. Appl.*, vol. 53, no. 4, pp. 3467–3475, Jul. 2017.

[93] K Alewine, and W Chen, “A review of electrical winding failures in wind turbine generators,” *IEEE Electr. Insul. Mag.*, vol. 28, no. 4, pp. 8–13, 2012.

[94] Jawad Faiz and Seyed Mohammad Mahdi Moosavi, “Detection of mixed eccentricity fault in doubly-fed induction generator based on reactive power spectrum,” *Iet Electr. Power Appl.*, vol. 11, no. 6, pp. 1076–1084, 2017.

[95] IEEE Committee Report, and IEEE, “Report of large motor reliability survey of industrial and commercial installations, Part I and Part II,” IEEE, 1985.

[96] B.M.Ebrahimi J. Faiz and M.B.B.Sharifian, “Different faults and their diagnosis techniques in three-phase squirrel-cage induction motors-A Review,” *J. Electromagn.*, vol. 26, pp. 543–569, 2006.

[97] A A S A I Kazzaz G. K. Singh, “Induction machine drive conditon mointoring and diagnosis research - survey,” *Electr. Power Syst. Res.*, vol. 64, pp. 145–158, 2003.

[98] V.Thorsen and M.Dalva, “Failure identification and analysis for highvoltage induction motors in the petrochemical industry,” *Ieee Trans. Ind. Appl.*, vol. 35, no. 4, pp. 810–818, 1999.

[99] Jawad Faiz and S M M Moosavi, “Eccentricity fault detection – From induction machines to DFIG—A review,” *Renew. Sustain. Energy Rev.*, vol. 55, pp. 169–179, 2016.

[100] Xiaohua Bao Yang Zhou Chong Di, and Lang Wang, “Analysis of Dynamic Unbalanced Magnetic Pull in Induction Motor With Dynamic Eccentricity During Starting Period,” *IEEE Trans. Magn.*, vol. 52, no. 7, 2016.

[101] Garcia-EscuderoLA Morinigo-SoteloD Duque-PerezO,Perez-Alonso M., “Practical aspects of mixed-eccentricity detection in PWM voltage-source-inverter-fed induction motors,” *IEEE Trans. Ind. Electron.*, vol. 57, pp. 252–262, 2010.

[102] Ilamparithi T C Nandi S Sang Bin L.,Doosoo H., “Detection of eccentricity faults in induction machines based on name plate parameters ,” *IEEE Trans. Ind. Electron.*, vol.

58, pp. 1673–1683, 2011.

[103] E Irgat, A Ünsal, and H T Canseven, “Detection of Eccentricity Faults of Induction Motors Based on Decision Trees,” in *2021 13th International Conference on Electrical and Electronics Engineering (ELECO)*, 2021, pp. 435–439.

[104] Israel Zamudio-Ramirez, Roque A.Alfredo Osornio-Rios, Jose Alfonso Antonino-Daviu, Hubert Razik, and Rene de Jesus Romero-Troncoso, “Magnetic Flux Analysis for the Condition Monitoring of Electric Machines: A Review,” *IEEE Trans. Ind. Informatics*, 2021.

[105] Bashir Mahdi Ebrahimi, Mehrsan Javan Roshtkhari, Jawad Faiz, and Seyed Vahid Khatami, “Advanced eccentricity fault recognition in permanent magnet synchronous motors using stator current signature analysis,” *IEEE Trans. Ind. Electron.*, vol. 61, no. 4, pp. 2041–2052, 2014.

[106] Martin Blödt, Jérémi Regnier, and Jean Faucher, “Distinguishing load torque oscillations and eccentricity faults in induction motors using stator current wigner distributions,” *IEEE Trans. Ind. Appl.*, vol. 45, no. 6, pp. 1991–2000, 2009.

[107] D Shah, S Nandi, and P Neti, “Stator-Interturn-Fault Detection of Doubly Fed Induction Generators Using Rotor-Current and Search-Coil-Voltage Signature Analysis,” *Ieee Trans. Ind. Appl.*, vol. 45, no. 5, pp. 1831–1842, 2009.

[108] V. Fernao Pires, Daniel Foito, J. F. Martins, and A. J. Pires, “Detection of stator winding fault in induction motors using a motor square current signature analysis (MSCSA),” *Int. Conf. Power Eng. Energy Electr. Drives*, vol. 2015-Septe, no. 1, pp. 507–512, 2015.

[109] Reemon Z Haddad, Cristian A Lopez, Joan Pons-llinares, Jose Antonino-daviu, Elias G Strangas, and Universidad Politecnica De Valencia, “Outer Race Bearing Fault Detection in Induction Machines Using Stator Current Signals,” pp. 801–808, 2015.

[110] Julien Maitre, Sebastien Gaboury, Bruno Bouchard, and Abdenour Bouzouane, “A New Computational Approach for Inter-Turn Short Circuit Recognition in Induction Machines Using currents analysis and Multi-Class Support Vector Machine,” pp. 1–6.

[111] Wajdi Saadaoui, and Kahled Jelassi, “Induction motor bearing damage detection using stator current analysis,” *2011 Int. Conf. Power Eng. Energy Electr. Drives*, no. May, pp. 1–6, 2011.

[112] Antonio Garcia Espinosa, Javier A. Rosero, Jordi Cusidó, Luis Romeral, and Juan Antonio Ortega, “Fault detection by means of Hilbert-Huang transform of the stator current in a PMSM with demagnetization,” *IEEE Trans. Energy Convers.*, vol. 25, no. 2, pp. 312–318, 2010.

[113] S. J. Oviedo, J. E. Quiroga, and C. Borras, “Experimental evaluation of motor current signature and vibration analysis for rotor broken bars detection in an induction motor,” in *International Conference on Power Engineering, Energy and Electrical Drives*, 2011.

[114] Tristan Plante, Lucas Stanley, Ashkan Nejadpak, and Cai Xia Yang, “Rotating machine fault detection using principal component analysis of vibration signal,” 2016.

[115] Aurelien Prudhom, Jose Antonino-Daviu, Hubert Razik, and Vicente Climente-Alarcon, “Time-frequency vibration analysis for the detection of motor damages caused by bearing currents,” *Mech. Syst. Signal Process.*, vol. 84, pp. 747–762, 2017.

[116] Iman Sadeghi, Hossein Ehya, Jawad Faiz, and Hossein Ostovar, “Online fault diagnosis of large electrical machines using vibration signal-a review,” in *2017 International Conference on Optimization of Electrical and Electronic Equipment (OPTIM) & 2017 Intl Aegean Conference on Electrical Machines and Power Electronics (ACEMP)*, 2017, pp. 470–475.

[117] J Seshadrinath, B Singh, and B K Panigrahi, “Vibration analysis based interturn fault diagnosis in induction machines,” *IEEE Trans. Ind. Informatics*, vol. 10, no. 1, pp. 340–350, 2014.

[118] Carlos Collantes Rivero, “Air Gap Monitoring in Motors and Generators,” *Power-MI Blog*, 2020. [Online]. Available: https://power-mi.com/content/air-gap-monitoring-

motors-and-generators. [Accessed: 29-Jul-2021].

[119] M Sasic, G C Stone, J Stein, and C Stinson, "Detecting Turn Shorts in Rotor Windings: A New Test Using Magnetic Flux Monitoring," *IEEE Ind. Appl. Mag.*, vol. 19, no. 2, pp. 63–69, 2013.

[120] R. Romary, R. Pusca, J. P. Lecointe, and J. F. Brudny, "Electrical machines fault diagnosis by stray flux analysis," in *2013 IEEE Workshop on Electrical Machines Design, Control and Diagnosis (WEMDCD)*, 2013, pp. 247–256.

[121] Zheng Liu, "Stray Flux Based Health Monitoring of Electrical Machines," Newcastle University, 2018.

[122] Gérard-André Capolino, Raphael Romary, Humberto Henao, and Rémus Pusca, "State of the Art on Stray Flux Analysis in Faulted Electrical Machines," *2019 IEEE Work. Electr. Mach. Des. Control Diagnosis*, vol. 1, pp. 181–187, 2019.

[123] Ciprian Harlisca, Lorand Szabo, Lucia Frosini, and Andrea Albini, "Bearing faults detection in induction machines based on statistical processing of the stray fluxes measurements," in *2013 9th IEEE International Symposium on Diagnostics for Electric Machines, Power Electronics and Drives (SDEMPED)*, 2013, pp. 371–376.

[124] Ciprian Harlisca, Lorand Szabo, Lucia Frosini, and Andrea Albini, "Diagnosis of rolling bearings faults in electric machines through stray magnetic flux monitoring," in *2013 8TH INTERNATIONAL SYMPOSIUM ON ADVANCED TOPICS IN ELECTRICAL ENGINEERING (ATEE)*, 2013, pp. 1–6.

[125] Lucia Frosini, Ciprian Harlisca, and Lorand Szabo, "Induction Machine Bearing Fault Detection by Means of Statistical Processing of the Stray Flux Measurement," *IEEE Trans. Ind. Electron.*, vol. 62, no. 3, pp. 1846–1854, Mar. 2015.

[126] O. Imoru, L. Mokate, A. A. Jimoh, and Y. Hamam, "Diagnosis of rotor inter-turn fault of electrical machine at speed using stray flux test method," in *AFRICON 2015*, 2015, pp. 1–5.

[127] O. Imoru *et al.*, "Diagnosis of rotor inter-turn fault of electrical machine at speed using stray flux test method," *2013 - 8th Int. Symp. Adv. Top. Electr. Eng. ATEE 2013*, vol. 62, no. 3, pp. 484–489, 2013.

[128] M. R. Barzegaran, A. Mazloomzadeh, and O. A. Mohammed, "Identification of short-circuit location in induction motors using radiated electromagnetic field signatures," in *2013 International Conference on Electrical Machines and Systems (ICEMS)*, 2013, pp. 484–489.

[129] O. Vitek, M. Janda, V. Hajek, and P. Bauer, "Detection of eccentricity and bearings fault using stray flux monitoring," in *8th IEEE Symposium on Diagnostics for Electrical Machines, Power Electronics & Drives*, 2011, pp. 456–461.

[130] A Ceban, R Pusca, and R Romary, "Study of Rotor Faults in Induction Motors Using External Magnetic Field Analysis," *IEEE Trans. Ind. Electron.*, vol. 59, no. 5, pp. 2082–2093, 2012.

[131] Pavel Ripka, and Michal Janošek, "Advances in magnetic field sensors," in *IEEE Sensors Journal*, 2010.

[132] Oliver Tonks, and Qing Wang, "The detection of wind turbine shaft misalignment using temperature monitoring," *CIRP J. Manuf. Sci. Technol.*, vol. 17, pp. 71–79, 2017.

[133] M J Picazo-Ródenas, J Antonino-Daviu, V Climente-Alarcon, R Royo-Pastor, and A Mota-Villar, "Combination of Noninvasive Approaches for General Assessment of Induction Motors," *Ieee Trans. Ind. Appl.*, vol. 51, no. 3, pp. 2172–2180, 2015.

[134] "Use of the infrared data for heating curve computation in induction motors: Application to fault diagnosis," *Eng. Fail. Anal.*, vol. 35, pp. 178–192, Dec. 2013.

[135] Wenxian Yang, P. J. Tavner, and Michael Wilkinson, "Wind turbine condition monitoring and fault diagnosis using both mechanical and electrical signatures," in *2008 IEEE/ASME International Conference on Advanced Intelligent Mechatronics*, 2008, pp. 1296–1301.

[136] P Guo, D Infield, and X Yang, "Wind Turbine Generator Condition-Monitoring Using Temperature Trend Analysis," *Sustain. Energy, IEEE Trans.*, vol. 3, no. 1, pp. 124–133, 2012.

[137] Sudhanshu Goel, Aparna Akula, Ripul Ghosh, and Balwinder Singh Surjan, "Condition monitoring of transformer using oil and winding temperature analysis," *2016 IEEE Uttar Pradesh Sect. Int. Conf. Electr. Comput. Electron. Eng. UPCON 2016*, pp. 496–500, 2017.

[138] M. J. Picazo-Rodenas, Jose Antonino Daviu, Pau Redon, Hubert Razik, and David Lopez-Perez, "Use of isothermal representation for infrared-based fault detection in induction motors," in *2017 IEEE 11th International Symposium on Diagnostics for Electrical Machines, Power Electronics and Drives (SDEMPED)*, 2017, pp. 591–599.

[139] David Lopez-Perez, and Jose Antonino-Daviu, "Application of Infrared Thermography to Failure Detection in Industrial Induction Motors: Case Stories," *IEEE Trans. Ind. Appl.*, vol. 53, no. 3, pp. 1901–1908, 2017.

[140] O Munoz-Ornelas, D A Elvira-Ortiz, R A Osornio-Rios, R J Romero-Troncoso, and L A Morales-Hernandez, "Methodology for thermal analysis of induction motors with infrared thermography considering camera location," in *IECON 2016 - 42nd Annual Conference of the IEEE Industrial Electronics Society*, 2016, pp. 7113–7118.

[141] Gurmeet T Singh Ch Anil Kumar VNA Naikan, "Fault diagnosis of Induction motor cooling system using infrared thermography," pp. 11–14, 2016.

[142] Qasim Khan, Asfar A. Khan, and Furkan Ahmad, "Condition monitoring tool for electrical equipment — Thermography," *2016 Int. Conf. Electr. Electron. Optim. Tech.*, pp. 2802–2806, 2016.

[143] By Yu-wei Alan Wang, Terence Hazel, and Ronny Hjørnevik, "Equipment Monitoring Using Thermography Cameras," pp. 2–11, 2017.

[144] Yu-wei Alan Wang, Terence Hazel, and Ronny Hjørnevik, "EQUIPMENT MONITORING FOR TEMPERATURE RELATED FAILURES," pp. 1–9.

[145] D.K. Chaturvedi, M.S. Iqbal, and M. Pratap, "Intelligent health monitoring system for three phase induction motor using infrared thermal image," *Int. Conf. Energy Econ. Environ. - 1st IEEE Uttar Pradesh Sect. Conf. UPCON-ICEEE 2015*, pp. 0–5, 2015.

[146] Y W A Wang, T Hazel, R Hjornevik, and O Fjeld, "Equipment Monitoring Using Thermography Cameras: Remote Detection of Temperature-Related Failures," *IEEE Ind. Appl. Mag.*, vol. PP, no. 99, pp. XX3–XX3, 2017.

[147] ABB, "FOCS applications and benefits," 2014. [Online]. Available: http://new.abb.com/power-electronics/focs/applications-and-benefits. [Accessed: 23-Nov-2017].

[148] Marcelo M., Regina C. S. B. Allil, Bessie A., and Fbio V. B. de Nazar, "A Guide to Fiber Bragg Grating Sensors," in *Current Trends in Short- and Long-period Fiber Gratings*, InTech, 2013.

[149] "ABB Fiber-Optic Current Sensor - FOCS for high DC currents - Power electronics," 2014. [Online]. Available: http://new.abb.com/power-electronics/focs. [Accessed: 23-Nov-2017].

[150] J.M. Corres, J. Bravo, F.J. Arregui, and I.R. Matias, "Unbalance and harmonics detection in induction motors using an optical fiber sensor," *IEEE Sens. J.*, vol. 6, no. 3, pp. 605–612, Jun. 2006.

[151] Matias I.R Corres, Jesus M. Bravo, J., Arregui, F.J., "Vibration monitoring in electrical engines using an in-line fiber etalon," *Sensors Actuators A Phys.*, vol. 132, no. 2, pp. 506–515, Nov. 2006.

[152] Michael Khmelnitsky, Shlomi Konforti, Jacob Bortman, Moshe Tur, Iddo Kressel, and Renata Klein, "Bearing health monitoring using optical fiber sensors," in *Advances in Technology to Support End User Mission - Proceedings of the 2016 Joint Conference/Symposium of the Society for Machinery Failure Prevention Technology*

and the International Society of Automation, 2016.

[153] Kevin Jones, Chris Staveley, and Jean-Francois Vialla, “Condition monitoring of a subsea pump using fibre optic sensing,” p. 91579Q, 2014.

[154] K De Morais Sousa, A A Hafner, H José Kalinowski, and J C C Da Silva, “Determination of temperature dynamics and mechanical and stator losses relationships in a three-phase induction motor using fiber bragg grating sensors,” *IEEE Sens. J.*, vol. 12, no. 10, pp. 3054–3061, 2012.

[155] Kleiton Morais Sousa, Igor Brutkowski Vieira da Costa, Ednilson Soares Maciel, Joaquim Eloir Rocha, Cicero Martelli, and Jean Carlos Cardozo da Silva, “Broken Bar Fault Detection in Induction Motor by Using Optical Fiber Strain Sensors,” *IEEE Sens. J.*, vol. 17, no. 12, pp. 3669–3676, Jun. 2017.

[156] Juan David Lopez, Alex Dante, Alcides O. Cremonezi, Rodrigo M. Bacurau, Cesar C. Carvalho, Regina Celia Da Silva Barros Allil, Elnatan C. Ferreira, and Marcelo Martins Werneck, “Fiber-Optic Current Sensor Based on FBG and Terfenol-D with Magnetic Flux Concentration for Enhanced Sensitivity and Linearity,” *IEEE Sens. J.*, 2020.

[157] M. Fabian, J. Borg Bartolo, Martin Ams, C. Gerada, T. Sun, and K. T. V. Grattan, “Vibration measurement of electrical machines using integrated fibre Bragg gratings,” *SPIE Int. Conf. Opt. Fibre Sensors*, vol. 90, no. 3, p. 963417, 2015.

[158] Cicero Martelli, Erlon Vagner Silva, Kleiton De Morais Sousa, Felipe Mezzadri, Jonas Somenzi, Marcos Crespin, and Hypolito José Kalinowski, “Temperature sensing in a 175MW power generator,” *OFS2012 22nd Int. Conf. Opt. Fiber Sensors*, vol. 8421, pp. 84212F-84212F–4, 2012.

[159] Kleiton de Morais Sousa, Angelo Alfredo Hafner, Marcos Crespim, Jonas Somenzi, Valmir de Oliveira, Hypolito Jose Kalinowski, and Jean Carlos Cardozo da Silva, “Fiber Bragg grating sensing applications in temperature monitoring of three-phase induction motors,” *2011 SBMO/IEEE MTT-S Int. Microw. Optoelectron. Conf. (IMOC 2011)*, vol. 600, pp. 862–866, 2011.

[160] T. Sun, M. Fabian, Y. Chen, M. Vidakovic, S. Javdani, K. T. V. Grattan, J. Carlton, C. Gerada, and L. Brun, “Optical fibre sensing : a solution for industry,” *Proc. SPIE*, vol. 10323, no. 103231H, pp. 1–4, 2017.

[161] M. Sasic, H. Jiang, and G. C. Stone, “Requirements for fiber optic sensors for stator endwinding vibration monitoring,” *Proc. 2012 IEEE Int. Conf. Cond. Monit. Diagnosis, C. 2012*, no. September, pp. 118–121, 2012.

[162] N.M. Theune, M. Muller, H. Hertsch, J. Kaiser, M. Willsch, P. Krammer, and T. Bosselmann, “Investigation of stator coil and lead temperatures on high voltage inside large power generators via use of fiber Bragg gratings,” *Proc. IEEE Sensors*, vol. 2, pp. 1603–1607, 2002.

[163] Ping Lu, Kevin Byerly, Michael Buric, Paul Zandhuis, Chenhu Sun, A. Leary, R. Beddingfield, M. E. McHenry, and Paul R. Ohodnicki, “Distributed fiber-optic sensor for real-time monitoring of energized transformer cores,” 2017, vol. 10194, p. 101941S.

[164] Jincy Johny, Jade Summers, Kaushalkumar Bhavsar, Ginson P Joseph, Wai Keung Fung, and Radhakrishna Prabhu, “Theoretical investigation of positional influence of FBG sensors for structural health monitoring of offshore structures,” in *OCEANS 2017 - Aberdeen*, 2017, pp. 1–5.

[165] Fabrizio Marignetti, Enzo de Santis, Saverio Avino, Gianni Tomassi, Antonio Giorgini, Pietro Malara, Paolo De Natale, and Gianluca Gagliardi, “Fiber Bragg Grating Sensor for Electric Field Measurement in the End Windings of High-Voltage Electric Machines,” *IEEE Trans. Ind. Electron.*, vol. 63, no. 5, pp. 2796–2802, May 2016.

[166] Joao Paulo Bazzo, Felipe Mezzadri, Erlon Vagner Da Silva, Daniel Rodrigues Pipa, Cicero Martelli, and Jean Carlos Cardozo Da Silva, “Thermal Imaging of Hydroelectric Generator Stator Using a DTS System,” *IEEE Sens. J.*, vol. 15, no. 11, pp. 6689–6696, 2015.

[167] Jesus M. Corres, Javier Bravo, Francisco J. Arregui, and Ignacio R. Matias, “Unbalance and harmonics detection in induction motors using an optical fiber sensor,” *IEEE Sens. J.*, vol. 6, no. 3, pp. 605–612, 2006.

[168] Shlomi Konforty, Michael Khmelnitsky, Iddo Kressel, Renata Klein, Moshe Tur, and Jacob Bortman, “Bearing health monitoring using optical fiber sensors,” in *4TH EUROPEAN CONFERENCE OF THE PROGNOSTICS AND HEALTH MANAGEMENT SOCIETY*, 2016, pp. 1–7.

[169] Kleiton Morais Sousa, Uilian Jose Dreyer, Cicero Martelli, and Jean Carlos Cardozo Da Silva, “Dynamic Eccentricity Induced in Induction Motor Detected by Optical Fiber Bragg Grating Strain Sensors,” *IEEE Sens. J.*, vol. 16, no. 12, pp. 4786–4792, 2016.

[170] Ying Xie, Chenglin Gu, and Wenping Cao, “Study of broken bars in three-phase squirrel-cage induction motors at standstill,” *Int. Trans. Electr. Energy Syst.*, vol. 23, no. 7, pp. 1124–1138, Oct. 2013.

[171] M Fabian, D Hind, C Gerada, T Sun, and K T V Grattan, “Multi-parameter monitoring of electrical machines using integrated fibre Bragg gratings,” *2017 25th Opt. Fiber Sensors Conf.*, vol. 44, no. 0, pp. 1–4, 2017.

[172] David Hind, Chris Gerada, Michael Galea, James Borg Bartolo, Matthias Fabian, Tong Sun, and Kenneth T. V. Grattan, “Use of optical fibres for multi-parameter monitoring in electrical AC machines,” in *2017 IEEE 11th International Symposium on Diagnostics for Electrical Machines, Power Electronics and Drives (SDEMPED)*, 2017, pp. 208–212.

[173] Li Wei, Zude Zhou, Yuegang Tan, Lei Yuan, and Tingting Hu, “Fiber bragg grating based rotating speed measurement system,” in *2011 International Conference on Electric Information and Control Engineering*, 2011, pp. 1387–1390.

[174] C. Hudon, M. Levesque, M. Essalihi, and C. Millet, “Investigation of rotor hotspot temperature using Fiber Bragg Gratings,” in *2017 IEEE Electrical Insulation Conference (EIC)*, 2017, pp. 313–316.

[175] Peng Wang, Jie Liu, Fangchao Song, and Hong Zhao, “Quasi-distributed temperature measurement for stator bars in large generator via use of Fiber Bragg Gratings,” *Proc. 6th Int. Forum Strateg. Technol. IFOST 2011*, vol. 2, pp. 810–813, 2011.

[176] Anees Mohammed, Juan I. Melecio, and Sinisa Djurovic, “Open-Circuit Fault Detection in Stranded PMSM Windings Using Embedded FBG Thermal Sensors,” *IEEE Sens. J.*, vol. 19, no. 9, pp. 3358–3367, May 2019.

[177] Jesse De Pelegrin, Uilian Jose Dreyer, Cicero Martelli, and Jean Carlos Cardozo Da Silva, “Optical Fiber Sensor Encapsulated in Carbon Fiber Reinforced Polymer for Fault Detection in Rotating Electrical Machines,” *IEEE Sens. J.*, 2020.

[178] Matthew Schwartz, “Refraction and Reflection,” *Lecture note*. [Online]. Available: https://scholar.harvard.edu/files/schwartz/files/lecture15-refraction.pdf. [Accessed: 10-Oct-2021].

[179] Klaus Bohnert, and Richard Thomas, “3 Light measures current.”

[180] ABB, “Fiber-Optic Current Sensor: Make light work of DC current measurement,” 2011.

[181] National Instruments, “Fundamentals of Fiber Bragg Grating (FBG) Optical Sensing - National Instruments,” 2016. [Online]. Available: http://www.ni.com/white-paper/11821/en/. [Accessed: 27-Nov-2017].

[182] Raman. Kashyap, *Fiber Bragg gratings*. Academic Press, 2010.

[183] Carlos A. J. Gouveia, Jose M., and Pedro A.S., “Refractometric Optical Fiber Platforms for Label Free Sensing,” in *Current Developments in Optical Fiber Technology*, InTech, 2013.

[184] Stephen W. James, and Ralph P. Tatam, “Optical fibre long-period grating sensors: Characteristics and application,” *Meas. Sci. Technol.*, vol. 14, no. 5, 2003.

[185] Jacques Albert, Sandrine Lepinay, Christophe Caucheteur, and Maria C. DeRosa, “High resolution grating-assisted surface plasmon resonance fiber optic aptasensor,”

Methods, vol. 63, no. 3, pp. 239–254, Oct. 2013.

[186] Amnon Yariv, and Harry V Winsor, “Proposal for detection of magnetic fields through magnetostrictive perturbation of optical fibers,” *Opt. Lett.*, vol. 5, no. 3, pp. 87–89, Mar. 1980.

[187] Aaron Mueller, Suha Mubarak Lasassmeh, and Chiu Tai Law, “Novel Chirped Fiber Optic Current Sensor,” in *Frontiers in Optics 2012/Laser Science XXVIII*, 2012, p. FM3H.4.

[188] Juan D. Lopez, Alex Dante, Rodrigo M. Bacurau, Alcides O. Cremonezi, Roberto W. Mok, Cesar C. Carvalho, Regina C.S.B. Allil, Elnatan Chagas Ferreira, and Marcelo M. Werneck, “Fiber-Optic Current Sensor Based on FBG and Optimized Magnetostrictive Composite,” *IEEE Photonics Technol. Lett.*, 2019.

[189] Huafu Pei, Junhao Jing, and Siqi Zhang, “Experimental study on a new FBG-based and Terfenol-D inclinometer for slope displacement monitoring,” *Meas. J. Int. Meas. Confed.*, 2020.

[190] Yunqi Liu, Kin Seng Chiang, and Pak Lim Chu, “Multiplexing of temperature-compensated FBG magnetostrictive sensors with a self-seeded laser diode,” in *Optical Fiber Communication Conference*, 2004, p. FC4.

[191] Ricardo M Silva, G Chesini, C J Gouveia, A B Lobo Ribeiro, O Frazão, C M B Cordeiro, and P A S Jorge, “Magnetic field sensor with Terfenol-D thin-film coated FBG,” in *Proc.SPIE*, 2012, vol. 8421.

[192] Earl Callen, “Magnetostriction,” *J. Appl. Phys.*, 1968.

[193] A. H. Reid *et al.*, “Beyond a phenomenological description of magnetostriction,” *Nat. Commun.*, 2018.

[194] Jing Hua Liu, Cheng Bao Jiang, and Hui Bin Xu, “Giant magnetostrictive materials,” *Science China Technological Sciences*. 2012.

[195] Yanning Zhang, and Ruqian Wu, “Mechanism of large magnetostriction of galfenol,” in *IEEE Transactions on Magnetics*, 2011.

[196] WU Yi-jie, “Giant Magnetostrictive Materials and its Application Research State,” *Institute of Manufacture Engineering, Zhejiang University*, 2012. [Online]. Available: https://en.cnki.com.cn/Article_en/CJFDTotal-JDGC200404017.htm.

[197] tdvib, “Terfenol-D,” *Magnetostriction*, 2012. .

[198] “Magnetostriction and the phenomena of the curie point,” *Proc. R. Soc. London. Ser. A, Contain. Pap. a Math. Phys. Character*, 1929.

[199] S. Pascarelli, M. P. Ruffoni, A. Trapananti, O. Mathon, C. Detlefs, M. Pasquale, A. Magni, C. P. Sasso, F. Celegato, E. Olivetti, Y. Joly, and D. Givord, “4f charge-density deformation and magnetostrictive bond strain observed in amorphous TbFe2 by x-ray absorption spectroscopy,” *Phys. Rev. B - Condens. Matter Mater. Phys.*, 2010.

[200] Marcelo J. Dapino, “Magnetostrictive Materials,” in *Encyclopedia of Smart Materials*, John Wiley & Sons, Inc., 2002, pp. 600–620.

[201] Arthur E. Clark, Joseph P. Teter, and Marilyn Wun-Fogle, “Characterization of Terfenol-D for magnetostrictive transducers,” *J. Acoust. Soc. Am.*, 1991.

[202] Mark B. Moffett, Arthur E. Clark, Marilyn Wun-Fogle, Jan F. Lindberg, Joseph P. Teter, and Elizabeth A. McLaughlin, “Characterization of Terfenol-D for magnetostrictive transducers,” *J. Acoust. Soc. Am.*, 1990.

[203] “IEEE Standard on Magnetostrictive Materials: Piezomagnetic Nomenclature,” *IEEE Trans. Sonics Ultrason.*, 1973.

[204] DON A. BERLINCOURT, DANIEL R. CURRAN, and HANS JAFFE, “Piezoelectric and Piezomagnetic Materials and Their Function in Transducers,” in *Physical Acoustics*, 1964.

[205] Evangelos Hristoforou, and Aphrodite Ktena, “Magnetostriction and magnetostrictive materials for sensing applications,” *J. Magn. Magn. Mater.*, 2007.

[206] P. T. Squire, “Magnetomechanical measurements of magnetically soft amorphous materials,” *Meas. Sci. Technol.*, 1994.

[207] E. W. Lee, “Magnetostriction and magnetomechanical effects,” *Reports on Progress in Physics*. 1955.

[208] Naoya Saito, and Shigeki Nakagawa, “Stress-assisted reversal of perpendicular magnetization of thin films with giant magnetostriction constant,” in *IEEE Transactions on Magnetics*, 2008.

[209] Kleiton De Morais Sousa, Ricardo Zandonay, Erlon Vagner Da Silva, Cicero Martelli, and Jean Carlos Cardozo Da Silva, “Application of fiber bragg grating to determine the terfenol-D magnetostriction characteristics for sensor development,” *J. Microwaves, Optoelectron. Electromagn. Appl.*, 2014.

[210] Kleiton de Morais Sousa, Ricardo Zandonay, Erlon Vagner da Silva, Cicero Martelli, and Jean Carlos Cardozo da Silva, “Determination of Terfenol-D magnetostriction characteristics for sensor application using fiber Bragg grating,” in *Second International Conference on Applications of Optics and Photonics*, 2014.

[211] G.N. Smith, T. Allsop, K. Kalli, C. Koutsides, R. Neal, K. Sugden, P. Culverhouse, and I. Bennion, “Characterisation and performance of a Terfenol-D coated femtosecond laser inscribed optical fibre Bragg sensor with a laser ablated microslot for the detection of static magnetic fields,” *Opt. Express*, 2011.

[212] S M J R Fatemi, H Henao, and G A Capolino, “Gearbox monitoring by using the stray flux in an induction machine based electromechanical system,” in *MELECON 2008 - The 14th IEEE Mediterranean Electrotechnical Conference*, 2008, pp. 484–489.

[213] Zheng Liu; Guiyun Tian; Wenping Cao; Xuewu Dai; Brian Shaw; Robert Lambert, “Non-invasive load monitoring of indcution motor drives using magnetic flux sensors,” *IET Power Electron.*, vol. 10, no. 2, pp. 189–195, 2017.

[214] Zheng Liu, “Stray Magnetic Field Based Health Monitoring of Electrical Machines,” *Doctoral Thesis*, 2018. [Online]. Available: https://theses.ncl.ac.uk/jspui/bitstream/10443/4105/1/Lui%2C Z%2C 2018.pdf. [Accessed: 17-Nov-2021].

[215] Vicente Biot-Monterde, Ángela Navarro-Navarro, Jose A. Antonino-Daviu, and Hubert Razik, “Stray flux analysis for the detection and severity categorization of rotor failures in induction machines driven by soft-starters,” *Energies*, vol. 14, no. 18, 2021.

[216] Jinjiang Wang, Robert X. Gao, and Ruqiang Yan, “Broken-rotor-bar diagnosis for induction motors,” *J. Phys. Conf. Ser.*, vol. 305, no. 1, 2011.

[217] Zuolu Wang, Jie Yang, Haiyang Li, Dong Zhen, Yuandong Xu, and Fengshou Gu, “Fault identification of broken rotor bars in induction motors using an improved cyclic modulation spectral analysis,” *Energies*, vol. 12, no. 17, 2019.

[218] Vanesa Fernandez-Cavero, Luis A. García-Escudero, Joan Pons-Llinares, Miguel A. Fernández-Temprano, Oscar Duque-Perez, and Daniel Morinigo-Sotelo, “Diagnosis of broken rotor bars during the startup of inverter-fed induction motors using the dragon transform and functional anova,” *Appl. Sci.*, vol. 11, no. 9, 2021.

[219] H Arabacı, and O Bilgin, “Diagnosis of broken rotor bar faults by using frequency spectrum of stator current envelope,” in *2012 XXth International Conference on Electrical Machines*, 2012, pp. 1643–1646.

[220] Yaskawa, “Variable Frequency Drive Control Methods,” 2014. [Online]. Available: https://www.yaskawa.com/delegate/getAttachment?documentId=WP.AFD.13&cmd=documents&documentName=WP.AFD.13.pdf. [Accessed: 22-Apr-2022].

[221] Elena G. Turitsyna, Adenowo Gbadebo, and John A. R. Williams, “A technique for mitigating the effect of the writing-beam profile on fibre Bragg grating fabrication,” *Opt. Express*, vol. 23, no. 10, pp. 12628–12635, 2015.

[222] Belema P. Alalibo, Wen Ping Cao, Adenowo Gbadebo, Lassi Aarniovuori, and Kewei Cai, “Investigation of the effect of bonding points on metal surface-mounted FBG

sensors for electric machines," *Prog. Electromagn. Res. C*, 2019.

[223] Van Than Dung, and Tegoeh Tjahjowidodo, "A direct method to solve optimal knots of Bspline curves: An application for non-uniform B-spline curves fitting," *PLoS One*, 2017.

[224] Adenowo A. Gbadebo, Elena G. Turitsyna, and John A. R. Williams, "Fabrication of precise aperiodic multichannel fibre Bragg grating filters for spectral line suppression in hydrogenated standard telecommunications fibre," *Opt. Express*, vol. 26, no. 2, p. 1315, 2018.

[225] Elena G. Turitsyna, Adenowo Gbadebo, and John A. R. Williams, "A technique for mitigating the effect of the writing-beam profile on fibre Bragg grating fabrication," *Opt. Express*, vol. 23, no. 10, p. 12628, 2015.

[226] Khadim Moin Siddiqui, "Modelling and Detection of Rotor Broken Bar Fault using Induction Motor Fed PWM Inverter," vol. 8491, pp. 353–358, 2012.

[227] Given S. Magagula, Agha F. Nnachi, and Aloys O. Akumu, "Broken Rotor Bar Fault Simulation and Analysis in D-q Reference Frame," *2020 IEEE PES/IAS PowerAfrica, PowerAfrica 2020*, pp. 6–9, 2020.

[228] Ciobanu Anca, and Helerea Elena, "Analysis of magnetic field distribution in induction motors with broken rotor bars," *2013 4th Int. Symp. Electr. Electron. Eng. ISEEE 2013 - Proc.*, pp. 1–6, 2013.

[229] Sinisa Mohammed, Anees, Djurovic, "Rotor Condition Monitoring Using Fibre Sensing Technology," in *PEMD 2020 10th International Conference on Power Electronics, Machines and Drives - 01–03, December 2020, East Midlands Conference Centre, Nottingham, UK*, 2021, p. Accepted for publication.

[230] Jing Zhao, Chenghai Li, and Quansong Mou, "Calculation of Inter-Turn Short Circuit Current of a Permanent Magnet Synchronous Machine," in *2019 22nd International Conference on Electrical Machines and Systems, ICEMS 2019*, 2019.

[231] C Rojas, M G Melero, M F Cabanas, J M Cano, G A Orcajo, and F Pedrayes, "Finite element model for the study of inter-turn short circuits in induction motors," in *2007 IEEE International Symposium on Diagnostics for Electric Machines, Power Electronics and Drives, SDEMPED*, 2007.

[232] Xuyang Liu, Wenchao Miao, Qi Xu, Libing Cao, Chunhua Liu, and Philip W T Pong, "Inter-Turn Short-Circuit Fault Detection Approach for Permanent Magnet Synchronous Machines Through Stray Magnetic Field Sensing," *IEEE Sens. J.*, vol. 19, no. 18, 2019.

[233] M Arkan, D Kostic-Perovic, and P J Unsworth, "Modelling and simulation of induction motors with inter-turn faults for diagnostics," *Electr. Power Syst. Res.*, vol. 75, no. 1, 2005.

Appendix A

List of Publications

1. **Belema P Alalibo,** Bing Ji, and Wenping Cao, “Short Circuit and Broken Rotor Faults Severity Discrimination in Induction Machines Using Non-invasive Optical Fiber Technology,” *Energies*, vol. 15, no. 2, 2022.
2. Cao, W., **Alalibo, B. P.**, Ji, B., Chen, X., & Hu, C. (2022). Optical FBG-T Based Fault Detection Technique for EV Induction Machines. Journal of Physics: Conference Series, 2195(1), [012045]. https://doi.org/10.1088/1742-6596/2195/1/012045
3. **Belema P. Alalibo**, Wen-ping Cao, Bing Ji, A. Gbadebo, N. Sahoo, K. Zhou (2021). Investigation of the Use of FBG-T Fibre Sensor for Detecting Broken Bar Fault in Induction Machine. *International Joint Conference on Energy, Electrical and Power Engineering*, Huangshan City, China, 5 – 7 Nov 2021.
4. **Belema P. Alalibo**, Wen-ping Cao, Bing Ji, A. Gbadebo, and K. Zhou (2021). FBG-T Sensor for Non-intrusive Broken Rotor Fault Severity Detection in Induction Machines. *International Joint Conference on Energy, Electrical and Power Engineering*, Huangshan City, China, 5 – 7 Nov 2021.
5. **B. P. Alalibo**, W. P. Cao, A. Gbadebo, L. Aarniovuori, and K. Cai, “Investigation of the effect of bonding points on metal surface-mounted FBG sensors for electric machines,” *Progress in Electromagnetics Research*, vol. 97, pp. 255–265, Aug. 2019.
6. **Belema P. Alalibo**, Wenping Cao and Zheng Liu (2019) Bi-Signature optical spectroscopy for online fault detection in electrical machines. *The Journal of Engineering*, 2019 (17), pp.3634-3638.
7. Bukhari, Abid Ali Shah, **Alalibo, Belema Prince**, Cao, Wenping, Lin, Zhengyu, Shaikh, Shahid Hussain, Soomro, Toufique Ahmed, Ansari, Shahzeb and Jandan, Fayyaz Ali (2019). Switched reluctance motor design for electric vehicles based on harmonics and back EMF analysis. *The Journal of Engineering*, 2019 (17), pp. 4220-4225.
8. Cai, K.; **Alalibo, B.P**.; Cao, W.; Liu, Z.; Wang, Z.; Li, G. Hybrid Approach for Detecting and Classifying Power Quality Disturbances Based on the Variational Mode Decomposition and Deep Stochastic Configuration Network. *Energies* 2018, 11, 3040.
9. L. Aarniovuori, H. Kärkkäinen, M. Niemelä, J. Pyrhonen, **B. Alalibo** and W. Cao, "Modelling a Vector Controlled Induction Motor in Simulink," *2018 X International Conference on Electrical Power Drive Systems (ICEPDS)*, Novocherkassk, 2018, pp. 1-8.

10. **Belema P. Alalibo**, Wen-ping Cao, Zheng Liu, Nan Yang (2017). Finite Element and Spectral Analyses of Induction Machine Faults using Comsol with Matlab. *Engineering Science and Technology International Research Journal*, vol.1,pg. 1-10.

STEP 2021

December 4, 2021 Online Conference

Certificate of Participation

BEST PAPER AWARD

IS PRESENTED TO

Wenping Cao, Belema P. Alalibo, Bing Ji,

Xiangping Chen and Cungang Hu

FOR THE PAPER

Optical FBG-T Based Fault Detection Technique for EV

Induction Machines

2021 International Conference on Smart Transportation, Energy and

Power (STEP 2021)

AEIC Academic Exchange Information Center

December 4, 2021